Trinity College Dublin
Coláiste na Tríonóide, Baile Átha Cliath
The University of Dublin

Non-equilibrium transport properties of quasiperiodic models

Cecilia Chiaracane

School of Physics

A thesis submitted in partial fulfilment of the requirements towards the degree of Doctor of Philosophy in Physics

Hilary Term 2023

Declaration

I declare that this thesis has not been submitted as an exercise for a degree at this or any other university and it is entirely my own work.

I agree to deposit this thesis in the University's open access institutional repository or allow the library to do so on my behalf, subject to Irish Copyright Legislation and Trinity College Library conditions of use and acknowledgement.

Signed: _____ Date: _____

Non-equilibrium transport properties of quasiperiodic models

Cecilia Chiaracane

Hilary Term 2023

Abstract

The advances in the manipulation of ultracold atoms trapped by optical lattices has established this set-up as a promising analogue simulator of quantum Hamiltonians. The extended coherence times allow for the monitoring of relaxation processes from non-equilibrium initial configurations, driven exclusively by intrinsic mechanisms. Furthermore, two-terminal transport measurements analogous to solid state physics are now routinely performed. This has opened an era of renewed intense activity towards the topics of non-equilibrium dynamics and transport, and fundamental questions on localisation and thermalisation in isolated many-body systems. Quasiperiodic models, long been known, have recently gained relevance due to their realisation in experiments on the same platform, which fall in this large body of investigations. Quasiperiodic potentials are incommensurate with the underlying periodicity of the lattice, neither periodic nor disordered, yet deterministic. This can lead, even in one-dimension and absence of interactions, to a localisation transition (in the Aubry-André-Harper or AAH model), an energy-dependent transition or "mobility edge" (generalised AAH or GAAH model), and critical states yielding anomalous diffusion (Fibonacci model). The majority of previous studies have been focused on spin or particle currents, we dedicate most of the thesis to extend the characterisation of their transport properties, with an emphasis on their thermal features. We first explore the capability of quasiperiodic models as working mediums in two-terminal quantum autonomous thermal machines, that convert heat to work through non-equilibrium steady-state currents of microscopic particles. In particular, we show that the mobility edge in the GAAH model can function as an energy filter, and demonstrate large thermoelectric effects, exceeding existing predictions by several orders of magnitude. We further investigate the interplay with dephasing noise from incoherent scattering. Heat and electric currents in the Fibonacci model turn from anomalous to standard diffusive. However, the conductivities exhibit a non-trivial dependence on the dephasing strength, which can be exploited to enhance the performance of the device. These findings open the route to a new class of efficient and versatile quasiperiodic steady-state thermoelectric engines. Quasiperiodic models further provide a testbed to investigate the possibility of many-body localisation (MBL). While the AAH model displays single-particle localisation and signatures of a possible MBL phase have been observed in presence of interactions, the lack of parallel experiments leaves to debate whether the anomalous diffusion survives in the interacting Fibonacci model. We contribute by studying real-time spread of density-density correlations at infinite temperature via dynamical quantum typicality, an approach not previously applied to quasiperiodic systems. Our findings suggest a possible crossover to MBL preceded by a regime of anomalous subdiffusive transport. In the last part of the thesis, we perform a similar numerical study in frequency rather than time domain. Inspired by further experimental results on ultracold atoms, we probe the transport properties of the XXZ model in presence of a integrability-breaking term with initial spin helix states, characterised by a winding magnetisation profile. Within the eigenstate thermalisation hypothesis framework, we evaluate correlation functions on statistical ensembles and on single states using the kernel polynomial method.

List of publications

The results exposed in this thesis are based on the following publications:

1. **C. Chiaracane**, M. T. Mitchison, A. Purkayastha, G. Haack, and J. Goold, *Quasiperiodic quantum heat engines with a mobility edge,* Phys. Rev. Research **2**, 013093 (2020)

2. **C. Chiaracane**, F. Pietracaprina, A. Purkayastha, and J. Goold, *Quantum dynamics in the interacting Fibonacci chain,* Phys. Rev. B **103**, 184205 (2021)

3. **C. Chiaracane**, A. Purkayastha, M. T. Mitchison, and J. Goold, *Dephasing-enhanced performance in quasiperiodic thermal machines,* Phys. Rev. B **105**, 134203 (2022)

4. **C. Chiaracane**, K. Zawadzki, M. T. Mitchison, S. R. Clark, and J. Goold, *Non-equilibrium spin helix states in single-impurity XXZ model* in preparation

Contents

List of Figures

Introduction

In recent years, the tendency towards miniaturisation and the unprecedented level of control reached over nanoscale systems has reinvigorated scientific activity in the study of microscopic thermal machines, for which quantum effects can become relevant [1, 2] and may even be exploited [3–10]. Thermoelectric engines offer the most practical application, converting heat into electric power. They do not rely on macroscopic moving parts, instead, they operate through non-equilibrium steady-state currents of microscopic particles, e.g. electrons or atoms, flowing between two reservoirs. In order to explore this mechanism, mesoscopic physics experiments have been extended beyond the traditional investigation of charge transport, and it is nowadays possible, on platforms ranging from superconducting circuits [11] and semiconductor quantum dots [12], to molecular junctions [13], to manipulate and detect heat currents. Furthermore, transport measurements analogous to solid state physics are now routinely performed on ultracold atom set-ups, where a two-terminal device generating a particle current from a temperature bias has been realised [14]. The high tunability of the microscopic details available in all of these systems constitutes a strong motivation to theoretically explore the capability as working medium of exotic physical models displaying non-trivial spectral and transport properties, with the ultimate purpose of inspiring the design of tailored quantum matter that could enhance the performance of future computers and heat-conversion devices.

In mesoscopic physics the interplay between transport and disorder is well studied and has been shown to enhance thermoelectric performances in low dimensional systems [15–19], while bulk thermoelectrics are generally quite inefficient [20]. Disorder breaks translational symmetry and inevitably modifies the Bloch wave picture [21], which depicts extended single particle states and periodic energy band structure. The

presence of random disorder gives rise to a metal-insulator transition, a phenomenon induced by the quantum coherent scattering of the electrons against the impurities, and known as Anderson localisation. While in three-dimensional systems a critical energy depending on the disorder strength, the so-called mobility edge, separates localised from extended states associated with diffusion [22], in one dimension, instead, all the eigenstates get spatially localised when even an infinitesimal amount of uncorrelated disorder is introduced, and the wires switch from ballistic conductors to insulators [23].

A wider variety of behaviours, even in one dimension, emerges in quasiperiodic potentials, neither periodic nor disordered, yet deterministic while incommensurate with the underlying periodicity of the lattice. These systems possess highly non-trivial singular continuous spectra with fractal or self-similar structure [24], which lead to the appearance of critical states, neither extended nor localised [25, 26]. Originally, their properties were appealing to mainly mathematicians and mathematical physicists [27–29], however, they have gathered broader attention in the context of quantum transport with numerous studies, although limited to particle or spin, which have established them as primary examples of anomalous behaviour [30–32]. The paradigmatic example is the Aubry-André-Harper (AAH) model, where a cosine potential, modified by an irrational factor in its argument, induces a transition from a completely delocalised phase with ballistic currents to a completely localised phase as the strength of the quasiperiodic potential is increased [33]. At the critical point, transport is subdiffusive. The addition of perturbations, such as beyond-nearest-neighbour hopping, or modifications to the on-site potential function, leads in many cases to the occurrence of a mobility edge [34–36]. A closely related model is the Fibonacci chain, where the lattice energies are generated by a substitution rule. The Fibonacci model has unusual properties such as a critical energy spectrum across all energy scales [37], without a localisation transition. This spectral criticality gives rise to anomalous transport exponents which vary continuously with the potential strength, so that it is possible to tune the transport regime from superdiffusive to subdiffusive.

In this thesis, we extend the study of quantum transport in one-dimensional quasiperiodic models to thermoelectricity, involving the simultaneous appearance of electric currents coupled to the temperature bias, and heat currents to the voltage bias. We thus perform the first characterisation of the heat-to-work conversion in quantum

autonomous thermal machines which employ the models described above as working medium. We focus mainly on two mechanisms to increase the efficiency of the device: energy filtering and dephasing enhanced transport.

Energy filtering is a central concept in thermoelectric energy conversion: allowing only particles in a finite energy window to flow induces a strong thermoelectric response [38, 39]. This effect is generally realised either by engineering the thermodynamic variables of the reservoirs attached to the system [40] or by tuning the transport characteristics of the sample so that it displays an energy-dependent transmission probability. We follow the latter approach by exploiting the spectral characteristics of the central system; in particular, the mobility edge of a generalised AAH model.

The presence of dephasing noise from the environment, in the form of loss of phase coherence with possible momentum and energy exchange, has been demonstrated to assist transport in various contexts. The examples of such environmental-assisted or dephasing-enhanced transport include natural photosynthetic complexes [41, 42], molecular junctions [43–45], photonic crystals [46, 47], trapped ions [48], and also boundary-driven spin chains at infinite temperature [49–51]. However, the implications of this effect for thermoelectricity — an intrinsically finite-temperature phenomenon — have received comparatively little attention. We further ask in this thesis if the inevitable presence of dephasing noise due to inelastic scattering can be used to enhance thermoelectric performance when interplays with the quasidisorder of quasiperiodic potentials.

Up to this point, we have discussed quasiperiodic models in the non-interacting regime, and in the context of autonomous thermal machines, where transport is driven by the temperature and voltage biases between the thermal reservoirs attached to the system. Quasiperiodic models, however, have also gained relevance in a different configuration, where the system is isolated from the external environment and evolves according to its intrinsic unitary dynamics from an initial non-equilibrium state. They have in fact been realised with tunable interaction strength in a series of experiments on ultracold atoms trapped by optical lattices [52–56]. In light of recent advances in the degree of tunability, the ability of manipulating their initial configuration, and in the coherence times reached, ultracold atoms represent the most promising and versatile platform to probe dynamical properties of strongly correlated systems [57–59], and investigate fundamental questions as the possible existence of a localised phase, non-equilibium

phenomena, and thermalisation [60–64]. A sufficiently-complex many-body system initially engineered away from equilibrium thermalises when local observables attain, typically in the long-time limit, an equilibration value that coincides with the expectation value given by the ensembles of statistical mechanics. This mechanism is nowadays understood in the framework of the eigenstate thermalisation hypothesis (ETH), that still lacks a formal proof [65]. In integrable systems, the extensive set of local conserved quantities prevents them from following this prescription, but they have been shown to thermalise if subject to integrability-breaking perturbations [66, 67]. In this case, however, thermalisation is anomalous, meaning that the statistical properties of the unperturbed integrable model end up embedded in the perturbed one, with a process still to be completely unraveled [66]. On the other hand, when a generic system is perturbed by sufficiently strong disorder, it transitions towards a many-body localisation (MBL) phase, and remains a perfect insulator at finite temperature, failing to thermalise. This picture presents many open problems, concerning, among the others, the conditions for the occurrence of MBL, out-of-equilibrium phenomena and the related transport behaviour, and the effect of finite temperature [64].

The experiments simulating quasiperiodic models fall in this large body of investigations. In the interacting AAH model, it has been verified that its single particle localisation gives rise to a possible MBL phase [53–56], however, understanding how it is different from such a phase induced by random disorder is still under study [68–70]. The complex interplay between interactions, localisation and quasiperiodic order is largely left to be uncovered. Another natural question emerging is what happens to the anomalous transport behaviour of the quasiperiodic models in presence of many-body interactions. Differently from the AAH, the non-interacting Fibonacci model does not display a delocalisation-localisation transition, and its eigenstates are critical over the whole parameter diagram. In this case, a localised phase would represent a purely many-body effect. Different answers have been proposed in the literature, ranging from a transition towards MBL [71], to metal-insulator transitions at low energies [72], to persistence of the anomalous diffusion [73]. Motivated by the lack of experimental results, we characterise quantum dynamics in the isolated interacting Fibonacci chain with a further approach not previously applied on quasiperiodic systems. Dynamical quantum typicality allows to extract information on the equilibrium transport properties of the system from a numerical quench experiment involving pure

states that can act as "typical" of the statistical ensemble [74].

Quantum quenches are a common protocol adopted on ultracold atom platforms to probe in the laboratory the dynamical aspects of the simulated Hamiltonians. The system is prepared in a non-equilibrium state, characterised by a non-uniform profile, and local observables are monitored as it unitarily evolves in time. The same scheme has been recently followed by Jepsen *et al.* in an exciting experiment exploring the transport regimes of the quantum XXZ model over an unprecedented range of anistotropies [75]. Here, initial spin helix states were implemented by imprinting a winding magnetization profile along the atoms, with adjustable wavelength. Remarkably, spin helix states exhibit a dependence of their mean energy on the wavelength, or helicity, and are described by pure states. Inspired by the experiment, which has demonstrated a behaviour in striking contrast with the predictions of linear-response regime, we explore in the last part of the thesis the transport properties of spin helix states in a XXZ spin chain with an integrability-breaking local perturbation. We adopt the kernel polynomial method (KPM) [76] to access dynamical properties as correlation functions in the frequency domain. Within ETH, spin helix states can in principle operate as energy resolved probes to extract transport exponents at finite temperature. We investigate this prospect and, furthermore, the applicability of KPM in the study of far-from-equilibrium dynamics.

We start by introducing in Ch. 1 the notion of quasiperiodic order, and the spectral properties of the quasiperiodic models that will be studied: the AAH model, one of its generalisations, and the Fibonacci chain. In Ch. 2, we discuss the theoretical frameworks which we employ in our investigation. The non-equilibrium steady-state heat and electric currents arising in the quantum thermal machine are evaluated through Landauer-Büttiker integrals. In presence of many body interactions, transport will be studied within the Green-Kubo formalism for isolated systems. In particular, in both set-ups we focus on the linear response regime, where it is possible to define an Onsager matrix, which relates the currents to the generalised forces driving transport. We also provide details on techniques which facilitate our numerical simulations, and, in particular, we spend the last part of the chapter presenting the KPM and its applicability in the spectral and dynamical study of quantum Hamiltonians. We proceed then with the electric and heat transport characterisation of quasiperiodic models. Ch. 3 is dedicated to the construction of a heat engine which exploits the mobility

edge in the generalised AAH model as energy filter. In Ch. 4, we analyse the performance of a heat engine employing a Fibonacci chain as working medium, and the effect of introducing dephasing from incoherent scattering events, encoded by Büttiker probes. In Ch. 5, we focus again on the Fibonacci model, but in the limit of isolated environment and in presence of many-body interactions. We investigate its dynamics through real-time spread of density-density correlations, in order to understand whether the anomalous diffusion present in the non-interacting system survives after introducing interactions. In Ch. 6, we perform a similar numerical experiment, analysed, however, in the frequency rather than time domain. We reproduce initial spin helix patterns in a XXZ model with local integrability-breaking, and exploit ETH to investigate if transport properties can be probed in an energy resolved way from these exotic states. Finally, we summarise our results in the Conclusions and offer an outlook on possible future works.

Chapter 1

Quasiperiodic models

In this Chapter, we discuss the notion of quasiperiodicity and, in particular, of quasiperiodic order in quantum mechanics, which can be dated back to the discovery of quasicrystals and has been investigated in recent experiments in photonics and ultracold atom physics. We then introduce the three examples of one-dimensional quasiperiodic systems mostly studied in the thesis: the Aubry-André-Harper model with one of its generalised versions and the Fibonacci chain.

1.1 Quasiperiodicity in quantum mechanics

The study of solid state matter has been traditionally based upon the idea of a periodic arrangement of the atoms in space. The structure of a solid, or crystal, is generated by repeated translations along the principal axes of a basic building block, the unit cell, and classified in a finite number of crystallographic groups according to the symmetries of the pattern. As a consequence of translational invariance, the solutions to the single-particle Schrödinger equation are extended states known as Bloch waves, in the form of plane waves modulated by an envelope with the same periodicity of the atomic lattice. This picture has succeeded since 1929 in explaining and predicting most of the relevant bulk properties of materials, from optical indexes to electric conductances, neverthless it has set as standard the correspondence between solid matter, periodicity and order. The paradigm was first questioned in the context of life science, in the debate around the structure of DNA. The most common hypothesis was that the repetition of the four different kinds of nucleotides forming DNA would occur

in a regular fashion. A trivially periodic macromolecule, however, would be unable to store the amount of information required for cell functions, given the constrains on the patterns determined by translational symmetry. In his famous series of lectures of 1943 "What Is Life? The Physical Aspect of the Living Cell", Schrödinger introduced for the first time the notion of one-dimensional aperiodic crystal, by suggesting that genetic material could be instead organised in sequences with a well-defined order but without the appearence of periodic repetitions [77].

Such structures, despite their precursors in medieval Islamic architecture [78] or Kepler's treatises [79], begun to be sistematically investigated only in the 1960s, when the first aperiodic pattern was created [80]. Geometry tells us that not all symmetries under rotation are compatible with translational invariance. In two dimensions, the square lattice is invariant under rotations of $2\pi/4$, or four-fold rotation, and the triangular lattice under rotations of $2\pi/3$, or three-fold rotation. Other n-fold rotational symmetries, instead, such as five- or seven-fold, are forbidden. The restriction becomes evident in Fig. 1.1a when trying to tile a plane with a series of pentagons, invariant under five-fold rotation, without any gap or overlap. We are forced to introduce new tiles with shapes that do not posses five-fold symmetry, as in Fig. 1.1b, where two pentagons and a rhombus can be translated until the whole space is covered in octagonal patches, highlighted in red. Other attempts at solving the puzzle can be made by applying a substitution or inflation rule. The original tile is inflated and divided in a collection of smaller tiles. We proceed then to enlarge every shape and dissect it again, in such a way to cover larger and larger portions of space. A special series of substitutions was designed by Penrose in 1974 [81] and led to the discovery of an aperiodic or quasiperiodic tiling which is now one of the most commonly represented examples, known as P1 tiling. In Fig. 1.2a, we show the entire set of substitution rules. A pentagon can be subdivided into six smaller ones in a flower arrangement, plus five triangular gaps. The tiles are enlarged and the rule is applied again to each of the pentagons, leaving gaps in the shape of diamonds. By inflating and adding a new substitution rule for the diamond shape, in the second row of Fig. 1.2a, star and "paper-boat" gaps appear, for which other substitutions are defined in the third and last row. Reiterating the substitutions, we generate a figure as Fig. 1.2b, which is by construction self-similar, repeating a similar pattern at different length scales. In the limit of infinite repetitions, we can cover the whole plane. The tiling is de-

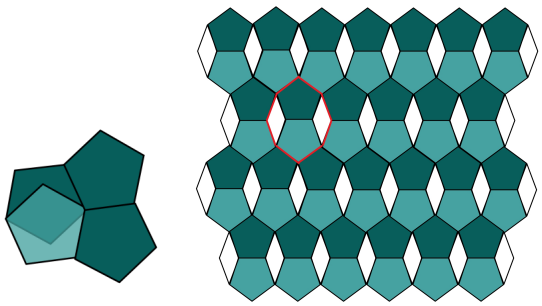

(a) (b)

Figure 1.1: (a) It is impossible to translate a pentagon in such a way to cover the whole plane without leaving any gap. (b) Here a periodic tiling with octagonal unit cell, highlighted in red, is created by admitting rhombic tiles, which do not posses five-fold symmetry.

terministic, since given by a precise set of rules, but despite looking almost identical it does not repeat exactly as we move along a line in any direction, as we shown in Fig. 1.2c by trying to overlap two copies of the tiling (in red and blue) with different origins. Several quasiperiodic tilings were devised by Penrose and others [79, 82, 83]. Nevertheless, these structures were believed to be pure mathematical artefacts.

Quasiperiodicity remained in the realm of mathematics until the observation in 1984 of a discrete diffraction pattern which could not be mapped into any of the crystallographic groups [84]. In particular, Shechtman synthesised an AlMn sample which exhibited the forbidden five-fold rotational symmetry. Later, he and his collaborators understood that the atoms in this alloy are organised in a quasiperiodic fashion, similarly to the P1 tiling. Since then, other structures with quasiperiodic rather than periodic order were found in the laboratory [85, 86], and the term quasicrystal was coined [87]. Nowadays, the study of their properties is an active field in condensed matter physics [88–91] and the first natural quasicrystal was observed in a meteorite sample [92, 93].

A function of space $g(\mathbf{x})$ can be expressed in Fourier components as

$$g(\mathbf{x}) = \sum_{\mathbf{K}} f_{\mathbf{K}} e^{i\mathbf{K}\cdot\mathbf{x}}, \tag{1.1}$$

where $\mathbf{K}$ indicates the spatial frequency in the Fourier space. When it describes a physical quantity on a crystal of dimension D, with lattice structure generated by the basis vectors $\{\mathbf{a}_j\}_{j=1}^{D}$, $g(\mathbf{x})$ will inherit the same periodicity of the lattice. Every

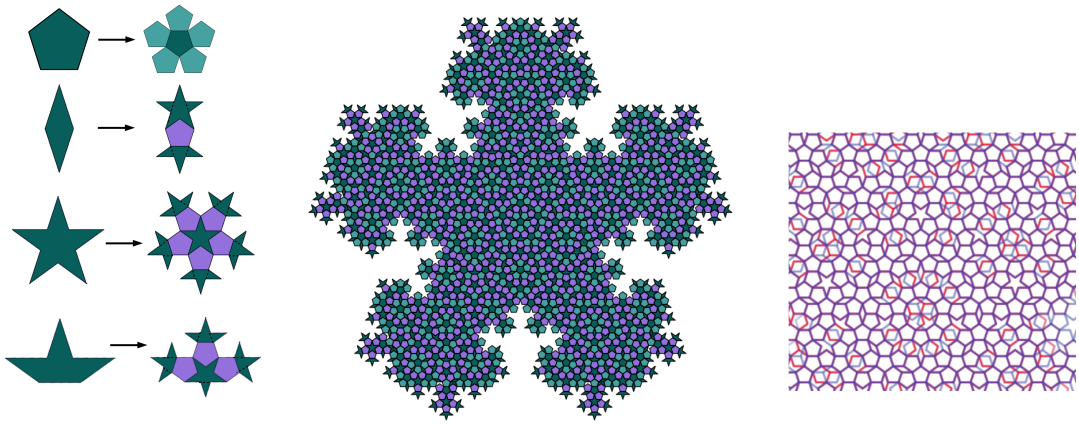

(a) (b) (c)

Figure 1.2: (a) The set of substitution rules defining the Penrose P1 tiling. (b) The aperiodic P1 tiling after iterating the substitution rules 4 times. The pattern is self-similar: the same kinds of shapes appear at different length scales, zooming in and out of the figure. (c) Two copies of the P1 tiling with different origins (in red and blue). Despite the pattern seems to repeat identically in space, it is impossible to find a translation which makes the two copies overlap completely in purple. Any translation will leave the aperiodic tiling almost invariant.

spacial frequency or wavevector $\mathbf{K}$ is thus given by the following linear combination

$$\mathbf{K} = \sum_{j=1}^{d} m_j \mathbf{b}_j, \tag{1.2}$$

where d equals the spatial dimension D, m_j are integers and the set of $\{\mathbf{b}_j\}_{j=1}^{d}$ spans the reciprocal lattice, related to the direct one via $\mathbf{a}_i \cdot \mathbf{b}_j = 2\pi\delta_{ij}$. In a diffraction experiment on a crystal, as stated by Bragg's law, the difference in wavevectors between incoming and outgoing X-rays must be a vector belonging to the reciprocal lattice. Therefore, the peaks in the emission are always discrete and can be used to infer the lattice structure. In a quasicrystal, the atomic distribution can be instead described by a quasiperiodic function. A function is by definition quasiperiodic when its Fourier components are not uniformly spaced as in the periodic case, but whose spacing can still be described by a finite set of lengths [94]. In other words, the spatial frequency $\mathbf{K}$ in the Fourier components of a quasiperiodic structure will still be given by the same expression of Eq. (1.2), however the number of reciprocal basis vectors exceeds the spatial dimension, $d > D$. Naturally, quasiperiodic functions represent the continuous description of aperiodic tilings. Almost periodic functions constitute, instead, despite the confusion in the notation, a larger family which includes also the case where an infinite set of $\mathbf{b}_j$ is needed to describe the Fourier frequencies in Eq. (1.2). From the

formal definition of quasiperiodic function, we derive two consequences. First, the diffraction from a quasiperiodic structure gives discrete Bragg spots, as first observed by Shechtman. Then, any quasiperiodic function characterised by d in Eq. (1.2) can be considered as a D-dimensional cut of a periodic function in d dimensions. The simplest example to consider is a one-dimensional function, $D = 1$,

$$f(x) = \cos x + \cos bx. \tag{1.3}$$

The Fourier transform consists of two delta functions. However, if $b = P/Q$ is rational with integers P, Q, $f(x)$ has period $2\pi Q$ and the frequencies can be expressed by using a single reciprocal lattice vector $b_1 = 1/Q$. When b is irrational, $f(x)$ is quasiperiodic. The two frequencies characterising $f(x)$ are uncommensurate, thus in the Fourier space they need to be expressed by two b_1 and b_2 with different length, meaning that $d = 2$. Nevertheless, the function can be seen as a cut along the axis $y = bx$ of the periodic two-dimensional $f(x, y) = \cos(x) + \cos(y)$.

The discovery of quasicrystals spurred the interest in the effects of quasiperiodicity on the spectral and transport properties of physical models. Given the inapplicability of the Bloch theorem, most studies were limited to one-dimension and made use of the tight-binding approximation, considering a discretised version of the Schrödinger equation as

$$t_{n,n+1}\psi_{n+1\ell} + t_{n,n-1}\psi_{n-1\ell} + V_n\psi_{n\ell} = E_\ell\psi_{n\ell}, \qquad \ell = 1, \dots, N \tag{1.4}$$

where $\psi_{n\ell}$ is the ℓ-th single-particle wavefunction, corresponding to the eigenvalue E_ℓ, evaluated at the lattice site n, N the length of the chain, $t_{n,n\pm1}$ the hopping terms, and V_n the on-site potential. Quasiperiodic models are realised with a set of $\{t_{n,n\pm1}\}_n$ or $\{V_n\}_n$ either generated by a substitution rule, analogously to the scheme followed for the aperiodic tilings, as in the case of the Fibonacci and Thue-Morse chains [26, 90], or by superimposing two or more periodic functions with incommensurate periods as Eq. (1.4), for example in the case of the Aubry-André-Harper model [33]. This series of works provided through exact and numerical methods an insight over the properties of quasiperiodic models, which are now known to exhibit highly fragmented spectra with self-similar properties [24, 25, 95], and neither extended nor localised critical states [26, 96, 97], associated to non-trivial transport properties that deviate from

standard ballistic or diffusive behaviour [30]. These properties were eventually observed on experiments conducted over a wide range of platforms, which have re-ignited in the last years the interest in the family of one-dimensional quasiperiodic models. The expected structure of the density of states of the Fibonacci model was studied in a polariton gas in one-dimensional cavities [98], and following experiments on the same type of system investigated localisation properties and topological invariants [99, 100]. Topologically protected modes were observed also on another type of set-up, where the effective potential for the light beam is modulated to be quasiperiodic by tuning the refraction indexes of optical waveguides [101–103]. On the same platform, the topological equivalence between the Fibonacci model and a two-dimensional quantum Hall system was explicitely demonstrated [104]. Quasiperiodic models have further been realised by trapping ultracold atoms in bichromatical optical lattices with uncommensurate wavelengths. On a deep primary lattice, the optical potential can be directly mapped onto the Aubry-André-Harper model [105, 106]. The localisation transition characteristic of the model was observed by measures of the imbalance in time [52, 54]. More complex spectral features, as an energy-dependent localisation transition, or "mobility edge", were engineered by lowering the depth of the primary lattice in such a way to allow hopping processes beyond nearest-neighbours [53], by modyfing the effective potential [35], or introducing many-body interaction terms [55, 56, 107].

1.2 Aubry-André-Harper model

The paradigmatic example of quasiperiodic model is a one-dimensional lattice subject to a harmonic perturbation incommensurate with the underlying periodicity of the lattice. The problem was studied by Aubry and André in the tight-binding approximation [33], considering a single-particle Schrödinger equation as Eq. (1.4) with constant hopping term t_h and on-site energies given by V_n^{AAH},

$$t_h(\psi_{n+1\ell} + \psi_{n-1\ell}) + V_n^{AAH}\psi_{n\ell} = E_\ell\psi_{n\ell} \qquad V_n^{AAH} = 2\lambda\cos(2\pi nb + \varphi), \tag{1.5}$$

where λ is the amplitude or strength of the potential, φ an arbitrary global shift in phase, and b an irrational number that prevents the potential from repeating itself exactly along the lattice. As we will review in the following, the most striking feature of the model is a localisation transition, where all the eigenstates are localised at

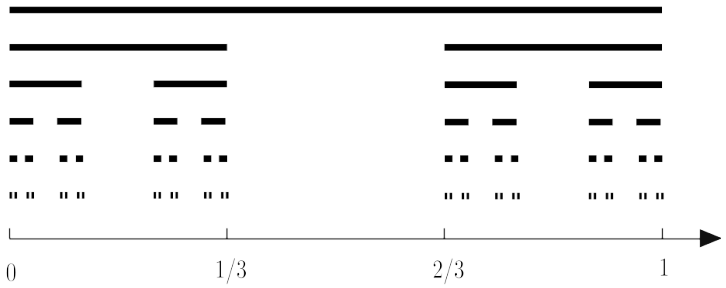

Figure 1.3: Construction of the Cantor set: an initial segment is divided into 3 subsegments, and the middle one removed (here the segments are chosen of equal length). The two steps are then repeated iteratively for each of the remaining intervals.

potential strengths λ above a certain critical value, and all extended for λ below.

The spectrum of the Aubry-André-Harper (AAH) model displays a rich structure, which has been the object of numerous studies in mathematical physics [29, 108–110]. The topic reached such popularity in 1981 that the mathematician Mark Kac promised ten Martini cocktails as reward to anyone who would prove the spectrum to be a Cantor set [27]. A Cantor set is the prototype of a fractal, which can be visualised considering first a segment, for example the points in the interval $[0, 1]$. The segment is divided in three parts, and the middle sub-segment removed, leaving in this case the set of points in $[0, 1/3] \cup [2/3, 1]$. The same two steps are then repeated for each of the remaining sub-segments $[0, 1/3]$ and $[2/3, 1]$ separately. The result after few iterations is illustrated in Fig. 1.3. The Cantor set contains all the points from the initial interval $[0, 1]$ which were not deleted at any step in the infinite series of iterations. The final structure is self-similar: it exhibits a similar pattern at increasingly smaller scales. The spectrum of the AAH model possesses analogous self-similar structure.

The famous "ten Martini problem" was solved by Avila and Jitomirskaya only fourteen years later, in 2005 [28]. Nevertheless, it is possible to anticipate the fractal nature of the spectrum via a more intuitive argument which exploits approximants to irrational numbers by continued fractions of integers. The golden ratio $\tau = (\sqrt{5} + 1)/2$, for example, can be defined iteratively as

$$\tau = 1 + \cfrac{1}{1 + \cfrac{1}{1 + \cfrac{1}{1 + \cfrac{1}{\ddots}}}}. \tag{1.6}$$

When we approximate b in Eq. (1.5) with a ratio P/Q between integers P, Q, the

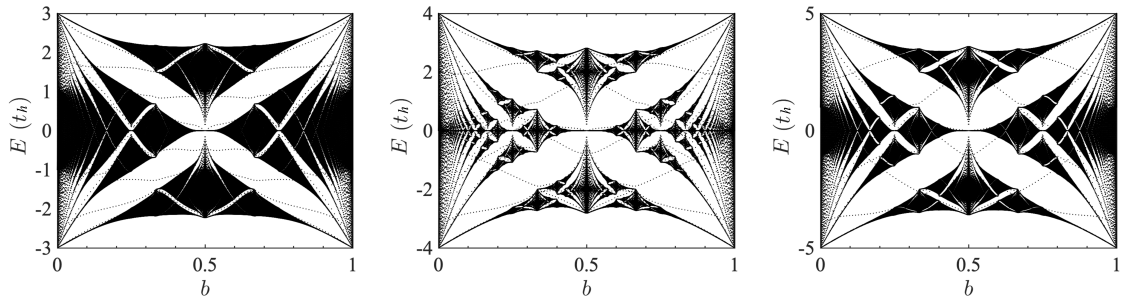

Figure 1.4: Eigenspectra of the AAH model at changing irrational parameter b for $N = 300$ sites, with $t_h = 1$, $\varphi = 0$, and (a) $\lambda = 0.5t_h$, (b) $\lambda = t_h$, and (c) $\lambda = 1.5t_h$. In (b), the spectrum reproduces the Hofstadter butterfly fractal.

potential is periodic, thus it defines a unit cell of length Q and a Brillouin zone in the reciprocal space with size $2\pi/Q$. The band structure of this periodic system will have Q bands with gaps at the boundaries of the Brillouin zone $\pm\pi/Q$. When we improve the approximation by increasing Q, the Brillouin zone becomes smaller, opening more sub-bands. Therefore, in the incommensurate limit, with $Q \to \infty$, the bands become more and more fragmented, separated by an infinite amount of gaps which will not close in the thermodynamic limit [111].

In Fig. 1.4, we show the spectrum of the AAH model as a function of b, for three different values of the potential strengths. The plots for $\lambda < t_h$ and for $\lambda > t_h$ look similar. At $\lambda = t_h$, instead, the figure reproduces the famous Hofstadter butterfly. The fractal is well known to describe the energy levels of an electron transversing a square lattice when subject to a uniform perpendicular magnetic field [112, 113]. The AAH model, in fact, can also be seen as cut of the Harper model, a one-dimensional projection along a line of a two-dimensional periodic system. In this picture, the parameter b corresponds to the ratio between the magnetic flux piercing the unit cell and the magnetic flux quantum. Beside designating a precise mapping to the Harper model, the value $\lambda = t_h$ marks the point in the parameter space where the system becomes self-dual under a transformation closely related to a discrete Fourier transform [33].

In order to clarify the self-duality and gain an insight on the phase diagram of the model, we follow the seminal work of Aubry and André. In the infinite system limit,

the solutions to an eigenvalue equation as Eq. (1.4) can either satisfy

$$\sum_n |\psi_{n\ell}|^2 < \infty, \tag{1.7}$$

or give a divergence in

$$\sum_n |\psi_{n\ell}|^2 = \infty. \tag{1.8}$$

The former condition physically indicates a localised state, which decays exponentially at large length scales $\psi_{n\ell} \sim e^{-\gamma_{\mathcal{L}}|n-n_0|}$, with $\gamma_{\mathcal{L}} > 0$ a characteristic exponent known as Lyaponuv exponent and defined as [114]

$$\gamma_{\mathcal{L}}(\psi_\ell) = -\lim_{n\to\infty} \frac{\ln\left(|\psi_{n+1\ell}|^2 + |\psi_{n\ell}|^2\right)}{2n}. \tag{1.9}$$

The latter signals an extended states, such a plane wave $\psi_{n\ell} \sim e^{inQ}$ for some wavenumber Q, which would have $\gamma_{\mathcal{L}} = 0$. General solutions to the tight-binding AAH model in Eq. (1.5) can be expressed as

$$\begin{aligned} \psi_{n\ell} &= e^{in\phi} \sum_m f_{m\ell} e^{im(2\pi nb+\varphi)}, \\ f_{m\ell} &= e^{im\varphi} \sum_n \psi_{n\ell} e^{in(2\pi m+\phi)}. \end{aligned} \tag{1.10}$$

We notice that if $f_{m\ell}$ is localised in the reciprocal space $\sum_m |f_{m\ell}|^2 < \infty$, $\psi_{n\ell}$ will be extended, and viceversa. This statement is true only when b is irrational, otherwise for $b = P/Q$ the reciprocal space series would have only a finite set of unique terms, since $f_{(m+Q)\ell} = f_{m\ell} e^{-iQ\varphi}$. Therefore, $f_{m\ell}$ would always be localised, and $\psi_{n\ell}$ always extended, as in the periodic case. If we insert Eq. (1.10) in Eq. (1.5), we derive that the components $f_{m\ell}$ must satisfy

$$\lambda(f_{m+1\ell} + f_{m-1\ell}) + 2t_h \cos(2\pi bm + \phi) f_{m\ell} = E_\ell f_{m\ell}, \tag{1.11}$$

which exhibits the same structure of Eq. (1.5) in real space, with interchanged λ and t_h. The two expressions become dual when $\lambda = t_h$ and $\varphi = \phi$. The transformation in Eq. (1.10) exchanges the localisation properties of the eigenfunctions, thus, if a localisation transition occurs, it must be at $\lambda = t_h$, the point where the transformation maps the eigenstate equation into itself. Aubry and André showed that the

eigenfunctions $\psi_{n\ell}$ are extended for all ℓ when $\lambda < t_h$ and conjectured the presence of a localised phase at $\lambda > t_h$, with all the $\psi_{n\ell}$ localised. In particular, their conjecture is based on the positivity of the Lyapanouv exponent and makes use of the Thouless formula [115], which connects the exponent to the density of states of the system

$$\rho(E) = \frac{1}{N} \sum_{\ell} \delta(E - E_\ell). \tag{1.12}$$

For Eq. (1.5), the formula reads

$$\gamma_{\mathcal{L}}(\psi_\ell) = \int dE \ln \left| \frac{E_\ell - E}{t_h} \right| \rho(E), \tag{1.13}$$

while for Eq. (1.11), since the energy and thus $\rho(E)$ remain the same, it reads

$$\gamma_{\mathcal{L}}(f_\ell) = \int dE \ln \left| \frac{E_\ell - E}{\lambda} \right| \rho(E). \tag{1.14}$$

The two exponents are thus related by $\gamma_{\mathcal{L}}(\psi_\ell) = \gamma_{\mathcal{L}}(f_\ell) + \ln(\lambda/t_h)$. According to the transformation in Eq. (1.10), if $f_{m\ell}$ is extended ($\gamma_{\mathcal{L}}(f_\ell) = 0$), then $\psi_{n\ell}$ must be localised with $\gamma_{\mathcal{L}}(\psi_\ell) = \ln(\lambda/t_h) > 0$, implying that this can be verified only at $\lambda > t_h$. Viceversa, when $\gamma_{\mathcal{L}}(\psi_\ell) = 0$ we must have $\gamma_{\mathcal{L}}(f_\ell) = -\ln(\lambda/t_h) > 0$, and this condition is only met when $\lambda < t_h$. This argument indicates that a transition would occur for all the eigenstates at the same potential strength, independently of the energy E. A formal proof of the existence of the localised phase was provided later from the decomposition of the spectrum in the case where the irrational number b is Diophantine [110], meaning that for every rational number P/Q with $Q > 0$ there must exist $C, r > 0$ such that

$$\left| b - \frac{P}{Q} \right| \geq \frac{C}{Q^{2+r}}. \tag{1.15}$$

As a consequence, the studies on the AAH model always consider a Diophantine parameter b, which is a sufficient condition for a sharp localisation transition. In particular, a conventional choice is the golden ratio τ [111], which will be adopted in the following. We show examples of eigenfunctions in Fig. 1.5, by plotting their probability density $|\psi_{n\ell}|^2$ over each site n in the three regimes of localisation. In Fig. 1.5a, where $\lambda < t_h$, the components of the eigenfunction appears roughly equally distributed along the chain. When $\lambda > t_h$, the eigenfunctions have only one or few components

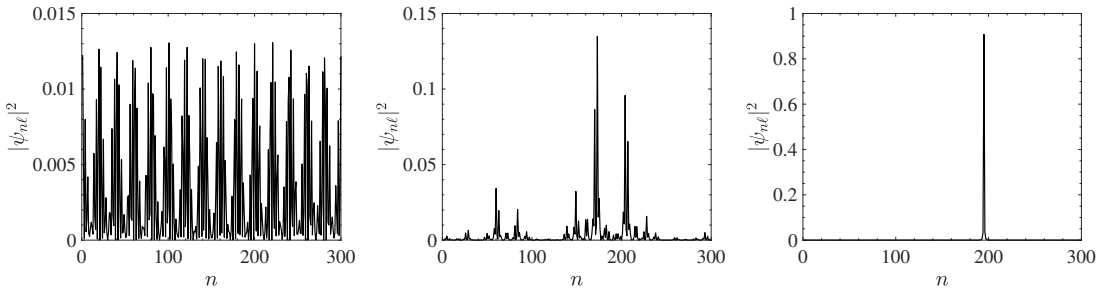

(a) (b) (c)

Figure 1.5: Examples of AAH model eigenstate probability density over the chain sites for (a) $\lambda = 0.5t_h$, (b) $\lambda = t_h$, and (c) $\lambda = 1.5t_h$. The remaining parameters are $t_h = 1$, $b = \tau$, $\varphi = 0$, and $N = 300$.

over close sites which are different from zero, as shown in Fig. 1.5c. At the critical point $\lambda = t_h$, we observe in Fig. 1.5b the structure of the eigenfunction repeating itself at smaller energy-scales. This type of states are netiher extended nor localised, and are called critical or multifractal [26]. They will be formally characterised in the next section.

Numerical simulations and experiments deal with systems of finite size and numbers which can only be represented by a finite amount of digits and thus not truly irrational. A truly incommensurate potential is then impossible to realise if not through an analytical formula. Nevertheless, the AAH model can always be studied on finite system of size N with $b = P/Q$ a rational number, when $Q > N$ in such a way that the potential has still a different value on every site and periodic replicas are avoided [105]. Finally, we mention that the global phase φ is not relevant in determining the localisation transition. However, it is closely connected to the topological properties of the model [102, 116], which will not be investigated in the thesis.

1.2.1 Inverse Participation Ratio

The degree of localisation of the eigenstate at energy E_ℓ can be well characterised by its inverse participation ratio (IPR), given by

$$\mathrm{IPR}(E_\ell) = \sum_{n=1}^{N} |\psi_{n\ell}|^4. \tag{1.16}$$

The expression provides a measure of the portion of lattice sites where the amplitude of the wavefunction differs from zero. In one-dimensional systems, the IPR of localised

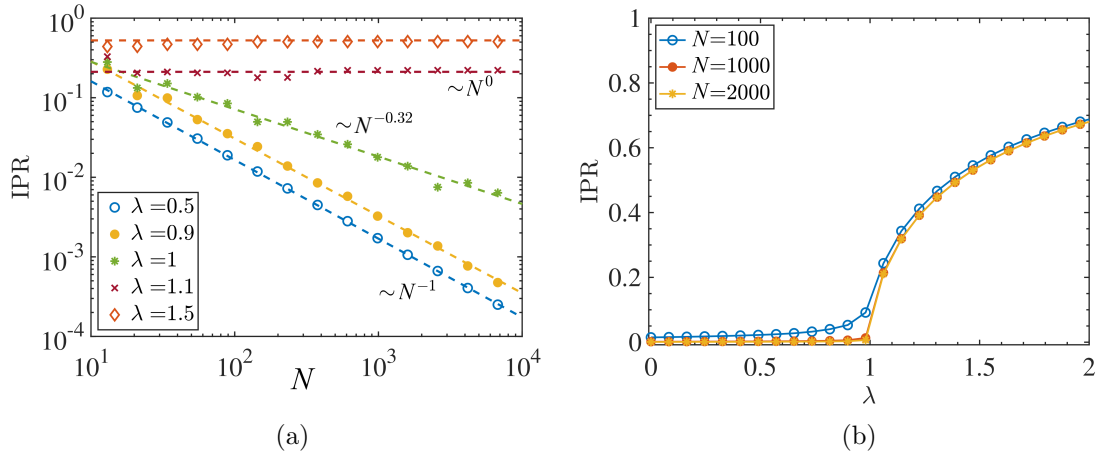

Figure 1.6: (a) Scaling of the IPR in the AAH model ($t_h = 1$, $b = \tau$, $\varphi = 0$) for the eigenstates in the middle of the eigenspectrum $\ell = N/2$ at different values of potential strength λ (markers). The dashed lines indicate the numerical fits $f_x \sim N^{-x}$ which yield $x = 1$ for $\lambda < 1$, $x \sim 0$ for $\lambda > 1$, and 0.32 at the critical point $\lambda = 1$. (b) IPR as a function of λ computed at fixed system sizes N. The localisation transition can be observed at $\lambda = 1$.

states is finite and does not scale with the system size N, while for extended states it is of order N^{-1}, thus vanishingly small in the thermodynamic limit. States with multifractal behaviour, instead, show IPR$\sim N^{-p}$, with $0 < p < 1$ [114].

We analyse the localisation transition in the AAH model by computing the scaling with system size N of the IPR for various values of λ. In Fig. 1.6a, we look at the eigenstates with energy lying in the middle of the spectrum, $\ell = N/2$, and observe the three expected types of scaling: N^{-1} for $\lambda < t_h$, absence of scaling or N^0 for $\lambda > t_h$, and N^{-p} with $p \sim 0.32$ for $\lambda = t_h$, indicating a multifractal state. The same distinct behaviours persist qualitatively in the three regimes for any general index ℓ. In particular, the scaling exponent of the multifractal states ranges between ~ 0.3 and ~ 0.6. In Fig. 1.6b, we represent the localisation diagram for the system at fixed sizes $N = 100, 1000, 2000$, by averaging the IPR over all the eigenstates. For $\lambda < t_h$ all single-particle eigenstates are completely delocalised with vanishing IPR, while for $\lambda > t_h$, all the single-particle eigenstates are localised with IPR close to the maximum value of 1. At the critical point $\lambda = t_h$, the IPR assumes intermediate values.

1.3 Generalised Aubry-André-Harper models

The first extension to the AAH model was introduced by Soukoulis and Economou, who added to the lattice a second harmonic perturbation with incommensurate fre-

quency [117]. A further generalisation considered tunnelling terms to the next-nearest neighbours [118]. Such models are not longer self-dual under the transformation defined in Eq. (1.10) by Aubry and André. Nevertheless, the authors collected numerical evidence of the appearance of a "mobility edge", a critical energy separating localised and extended eigenstates in the same spectrum. A mobility edge is present also in the three-dimensional Anderson model [119, 22]. The appearance of a rich localisation behaviour in the first experiments with ultracold atoms in incommensurate optical lattices [53–55] has fuelled again the theoretical study of a series of generalisations of the AAH model. The first motivation is to model more accurately the experiments when performed at different reciprocal depth of the potentials [120], out of the deep lattice regime which can be directly mapped to the original tight-binding model [105]. Secondly, the exploration of such generalisations is driven by the possibility to realise a wide variety of non-trivial localisation properties even in one-dimension and in absence of many-body interactions. Several works have focused on hopping terms beyond nearest neighbours [121, 122], decaying with a power law [123, 124] or with gaussian and exponential envelopes [125, 126]. Other generalisations consider additional deformations to the harmonic functions in the potential [36, 68, 127–129], or more complicated geometries, as coupled AAH chains generating a two-dimensional system [130, 34].

We focus on a particular generalised AAH (GAAH) model, which has been recently realised in an ultracold atom experiment [35]. The on-site energies V_n^{AAH} in Eq. (1.5) are replaced by [36]

$$V_n^{GAAH} = \frac{2\lambda\cos(2\pi bn+\varphi)}{1-\alpha\cos(2\pi bn+\varphi)}, \tag{1.17}$$

with $\alpha \in]-1,1[$. At $\alpha = 0$, the potential recovers the standard AAH model, and it exhibits a localisation transition at the self-dual point $\lambda = t_h$, independent on the energy. For $\alpha \neq 0$, the perturbation at the denominator breaks the duality symmetry defined in the previous section. For the specific model, it is possible to identify a new transformation under which the model can be shown to be self-dual at energies [36]

$$E_c = \frac{2}{\alpha}\text{sign}(\lambda)(|t_h| - |\lambda|). \tag{1.18}$$

We notice that the self-dual point is different at different values of λ. For a single realisation of the potential we can then observe a transition from localised to extended

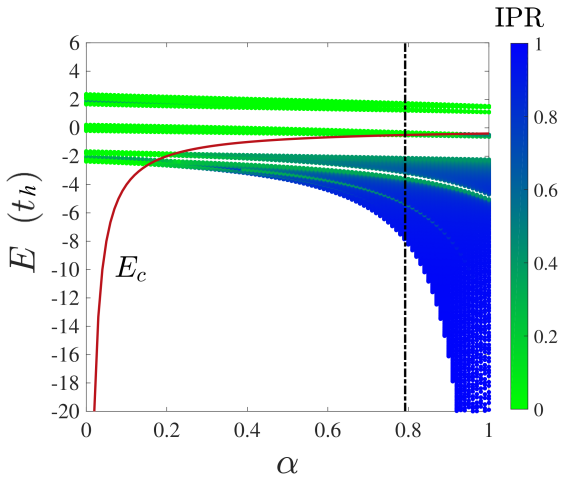

Figure 1.7: Eigenenergy spectra of the GAAH model with $b = (\sqrt{5}+1)/2$, $\lambda = -0.8$ and $\varphi = 0$ as a function of α, for a chain of $N = 987$ sites. The IPR of the corresponding eigenstate is shown by a color map, with green for extended, blue for completely localised states. The red line represents the mobility edge E_c given by Eq. (1.18), which separates localised from delocalised states. The dashed black line indicates a single realisation of the model at $\alpha = 0.792$.

states now dependent on the energy. The E_c defines the so-called mobility edge, separating localised from extended regions. Given the analytical expression in Eq. (1.18), the position of the mobility edge can be tuned by changing λ and α. In Fig. 1.7, we show examples of the energy spectra of the GAAH model for various α at a chosen λ. For each eigenvalue, the corresponding IPR is represented on a blue-green color map, and the analytical expression for the mobility edge E_c separating the localised region from the extended region is marked by a continuous red line. The extended region appears green (IPR = 0), while the localised region mostly blue (IPR = 1). The eigenstates whose energies lie on the mobility edge are critical in nature [36]. However, the regions in a darker shade of green ($0.4 \lesssim$ IPR) visible in Fig. 1.7 away but below the mobility edge are an effect of the finite system size. The corresponding eigenstates prove to be localised when studying the IPR scaling at large enough N.

1.4 Fibonacci chain

Following the work of Aubry and André, the spectral and dynamical properties of a wide range of quasiperiodic potentials begun to be explored in the tight-binding limit. Another popular example was the Fibonacci chain [96, 97], that more recently has been used to model different types of synthetic DNA macromolecules [131, 132] and to implement a topological pump on a photonic waveguide array [102, 104]. Exact and

perturbative solutions have been obtained to describe its eigenspectra [133, 134]. Here we provide an overview on how to build the quasiperiodic model, and its localisation features. There exist a diagonal and a off-diagonal versions of the Fibonacci model, where the quasiperiodic order is respectively applied on the hopping terms $t_{n,n\pm1}$, or on the on-site energies V_n in Eq. (1.4). We focus on the diagonal Fibonacci chain, where the hopping terms are constant $t_{n,n\pm1} = t_h$, and the on-site potential assumes only two alternating values, $V_n \in \{u_A, u_B\}$. The way in which the amplitudes alternate along the sites of the chain $C = [V_1\ V_2\ V_3 \dots V_N]$ is determined by the Fibonacci sequence [37].

The sequence of u_A and u_B can be built in different but equivalent ways, which have been extensively studied in combinatorics on binary words, where u_A and u_B are interpreted as two symbols forming strings or words when concatenated [135]. We start from the two basic blocks $C_0 = [u_B]$ and $C_1 = [u_A]$. The next string or word of the Fibonacci sequence is generated by concatenation of the previous two, thus $C_2 = C_1C_0 = [u_A\ u_B]$, $C_3 = C_2C_1 = [u_A\ u_B\ u_A]$, $C_4 = C_3C_2 = [u_A\ u_B\ u_A\ u_A\ u_B]$, etc. The string at the m-th iteration is $C_m = C_{m-1}\, C_{m-2}$. The length of the string is determined by the number of symbols it contains and indicated by $|C_m|$. By construction, the length of a Fibonacci word always belongs to the Fibonacci number sequence, $|C_m| = F_m$, where $F_m \in \{1, 1, 2, 3, 5, \dots\}$. The complexity function $P(m)$ of the sequence is instead defined as the total number of factors, prefixes and suffices of C_m. A word W will be a factor of a longer word C_m, or its prefix or suffix, if there exist other X, Y such that $C_m = XWY$, or, respectively, $C_m = WX$ or $C_m = XW$. The quantity $P(m)$ measures then the "randomness" of the sequence, since it increases with the variety of different factors appearing at every iteration with $P(m) \leq P(m+1)$, and $1 \leq P(m) \leq 2^m$ in case of a binary sequence. Periodic sequences, or sequences that become periodic after a certain m, have little complexity and bounded complexity function for $m \to \infty$. The complexity function of the Fibonacci sequence and other quasiperiodic sequences grows linearly $P(m) = m + 1$ [135], thus they are considered the closest non-periodic structure to periodicity.

The Fibonacci sequence can also be generated by applying the following substitution

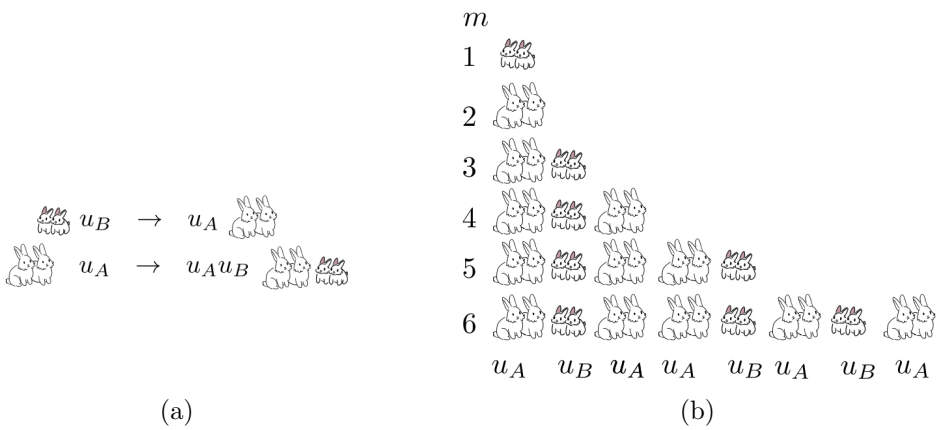

(a) (b)

Figure 1.8: A schematic overview on the construction method for the Fibonacci sequence. (a) The Fibonacci substitution rules. In order to generate the next string, one replaces each u_B (indicated by the pair of bunnies) with u_A (a pair of grown-up rabbits), and each u_A by $u_A u_B$. (b) The next iteration of the Fibonacci sequence is built by applying the substitution rules to each of the elements.

rules on each element of C_m,

$$u_B \rightarrow u_A \tag{1.19}$$

$$u_A \rightarrow u_A u_B, \tag{1.20}$$

starting again from $C_0 = [u_B]$. These substitution rules were first ideated by the mathematician Lorenzo Pisano alias Fibonacci in the Late Middle Ages, with the idea of modelling the growth of a population of rabbits. He simplified the problem by considering that at each generation every pair of baby bunnies, symbolised by u_B, will grow into a pair of adult rabbits, symbolised by u_A, and that every pair of rabbits (u_A) will additionally generate a new born pair of bunnies ($u_A u_B$). The construction method is illustrated schematically in Fig. 1.8. At the m-th iteration, the number of u_A is given by the length of the chain in the previous generation, which is the Fibonacci number F_{m-1}. The number of u_B, instead, will be equal to the previous number of u_A, thus F_{m-2}. Despite the fact that we cannot generate a larger portion of a Fibonacci chain by repeating smaller parts of it, as in the periodic case, a long-range order arises anyway if we consider the ratio between occurrences of u_A and u_B. In the limit of infinite repetition C_∞, in fact, this ratio will reach convergence to a finite value,

$$\lim_{m\to\infty} \frac{F_m}{F_{m-1}} = 1/\tau, \tag{1.21}$$

an irrational number given by the inverse of the golden ratio.

Finally, it is possible to derive a closed formula in the case of the indefinitely extended Fibonacci sequence $C_\infty = [V_1, V_2, \dots, V_n, \dots]$ as following [37, 32],

$$V_n = u_B + (u_A - u_B)\chi_n, \qquad \chi_n = \left[\frac{n+1}{\tau}\right] - \left[\frac{n}{\tau}\right], \tag{1.22}$$

with $[\,\cdot\,]$ taking the integer part of the argument.

The quasiperiodic order exhibited by the Fibonacci sequence affects the spectral and transport features of the corresponding model in a non-trivial way. As mentioned earlier, the Fibonacci chain is built by taking a one-dimensional tight-binding model with constant hopping terms, and using a string C_m from the sequence to read the on-site energies. The symbols u_A and u_B thus represent two different values the potential can assume at each site, and their alternation in a chain of size $N = F_m$ is determined by how they are listed in C_m. Applying the same argument used for the AAH model, it is possible to anticipate that the structure of the spectrum of the Fibonacci chain is fractal. The two models, in fact, were shown to be connected by a unified characteristic function [101, 136]. The inverse of the golden ratio $1/\tau$ in Eq. (1.22) can be replaced with a series of rational approximants, which at the m-th step reads F_m/F_{m-1}, and converges correctly for $m \to \infty$, as explicitly shown in Eq. (1.21), or, equivalently, in Eq. (1.6) as continued fraction. Therefore, the spectrum of the Fibonacci chain is also a Cantor set, with self-similar properties and dense gaps opening at smaller and smaller energy scales, even in the limit of a chain of infinite length [24, 137]. A key difference with respect to the AAH model is that the Fibonacci chain does not exhibit a localisation transition. Even an infinitesimal amount of potential strength is enough to make all the eigenfunctions critical or multifractal [134], for every choice of u_A and u_B [25]. For such reason, it is generally adopted a single parameter to control the potential strength,

$$u = u_A = -u_B. \tag{1.23}$$

As we see in Fig. 1.9a, the IPR scaling indicates multifractality at any value of u. Furthermore, it is known that the scaling exponent p changes continuously as a function of the potential strength, as we notice in Fig. 1.9b, varying from $p = 1$ for $u = 0$ (extended states), to $p \to 0$ only in the limit $u \to \infty$. This feature is reflected on the transport properties of the model, which will be investigated in the next sections.

In Fig. 1.9a, the lengths N belong to the Fibonacci number sequence. However,

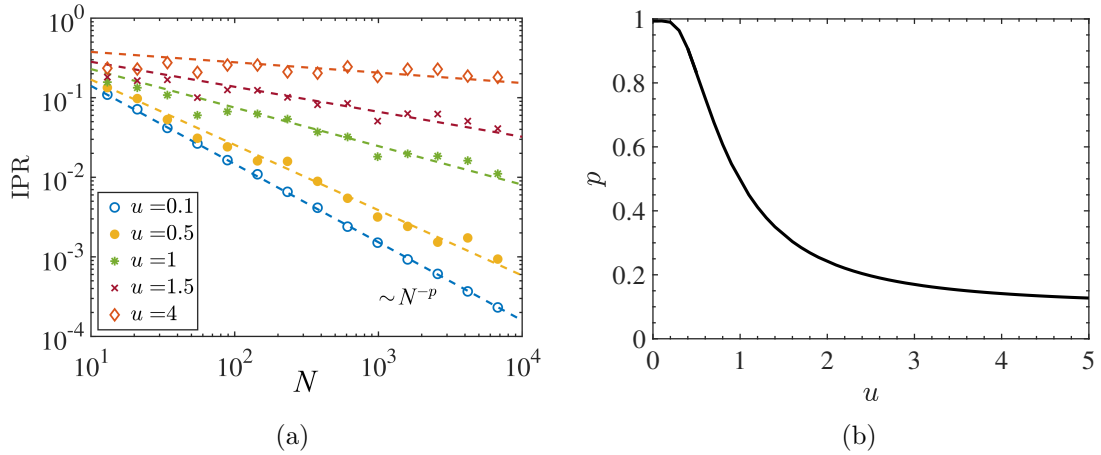

Figure 1.9: (a) Scaling of the IPR with system size for the eigenstates of the Fibonacci chain in the middle of the spectrum $\ell = N/2$, at different values of potential strength u, and $t_h = 1$. Each set of data is fitted by $f \sim N^{-p}$, indicated in dashed lines. (b) The scaling exponent of the IPR extracted from the fits in (a) is plotted as a function of u, showing that it varies continuously by tuning the potential strength.

as discussed earlier, experiments and more complex numerical simulations can be strongly limited in system size and usually involve chains of generic length N. In order to treat the Fibonacci potential within small system sizes and reduce the sample-to-sample fluctuations, one usually adopts the averaging procedure used in Refs. [134, 32]. The idea is to consider the sequence of infinite length C_∞ and cut finite samples of length N out of it. Physical quantities are calculated as statistical averages over the different realisations of potential obtained. Given the quasiperiodicity of the sequence, there is a finite but limited amount of non-equivalent samples of length N that can be cut out from different sections of C_∞. In particular, it can be proved the existence of $N + 1$ such realisations, among which one (for even N) or two (for odd N) are reflection symmetric around the center of the chain, while the others possess a symmetric partner each [135]. As already noticed in the context of binary random disorder, reflection symmetry makes difficult to compare the results with those from the other samples [138], while symmetric partners have same eigenvalues and eigenstates. Therefore, after discarding these configurations, there are $N/2$ (if N is even) or $(N - 1)/2$ (for N odd), realisations of the potential to average over.

Chapter 2

Methods

In this Chapter, we present a general overview on the theoretical and numerical tools used to obtain the main results of the thesis. In Sec. 2.1, we review the Landauer-Büttiker framework to describe coherent transport in a non-interacting open system, including technical details on how to compute through Green's function approach the main ingredient of the formalism, i.e. the transmission function, in the case of a fermionic chain with arbitrary on-site potential. Moreover, we provide a general treatment of thermoelectric transport in linear response for a system in the two-terminal configuration and a description of how it can operate as a quantum heat engine, converting heat-to-work through the flowing of non-equilibrium steady-state microscopic currents. We discuss the quantities relative to the conversion, such as transport coefficients, power, and efficiency within the Landauer-Büttiker framework, focusing on the characteristics that the transmission function of the working medium must exhibit in order to maximise the performance of the machine. In Sec. 2.2, we move to isolated many-body systems, in particular, quantum spin chains, and study transport through their unitary dynamics starting from an initial perturbation. We review the general framework of linear response theory and provide an expression for the Onsager coefficients within the Green-Kubo formalism. We consider then the electrical conductivity and discuss how it dictates the transport regimen of the system. Finally, we show how we can gather numerical evidence on the transport properties of the system by connecting the conductivity to the the spread of density correlations, and with the introduction of the notion of quantum dynamical typicality. This approach allows to infer thermal equilibrium properties of the system from the dynamics of a single pure

state, which act as "typical" representative of the statistical ensemble. Finally, in Sec. 2.3, we describe how to derive physical quantities in the energy domain through an expansion in Chebyshev polynomials via the kernel polynomial method. In particular, we show how to employ this technique for spectral properties such as local and global density of states, expectation values in the microcanonical ensemble, and dynamical quantities such as correlation functions.

2.1 Landauer-Büttiker formalism

The formalism, first elaborated by Landauer [139] and later extended by Büttiker to set-ups with multiple terminals [140], constitutes a simple and elegant description of quantum transport. It establishes an explicit connection between the microscopic scattering probabilities of the particles and the conducting properties of the system under study. This framework can be applied to non-interacting or effectively non-interacting particles, as in the case of a mean-field characterisation, and when the scale of the problem is smaller than the lengths at which the particles relax to local thermal equilibrium and no longer possess memory of their phase. In these conditions, transport is said to be "coherent". Due to the simplicity of the picture, and the possibility to generalise it to arbitrary potentials and complex geometries, the Landauer-Büttiker framework has been a fundamental tool for interpreting the results from mesoscopic physics experiments [141–143] and for modelling a wide range of nanostructures, from molecules to quantum dots [16, 17, 144, 145].

We consider the system of interest as a central scattering region S which receives spinless electrons from fermionic reservoirs connected through metallic leads. The reservoirs are large compared to the central system, thus they can at any time be regarded as in thermal equilibrium with well defined chemical potential μ_ν and temperature T_ν. In particular, we focus on a two-terminal set-up, with a left ($\nu = L$), and a right ($\nu = R$) reservoir. The electrons leave the reservoirs and undergo purely elastic scattering events, preserving their energy and phase during the collisions, until they escape again the central region. Any energy dissipation and entropy production is then limited to the reservoirs. The Landauer-Büttiker formalism captures the situation where the system has already reached a non-equilibrium steady state with constant currents induced by the differences in chemical potential and temperature.

The particle J_N and energy J_E currents from the reservoirs to the system can be defined in terms of the particles dN^ν and energy dU^ν leaving or entering reservoir $\nu = L, R$ per unit of time,

$$J_N = -\frac{dN^L}{dt} = \frac{dN^R}{dt}, \qquad J_E = -\frac{dU^L}{dt} = \frac{dU^R}{dt}, \tag{2.1}$$

where we used the fact that both quantities are conserved in the central system, meaning $dN^L + dN^R = 0$ and $dU^L + dU^R = 0$. In particular, with this sign convention the currents are positive when flowing from the left to the right. The same applies to the electric current $J_e = eJ_N$, with e the charge of the electron. Within the Landauer-Büttiker framework, the currents can be computed as

$$J_e = \frac{2e}{h} \int dE\ \tau_{LR}(E)[f_L(E) - f_R(E)], \tag{2.2}$$

$$J_E = \frac{2}{h} \int dE\ E\ \tau_{LR}(E)[f_L(E) - f_R(E)], \tag{2.3}$$

where the factor 2 is due to the spin degeneracy, and

$$f_\nu(E) = \{1 + \exp[(E - \mu_\nu)/k_B T_\nu]\}^{-1} \tag{2.4}$$

is the Fermi-Dirac distribution of bath ν, with h and k_B the Planck and Boltzmann constants, respectively. The transmission function $\tau_{LR}(E)$ encodes the probability for an electron at energy E to tunnel from the left to the right reservoir through the central region. The factor $[f_L(E) - f_R(E)]$ evaluates the number of available states to be occupied by the tunnelling electrons. While electric and energy currents are conserved, the heat currents in the two leads might differ if the electrons perform work while in the central system, as depicted in Fig. 2.1. Making use of the first law of thermodynamics,

$$dU^\nu = dQ^\nu + dW^\nu \qquad \nu = L, R, \tag{2.5}$$

where $dW^\nu = \mu_\nu dN^\nu$ is the work done to reservoir ν, and dQ^ν the heat flowing into it. From the expressions in Eq. (2.1), the heat currents from or into (depending on

the sign) the reservoirs are [146, 147]

$$J_q^L = -\frac{dQ^L}{dt} = J_E - \mu_L J_N,$$
$$J_q^R = \frac{dQ^R}{dt} = J_E - \mu_R J_N. \tag{2.6}$$

Therefore, the difference between the heat currents reads

$$J_q^L - J_q^R = -J_N \Delta\mu. \tag{2.7}$$

The entropy production in each reservoir is defined as

$$\dot{\mathcal{S}}_\nu dt = \frac{dQ^\nu}{T_\nu}, \quad \nu = L, R, \tag{2.8}$$

thus the total entropy production rate in the extended system, since it is zero in the central region, can be related to the heat currents through

$$J_q^L = -T_L \dot{\mathcal{S}}_L, \quad J_q^R = T_R \dot{\mathcal{S}}_R, \tag{2.9}$$
$$\dot{\mathcal{S}} = \dot{\mathcal{S}}_L + \dot{\mathcal{S}}_R = -\frac{J_q^L}{T_L} + \frac{J_q^R}{T_R}. \tag{2.10}$$

We recover the corresponding integral in the Landauer-Büttiker formalism by inserting Eqs. (2.2) and (2.3) into Eq. (2.6),

$$J_q^\nu = \frac{2}{h} \int dE (E - \mu_\nu) \tau_{LR}(E) [f_L(E) - f_R(E)]. \tag{2.11}$$

The fundamental ingredient of the framework is the transmission function $\tau_{LR}(E)$, which encodes the microscopic details of the central system and its coupling to the reservoirs. The original approach is to consider incoming and outgoing modes by solving a scattering problem, and explicitly extract the transmission coefficients from the amplitudes of the resulting wavefunction [148]. We focus, instead, on a method which is more efficient from the numerical point of view, reformulating the situation in non-equilibrium Green's function formalism.

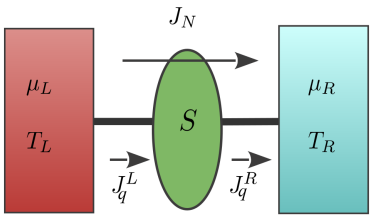

Figure 2.1: Schematic of a typical configuration to study quantum transport. The quantum system of interest S is connected to two reservoirs at thermal equilibrium. When the system has reached a non-equilibrium steady state, it is possible to compute the constant particle J_N, electric $J_e = eJ_N$, and heat currents J_q^L and J_q^R, respectively in the left and right lead, within the Landauer-Büttiker framework.

2.1.1 Green's function approach to transmission

The class of systems usually studied in the configuration of Fig. 2.1 are typically well described by a tight-binding approximation, which can be expressed in matrix representation and gives discrete energy levels. On the other hand, the reservoirs are assumed to be infinitely large when compared to the central system S, thus their energy spectrum is effectively continuous. In the Green's function formalism, the effect of the reservoirs L and R can be included in the matrix representation of the discrete-level system S and the transmission function be expressed in a convenient form for numerical simulations. We focus on one-dimensional models or wires of non-interacting electrons whose Hamiltonian in second quantisation is given by

$$\hat{H}_S = \sum_{n=1}^{N-1} t_h(\hat{a}_n^\dagger \hat{a}_{n+1} + \text{h.c}) + \sum_{n=1}^{N} V_n \hat{a}_n^\dagger \hat{a}_n, \tag{2.12}$$

where t_h is the tunnelling or hopping constant, V_n is the on-site energy of site n, and $\hat{a}_n$ is the fermionic annihilation operator of site n. When the system is isolated, it is straightforward to rewrite the single-particle eigenvalue problem $\hat{H}_S |\psi_\ell\rangle = E_\ell |\psi_\ell\rangle$ in matrix form on the site basis $\{|n\rangle\}_n = \{\hat{a}_n^\dagger |0\rangle\}_n$, with $|0\rangle$ the vacuum state. The matrix takes the form

$$\hat{H}_S = \sum_{nm} [\mathbf{H}_S]_{nm} \hat{a}_n^\dagger \hat{a}_m. \tag{2.13}$$

In particular, we recover with $\sum_{nm} [\mathbf{H}_S]_{nm} \psi_{m\ell} = E_\ell \psi_{n\ell}$ the same set of equations seen in Eq. (1.4) to study quasiperiodic models, if $t_{n,n-1} = t_h$. In this case, $\mathbf{H}_S$ is a $N \times N$ symmetric and tridiagonal matrix, with diagonal entries $\{V_n\}_n$ and off-diagonal entries equal to t_h. The retarded single-particle Green's function of the isolated system

is defined as

$$\mathbf{G}_S^r(E) = \big[\mathbf{E} - \mathbf{H}_S\big]^{-1}, \tag{2.14}$$

where we indicate $\mathbf{E} = (E + i\eta^+)\mathbb{1}$, with $\eta^+ = 0^+$ an infinitesimally small positive number and $\mathbb{1}$ the $N \times N$ identity matrix. The advanced Green's function $\mathbf{G}_S^a(E)$ is defined analogously to Eq. (2.14), with $\mathbf{E} = (E - i\eta^+)\mathbb{1}$. In the rest of the dissertation, however, we consider systems with time-reversal symmetry. As a consequence, the advanced Green's function is always equal to the hermitian conjugate of the retarded Green's function $\mathbf{G}_S^a(E) = [\mathbf{G}_S^r(E)]^\dagger$. Therefore, in the following we refer to $\mathbf{G}_S^r(E)$ simply as Green's function (GF) and drop the r apex. The local density of states on site n can be then expressed as

$$\rho_n(E) = \sum_\ell |\psi_{n\ell}|^2 \delta(E - E_\ell), \tag{2.15}$$

$$\rho_n(E) = -\frac{1}{\pi}\mathrm{Im}[\mathbf{G}_S(E)]_{nn}, \tag{2.16}$$

while the global density of states $\rho(E)$ defined in Eq. (1.12) is obtained by

$$\rho(E) = -\frac{1}{\pi}\mathrm{Tr}\big\{\mathrm{Im}\mathbf{G}_S(E)\big\}. \tag{2.17}$$

In the previous section we studied the spectral properties of isolated one-dimensional systems in the tight-binding approximation. We now connect the tight-binding chain to the two reservoirs, and consider the following total Hamiltonian

$$\hat{H} = \hat{H}_S + \sum_{\nu=L,R} \big(\hat{H}_\nu + \hat{H}_{S\nu}\big), \tag{2.18}$$

which includes also the Hamiltonian of the reservoirs $\hat{H}_\nu$ and their coupling to the system $\hat{H}_{S\nu}$. Each of the reservoirs is described by a quadratic fermionic Hamiltonian with infinitely many degrees of freedom,

$$\hat{H}_\nu = \sum_\ell E_{\ell\nu}\hat{D}_{\ell\nu}^\dagger \hat{D}_{\ell\nu}, \qquad \nu = L, R \tag{2.19}$$

where $E_{\ell\nu}$ are the single-particle eigenenergies of the leads and $\hat{D}_{\ell\nu}$ are annihilation operators for the corresponding eigenmodes. For the moment, we will not make any assumption on the structure of the system-reservoir coupling. The total Hamiltonian

can also be represented in matrix form analogously to Eq. (2.13), with the following block structure [148],

$$\mathbf{H} = \begin{pmatrix} \mathbf{H}_L & \mathbf{H}_{SL} & 0 \\ \mathbf{H}_{SL}^\dagger & \mathbf{H}_S & \mathbf{H}_{SR}^\dagger \\ 0 & \mathbf{H}_{SR} & \mathbf{H}_R \end{pmatrix}, \tag{2.20}$$

whose diagonal entries are the hamiltonian matrices of the system and left and right reservoirs $\mathbf{H}_S$, $\mathbf{H}_L$, $\mathbf{H}_R$, while the off-diagonal entries are the coupling terms $\mathbf{H}_{S\nu}$. As a consequence, the GF for the total extended system shows an analogous block structure,

$$\mathbf{G}(E) = \big[\mathbf{E} - \mathbf{H}\big]^{-1},$$

$$\begin{pmatrix} \mathbf{E} - \mathbf{H}_L & -\mathbf{H}_{SL} & 0 \\ -\mathbf{H}_{SL}^\dagger & \mathbf{E} - \mathbf{H}_S & -\mathbf{H}_{SR}^\dagger \\ 0 & -\mathbf{H}_{SR} & \mathbf{E} - \mathbf{H}_R \end{pmatrix} \begin{pmatrix} \mathbf{G}_L(E) & \mathbf{G}_{SL}(E) & 0 \\ \mathbf{G}_{LS}(E) & \mathbf{G}_S(E) & \mathbf{G}_{RS}(E) \\ 0 & \mathbf{G}_{SR}(E) & \mathbf{G}_R(E) \end{pmatrix} = \mathbb{1}. \tag{2.21}$$

As reviewed in Ref. [148], we derive the GF for the central system $\mathbf{G}_S(E)$ by using the two following equations from the above linear system,

$$(\mathbf{E} - \mathbf{H}_L)\mathbf{G}_{SL}(E) - \mathbf{H}_{SL}\mathbf{G}_S(E) = 0, \tag{2.22}$$

$$-\mathbf{H}_{SR}\mathbf{G}_S(E) + (\mathbf{E} - \mathbf{H}_R)\mathbf{G}_{SR}(E) = 0, \tag{2.23}$$

in order to replace $\mathbf{G}_{SL}(E)$ and $\mathbf{G}_{SR}(E)$ in

$$-\mathbf{H}_{SL}^\dagger\mathbf{G}_{SL}(E) + (\mathbf{E} - \mathbf{H}_S)\mathbf{G}_S(E) - \mathbf{H}_{SR}^\dagger\mathbf{G}_{SR}(E) = \mathbb{1}. \tag{2.24}$$

With this substitution, we arrive to the definition of retarded single-particle non-equilibrium Green's function (NEGF) for the central system,

$$\mathbf{G}_S(E) = \Big[\mathbf{E} - \mathbf{H}_S - \sum_\nu \mathbf{\Sigma}_\nu(E)\Big]^{-1}, \tag{2.25}$$

where we introduce the notion of self-energy,

$$\mathbf{\Sigma}_\nu(E) = \mathbf{H}_{S\nu}^\dagger(\mathbf{E} - \mathbf{H}_\nu)^{-1}\mathbf{H}_{S\nu} = \mathbf{H}_{S\nu}^\dagger\mathbf{G}_\nu(E)\mathbf{H}_{S\nu}. \tag{2.26}$$

The self-energy encodes the presence of the reservoirs, thus it depends only on the GF of the isolated reservoirs $\mathbf{G}_\nu(E) = (\mathbf{E} - \mathbf{H}_\nu)^{-1}$ and on their coupling to the central system. We notice that the NEGF in Eq. (2.25) can be rewritten in the same form as the GF for an isolated system whose effective Hamiltonian $\tilde{\mathbf{H}}_S = \mathbf{H}_S + \sum_\nu \mathbf{\Sigma}_\nu(E)$ is not hermitian. The eigenvalues of the effective Hamiltonian can thus be complex: $\tilde{E}_\ell = E_\ell - \Delta_\ell - i\gamma_\ell/2$, where Δ_ℓ translates into a shift for the original eigenvalues, while the imaginary part γ_ℓ reflects the fact that the electrons injected into the central scattering region will eventually leave it to re-enter the baths [149]. The time dependence of the eigenvectors of the effective Hamiltonian $\boldsymbol{\psi}_\ell = \{\psi_{n\ell}\}_{n=1}^N$ is modified to $e^{-iE_\ell t/\hbar} \to e^{-i(E_\ell - \Delta_\ell)t/\hbar} e^{-\gamma_\ell t/2\hbar}$, and the probability density decays as $|\boldsymbol{\psi}_\ell(t)|^2 \sim e^{-\gamma_\ell t/\hbar}$. The quantity γ_ℓ is then proportional to the inverse average time spent by the particle in state ℓ inside the central region, or, equivalently, the rate at which particles escape into the reservoirs.

After introducing the level-width function, or bath spectral density,

$$\mathbf{\Gamma}_\nu(E) = i[\mathbf{\Sigma}_\nu^\dagger(E) - \mathbf{\Sigma}_\nu(E)], \tag{2.27}$$

the transmission function is given by the Fisher-Lee formula [148–150],

$$\tau_{LR}(E) = \mathrm{Tr}\big\{\mathbf{\Gamma}_L(E)\mathbf{G}_S^\dagger(E)\mathbf{\Gamma}_R(E)\mathbf{G}_S(E)\big\}. \tag{2.28}$$

The crucial aspect in the derivation of the transmission function is the evaluation of the self-energies and level-width functions, which are represented by matrices of infinite dimension. A blunt truncation in the degrees of freedom involves the risk of describing a closed extended system, instead of the original system of interest S in open configuration. However, in most relevant cases it is possible to apply approximations which make the problem tractable. First, we assume in Eq. (2.18) a bilinear system-reservoir coupling of the form

$$\hat{H}_{SL} + \hat{H}_{SR} = \sum_{\ell\ell'} (t_{\ell L}\hat{a}_1^\dagger \hat{D}_{\ell L} + t_{\ell' R}\hat{a}_N^\dagger \hat{D}_{\ell' R} + \mathrm{h.c}), \tag{2.29}$$

where $t_{\ell L}$ and $t_{\ell' R}$ describe the amplitude for electrons respectively in the ℓ-th mode of lead L and ℓ'-th of lead R to tunnel onto the wire. Only the first site of the system is coupled to the left lead L and only the last one is coupled to the right lead R. In

this case, the level width functions or bath spectral densities have only one non-zero element each, $\left[\mathbf{\Gamma}_L(E)\right]_{11} = \mathfrak{J}_L(E)$ and $\left[\mathbf{\Gamma}_R(E)\right]_{NN} = \mathfrak{J}_R(E)$, which assumes the form of a weighted density of states,

$$\mathfrak{J}_\nu(E) = 2\pi \sum_\ell |t_{\ell\nu}|^2 \delta(E - E_{\ell\nu}). \tag{2.30}$$

We also make use of the the wide-band limit (WBL) approximation. The typical energy scales of the reservoirs are considered so large in comparison to those of the central system that it is effectively possible to take spectral densities independent of the energy and purely imaginary self-energies. We also consider identical values: $\mathfrak{J}_L(E) = \mathfrak{J}_R(E) = \gamma$, which we indicate in the following as the coupling strength. Given these approximations, the matrices $\mathbf{\Sigma}_L(E)$, $\mathbf{\Sigma}_R(E)$ and $\mathbf{\Gamma}_L(E)$, $\mathbf{\Gamma}_R(E)$ have the only non-zero element given by

$$\left[\mathbf{\Sigma}_L(E)\right]_{11} = \left[\mathbf{\Sigma}_R(E)\right]_{NN} = -i\gamma/2, \qquad \left[\mathbf{\Gamma}_L(E)\right]_{11} = \left[\mathbf{\Gamma}_R(E)\right]_{NN} = \gamma. \tag{2.31}$$

The expression for the transmission function from Eq. (2.28) thus simplifies to

$$\tau_{LR}(E) = \gamma^2 \left|[\mathbf{G}_S(E)]_{1N}\right|^2. \tag{2.32}$$

The most straightforward example to study is transport through a single level system, with energy ϵ_0. In this case, the NEGF in WBL approximation is a scalar,

$$G_S(E) = \frac{1}{E - \epsilon_0 - \sum_\nu \Sigma_\nu} = \frac{1}{E - \epsilon_0 - i\gamma}, \tag{2.33}$$

and the transmission function can be evaluated analytically,

$$\tau_{LR}(E) = \frac{\gamma^2}{[E - \epsilon_0]^2 + \gamma^2}. \tag{2.34}$$

As shown in Fig. 2.2, the result is a Lorentzian centred in $E = \epsilon_0$, where it reaches the maximum value of 1 at every γ. The coupling strength controls the broadening of the curve, thus the probabilities of transmission on a larger energy window.

When we consider larger system sizes, exact analytical solutions are not accessible even for trivial potentials, so one resorts to numerical inversion of the NEGF matrix. The computational cost of most algorithms for matrix inversion, however, has a scaling

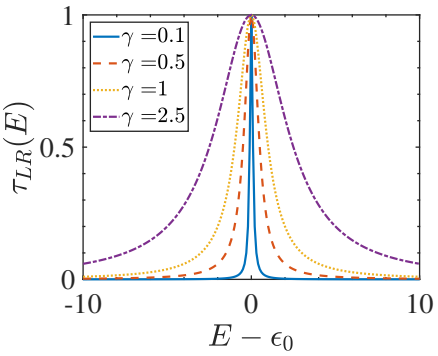

Figure 2.2: The transmission function for a single level model of energy ϵ_0 connected to two reservoirs in WBL approximation, whose analytical expression is given in Eq. (2.34). The coupling strength γ controls the broadening of the Lorentzian, centred in $E = \epsilon_0$ with maximum value of 1.

of $N^{2.8-3}$. As a consequence, simulations can become heavy if the energy grid on which the transmission function needs to be evaluated for the integrals in Eqs. (2.2), (2.3), and (2.11) is fine, as in the case of the fractal spectrum of quasiperiodic models. However, given the form of the coupling and the WBL approximation, the NEGF of Eq. (2.25) is a tridiagonal matrix as the original Hamiltonian. Therefore, it is possible to exploit iterative algorithms to extract the elements of the inverse of tridiagonal matrices, which scale linearly with N. In Fig. 2.3, we show example transmission functions for the Hamiltonian in Eq. (2.12) with constant on-site energies. A clean wire of N sites exhibits N discrete energy levels lying in $E \in [-2, 2]$ when $V_n = 0$ and $t_h = 1$. For $N = 10$, we notice in Fig. 2.3a a transmission function $\tau_{LR}(E)$ that in the limit of small γ consists of a series of δ-shaped peaks corresponding to the energy levels. As γ increases, the peaks broaden and eventually merge at the approximately constant maximum value 1. We observe the same effect for a wire of length $N = 100$, increasing the coupling from $\gamma = 0.1$ in Fig. 2.3b to $\gamma = 2.5$ in Fig. 2.3c. At both lengths, the transmission drops to zero outside of the energy window containing the spectrum.

2.1.2 Linear-response regime

The linear response regime is relevant for numerous experimental platforms, ranging from semiconductor [151, 152] and molecular electronics [144] to ultracold atoms [14], and, furthermore, permits to derive in a more compact way fundamental considerations about thermoelectric effects and the performance of thermoelectric devices.

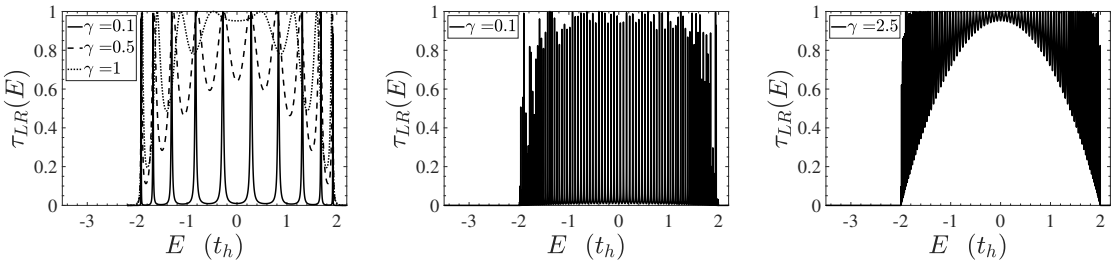

Figure 2.3: Transmission function for the clean one-dimensional tight-binding model when coupled in WBL approximation to two baths, with coupling strength γ ($V_n = 0$ and $t_h = 1$). (a) For $N = 10$ sites, we observe a series of peaks at the eigenergies of the system, which are δ-functions in the limit $\gamma \to 0$ and broaden as γ increases. For $N = 100$ the single peaks are still distinguishable for (b) $\gamma = 0.1$ and look partially merged at (c) $\gamma = 2.5$.

In order to reach this regime, the differences between the chemical potentials $\Delta\mu = \mu_L - \mu_R$ and temperatures $\Delta T = T_L - T_R$ of the two reservoirs in Fig. 2.1 must be small $|\Delta T| << T$, $|\Delta\mu| << k_B T$ [20] compared to the reference thermodynamic quantities $\mu = \mu_R$ and $T = T_R$. The currents can then be expressed as linear combinations of the generalised forces or affinities driving transport [20, 141, 146, 153]. The affinities are identified by considering the set of independent extensive variables $\{X_i\}$ which determine the thermodynamic entropy of the system $\mathcal{S} = \mathcal{S}(X_1, X_2, \dots)$. The entropy production rate can be then formulated as the product of extensive fluxes or currents $J_i = dX_i/dt$ and the affinities $\mathcal{F}_i = d\mathcal{S}/dX_i$ [146],

$$\dot{\mathcal{S}} = \sum_i \frac{d\mathcal{S}}{dX_i}\frac{dX_i}{dt} = \sum_i J_i \mathcal{F}_i. \tag{2.35}$$

There is a certain arbitrariness in defining the independent currents, however, in the study of thermoelectric effects, one usually considers the expression for the entropy production rate given in Eq. (2.10) to isolate J_e and J_q^L, as follows

$$\dot{\mathcal{S}} = \frac{1}{T_R}\left(J_q^L + \frac{J_e \Delta\mu}{e}\right) - \frac{J_q^L}{T_L} = \frac{J_e \Delta\mu}{eT_R} + J_q^L\left(\frac{1}{T_R} - \frac{1}{T_L}\right) = J_e\frac{\Delta\mu}{eT} + J_q^L \Delta\left(-\frac{1}{T}\right), \tag{2.36}$$

where we used Eq. (2.7). The relation between currents and affinities is compactly represented via the Onsager matrix [154] as

$$\begin{pmatrix} J_e \\ J_q \end{pmatrix} = \mathbf{L}\begin{pmatrix} \Delta\mu/eT \\ \Delta T/T^2 \end{pmatrix}, \quad \mathbf{L} = \begin{pmatrix} L_{11} & L_{12} \\ L_{21} & L_{22} \end{pmatrix}. \tag{2.37}$$

As evident from Eq. (2.7), the difference between the heat currents in the left J_q^L and right J_q^R lead is quadratic in the biases $\Delta\mu$, ΔT. The relations obtained within linear response regime are, instead, only accurate to first order in chemical potential and temperature difference, they thus introduce a conserved heat current $J_q = J_q^L \sim J_q^R$ irrespective of whether the system is absorbing or producing electrical work, with the same sign convention of J_N and J_e.

The Onsager coefficients are constrained by the Onsager reciprocal relations, and by the second law of thermodynamics. Firstly, Onsager proved that the diagonal coefficient L_{12} measured in an external magnetic field $\mathbf{B}$ is identical to L_{21} measured in the same reversed magnetic field $-\mathbf{B}$: $L_{12}(\mathbf{B}) = L_{21}(-\mathbf{B})$. If the system is time-reversal invariant, as in absence of external magnetic field, $L_{12} = L_{21}$ always holds [154]. Secondly, the non-negativity of the entropy production rate associated to the transport processes implies that

$$L_{11} \geq 0, \quad L_{22} \geq \frac{(L_{12} + L_{21})^2}{4L_{11}} \geq 0. \tag{2.38}$$

The electrical conductance G, the thermal conductance K, the Seebeck factor (or thermopower) S and the Peltier coefficient Π are defined as

$$G = \left(\frac{J_e}{\Delta V}\right)\bigg|_{\Delta T=0} = \frac{L_{11}}{T}, \tag{2.39}$$

$$K = \left(\frac{J_h}{\Delta T}\right)\bigg|_{J_e=0} = \frac{1}{T^2}\frac{\det \mathbf{L}}{L_{11}}, \tag{2.40}$$

$$S = -\left(\frac{\Delta V}{\Delta T}\right)\bigg|_{J_e=0} = \frac{1}{T}\frac{L_{12}}{L_{11}}, \tag{2.41}$$

$$\Pi = \left(\frac{J_q}{J_e}\right)\bigg|_{\Delta T=0} = \frac{L_{21}}{L_{11}}, \tag{2.42}$$

where we notice that in presence of time-reversal symmetry Π and S differs only by a factor $1/T$. As a consequence of the conditions in Eq. (2.38), the conductances are always positive

$$G \geq 0, \quad K \geq \frac{G(ST - \Pi)^2}{4T} \geq 0, \tag{2.43}$$

while the thermopower S and the Peltier coefficient Π can be negative. The currents

are then re-written as

$$J_e = G\Delta\mu/e + GS\Delta T, \tag{2.44}$$

$$J_q = G\ \Pi\Delta\mu/e + (K + GS\ \Pi)\Delta T. \tag{2.45}$$

with the transport coefficients fully characterising the thermoelectric effects in the non-equilibrium steady state. We explicitly see, in fact, that they couple the electric current to the temperature bias, and the heat current to the chemical potential difference. Moreover, G and K give an indication on the quantum heat and electric transport properties of the central system, as it will be specified in Sec. 2.2.2.

We remark again that the definition of the entropy production rate in Eq. (2.35) allows some freedom in choosing the independent currents and the related affinities. The same formulation described above can be built taking the electric and the energy currents J_e and J_E, instead of electric and heat J_e and J_q. In this case, the affinities are $\tilde{\mathcal{F}}_e = \mathcal{F}_e - \mu\mathcal{F}_q/e$, $\tilde{\mathcal{F}}_E = \mathcal{F}_q$. An analogous Onsager matrix $\tilde{\mathbf{L}}$ can then be derived, with the following relation between the two representations [155, 20],

$$\begin{aligned} L_{11} &= \tilde{L}_{11}, \\ L_{12} = L_{21} &= \tilde{L}_{12} - \frac{\mu}{e}\tilde{L}_{11}, \\ L_{22} &= \tilde{L}_{22} - \frac{2\mu}{e}\tilde{L}_{12} + \left(\frac{\mu}{e}\right)^2 \tilde{L}_{11}, \end{aligned} \tag{2.46}$$

where the same property under time-reversal symmetry holds $\tilde{L}_{12} = \tilde{L}_{21}$.

Within Landauer-Büttiker framework, we obtain the heat and electric currents in linear-response regime by Taylor-expanding at first order the Fermi-Dirac distributions around the reference thermodynamic variables $\mu = \mu_R$ and $T = T_R$,

$$f_L(E) \approx f(E) + \frac{\partial f}{\partial T}\Delta T + \frac{\partial f}{\partial \mu}\Delta\mu = f(E) - f'(E)\left[(E-\mu)\frac{\Delta T}{T} + \Delta\mu\right], \tag{2.47}$$

where

$$f'(E) = \frac{\partial f}{\partial E} = -\frac{1}{4k_BT}\frac{1}{\cosh^2[(E-\mu)/2k_BT]}, \tag{2.48}$$

is an even function centered around μ with a width of order k_BT, which, as shown in Fig. 2.4a, effectively defines the energy window contributing to transport.

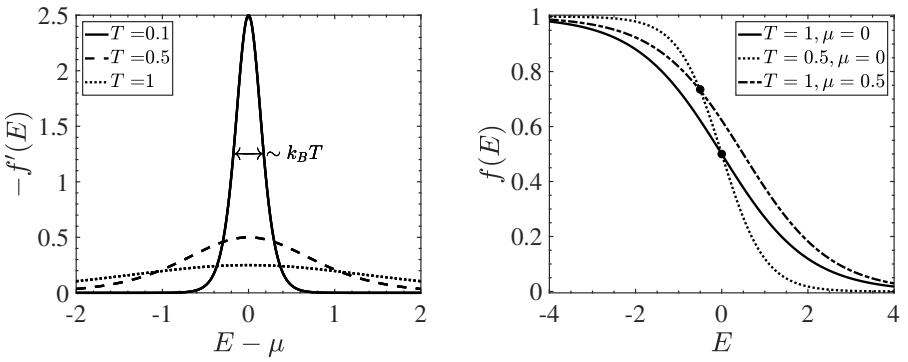

(a) (b)

Figure 2.4: (a) The Fermi-Dirac distribution derivative of Eq. (2.48), with a negative sign. We notice that it is an even function of $(E-\mu)$, different from zero only within an energy window of order $\sim k_BT$. It thus defines the effective energy window contributing to the transport coefficients integrals of Eq. (2.50). (b) Two Fermi-Dirac distributions $f_\nu(E)$ and $f_{\nu'}(E)$ intersect only at one energy E^* (highlighted with black dots in the plotted examples) unless $\mu_\nu = \mu_{\nu'}$ and $T_\nu = T_{\nu'}$, in which case $f_\nu(E) = f_{\nu'}(E)$ on the whole energy axis.

Comparing the result with Eq. (2.37), the Onsager coefficients can be expressed as

$$L_{11} = e^2 T I_0, \quad L_{12} = L_{21} = eTI_1, \quad L_{22} = TI_2, \tag{2.49}$$

where

$$I_k = \frac{2}{h}\int dE(E-\mu)^k \tau_{LR}(E)[-f'(E)]. \tag{2.50}$$

Within this framework, it is possible to formally illustrate by Sommerfeld expansion a result which was first derived phenomenologically, the Wiedemann-Franz (WF) law. The WF law states that in normal conductors at low temperatures the ratio of the thermal conductivity over the product of electrical conductivity and temperature $\mathcal{L}$,

$$\frac{K}{GT} = \mathcal{L}, \quad \mathcal{L}_0 = \frac{1}{3}\left(\frac{\pi k_B}{e}\right)^2, \tag{2.51}$$

is a universal constant known as Lorenz number $\mathcal{L}_0$. In order to derive the law, we Taylor-expand the transmission function $\tau_{LR}(E)$ in $(E-\mu)$, with the expectation that only the first few terms will be important

$$\tau_{LR}(E) = \tau_{LR}(\mu) + \sum_{m=1}^{\infty} \frac{(E-\mu)^m}{m!}\left[\frac{d^m \tau_{LR}(E)}{dE^m}\right]_{E=\mu}. \tag{2.52}$$

As mentioned earlier, $f'(E)$ is different from zero only within a few k_BT around $E=\mu$, thus the integrals of Eq. (2.50) are effectively computed over this limited range of

energies, where we can replace $\tau_{LR}(E)$ with the first terms of its Taylor expansion, provided that it is not too rapidly varying in this energy interval. Furthermore, since $f'(E)$ is an even function and $(E-\mu)f'(E)$ is odd, the leading order term in I_0 and I_2 depends on $\tau(\mu)$, while in I_1 it depends on the first derivative $\frac{d\tau_{LR}(E)}{dE}|_{E=\mu}$. We consider then only the leading order in k_BT of the Sommerfeld expansion [21], by assuming low temperature and making use of the known result

$$\int dE[-f'(E)]\frac{(E-\mu)^{2m}}{2m!} = a_m(k_BT)^{2m}, \tag{2.53}$$

where $a_m = (2-2^{-2(m-1)})\zeta(2m)$, with $\zeta(m)$ the Riemann zeta function. We will need $a_0 = 1$ for I_0, and $2a_1 = \pi^2/3$ for I_1 and I_2. It follows that

$$I_0 = \frac{2}{h}\tau_{LR}(\mu), \quad I_1 = \frac{2\pi^2}{3h}\frac{d\tau_{LR}(E)}{dE}\bigg|_{E=\mu}(k_BT)^2, \quad I_2 = \frac{2\pi^2}{3h}\tau_{LR}(\mu)(k_BT)^2. \tag{2.54}$$

Given that in the integrals I_k the energy range $(E-\mu)$ is contained within few k_BT, the truncation to the first order $m = 1$ of the transmission function in Eq. (2.52) implies also that

$$(k_BT)I_0 >> I_1, \quad I_2/(k_BT) >> I_1, \tag{2.55}$$

such that the expressions for the conductances from Eqs. (2.39) and (2.40) can be approximated to

$$G = e^2 I_0, \quad K = \frac{1}{T}\left(I_2 - \frac{I_1^2}{I_0}\right) \simeq \frac{I_2}{T}. \tag{2.56}$$

By inserting the results from Eq. (2.54) in the formulas above, we finally arrive to the WF law of Eq. (2.51). Beside restricting to low temperature, which allows us to stop at the first order of the Sommerfeld expansion, in order to derive the WF law we have made another essential assumption on the transmission function. We have considered a $\tau_{LR}(E)$ not singular and not too rapidly varying in the neighbourhood of $E = \mu$. Only in this case it is possible to consider the first order in Eq. (2.52) and proceed with the Sommerfeld expansion. As mentioned before, this assumption also implies Eq. (2.55), which translates directly into the fact that the chemical potential difference will contribute weakly to the heat current and the same for temperature bias to the electric current, having $L_{11}L_{22} >> (L_{12})^2$. Therefore, a violation of the WF law in a non-interacting systems at low temperature and small biases signals a strong dependence of the transmission function on the energy, determining the presence of

thermoelectric effects (since the condition in Eq. (2.55) cannot be applied) [156].

2.1.3 Autonomous thermal machines

If thermoelectric effects are present, with simultaneous flows of heat and electric currents, the two-terminal set-up we have discussed can function as an autonomous thermal machine, depending on the thermodynamic variables of the reservoirs. A quantum thermal machine operates without macroscopic elements such pistons, but through the flows of the non-equilibrium steady-state heat and electric currents. The machine is said to be autonomous when the "cycle" it performs is entirely induced by the differences in temperature and chemical potential between the two reservoirs, without any external drive. In such case, the central system constitutes the working medium of the device.

We first introduce the heat engine (h) configuration, already represented schematically in Fig. 2.1, assuming without loss of generality that the left reservoir is hotter than the right one, i.e. $T_L > T_R$, and that it is characterised by a lower chemical potential, i.e. $\mu_L < \mu_R$ or $\Delta\mu < 0$. The temperature difference induces an electrical current J_e from the left reservoir into the right one, against the voltage bias $\Delta V = \Delta\mu/e$. Per unit of time, the central system gains heat J_q^L from the left reservoirs, performs work P when electrons are moved from a low chemical potential to a higher one, and other heat J_q^R is dumped into the right reservoir. The power produced is then

$$P = -J_N\Delta\mu = -J_e\Delta V = J_q^L - J_q^R, \tag{2.57}$$

where in the last equality we used Eq. (2.7). The electrons do not necessarily flow from the hot to the cold reservoirs, in fact the direction of the currents depends on μ_ν and T_ν of each reservoir $\nu = L, R$. However, the sign convention establishes that the system behaves as an heat engine when J_e is driven against a potential difference and $P > 0$ is produced with $J_q^L, J_q^R > 0$, in such case the efficiency is given by

$$\eta^{(h)} = \frac{P}{J_q^L} = 1 - \frac{J_q^R}{J_q^L}, \tag{2.58}$$

analogously to the cyclic engine [147]. By replacing the heat currents with their relation to the entropy production rates in Eq. (2.9) and applying again the second

law of thermodynamics $\dot{S} > 0$, we in fact verify that the definition is consistent with finite time thermodynamics,

$$\eta^{(h)} = \frac{-T_L\dot{S}_L - T_R\dot{S}_R}{-T_L\dot{S}_L} \leq 1 - \frac{T_R}{T_L} = \eta_C^{(h)}, \tag{2.59}$$

since bounded from above by the Carnot efficiency $\eta_C^{(h)}$. A process can reach the limit of Carnot efficiency only when it is perfectly reversible, such that $\dot{S} = 0$. Within the Landauer-Büttiker framework, as mentioned in the discussion on the WF law, the presence of thermoelectric effect and heat-to-work conversion are closely connected to the behaviour of the transmission function. It is known that the transmission function maximising the efficiency to the Carnot limit is a δ-function [38]. The result is general [157, 147] and can be derived by substituting in Eq. (2.10) the integrals for the heat currents of Eq. (2.11),

$$\dot{S} = k_B \int dE \tau_{LR}(E)[f_L(E) - f_R(E)] \ln \frac{f_L(E)[1 - f_R(E)]}{f_R(E)[1 - f_L(E)]}, \tag{2.60}$$

where we used the fact that $(E - \mu_\nu)/k_B T_\nu = (\{\ln[1 - f_\nu(E)] - \ln f_\nu(E)\}$. Since $\tau_{LR}(E) \geq 0$, the integrand is always non-negative. In order to get $\dot{S} = 0$, however, for each E we either need $\tau_{LR}(E) = 0$, or $[f_L(E) - f_R(E)] = 0$. We wish a non-trivial situation with finite transport, where $\tau_{LR}(E) \neq 0$. On the other hand, the term $[f_L(E) - f_R(E)]$, as shown in Fig. 2.4b, can be different from zero only on a single energy E^*, otherwise the two reservoirs would have the same distribution, implying again the absence of transport. From these considerations, it is evident that the transmission function determining $\dot{S} = 0$ can only be of the form $\tau_{LR}(E) = \delta(E - E^*)$, with E^* given by the further condition

$$f_L(E^*) = f_R(E^*), \quad E^* = \frac{T_L\mu_R - T_R\mu_L}{T_L - T_R}. \tag{2.61}$$

Equivalently, recasting the expression for E^*, Carnot efficiency is reached if we apply an optimal chemical potential difference between the reservoirs which depends on the δ-shaped transmission,

$$\Delta\mu = E^*(1 - T_R/T_L). \tag{2.62}$$

We have previously encountered a transmission function of similar nature, when dis-

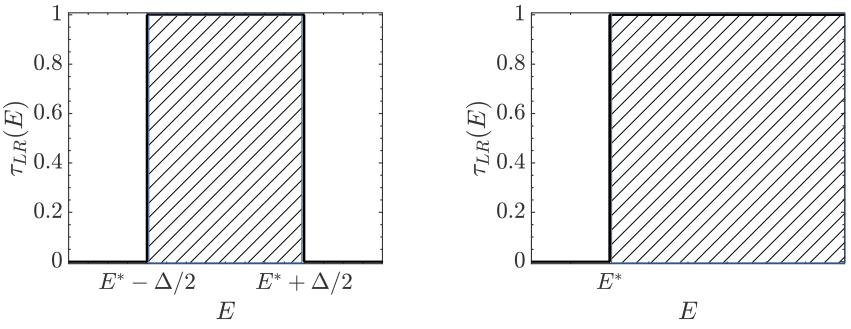

(a) (b)

Figure 2.5: (a) A boxcar transmission function, which is known to optimise the efficiency of the heat engine at a given finite power output. (b) As the required power output increases, the transmission function must be chosen with larger and larger width Δ. In the limit of a perfect step transmission function, the power output is maximised.

cussing the single-level model. If we look again at Fig. 2.2, it appears evident that in the limit of vanishing system-bath coupling $\gamma \to 0$ and tuning its energy level to $\epsilon_0 = E^*$, the efficiency of a heat engine with a single quantum dot as working medium approaches the Carnot limit [17, 12]. As mentioned after introducing the self-energies of Eq. (2.26) in Green's functions formalism, the broadening of the transmission function gives an indication of the rate at which the electrons escape the central system to re-enter the reservoirs. When the transmission function is a Dirac-δ, it takes an infinite average time for an electron to scatter across the central system, or, equivalently, it takes infinite time to operate the machine. This determines, as in the Carnot cyclic engine, zero power output. We show it explicitly by modelling the transmission function with the following boxcar function,

$$\tau_{LR}(E) = \begin{cases} 1 & \text{for} \quad E \in \left[E^* - \frac{\Delta}{2}, E^* + \frac{\Delta}{2}\right], \\ 0 & \text{otherwise}, \end{cases} \tag{2.63}$$

depicted in Fig. 2.5a. The associated power output can be calculated as [39, 158]

$$P = -\frac{2\Delta\mu}{h} \int_{E^*-\Delta/2}^{E^*+\Delta/2} dE[f_L(E) - f_R(E)] = -\frac{d[f_L(E) - f_R(E)]}{dE}\bigg|_{E=E^*} \frac{\Delta\mu}{h}\Delta^2 + \mathcal{O}(\Delta^3), \tag{2.64}$$

and thus vanishes in the limit of $\Delta \to 0$.

Any practical thermoelectric device, however, should give a finite power output, irre-

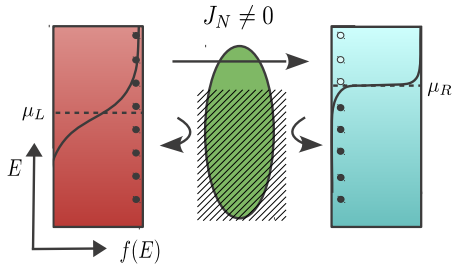

Figure 2.6: An efficient thermoelectric device can be obtained through the use of an energy filter in the central system, blocking the transport at certain energies. The temperature bias drives particle (hole) transport above (below) the chemical potential, leading to zero net electric current in the presence of particle-hole symmetry. Finite electric current and, consequently, output power are instead obtained by differentiating the dynamics of the particles at energies above and below the chemical potential. This mechanism can be realised through transmission functions as in Figs. 2.5a or 2.5b.

spective of its efficiency. This consideration has fuelled numerous studies in irreversible thermodynamics, investigating the transmission function optimised to generate the maximum efficiency at a given finite power output [147, 157–160]. While it can be already seen intuitively in Eq. (2.64), it has been formally proved that such $\tau_{LR}(E)$ is the boxcar function with finite width [158]. A finite power output signals that the engine is not in conditions of perfect reversibility, the efficiency will be thus strictly less than the Carnot limit. There is in fact a definite threshold between efficiency and produced power. The power output, as seen in Eq. (2.64), can be increased with the width of the boxcar transmission function, and it is maximised when the system lets through all particles above or below a certain energy with probability 1, but none at other energies, with a transmission function described by a step-function [39] as in Fig. 2.5b.

When the transmission function can be approximated by a boxcar or a step function, the central system is said to act as an energy filter. This is a mechanism to break the particle-hole symmetry that would otherwise impede thermoelectric power generation. Indeed, in the presence of particle-hole symmetry, heat is transported both by particles above the chemical potential and by holes below the chemical potential. The corresponding charge currents of the particles and the holes compensate each other, leading to zero net power output. As demonstrated in Fig. 2.6, blocking transport in the working medium within a certain energy range allows charge to flow only in one direction, i.e., against the voltage gradient.

In linear response regime, the effect of an energy filter can immediately seen mathe-

matically by using Eq. (2.50) to write the thermopower as

$$S = \frac{1}{eT}\frac{\int dE(E-\mu)\tau_{LR}(E)[-f'(E)]}{\int dE\tau_{LR}(E)[-f'(E)]}. \tag{2.65}$$

Given that $f'(E)$ is an even function of the energy, it is clear that the Seebeck factor will vanish whenever the transmission probability is also an even function. Breaking electron-hole symmetry in the transmission probability is therefore crucial to achieve a finite thermoelectric response. Linear response regime has the further advantage of simplifying all the relevant parameters for the characterisation of the heat-to-work conversion in terms of a single dimensionless parameter [161], the figure of merit

$$ZT = \frac{GS^2T}{K}. \tag{2.66}$$

In particular, the maximum thermodynamic efficiency reachable by the device can be parametrised as [20]

$$\eta^{(h)}_{max} = \eta^{(h)}_C \frac{\sqrt{ZT+1}-1}{\sqrt{ZT+1}+1}. \tag{2.67}$$

Larger values of ZT correspond to higher efficiencies or performance, giving the maximum theoretical limits for $ZT \to \infty$ The efficiency at maximum power in linear response regime can instead be expressed as [20]

$$\eta^{(h)}(P_{max}) = \frac{\eta^{(h)}_C}{2}\frac{ZT}{ZT+2}, \tag{2.68}$$

which for $ZT \to \infty$ tends to $\eta^{(h)}_C/2$. This value corresponds to the Curzon-Ahlborn efficiency [162, 163] expanded at the first order,

$$\eta_{CA} = 1 - \sqrt{\frac{T_L}{T_R}} \approx \frac{\eta_C}{2} + \frac{\eta_C^2}{8} + \mathcal{O}(\eta_C^3). \tag{2.69}$$

As demonstrated in Fig. 2.7, the figure of merit ZT represents then the fundamental index to categorise thermoelectrics [151, 164] (even though it may over- or underestimate the performance of the engine outside of the linear-response regime). Most current thermoelectric devices work with $ZT \approx 1$ and it is often stated that $ZT \approx 3$ would be required in order to compete with alternative technologies [20]. We further observe that the values of $ZT/S^2 = 1/\mathcal{L}$ are constrained to $1/\mathcal{L}_0$ unless the WF law of Eq. (2.51) is violated.

The power produced by the thermoelectric device, however, does not depend only on the characteristics of the device itself and its transmission function, but also on the load powered by it. The attached circuit acts as a resistance R_l, which contributes to determine J_e through the engine at a given applied bias. As a consequence of charge conservation, and if the load is connected in series, the current can be expressed as $J_e = -G_l \Delta V$, where $G_l = 1/R_l$ is the conductance of the load. The current J_e, and thus the power given to the load, is zero if either $R_l = 0$ ($G_l = \infty$), since it is then impossible to apply any potential difference, or $R_l = \infty$ ($G_l = 0$), where no electric current can flow. The voltage building up in the load to stop the current can be found by imposing Eq. (2.44) equal to zero. As it comes naturally from the definition of thermopower, the so-called stopping voltage in the load is $\Delta V_{stop} = -S\Delta T$ [20]. If we replace this expression in the power output $P = -J_e \Delta V$, we find a parabolic curve with maximum power output P_{max} reached when we apply

$$\Delta\mu = \frac{\Delta V_{stop}}{2e} = -\frac{1}{2} S\Delta T, \tag{2.70}$$

between the two reservoirs.

The same considerations on the transmission function which optimises the engine at a given power output can be applied when the device functions as a refrigerator (r) [39, 20]. In this case, the heat current is negative, with heat transported from the right (colder) to the left (hotter) bath, while power is supplied to the system ($P < 0$),

$$J_q < 0, \quad P < 0 \quad \text{(refrigerator regime)}. \tag{2.71}$$

The efficiency of the refrigeration is quantified by the coefficient of performance (COP)

$$\eta^{(r)} = \frac{J_q}{P} \leq \eta_C^{(r)} = \frac{T}{\Delta T}, \tag{2.72}$$

which is characterised by the same figure of merit ZT, and analogous expressions to Eq. (2.67).

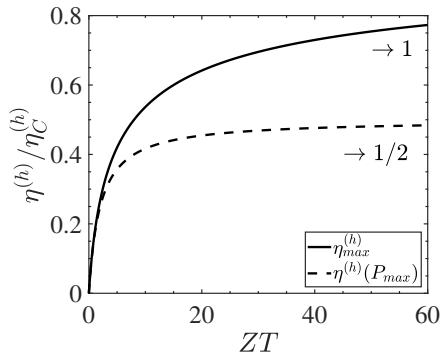

Figure 2.7: The maximum efficiency reachable by a heat engine in linear response regime $\eta_{max}^{(h)}$ (Eq. (2.67)) and the efficiency at maximum power output $\eta(P_{max})$ (Eq. (2.68)), both as a function of the figure of merit ZT. We notice that until approximately $ZT \sim 3$ the two curves lie on top of each other, however for $ZT \to \infty$, $\eta^{(h)}(P_{max}) \to \eta_C^{(h)}/2$, while $\eta_{max}^{(h)} \to \eta_C^{(h)}$ with a slower convergence.

2.2 Linear-response theory in isolated systems

Scattering theory and Landauer-Büttiker type formulae are essential to study transport at the mesoscopic scale and to provide an elegant and effective picture to understand thermoelectric effects on a wide range of experimental platforms. However, despite the possibility of mimicking some kinds of incoherent mechanisms, in their simplest form they represent tools for single-particle systems. In presence of many-body interactions, we need other frameworks to probe particle and thermal transport. In particular, we focus on strongly correlated one-dimensional lattice models in isolated environment. In linear response regime, the currents arise as a response to a weak perturbation which brings the system out of equilibrium [165]. The Green-Kubo formalism gives a relation between transport coefficients and the dynamical correlation function of the currents evaluated at thermal equilibrium [166]. Numerical simulations in this field are computationally heavy, due to the exponential growth in the degrees of freedom, and to the long scales necessary to perform the unitary time-evolution of the initial state, usually described by a density matrix. In this section, we first review the type of Hamiltonians under study in Sec. 2.2.1. Then, we discuss the generalities of Kubo formalism in Sec. 2.2.2 with the connection to the Onsager matrix, and how to classify the transport regimen according to the conductivity in Sec. 2.2.3. Finally, we present in Sec. 2.2.4 a technique to circumvent part of the difficulties in the numerics. Dynamical quantum typicality prescribes the possibility of using a single pure state to reproduce the properties of a full ensemble density matrix, and has been exploited

in numerous studies on quantum spin chains [74, 167–170].

2.2.1 Quantum spin chains

Quantum spin chains, collections of interacting spins embedded on a one-dimensional lattice, constitute a popular testbed to investigate the statistical mechanics of isolated systems and the effect of many-body interactions on transport. The prototypical Hamiltonian presents anisotropic interactions and arbitrary magnetic field $\{V_l\}_{l=1}^N$, and can be written as

$$\hat{H} = \sum_{l=1}^{N-1} [J_{xy}(\hat{s}_l^x \hat{s}_{l+1}^x + \hat{s}_l^y \hat{s}_{l+1}^y) + \Delta \hat{s}_l^z \hat{s}_{l+1}^z] + \sum_{l=1}^{N} V_l \hat{s}_l^z, \tag{2.73}$$

where $\hat{s}_l^\alpha$ are the spin-1/2 operators on site l, fulfilling the commutation relations $[\hat{s}_l^\alpha, \hat{s}_p^\beta] = i\epsilon_{\alpha\beta\gamma}\hat{s}_l^\gamma \delta_{lp}$. As clarified below, J_{xy} indicates the rate of spin exchange, and Δ the strength of the interactions. The most famous example of quantum spin chain is the XXZ model, where $V_l = 0$. The Hamiltonian is composed only of nearest-neighbour interactions, thus it can be split in local factors of the form

$$\begin{aligned} \hat{H} &= \sum_{l=1}^{N-1} \hat{h}_{l,l+1}, \\ \hat{h}_{l,l+1} &= J_{xy}(\hat{s}_l^x \hat{s}_{l+1}^x + \hat{s}_l^y \hat{s}_{l+1}^y) + \Delta \hat{s}_l^z \hat{s}_{l+1}^z + \frac{1}{2}(V_l \hat{s}_l^z + V_{l+1} \hat{s}_{l+1}^z), \end{aligned} \tag{2.74}$$

where the open boundary conditions imply the addition of a factor $V_1 \hat{s}_1^z/2$ to the first term $\hat{h}_{1,2}$, and $V_N \hat{s}_N^z/2$ to the last one $\hat{h}_{N-1,N}$. Although not diagonal on this basis, the Hamiltonian is commonly represented as a matrix operator on the basis of the eigenstates of $\bigotimes_{i=1}^N \hat{s}_i^z$. This is given by the complete set of all the $D = 2^N$ possible combinations to allocate up and down spins along the chain $\{|\uparrow_1 \uparrow_2 \dots \uparrow_N\rangle, |\downarrow_1 \uparrow_2 \dots \uparrow_N\rangle, |\downarrow_1 \downarrow_2 \dots \uparrow_N\rangle, \dots\}$, also called the "computational basis" [171]. The effects of the Hamiltonian on the states of the computational basis can be shown by recasting it as

$$\hat{H} = \sum_{l=1}^{N-1} \left[\frac{J_{xy}}{2}(\hat{s}_l^+ \hat{s}_{l+1}^- + \text{h.c}) + \Delta \hat{s}_l^z \hat{s}_{l+1}^z \right] + \sum_{l=1}^{N} V_l \hat{s}_l^z. \tag{2.75}$$

where $\hat{s}_l^{\pm} = \hat{s}_l^x \pm i\hat{s}_l^y$ are the raising and lowering operators. We observe that the Hamiltonian introduces attraction or repulsion terms depending if neighbouring spins are anti-aligned or aligned, for example

$$\Delta \hat{s}_l^z \hat{s}_{l+1}^z \left|\ldots \uparrow_l \downarrow_{l+1} \ldots\right\rangle = -\Delta \left|\ldots \uparrow_l \downarrow_{l+1} \ldots\right\rangle$$
$$,\Delta \hat{s}_l^z \hat{s}_{l+1}^z \left|\ldots \uparrow_l \uparrow_{l+1} \ldots\right\rangle = +\Delta \left|\ldots \uparrow_l \uparrow_{l+1} \ldots\right\rangle ,$$

and it moves neighbouring excitations along the chain, as in

$$\frac{J_{xy}}{2}(\hat{s}_l^+ \hat{s}_{l+1}^- + \hat{s}_l^- \hat{s}_{l+1}^+) \left|\ldots \uparrow_l \downarrow_{l+1} \ldots\right\rangle = \frac{J_{xy}}{2} \left|\ldots \downarrow_l \uparrow_{l+1} \ldots\right\rangle .$$

However, excitations are neither created or destroyed, signalling that the total magnetisation along z is conserved,

$$\hat{S}^z = \sum_{l=1}^{N} \hat{s}_l^z, \quad [\hat{H}, \hat{S}^z] = 0. \tag{2.76}$$

This symmetry is known as $U(1)$ symmetry, and allows to divide the Hilbert space in sectors and write the Hamiltonian as a block diagonal matrix, each block corresponding to a sector at fixed magnetisation $\langle \hat{S}^z \rangle$. Other operators, such as the generator of the dynamics $\hat{U}(t) = \exp(-i\hat{H}t/\hbar)$, do not mix different excitation sectors. The dimension of each of them is given by the number of possible ways to allocate N_{up} spin up that preserve $\langle \hat{S}^z \rangle$,

$$D^s = \begin{pmatrix} N \\ N_{up} \end{pmatrix} = \frac{N!}{N_{up}!(N - N_{up})!}. \tag{2.77}$$

Numerical simulations are often performed in the largest subsector rather than in the full Hilbert space. For chains with even number of spins, this subsector corresponds to $\langle \hat{S}^z \rangle = 0$ with $N_{up} = N/2$, while for odd number of spins $\langle \hat{S}^z \rangle = \pm 1$, $N_{up} = (N \pm 1)/2$.

The quantum spin chain Hamiltonian of Eq. (2.73) can be mapped into a system of interacting spinless fermions through Jordan-Wigner transformations [172]. In particular, we obtain the one-dimensional tight-binding Hamiltonian of Eq. (2.12), with $t_h = J_{xy}/2$ and the addition of a nearest neighbour density-density interaction

term $\hat{n}_l = \hat{a}_l^\dagger \hat{a}_l$,

$$\hat{H} = \sum_{l=1}^{N-1} \left[\frac{J_{xy}}{2} (\hat{a}_l^\dagger \hat{a}_{l+1} + \text{h.c}) + \Delta \hat{n}_l \hat{n}_{l+1} \right] + \sum_{l=1}^{N} V_l \hat{n}_l + \hat{h}_{BC}. \tag{2.78}$$

The term $\hat{h}_{BC}$ depends on the boundary conditions used, in case of open boundary conditions $\hat{h}_{BC} = (\hat{n}_1 + \hat{n}_L)/2$ up to a constant term. In this picture, the global symmetry concerns the total number of particles,

$$\hat{N} = \sum_{l=1}^{N} \hat{n}_l, \quad [\hat{H}, \hat{N}] = 0, \tag{2.79}$$

and the Hilbert space is divided in subsectors depending on the number of particles present $\langle \hat{N} \rangle = N_{up}$.

2.2.2 Green-Kubo formalism

When the quantum system of interest is isolated, its transport properties can be studied through Kubo formulae, which constitute the core of linear response theory. We consider the isolated system driven out of equilibrium by a small perturbation,

$$\hat{H}'(t) = \hat{H} - b(t)\hat{B}, \tag{2.80}$$

where $\hat{B}$ is a hermitian operator and $b(t)$ a weakly perturbing field with real values, also called the generalised force or affinity coupled to $\hat{B}$. We assume that $b(t)$ vanishes for $t \to -\infty$. Therefore, the system is initially at equilibrium with respect to the original $\hat{H}$, and then coherently evolves in time according to $\hat{H}'$. Linear-response theory describes the consequences of the perturbation on the measured quantities, thus how the expectation value of an observable $\hat{O}$ deviates from the thermal equilibrium value,

$$\delta \langle \hat{O}(t) \rangle = \langle \hat{O}(t) \rangle - \langle \hat{O} \rangle_{eq}. \tag{2.81}$$

Here, the expectation value $\langle \cdot \rangle_{eq} = \text{Tr}\{\cdot \hat{\rho}_{eq}\}$ is taken on the statistical mechanical ensemble described by $\hat{\rho}_{eq}$. When the unperturbed Hamiltonian is invariant under time-reversal symmetry, the response induced by the weakly perturbing field can be

expressed in first order through the so-called "Kubo formula" [165],

$$\delta \langle \hat{O}(t) \rangle = \int_{-\infty}^{\infty} \chi_{BO}(t-t') b(t') dt' + \mathcal{O}(b^2), \tag{2.82}$$

where the linear response function $\chi_{BO}(t-t')$, is a property of the unperturbed system at equilibrium. Due to the stationarity of $\hat{\rho}_{eq}$, the response function depends exclusively on $t-t'$, and is written as [173],

$$\chi_{BO}(t-t') = \frac{i}{\hbar} \theta(t-t') \langle [\hat{O}(t-t'), \hat{B}] \rangle_{eq}, \tag{2.83}$$

where $\theta(t)$ indicates the Heaviside step-function, $\theta(t) = 0$ for $t < 0$ and $\theta(t) = 1$ for $t > 0$. It is evident that $\chi_{BO}(t-t')$ describes the after-effect at time t on the observable $\hat{O}$ to the impulse that coupled the system to the perturbation $\hat{B}$ at an earlier time $t' < t$. For this reason, it is also called "causal" response function. One generally chooses $t' = 0$ without loss of generality.

The linear response function is related to the connected correlation function, defined as

$$C_{BO}(t) = \langle \hat{O}(t) \hat{B} \rangle_{eq} - \langle \hat{O}(t) \rangle_{eq} \langle \hat{B} \rangle_{eq}. \tag{2.84}$$

The correlation function can in general assume complex values, with $C_{BO}(-t) = C^*_{OB}(t)$. However, when the two observables coincide $\hat{O} = \hat{B}$, the autocorrelation $C_{OO}(t)$ is separable into a real and symmetric, and an imaginary and antisymmetric part by virtue of the relation $C_{OO}(-t) = C^*_{OO}(t)$. In order to characterise the correlation between the two observables through a real function, one defines the symmetrised noise or fluctuation function

$$S_{BO}(t) := \langle \{\hat{O}(t), \hat{B}\} \rangle_{eq} - 2 \langle \hat{O}(t) \rangle_{eq} \langle \hat{B} \rangle_{eq}, \tag{2.85}$$

where $\{\cdot, \cdot\}$ indicates the anticommutator. When $\hat{O} = \hat{B}$, this function is also even,

$$S_{OO}(t) = 2C^+_{OO}(t) = 2\,\mathrm{Re}\{C_{OO}(t)\}. \tag{2.86}$$

The symmetric component of the autocorrelation is given by $C^+_{OO}(t) = [C_{OO}(t) + C_{OO}(-t)]/2$. Analogously, the anticommutator determines another quantity, which is

purely imaginary and related to the linear response function in Eq. (2.83),

$$\chi''_{BO}(t) := \frac{1}{2\hbar}\langle[\hat{O}(t)|\hat{B}]\rangle_{eq}\,, \quad \chi_{BO}(t) = 2i\theta(t)\chi''_{BO}(t). \tag{2.87}$$

In the case $\hat{O} = \hat{B}$, it can be related to the imaginary or antisymmetric part of the autocorrelation $C^{-}_{BO}(t) = [C_{BO}(t) - C_{BO}(-t)]/2$, as follows

$$\chi''_{OO}(t) = \frac{1}{\hbar}C^{-}_{OO}(t) = \frac{i}{\hbar}\,\mathrm{Im}\{C_{OO}(t)\}. \tag{2.88}$$

The Fourier transform of $\chi''_{BO}(t)$ is called "spectral density",

$$\chi''_{BO}(\omega) = \int_{-\infty}^{\infty}\chi''_{BO}(t)e^{i\omega t}dt. \tag{2.89}$$

Particular care must be taken when transforming the linear response function to frequency space, since causality ensures analyticity only on the upper half of the complex plane. The Fourier transform of the linear response is called generalised susceptibility,

$$\chi_{BO}(\omega) = \lim_{\epsilon\to 0^+}\int_{-\infty}^{\infty}e^{i(\omega t - i\epsilon t)}\chi_{BO}(t), \tag{2.90}$$

where the exponential factor is inserted to ensure convergence. Despite the misleading notation sometimes adopted in the literature, $\chi''_{BO}(t)$ is not the imaginary part of $\chi_{BO}(t)$. The response function $\chi_{BO}(t)$ is purely real, since it describes the response of an observable, while the generalised susceptibility $\chi_{BO}(\omega)$ can be complex. In frequency space, the following relations hold [174],

$$\chi_{BO}(\omega) = \frac{1}{\pi}\lim_{\epsilon\to 0^+}\int_{-\infty}^{\infty}\frac{\chi''_{BO}(\omega')}{\omega' - \omega - i\epsilon}d\omega', \quad \chi''_{OO}(\omega) = \mathrm{Im}\{\chi_{OO}(\omega)\}. \tag{2.91}$$

In his early study [166], Kubo presents a different version of the linear response function,

$$\chi_{BO}(t) = \beta\theta(t)K_{\dot{B}O}(t), \quad \chi_{BO}(\omega) = \beta\int_{0}^{\infty}K_{\dot{B}O}(t)e^{i\omega t}dt, \tag{2.92}$$

where $\beta = 1/k_BT$ is the inverse temperature of the statistical equilibrium ensemble, and $\hat{\dot{B}} = [\hat{B}, \hat{H}]/(i\hbar)$.

The Kubo canonical correlation function,

$$K_{BO}(t) = \frac{1}{\beta}\int_0^\beta \langle \hat{B}\hat{O}(t + i\hbar\beta')\rangle_\beta \, d\beta', \tag{2.93}$$

was originally calculated in the canonical ensemble $\langle\cdot\rangle_\beta = \mathrm{Tr}\{\cdot\hat{\rho}_c^\beta\}$,

$$\hat{\rho}_c^\beta = \frac{e^{-\beta\hat{H}}}{\mathcal{Z}_c} \tag{2.94}$$

with $\mathcal{Z}_c = \mathrm{Tr}\{e^{-\beta\hat{H}}\}$ the partition function. Its definition can be extended to other ensembles, as the grand-canonical $\langle\cdot\rangle_{\beta,\mu} = \mathrm{Tr}\{\cdot\hat{\rho}_{gc}^{\beta\mu}\}$, with $\hat{\rho}_{gc}^{\beta\mu} = e^{-\beta(\hat{H}-\mu\hat{N})}/\mathcal{Z}_{gc}$. However, in such case it is necessary a connected correlation in the integrand $\langle \hat{B}\hat{O}(t + i\hbar\beta')\rangle_{eq} - \langle\hat{B}\rangle\langle\hat{O}(t + i\hbar\beta')\rangle_{eq}$ [175]. If we consider the canonical ensemble, the following relation holds in frequency space [174],

$$K_{BO}(\omega) = \frac{1 - e^{-\beta\omega\hbar}}{\beta\omega\hbar} C_{BO}(\omega). \tag{2.95}$$

Moreover, we notice that $K_{BO}(t)$ is always real, and even when $\hat{B} = \hat{O}$. In this case, then, its Fourier transform is given simply by

$$K_{OO}(\omega) = 2\int_0^\infty \cos\omega t K_{OO}(t)dt. \tag{2.96}$$

The general framework we have introduced helps building a formal parallelism between the two pictures in which we have seen transport in linear response regime: the open setting, where non-equilibrium steady-state currents are established after the system has been attached to reservoirs, or the closed environment, where a perturbation induces correlation in the isolated system initially at equilibrium. While in the former case, treated in Sec. 2.1.2, we focus on extensive current $J_a = \langle\hat{J}_a\rangle$ associated to the conserved quantity or charge X_a, in the isolated system one assumes local equilibrium and a continuity equation between the current and the charge densities j_a and ϱ_a,

$$\frac{d\hat{\varrho}_a(t)}{dt} = \frac{i}{\hbar}[\hat{H}, \hat{\varrho}_a] = -\nabla\hat{j}_a(t), \tag{2.97}$$

where the variation in the charge density is induced by a local affinity f_a, expressed also in terms of a gradient. Analogously to Eq. (2.37), independent current densities

can be written as linear combination of the corresponding local affinities. Fermionic Hamiltonians as Eq. (2.78), irrespective of $\Delta = 0$ or $\Delta \neq 0$ (or, equivalently, spin Hamiltonians as Eq. (2.73) by Jordan-Wigner transformation), allow to express the global conserved quantity $\hat{N} = \sum_l \hat{n}_l$, charge or total number of particles, and the total energy $\hat{H} = \sum_l \hat{h}_{l,l+1}$ as sums of local operators on different sections (as seen explicitly in Eq. (2.74) for the spin chain). It is then possible to define a continuity equation at each section's edge. Formally, up to boundary terms, one has respectively for the particle/charge current and the energy current

$$e\frac{d\hat{n}_l}{dt} = \frac{ie}{h}[\hat{H}, \hat{n}_l] = \hat{j}_{e,l-1} - \hat{j}_{e,l}, \quad \hat{J}_e = \sum_l \hat{j}_{e,l} \tag{2.98}$$

$$\frac{d\hat{h}_{l,l+1}}{dt} = \frac{i}{h}[\hat{H}, \hat{h}_{l,l+1}] = \hat{j}_{E,l} - \hat{j}_{E,l+1}, \quad \hat{J}_E = \sum_l \hat{j}_{E,l}. \tag{2.99}$$

Their related affinities can be shown to be $\tilde{f}_e = -\nabla(\mu/eT)$, and $\tilde{f}_E = \nabla(1/T)$ [175], thus

$$j_a = \sum_b \tilde{\lambda}_{ab}\tilde{f}_b, \quad a, b = e, E. \tag{2.100}$$

The coefficients $\tilde{\lambda}_{ab}$ form an Onsager matrix $\tilde{\boldsymbol{\lambda}}$ equivalent to $\tilde{\mathbf{L}}$ in Eq. (2.46), and in the thermodynamic limit can be computed in terms of the Kubo correlation function introduced in Eq. (2.93), as follows [20, 155, 175]

$$\tilde{\lambda}_{ab} = \lim_{\omega\to 0} \mathrm{Re}\{\tilde{\lambda}_{ab}(\omega)\}, \quad \tilde{\lambda}_{ab}(\omega) = \beta \lim_{t\to\infty} \lim_{N\to\infty} \frac{1}{N} \int_0^t dt' e^{i\omega t'} K_{J_a \dot{B}_b}(t'). \tag{2.101}$$

We notice that the above expression has a similar form to Eq. (2.92), with $\hat{B}_b$ the operator coupling the affinity $\tilde{f}_b$ to the system, in this case $\hat{\dot{B}}_e = T\hat{J}_q$ and $\hat{\dot{B}}_E = T\hat{J}_E$ [175]. The Onsager coefficients $\tilde{\lambda}_{ab}$ determine the corresponding transport coefficients, according to relations analogous to Eqs. (2.39) - (2.42), involving conductivities instead of conductances. In absence of direct coupling between energy and electric current density ($\tilde{\lambda}_{12} = \tilde{\lambda}_{21} = 0$), the electrical and thermal conductivities are given by the generalised Green-Kubo formulae,

$$\sigma_{GK} = \frac{\tilde{\lambda}_{ee}}{T} \tag{2.102}$$

$$\tilde{\kappa}_{GK} = \frac{\tilde{\lambda}_{EE}}{T^2}. \tag{2.103}$$

The order of the limits in Eq. (2.101) is crucial to obtain the closed-system conductivities. First, one takes the limit of infinite system size N, and only then the limit of infinite time, to avoid probing finite size effects instead of targeting the bulk. In this way, the system can be considered effectively isolated, with no effect from any bath. In an open environment, the system first reaches the non-equilibrium steady state in the infinite time limit, and then the currents are evaluated $J_e = \langle \hat{J}_e \rangle$, $J_E = \langle \hat{J}_E \rangle$ at finite size (as we noticed in the prescription of the Landauer-Büttiker integrals in Eq. (2.50) for non-interacting systems). In case of diffusion, the macroscopic current in the open system obeys the phenomenological laws,

$$J_e = \sigma \Delta\mu / eN, \tag{2.104}$$

with open system conductivity σ (equivalent considerations can be made for κ and K in heat representation, or $\tilde{\kappa}$ and $\tilde{K}$ in energy representation). In the thermodynamic limit, we have the equivalence

$$\sigma = \lim_{N\to\infty} NG. \tag{2.105}$$

In case of diffusive transport, the conductivity σ is constant and independent of N, hence the corresponding conductance scales as

$$G \sim N^{-\alpha_G}, \tag{2.106}$$

with $\alpha_G = 1$. For ballistic transport, the current is independent of system size, thus $\alpha_G = 0$. Anomalous behaviours emerge when $0 < \alpha_G < 1$, when transport is said to be superdiffusive, or $\alpha_G > 1$, when transport is said subdiffusive. We notice that in the ballistic and superdiffusive case, the conductivity diverges, while it is zero in case of subdiffusion or in absence of transport, where $G \sim e^{-N}$. The same classification can be applied to heat transport according to the scaling exponent of the thermal conductance,

$$K \sim N^{-\alpha_K}. \tag{2.107}$$

The classification of transport in the open system setting is generally expected to agree with what we will extract from the Kubo formulae in the case of isolated system. However, there can be situations in which the effect of the boundary between the system and the bath leads to different predictions [176].

2.2.3 Classification of transport

We focus again in this section on the electrical conductivity from the Green-Kubo formula. In order to procede with the discussion, we re-write Eq. (2.101) and Eq. (2.102) at finite ω as [175],

$$\begin{aligned}\sigma_{GK}(\omega) &= \lim_{t\to\infty}\lim_{N\to\infty}\frac{1}{N}\,\mathrm{Re}\left\{\int_0^t dt' e^{i\omega t'} K_{J_eJ_e}(t')\right\} \\ &= \frac{1-e^{-\beta\omega\hbar}}{\omega\hbar}\lim_{t\to\infty}\lim_{N\to\infty}\frac{1}{N}\,\mathrm{Re}\left\{\int_0^t dt' e^{i\omega t'} C_{J_eJ_e}(t')\right\},\end{aligned} \tag{2.108}$$

where we have exploited the symmetry property of the Kubo correlation function from Eq. (2.96), and its relation with the connected correlation in Eq. (2.95). In order to classify transport, we want to evaluate the real conductivity at small frequencies, $\sigma_{GK}(\omega\to 0)$. The conductivity is usually decomposed into a singular and a regular part,

$$\sigma_{GK}(\omega) = 2\pi D_{ee}^W \delta(\omega) + \sigma_{GK}^{reg}(\omega), \tag{2.109}$$

where the Drude weight is given by

$$D_{ee}^W = \frac{\beta}{2}\lim_{t\to\infty}\lim_{N\to\infty}\frac{1}{t}\int_0^t dt'\,\mathrm{Re}\{C_{J_eJ_e}(t')\}. \tag{2.110}$$

A finite Drude weight implies a correlation function that does not decay to zero in the limit of infinite time, but reaches a plateau and gives a conductivity which diverges linearly with system size in the thermodynamic limit, physically translating into ballistic transport. The non-zero plateau is typically an indication of the existence of an extensive number of conserved local quantities in the system [177, 178], which is then said "integrable". A vanishing Drude weight, instead, is associated with diffusive or anomalous behaviour. If $D_{ee}^W = 0$, we distinguish then three possibilities:

(i) if $\sigma_{GK}^{reg}(0)/\beta$ is finite, it is possible to write a phenomenological law $J_e = -De\nabla n$, where D is the diffusion coefficient and ∇n the gradient in the particle density, and in such case, transport is diffusive,

(ii) if $\sigma_{GK}^{reg}(\omega\to 0)/\beta \to \infty$ (with a slower divergence than $|\omega|^{-1}$, since the Drude weight is zero), then transport is superdiffusive,

(iii) if $\sigma_{GK}^{reg}(0)/\beta = 0$, transport is subdiffusive.

If $D_{ee}^{W}/\beta \neq 0$, then the transport regimes listed in (i)-(iii) should be interpreted as subleading corrections to ballistic transport [175].

Taking the limit $\omega \to 0$ in Eq. (2.109), we finally arrive to

$$\sigma_{GK}(\omega \to 0) = \beta \lim_{t\to\infty} \lim_{N\to\infty} \frac{1}{N} \mathrm{Re}\left\{ \int_0^t dt' C_{J_e J_e}(t') \right\}. \tag{2.111}$$

If the Hamiltonian of the system has time translation and time-reversal symmetry, the electrical conductivity at zero frequency $\omega \to 0$ can be related to the spread of density-density correlations, or density spatial variance

$$\Sigma^2(t) = 4 \sum_{p,q=1}^{N} (p-q)^2 C_{pq}(t) \tag{2.112}$$

where we define the density-density correlation,

$$C_{pq}(t) = \langle \hat{n}_p(t) \hat{n}_q \rangle_{eq} - \langle \hat{n}_p(t) \rangle_{eq} \langle \hat{n}_q \rangle_{eq}, \tag{2.113}$$

evaluated on the thermal statistical ensemble, which encodes macroscopic thermodynamic variables as T and μ. Since we consider systems in open boundary conditions, the position operator $\hat{x}$ is well-defined [179], and can be used to write the total particle current $\hat{J} = \hat{J}_e/e$,

$$\hat{x} = \sum_{p=1}^{N} p \hat{n}_p, \quad \hat{J} = \frac{d\hat{x}}{dt}. \tag{2.114}$$

Then, starting from the equivalence

$$\langle \hat{J}(t_1) \hat{J}(t_2) \rangle_{eq} = \frac{d}{dt_1} \frac{d}{dt_2} \left(\sum_{p,q=1}^{N} pq \langle \hat{n}_p(t_1) \hat{n}_q(t_2) \rangle_{eq} \right), \tag{2.115}$$

and using time translational invariance of the equilibrium state to change variable to $t = t_1 - t_2$, we obtain

$$\langle \hat{J}(t) \hat{J} \rangle_{eq} = -\frac{d^2}{dt^2} \left(\sum_{p,q=1}^{N} pq \langle \hat{n}_p(t) \hat{n}_q \rangle_{eq} \right). \tag{2.116}$$

Now, we apply the substitution $2pq = p^2 + q^2 - (p-q)^2$, considering the fact that the

Hamiltonian is number conserving $\frac{d\left(\sum_{p=1}^{N}\hat{n}_p(t)\right)}{dt}=0$, hence

$$\langle\hat{J}(t)\hat{J}\rangle_{eq}=\frac{1}{2}\frac{d^2}{dt^2}\left(\sum_{p,q=1}^{N}(p-q)^2\langle\hat{n}_p(t)\hat{n}_q\rangle_{eq}\right),$$
$$\int_0^t dt'\langle\hat{J}(t')\hat{J}\rangle_{eq}=\frac{1}{2}\frac{d}{dt}\left(\sum_{p,q=1}^{N}(p-q)^2\langle\hat{n}_p(t)\hat{n}_q\rangle_{eq}\right). \tag{2.117}$$

Therefore Eq. (2.111) becomes,

$$\sigma_{GK}(\omega\to 0)=\frac{\beta}{2}\lim_{t\to\infty}\lim_{N\to\infty}\frac{1}{N}\frac{d}{dt}\,\mathrm{Re}\left\{\sum_{p,q=1}^{N}(p-q)^2C_{pq}(t)\right\}. \tag{2.118}$$

Further simplification are possible if the system exhibits translational invariance in the thermodynamic limit. In such case, $C_{pq}(t)$ becomes almost independent on q for large enough system sizes, $N\to\infty$. Therefore, we can fix $q=N/2$. Furthermore, we take the limit of infinite temperature, where the correlation function and thus the spatial variance in Eq. (2.112) are real,

$$\lim_{\beta\to 0}\frac{1}{\beta}\sigma_{GK}(\omega\to 0)=\frac{e^2}{8}\lim_{t\to\infty}\lim_{N\to\infty}\frac{1}{N}\frac{d}{dt}\Sigma^2(t), \tag{2.119}$$

where now the spread of correlation is evaluated on the thermal statistical ensemble at infinite temperature,

$$\Sigma^2(t)=4\sum_{p=1}\left(p-\frac{N}{2}\right)^2C_p(t), \tag{2.120}$$
$$C_p(t)=\langle\hat{n}_p(t)\hat{n}_{N/2}\rangle_\infty-\langle\hat{n}_p(t)\rangle\langle\hat{n}_{N/2}\rangle_\infty. \tag{2.121}$$

The scaling with time of $\Sigma^2(t)$ gives an indication of the nature of high-temperature transport in the system. It captures the influence of a finite Drude weight, implying ballistic transport, when $\Sigma(t)\sim t^\nu$, with $\nu=2$. Otherwise, once defined the time-dependent diffusion coefficient at high temperature,

$$\mathcal{D}(t)=\lim_{\beta\to 0}\lim_{N\to\infty}\frac{1}{N}\int_0^t dt'C_{JJ}(t'), \tag{2.122}$$

we can further derive the following relation,

$$\frac{d\Sigma^2(t)}{dt} = 8\mathscr{D}(t). \tag{2.123}$$

When transport is diffusive, the diffusion coefficient must be constant, $\mathscr{D}(t) = \mathscr{D}$ and hence $\Sigma^2(t) = 8\mathscr{D}t$. If $\mathscr{D}(t)$ diverges with a power less than 1, then transport is superdiffusive. If, instead, $\mathscr{D}(t)$ decreases with time, it points to subdiffusion, while $\mathscr{D}(t) = 0$ determines lack of transport. Therefore, the spatial variance is assumed to grow with a power law, whose exponent depends in general on the transport regime,

$$\Sigma^2(t) \sim t^{\nu} \begin{cases} \nu = 2 & \text{ballistic transport,} \\ 1 < \nu < 2 & \text{superdiffusion,} \\ \nu = 1 & \text{diffusion,} \\ 0 < \nu < 1 & \text{subdiffusion,} \\ \nu = 0 & \text{no transport.} \end{cases} \tag{2.124}$$

Although $\nu = 1$ is a necessary condition for diffusion, the spatial variance yields no information on the width of the profile, while the presence of diffusive transport can be strictly verified only when the full spatial dependence of the profile is described by the diffusion equation [175]. Furthermore, despite the crucial order in taking the limits, first infinite system size and only then infinite time, in numerics the system size will always be finite. In order to compute the exponent ν numerically, one usually evaluates the scaling of $\Sigma^2(t)$ at finite system sizes, up to times before finite-size effects become substantial. In the next section, we further introduce a notion that will allow us to replace the ensemble average in $\Sigma^2(t)$ with a single pure state, the dynamical quantum typicality.

We conclude this section by mentioning a simple scaling analysis [50] to connect quantitatively the exponent ν linked to the Green-Kubo conductivity in the isolated system, with the scaling exponent of the conductance α_G in the open system setting, seen in Eq. (2.106). The argument leads to a relation which holds in general, but not necessarily in cases where the effect of the boundary between the baths and the system invalidates the exchange of infinite time and infinite system size limits in computing open and isolated system conductivities, as in presence of multifractal

states [176, 32]. Given the power law growth in time of the spread of correlation, the time taken by a single exciton to go across the system scales as $t_N \sim N^{2/\nu}$. The current at fixed density can be written then as $J_e \sim N/t_N \sim N^{-\alpha_G}$, determining the following relation [180, 175]

$$\nu = \frac{2}{\alpha_G + 1}. \tag{2.125}$$

In particular, for a non-interacting chain of fermions as in Eq. (2.78) with $\Delta = 0$, the exponent α_G can be extracted within the Landauer-Büttiker framework. The exponent ν, instead, can be more simply evaluated from the scaling of the mean square displacement of an initially localised wavepacket,

$$\Delta x^2(t) = \sum_l \left[(l - N/2)^2 \ |\Psi_l(t)|^2\right] \sim t^\nu, \tag{2.126}$$

with $|\Psi(0)\rangle = \sum_l \Psi_l(0)\hat{a}_l^\dagger |0\rangle$, $|0\rangle$ the vacuum state, and $\Psi_l(0) = \delta_{lN/2}$. The spread of correlation $\Sigma^2(t)$ can in fact be shown (in Appendix A) to reduce to the mean square displacement $\Delta x^2(t)$ in non-interacting systems. However, there can be situations in which the effect of the boundary between the system and the bath leads to different predictions, which diverge from the relation in Eq. (2.125).

2.2.4 Typicality and density correlations

When the Hamiltonian includes many-body interactions, the evaluation of its dynamics is arduous to compute numerically due to the exponential increase of the Hilbert space dimension $D = \dim\mathcal{H}$ with the number of degrees of freedom in the system, and remains challenging even when it can be restricted to symmetry sectors. Popular techniques, such as the time-dependent density matrix renormalisation group (tDMRG) [181] can push the simulations to large spin chains of sizes $N \sim 200$, but are limited to short times due to the growth of entanglement, and cannot generally reach the time scales required to study equilibrium properties. However, it is possible to exploit the concept of dynamical quantum typicality (DQT) to circumvent part of these difficulties. The approximation tells that it is possible to infer the dynamics of the system from a single pure state $|\psi\rangle$ drawn at random on an arbitrary basis $\{|\phi_k\rangle\}_{k=1}^D$, which is considered a "typical" representative of the statistical ensemble [182, 183]. We discuss below the idea of DQT and how it can be used to calculate

spread of density correlations following a perturbation over a thermal state, following the approach originally presented in Refs. [74, 168–170, 184]. As we discussed in the previous section, the spread of density correlation is often used to classify the transport regimes of isolated systems.

We write explicitly the typical state on an arbitrary basis $\{|\phi_k\rangle\}_k$ as

$$|\psi\rangle = \hat{R}\sum_{k=1}^{D}\xi_k\,|\phi_k\rangle\,, \qquad \xi_k = a_k + ib_k, \tag{2.127}$$

with $\hat{R}$ an arbitrary linear operator, and a_k and b_k mutually independent random variables from Gaussian distributions with zero mean and variance 1/2. Therefore, performing the statistical ensemble average, indicated henceforth by the overline, gives as result,

$$\overline{a_k} = \overline{b_k} = 0, \quad \overline{a_k^2} = \overline{b_k^2} = \frac{1}{2}, \tag{2.128}$$

and, exploiting the mutual independence of the two variables,

$$\overline{\xi_k^*\xi_j} = \delta_{kj}, \quad \overline{\xi_k^*\xi_j\xi_m^*\xi_n} = \delta_{kj}\delta_{mn} + \delta_{mj}\delta_{kn}. \tag{2.129}$$

It can be shown from the properties of the coefficients that the statistical averaged expectation value of an arbitrary Hermitian operator $\hat{O}$ in the typical state is equivalent to the expectation value taken with respect to a density matrix $\hat{\rho}$, as follows

$$\begin{aligned}\overline{O} = \overline{\langle\psi|\hat{O}|\psi\rangle} &= \sum_{k,j=1}^{D}\overline{\xi_k^*\xi_j}\,\langle\phi_k|\hat{R}^\dagger\hat{O}\hat{R}|\phi_j\rangle = \sum_{k=1}^{D}\langle\phi_k|\hat{R}^\dagger\hat{O}\hat{R}|\phi_k\rangle \\ &= \mathrm{Tr}\{\hat{R}^\dagger\hat{O}\hat{R}\} = \mathrm{Tr}\{\hat{R}\hat{R}^\dagger\hat{O}\} = \mathrm{Tr}\{\hat{\rho}\hat{O}\},\end{aligned} \tag{2.130}$$

where the density matrix is then defined as

$$\hat{\rho} = \hat{R}\hat{R}^\dagger. \tag{2.131}$$

Since the density matrix is positive semi-definite, it can always be written in the above form. Thus, any mixed state $\hat{\rho}$ can be represented in terms of an ensemble of typical pure states, once found the appropriate $\hat{R}$. The variance of sample to sample

fluctuations in taking the statistical average over the distribution

$$\sigma_O^2 = \overline{\left(\langle\psi|\hat{O}|\psi\rangle\right)^2} - \left(\overline{O}\right)^2, \tag{2.132}$$

can be shown to assume a simple expression using again the properties of the coefficients in Eq. (2.129). The first term in the variance becomes

$$\begin{aligned}\overline{\left(\langle\psi|\hat{O}|\psi\rangle\right)^2} &= \sum_{k,j,m,n=1}^{D} \overline{\xi_k^*\xi_j\xi_m^*\xi_n}\, \langle\phi_k|\hat{R}^\dagger\hat{O}\hat{R}|\phi_j\rangle\, \langle\phi_m|\hat{R}^\dagger\hat{O}\hat{R}|\phi_n\rangle \\ &= \sum_{k,j,m,n=1}^{D} (\delta_{kj}\delta_{mn} + \delta_{mj}\delta_{kn})\, \langle\phi_k|\hat{R}^\dagger\hat{O}\hat{R}|\phi_j\rangle\, \langle\phi_m|\hat{R}^\dagger\hat{O}\hat{R}|\phi_n\rangle \\ &= (\overline{O})^2 + \mathrm{Tr}\{(\hat{\rho}\hat{O})^2\}. \end{aligned} \tag{2.133}$$

The variance is thus given by

$$\sigma_O^2 = \mathrm{Tr}\{(\hat{\rho}\hat{O})^2\}, \tag{2.134}$$

and can be bounded from above by applying the triangle inequality to the two operators $\hat{O}_1 = \hat{O}\hat{\rho}$ and $\hat{O}_2 = \hat{\rho}\hat{O}$,

$$\begin{aligned}&|\mathrm{Tr}\{\hat{O}_1^\dagger\hat{O}_2\}|^2 \leq \mathrm{Tr}\{\hat{O}_1^\dagger\hat{O}_1\}\mathrm{Tr}\{\hat{O}_2^\dagger\hat{O}_2\}, \\ &|\mathrm{Tr}\{(\hat{\rho}\hat{O})^2\}|^2 \leq \left(\mathrm{Tr}\{\hat{\rho}^2\hat{O}^2\}\right)^2 \quad \Longrightarrow \quad \sigma_O^2 \leq \mathrm{Tr}\{\hat{\rho}^2\hat{O}^2\}. \end{aligned} \tag{2.135}$$

We can further bound the variance by carrying out the trace on the eigenbasis of the operator $\hat{O}\,|o_k\rangle = o_k\,|o_k\rangle$,

$$\begin{aligned}\sigma_O^2 \leq \mathrm{Tr}\{\hat{\rho}^2\hat{O}^2\} &= \sum_{k=1}^{D} \langle o_n|\hat{\rho}^2|o_k\rangle \\ &\leq \left(\max\{o_k\}\right)^2 \sum_{k=1}^{D} o_k^2\, \langle o_n|\hat{\rho}^2|o_k\rangle = \|\hat{O}\|^2\mathrm{Tr}\{\hat{\rho}^2\}, \end{aligned} \tag{2.136}$$

with $\|\hat{O}\|^2 = \left(\max\{o_k\}\right)^2$, and $\mathrm{Tr}\{\hat{\rho}^2\}$ the purity of the state $\hat{\rho}$. For highly mixed state in a high dimensional Hilbert space $\mathrm{Tr}\{\hat{\rho}^2\} \ll 1$. In such cases, the sample to sample fluctuations in doing the ensemble average also become small, so that, for a large enough system size, a small number of realisations is enough to calculate expectation values of operators [185].

Canonical ensemble averages $\langle\hat{O}\rangle_\beta = \mathrm{Tr}\{\hat{O}\hat{\rho}_c^\beta\}$, introduced in Eq. (2.94), can be then

evaluated as

$$\langle \hat{O} \rangle_\beta = \overline{\langle \psi_\beta | \hat{O} | \psi_\beta \rangle}, \tag{2.137}$$

where the so-called "canonical thermal pure quantum state" [186] is taken as

$$|\psi_\beta\rangle = \frac{e^{-\beta \hat{H}/2}}{\sqrt{\mathcal{Z}_c}} \sum_{k=1}^{D} \xi_k \, |\phi_k\rangle \, . \tag{2.138}$$

In particular, in the infinite temperature limit, the partition function $\mathcal{Z}_c$ is known, and, since the state is completely mixed, essentially one typical state realisation can be used as representative of the whole ensemble:

$$\hat{\rho}_c^\infty = \frac{\mathbb{1}}{D}, \qquad |\psi_\infty\rangle = \frac{1}{\sqrt{D}} \sum_{k=1}^{D} \xi_k \, |\phi_k\rangle \, . \tag{2.139}$$

The formulation described above does not depend on any specific property of the operator $\hat{O}$, that can also be constituted by a combination of operators in the Heisenberg picture, so that both the dynamics, as well as correlation functions can be obtained. For these reasons, it is referred to as "dynamical quantum typicality" (DQT).

Here, we focus on the density-density correlations, defined in Eq. (2.113), evaluated in the thermal statistical ensemble at infinite temperature for a system of interacting fermions as in the Hamiltonian of Eq. (2.78). In the framework of linear response theory, in fact, correlation functions can be connected to the transport properties of the isolated system in the thermodynamic limit. At infinite temperature, the correlation function is real, and it reads

$$\begin{aligned} C_{pq}(t) &= \langle \hat{n}_p(t) \hat{n}_q \rangle_\infty - \langle \hat{n}_p \rangle_\infty \langle \hat{n}_q \rangle_\infty = \frac{\mathrm{Tr}\{\hat{n}_p(t)\hat{n}_q\}}{2^N} - \frac{\mathrm{Tr}\{\hat{n}_p\}}{2^N} \frac{\mathrm{Tr}\{\hat{n}_q\}}{2^N} \\ &= \frac{\mathrm{Tr}\{\hat{n}_p(t)\hat{n}_q\}}{2^N} - \frac{1}{4}, \end{aligned} \tag{2.140}$$

where we have used $D = 2^N$, and $\mathrm{Tr}\{\hat{n}_l\} = 2^{N-1}$. We can further simplify by using $\hat{n}_q^2 = \hat{n}_q$,

$$\begin{aligned} C_{pq}(t) &= \frac{\mathrm{Tr}\{\hat{n}_p(t)\hat{n}_q\hat{n}_q\}}{2^N} - \frac{1}{4} = \frac{\mathrm{Tr}\{\hat{n}_q\hat{n}_p(t)\hat{n}_p\}}{2^N} - \frac{1}{4} \\ &= \overline{\langle \psi_q | \hat{n}_l(t) | \psi_q \rangle} - \frac{1}{4} \approx \langle \psi_q | \hat{n}_l(t) | \psi_q \rangle - \frac{1}{4}. \end{aligned} \tag{2.141}$$

In the last line, we have exploited typicality with [168–170]

$$|\psi_q\rangle = \hat{n}_q\,|\psi_\infty\rangle\,, \tag{2.142}$$

and considered that, at large system sizes, one single realisation of $|\psi_\infty\rangle$ is enough to guarantee negligible sample to sample fluctuations. After we normalise the above state,

$$|\tilde{\psi}_q\rangle = \frac{1}{\sqrt{C}}\,|\psi_q\rangle\,, \quad C = \langle\psi_\infty|\hat{n}_q|\psi_\infty\rangle \approx \overline{\langle\psi_\infty|\hat{n}_q|\psi_\infty\rangle} = \frac{\mathrm{Tr}\{\hat{n}_q\}}{2^N} = \frac{1}{2}$$
$$\implies |\tilde{\psi}_q\rangle = \sqrt{2}\tilde{\psi}_q, \tag{2.143}$$

the density-density correlation in the typicality approximation is given by

$$C^{typ}_{pq}(t) = \frac{1}{2}\Big(\,\langle\tilde{\psi}_q|\hat{n}_p(t)|\tilde{\psi}_q\rangle - \frac{1}{2}\Big). \tag{2.144}$$

We observe then that the density-density correlation $C_{pq}(t)$ can be inferred from the dynamics of the expectation value of $\hat{n}_p$ after a quench induced by the normalised projection of a typical state onto the subspace where the site q is occupied [168–170]. The subtraction of $1/2$ within the parentheses amounts to subtracting the background initial occupation of sites away from q, where $|\tilde{\psi}_q\rangle$ is initially localised. We notice, in fact, that for $p \neq q$

$$\langle\tilde{\psi}_q|\hat{n}_p|\tilde{\psi}_q\rangle \approx 2\,\langle\psi_q|\hat{n}_p|\psi_q\rangle = 2\,\langle\psi|\hat{n}_q\hat{n}_p\hat{n}_q|\psi\rangle = 2\,\langle\psi|\hat{n}_p\hat{n}_q|\psi\rangle$$
$$\approx 2\overline{\langle\psi|\hat{n}_p\hat{n}_q|\psi\rangle} = 2\frac{\mathrm{Tr}\{\hat{n}_p\hat{n}_q\}}{2^N} = \frac{1}{2}, \tag{2.145}$$

where in the last equality we use that $\mathrm{Tr}\{\hat{n}_p\hat{n}_q\} = 2^{N-2}$. The density-density correlation can finally be computed as

$$C^{typ}_{pq}(t) = \frac{1}{2}\Big(\,\langle\tilde{\psi}_q|\hat{n}_p(t) - \hat{n}_p(0)|\tilde{\psi}_q\rangle\,\Big). \tag{2.146}$$

When we fix $q = N/2$, as we will do in the computation of the $\Sigma^2(t)$ in Eq. (2.120), the initial density profile $\{\langle\tilde{\psi}_{N/2}|\hat{n}_p(0)|\tilde{\psi}_{N/2}\rangle\}_{p=1}^{N}$ is a non-equilibrium configuration that sees a peak at the center of the chain over a uniform background, which spreads

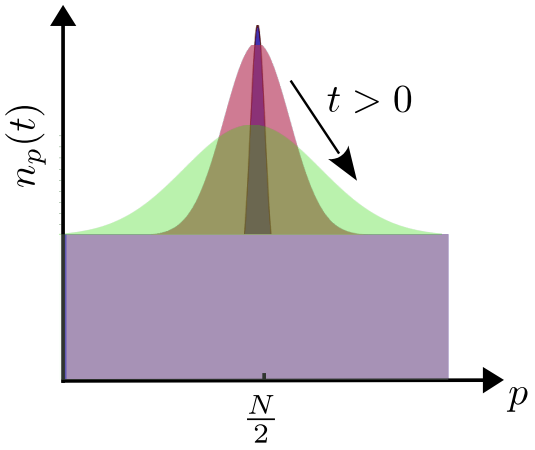

Figure 2.8: The correlation function $C_p(t)$ can be mapped via typicality to the evolution in time of a density profile $\{n_p(t)\}_{p=1}^{N}$ initially localised at the center of the chain over a uniform background which corresponds to the thermal expectation value.

along the chain over time, as depicted schematically in Fig. 2.8. The quantity

$$C_p^{typ}(t) = \frac{1}{2}\Big(n_p(t) - n_p(0)\Big), \quad q \neq 0, \tag{2.147}$$

where $n_p(t) = \langle\tilde{\psi}_{N/2}|\hat{n}_p(t)|\tilde{\psi}_{N/2}\rangle$, is thus used to derive the spread of correlations at infinite temperature,

$$\Sigma^2(t) = 4\sum_{p=1}^{N}\left(p - \frac{N}{2}\right)^2 C_p^{typ}(t). \tag{2.148}$$

Another mean of characterising transport that can be computed via DQT is the decay of density autocorrelation with time. The infinite temperature density autocorrelation at site $N/2$ is given by

$$\begin{aligned} C_{N/2}(t) &= \langle\hat{n}_{N/2}(t)\hat{n}_{N/2}\rangle_\infty - \langle\hat{n}_{N/2}(t)\rangle_\infty \langle\hat{n}_{N/2}\rangle_\infty \\ &= \frac{Tr[\hat{n}_{N/2}(t)\hat{n}_{N/2}]}{2^N} - \frac{Tr[\hat{n}_l]}{2^N} \approx C_{N/2}^{typ}(t) = \frac{1}{2}\Big(n_{N/2}(t) - \frac{1}{2}\Big). \end{aligned} \tag{2.149}$$

Via typicality, it corresponds to how the occupation at the middle site approaches its thermal value following the quench. The classification of transport according to the exponent in the time scaling of autocorrelation functions originates from the spin diffusion theory proposed to describe inelastic neutron scattering in magnetic systems at elevated temperature. However, the same phenomenology has been proved to have

some degree of universality for a large class of quantum Hamiltonians [170, 187]. The autocorrelation is assumed to exhibit a power-law decay,

$$C_{N/2}(t) \sim t^{-\nu'}, \tag{2.150}$$

where $\nu' = 1/2$ in case of diffusion. For a superdiffusive system $1/2 < \nu' < 1$, while $0 < \nu' < 1/2$ points to subdiffusive transport, and $\nu' = 0$ to absence of transport. In case of standard diffusion, this exponent ν' is related to the exponent ν in Eq. (2.124) as $\nu = 2\nu'$. However, for anomalous transport, these two exponents may not be directly related.

2.3 Kernel polynomial method

In discussing the DQT approach, we have already acquired a feeling of how demanding is the numerical analysis of strongly correlated quantum systems and the emergence of macroscopic features from their dynamics. In particular, the required computational resources scale exponentially with the system size. The kernel polynomial method (KPM) is a numerical technique to efficiently expand any function on a truncated series of Chebyshev polynomials. It can then be used to approximate spectral functions of Hamiltonians such as densities of states, but also expectation values and correlation functions in the microcanonical ensemble, without the use of exact diagonalisation (ED). As the expansion is carried out in the energy or frequency space and can be formulated iteratively, the KPM can compute results relative to the dynamics at large or infinite time with a high control on the accuracy. The method, already popular in condensed matter physics [188–191], has seen a sparse but increasing use in the quantum system community [192–194]. In this section, we introduce its generalities, following mainly Ref. [76], and apply it to the physical quantities of interest.

A regular function $f(x) : [-1, 1] \to \mathbb{R}$ can be expanded in series of Chebyshev polynomials $T_n(x) = \cos[n \arccos(x)]$ as,

$$f(x) = \frac{1}{\pi\sqrt{1-x^2}}\left[\mu_0 + 2\sum_{n=1}^{\infty} \mu_n T_n(x)\right], \tag{2.151}$$

where the μ_n indicate the coefficients or moments of the expansion,

$$\mu_n = \int_{-1}^{1} f(x)T_n(x)dx. \tag{2.152}$$

The expansion above can be performed with any series of polynomials forming an orthonormal basis. However, the method is focused on the Chebyshev ones as they show good convergence properties, and can conveniently be defined in an iterative way,

$$\begin{aligned} &T_0(x) = 1, \quad T_{-1}(x) = T_1(x) = x, \\ &T_{n+1}(x) = 2xT_n(x) - T_{n-1}(x). \end{aligned} \tag{2.153}$$

Moreover, they possess simple expressions for kernels preventing the arising of fluctuations near points where the functions is not continuous, known as Gibbs oscillations, when the expansion is truncated at finite order [76]. The usual procedure is to modify the moments with factors g_n depending on the order of expansion N_C,

$$f_{KPM}(x) = \frac{1}{\pi\sqrt{1-x^2}}\left[\mu_0 g_0 + 2\sum_{n=1}^{N_C-1}\mu_n g_n T_n(x)\right], \tag{2.154}$$

which is formally equivalent to taking the convolution of $f(x)$ with a kernel of the following form,

$$\begin{aligned} \mathcal{K}_{N_C}(x,y) &= \frac{1}{\pi^2\sqrt{1-x^2}}\frac{1}{\sqrt{1-y^2}}\left[g_0T_0(x)T_0(y) + 2\sum_{n=1}^{N_C-1} g_nT_n(x)T_n(y)\right], \\ f_{KPM}(x) &= \int_{-1}^{1}\pi\sqrt{1-y^2}\mathcal{K}_{N_C}(x,y)f(y)dy. \end{aligned} \tag{2.155}$$

A drastic truncation of the series corresponds to assuming every g_n equal to 1 (Dirichlet kernel). More sophisticated forms which guarantee uniform convergence of the approximation, meaning mathematically $\max_x|f(x) - f_{KPM}(x)| \xrightarrow{N_C\to\infty} 0$, can be found by requiring that the kernel is positive, normalised to 1, and that its second coefficient g_1 approaches 1 as $N_C \to 1$. The Jackson kernel is usually the best choice for the applications we will discuss below. Its explicit expression g_n^J, which can be found in Ref. [76], comes from the additional request of having optimal resolution, in the sense that it minimises the spread of the kernel over the xy plane,

or its squared width, to $1/(N_C)^2$. Applying the KPM with the Jackson kernel to a Dirac-δ function $\delta(x - x_0)$ with $x_0 \in]-1, 1[$ will result in a broadened gaussian peak $\delta_{KPM}(x - x_0) \approx \frac{1}{\sqrt{2\pi\sigma_x^2}} \exp\left[-(x - x_0)^2/(2\sigma_x^2)\right]$ with $\sigma_x = \pi/N_C$. It is evident then that the features of the function $f(x)$ on scale smaller than $1/N_C$ will appear undistinguishable in $f_{KPM}(x)$. As a further consequence, smoother functions will require less moments to be approximated.

Having introduced the core ideas of the KPM from a mathematical perspective, we focus now on its practical applications for the physics of quantum systems. We consider a generic Hamiltonian $\hat{H}$, which can include or not include many-body interaction terms. Normally, we would need to know the entire set of eigenvalues $\{E_k\}_{k=1}^D$ and eigenstates $\{|k\rangle\}_{k=1}^D$ in order to compute the spectral or dynamical properties of interest. We can now instead treat these quantities as functions of the energy and approximate them with the KPM. As a first step, however, we need to rescale the underlying Hamiltonian and energy axis to the domain of the Chebyshev polynomial, according to

$$\begin{aligned} \hat{\tilde{H}} = (\hat{H} - b)/a, \quad \tilde{E} = (E - b)/a \\ a = \frac{E_{max} - E_{min}}{2 - \epsilon}, \quad b = \frac{E_{max} + E_{min}}{2}, \end{aligned} \tag{2.156}$$

with E_{max} and E_{min} respectively the largest and smallest eigenvalues, and ϵ a small cut-off parameter introduced to avoid instabilities in case the spectrum includes the boundaries of the interval $[-1, 1]$. Henceforth, all the rescaled quantities will be denoted with a tilde. Once computed up to N_C moments, the approximation to N_C-th order of the function can be built as in Eq. (2.154), and then rescaled back to its original domain. The form of the moments μ_n will depend on the specific quantity considered. We proceed listing some recipes for relevant physical properties of the Hamiltonian. In the following, essential details will be provided to understand the computation of the quantities studied in Ch. 6, where the KPM proves crucial to evaluate transport properties from equilibrium and out-of-equilibrium correlation functions. However, the physical results can be interpreted also without the support of the remaining sections of this chapter.

2.3.1 Densities of states

The most basic application of the KPM for quantum system is the construction of the density of states (DOS), that reads

$$\rho(E) = \frac{1}{D}\sum_{k=1}^{D}\delta(E - E_k). \tag{2.157}$$

The moments of its KPM approximation $\tilde{\rho}(\tilde{E})$, evaluated according to Eq. (2.152), assume the following form

$$\begin{aligned}\mu_n &= \int_{-1}^{1}\tilde{\rho}(\tilde{E})\; T_n(\tilde{E})\; d\tilde{E} = \frac{1}{D}\sum_{k=1}^{D}T_n(\tilde{E}_k)\\ &= \frac{1}{D}\sum_{k=1}^{D}\langle k|T_n(\hat{\tilde{H}})|k\rangle = \mathrm{Tr}[T_n(\tilde{H})].\end{aligned} \tag{2.158}$$

Despite the presence in this formula of the trace over the whole Hilbert space of the Hamiltonian, the KPM maintains its advantage over ED techniques, since the moments can be approximated with high accuracy through a stochastic evaluation of trace [76].

An estimate of the trace can be provided by the average over a number $R \ll D$ of random states $|r\rangle$,

$$\mu_n = \mathrm{Tr}[T_n(\hat{\tilde{H}})] \approx \frac{1}{R}\sum_{r=1}^{R}\langle r|T_n(\hat{\tilde{H}})|r\rangle\,. \tag{2.159}$$

The states are drawn over an arbitrary basis $\{|\phi_k\rangle\}$, $|r\rangle = \sum_{k=1}^{D}\xi_{rk}\,|\phi_k\rangle$, with coefficients that are independent random variables whose statistical distribution ensures

$$\overline{\xi_{rk}} = 0, \quad \overline{\xi_{rk}\xi_{r'k'}} = 0, \quad \overline{\xi^*_{rk}\xi_{r'k'}} = \delta_{rr'}\delta_{kk'}. \tag{2.160}$$

These conditions are a reminiscence of the typicality discussed in Sec. 2.2.4, and, indeed, if we assume a gaussian distribution of the coefficients, it is possible to show with analogous considerations to Eq. (2.130) and Eq. (2.133) (for details, see Ref. [76]) that the sample-to-sample fluctuation in the estimation can be reduced to the following

$$\sigma^2_{\mu_n} = \frac{1}{R}\mathrm{Tr}[T_n(\tilde{H})^2]. \tag{2.161}$$

Therefore, the relative error σ_{μ_n}/μ_n scales as $\mathcal{O}(1/\sqrt{RD})$. Typically, DOS for the quantum spin chain Hamiltonians of Eq. (2.73) exhibit a smooth structure. As a consequence, few moments are in general required for this calculation.

The moments for the local DOS (LDOS) associated to the general state $|\psi\rangle$,

$$\rho_\psi(E) = \sum_{k=1}^{D} |\langle k|\psi\rangle|^2 \delta(E - E_k), \tag{2.162}$$

have instead a simpler expression, given by

$$\begin{aligned} \mu_n &= \int_{-1}^{1} \tilde{\rho}_\psi(\tilde{E}) T_n(\tilde{E}) d\tilde{E} = \sum_k T_n(\tilde{E}_k) |\langle \psi|k\rangle|^2 \\ &= \sum_k \langle k|T_n(\hat{\tilde{H}})|k\rangle \langle k|\psi\rangle \langle \psi|k\rangle = \langle \psi|T_n(\hat{\tilde{H}})|\psi\rangle \,. \end{aligned} \tag{2.163}$$

The evaluation of the expectation value of the n-th order polynomial on a single state can be further simplified by using the iterative definition of Eq. (2.153),

$$\begin{aligned} |t_0\rangle &= |\psi\rangle \,, \\ |t_1\rangle &= \tilde{H} \, |t_0\rangle \,, \\ |t_{n+1}\rangle &= 2\tilde{H} \, |t_n\rangle - |t_{n-1}\rangle \,. \end{aligned} \tag{2.164}$$

As a result, $\mu_n = \langle t_0|t_n\rangle$, which implies only matrix-vector multiplications. The same simplification can be used when considering a random state $|r\rangle$.

2.3.2 Ensemble expectation values

The evaluation of expectation value of an observable $\hat{O}$ in the microcanonical ensemble,

$$O_{mc}(E) = \langle \hat{O} \rangle_E = \mathrm{Tr}\{\hat{O}\hat{\rho}^E_{mc}\}, \tag{2.165}$$

where

$$\hat{\rho}^E_{mc} = \frac{1}{\rho(E)} \sum_{k=1}^{D} \delta(E - E_k) \, |k\rangle \langle k| \,, \tag{2.166}$$

is relevant for the study of thermalisation in the isolated system, as we will see later through the dissertation. Within the KPM, the moments to derive $O_{mc}(E)$ up to the

normalising factor $\rho(E)$ are given by

$$\begin{aligned}\mu_n &= \sum_k \int_{-1}^{1} \delta(\tilde{E} - \tilde{E}_k) \langle k|\hat{O}|k\rangle T_n(\tilde{E}) d\tilde{E} \\ &= \sum_k \langle k|\hat{O}|k\rangle \langle k|T_n(\hat{\tilde{H}})|k\rangle = \mathrm{Tr}\{\hat{O}T_n(\hat{\tilde{H}})\}. \end{aligned} \tag{2.167}$$

Another fundamental ensemble for the study of thermalisation is the diagonal ensemble associated to $|\psi\rangle$,

$$\hat{\rho}_{DE} = \sum_{k=1}^{D} |\langle k|\psi\rangle|^2 |k\rangle \langle k| . \tag{2.168}$$

The expectation value of the observable $O_{DE}(\psi) = \mathrm{Tr}\left\{\hat{O}\hat{\rho}_{DE}\right\}$ can be computed, as a result of operations analogous to those above, through

$$\mu_n = \langle\psi|\hat{O}T_n(\hat{\tilde{H}})|\psi\rangle . \tag{2.169}$$

2.3.3 Correlation functions

As verified throughout Sec. 2.2, correlation functions are fundamental objects to evaluate the dynamical properties of isolated systems. We consider in the following how to evaluate expressions as in Eq. (2.84) in the microcanonical ensemble, and on a single pure state. The KPM, however, provides an approximation in the energy domain, thus we first need to expand the functions in the energy eigenbasis. Moreover, we consider the case in which a single observable is present in the expression.

The microcanonical ensemble average of the correlation function for the arbitrary operator $\hat{O}$ can thus be written as

$$C_{mc}(t, E) = \langle \hat{O}(t)\hat{O}\rangle_E - \langle \hat{O}(t)\rangle \langle \hat{O}\rangle_E , \tag{2.170}$$

where $\langle\cdot\rangle_E = \mathrm{Tr}\{\cdot\hat{\rho}^E_{mc}\}$. We consider how to construct the approximation only for the first therm, since we have already treated terms as the second in the previous section.

We write an expansion on the energy eigenbasis, and obtain

$$\begin{aligned} C'_{mc}(t,E) = \langle \hat{O}(t)\hat{O}\rangle_E &= \frac{1}{\rho(E)}\sum_k \delta(E-E_k)\,\langle k|\hat{O}(t)\hat{O}|k\rangle \\ &= \frac{1}{\rho(E)}\sum_{kj} \delta(E-E_k)\,\langle k|\hat{O}(t)|j\rangle\,\langle j|\hat{O}|k\rangle \\ &= \frac{1}{\rho(E)}\sum_{kj} \delta(E-E_k)e^{-i(E_j-E_k)t/\hbar}|O_{kj}|^2, \end{aligned} \tag{2.171}$$

where henceforth we indicate $O_{kj} = \langle k|\hat{O}|j\rangle$. If we perform a Fourier transform of this expression,

$$C'_{mc}(\omega,E) = \int dt C'_{mc}(t,E)e^{i\omega t}, \tag{2.172}$$

we realise that it gives, as result,

$$\begin{aligned} C'_{mc}(\omega,E) &= \frac{1}{\rho(E)}\sum_{kj} \delta(E-E_k)\delta(\omega-(E_j-E_k))|O_{kj}|^2 \\ &= \frac{1}{\rho(E)}K(E,E+\omega), \end{aligned} \tag{2.173}$$

where we identify a suitable function to approximate with the KPM,

$$K(x,y) = \sum_{kj}\delta(x-E_k)\delta(y-E_j)|O_{kj}|^2. \tag{2.174}$$

Since it is a function of two variables, we need to generalise the KPM to multiple Chebyshev expansions,

$$\tilde{K}(x,y) = \frac{1}{\pi\sqrt{1-y^2}}\frac{1}{\pi\sqrt{1-x^2}}\sum_{n,m=0}^{N_C,M_C}\mu_{nm}h_{nm}g_n g_m T_n(x)T_m(y), \tag{2.175}$$

where the factor $h_{nm} = 4/[(1+\delta_{n0})(1+\delta_{m0})]$ takes care of the normalisation, and g_n, g_m are the corrections given by the kernels [76]. The moments of the Chebyshev expansion are given by,

$$\begin{aligned} \mu_{nm} &= \sum_{kj}\int dx \int dy\; T_n(x)T_m(y)\delta(x-\tilde{E}_k)\delta(y-\tilde{E}_j)|O_{kj}|^2 \\ &= \sum_{kj} T_n(\tilde{E}_k)T_m(\tilde{E}_j)|O_{kj}|^2 = \mathrm{Tr}\big\{T_n(\hat{\tilde{H}})\hat{O}T_m(\hat{\tilde{H}})\hat{O}\big\}, \end{aligned} \tag{2.176}$$

where we need to apply again the stochastic evaluation of trace. After plugging the

moments in Eq. (2.175), and rescaling back to the original energy range, we obtain a grid which represent the values of $K(x,y)$ on the xy plane. Schematically, if we evaluate $K(x,y)$ on a symmetric grid of $P \times P$ equally spaced points, with positive interval $\Delta = x_p - x_{p-1}$, we get

$$\begin{pmatrix} K(x_1,x_1) & K(x_1,x_1+\Delta) & K(x_1,x_1+2\Delta) & \dots & \dots \\ K(x_2,x_2-\Delta) & K(x_2,x_2) & K(x_2,x_2+\Delta) & \dots & \\ K(x_3,x_3-2\Delta) & K(x_3,x_3-\Delta) & K(x_3,x_3) & \dots & \dots \\ \dots & & \dots & \dots & \\ K(x_P,x_P-P\Delta) & \dots & & \dots & K(x_P,x_P) \end{pmatrix} \tag{2.177}$$

Comparing with Eq. (2.173), we see on the diagonal $K(x_p, y = x_p)$, or $K(E,E)$ evaluated for $\omega = 0$. In order to compute $C'_{mc}(E_j,\omega)$ as a function of ω and fixed $E = E_j$, we extract the j-th row corresponding to $x_j = E_j$. Viceversa, for $C'_{mc}(E,\omega_j)$ as a function of the energy at fixed frequency $\omega_j = j \times \Delta$, we need to consider the values on the j-th diagonal.

We examine now the correlation function evaluated on an arbitrary state $|\psi\rangle$,

$$C_\psi(t) = \langle\psi|\hat{O}(t)\hat{O}|\psi\rangle - \langle\psi|\hat{O}(t)|\psi\rangle \langle\psi|\hat{O}|\psi\rangle \,. \tag{2.178}$$

As above, before using the KPM it is necessary to apply some manipulations, starting from the expansion of the first term on the eigenbasis,

$$\begin{aligned} C'_\psi(t) = \langle\psi|\hat{O}(t)\hat{O}|\psi\rangle &= \sum_{klj} \langle\psi|k\rangle \langle k|\hat{O}(t)|l\rangle \langle l|\hat{O}|j\rangle \langle j|\psi\rangle \\ &= \sum_{klj} c_k^* c_j O_{kl} O_{lj} e^{-i(E_l - E_k)t/\hbar}, \end{aligned} \tag{2.179}$$

with coefficients given by $c_k = \langle k|\psi\rangle$. We derive then the Fourier transform,

$$C'_\psi(\omega) = \sum_{klj} \delta(\omega - (E_l - E_k))\; c_k^* c_j O_{kl} O_{lj}. \tag{2.180}$$

We further need to decouple the δ-function,

$$\begin{aligned} C'_\psi(\omega) &= \sum_{klj} \int_{-\infty}^{\infty} d\omega' \delta(\omega' - E_l)\delta(\omega' - (\omega + E_k)) c_k^* c_j O_{kl} O_{lj} \\ &= \int_{-\infty}^{\infty} d\omega' A(\omega' - \omega, \omega'), \end{aligned} \tag{2.181}$$

before identifying a suitable function for the KPM, i.e.

$$A(\omega' - \omega, \omega') = \sum_{klj} \delta(\omega' - E_l)\delta(\omega' - (\omega + E_k)) c_k^* c_j O_{kl} O_{lj}. \tag{2.182}$$

Analogously to the case of the microcanonical ensemble, after rescaling frequency domain and Hamiltonian, we double Chebyshev-expand the expression

$$\tilde{A}(x, y) = \sum_{klj} \delta(x - \tilde{E}_k)\delta(y - \tilde{E}_l) c_k^* c_j O_{kl} O_{lj}, \tag{2.183}$$

using the following moments,

$$\begin{aligned} \mu_{nm} &= \sum_{klj} \int dx \int dy \; T_n(x) T_m(y) \delta(x - \tilde{E}_k)\delta(y - \tilde{E}_l) c_k^* c_j O_{kl} O_{lj} \\ &= \sum_{klj} T_n(\tilde{E}_k) T_m(\tilde{E}_l) \; c_k^* c_j O_{kl} O_{lj} \\ &= \sum_{klj} \langle \psi | k \rangle \, T_n(\tilde{E}_k) \, \langle k | \hat{O} | l \rangle \, T_m(\tilde{E}_l) \, \langle l | \hat{O} | j \rangle \, \langle j | \psi \rangle \\ &= \langle \psi | T_n(\hat{\tilde{H}}) \hat{O} T_m(\hat{\tilde{H}}) \hat{O} | \psi \rangle \, . \end{aligned} \tag{2.184}$$

If we evaluate the function on a symmetric grid of $P \times P$ equally spaced points, with interval $\Delta = x_p - x_{p-1}$, we can write a structure analogous to Eq. (2.177). Comparing the variables in Eq. (2.182) and Eq. (2.183), we realise that to compute the correlation function, we need to perform the numerical integral in Eq. (2.181) for each ω. The correlation function $C_\psi(\omega_j)$ at $\omega_j = j \times \Delta$ is thus given by the integration of the values on the j-th diagonal starting from the center, in the upper part of the matrix for positive j, in the lower part for negative j.

Chapter 3

Quasiperiodic heat engine with mobility edge

In this and in the following chapters, we finally employ the theoretical frameworks and numerical techniques examined in Ch. 2 in order to investigate the electric and heat non-equilibrium transport properties of quasiperiodic potentials. We initially focus on the tight-binding GAAH model, whose spectral and localisation characteristics were already described in Sec. 1.3. After reviewing the known literature on the behaviour of its particle current at high temperature, we argue how the mobility edge displayed by the model can operate as an energy filter in a heat engine, according to the mechanism discussed in detail in Sec. 2.1.3. Motivated by this possibility, we study the thermoelectric response of the quasiperiodic chain when put into contact with two reservoirs at different finite temperature and chemical potential. We compute the transport coefficients in linear-response regime using the Landauer-Büttiker approach of Sec. 2.1.2 and quantify through them the performance of a GAAH heat engine as a function of temperature. We show in Sec. 3.1 how the remarkable properties of the model give rise to a versatile and efficient quantum thermal machine. Finally, we prove that the physics described here is not only limited to our chosen potential, but is also expected to hold true in more general cases. In particular, we model the mobility edge through a purely phenomenological transmission function in Sec. 3.2, while in Sec. 3.3 we obtain a qualitatively similar behaviour in the weak-coupling regime, where the scaling with system size of the wavefunctions can explicitly be encoded in the expressions for the currents. This chapter is based on the results originally presented in Ref. [195].

We write again for completeness the on-site potential of the GAAH tight-binding model, previously seen in Eq. (1.17),

$$V_n^{GAAH} = \frac{2\lambda \cos(2\pi b n + \varphi)}{1 - \alpha \cos(2\pi b n + \varphi)}, \tag{3.1}$$

where λ indicates the strength of the potential, φ a phase with no effect on the localisation properties, b the irrational Diophantine number establishing the quasiperiodicity, and $\alpha \in]-1, 1[$. For $\alpha = 0$, the GAAH model reduces to the AAH model, treated instead in Sec. 1.2. In the AAH model, the quasiperiodic nature of the potential leads to a delocalisation-localisation transition depending just on λ, which has been detected experimentally on a wide range of experimental platforms [55, 56, 105, 196]. The critical point of the transition in the AAH model occurs at $\lambda = t_h$, with t_h the first neighbour hopping constant. For $\lambda = t_h$, the multifractal states lead to anomalous transport behavior [31, 32, 176]. In these works, the exponent in the scaling of the particle current, calculated in an open environment either through a NEGF approach to the Landauer-Büttiker integrals or a phenomenological Lindblad master equation, is subdiffusive but assumes a different value depending on the set of finite system sizes chosen, generic or from the rational approximants to b. This feature is related to the number theoretic properties of the system size N, and it is extensively discussed in Ref. [32]. In the open setting, as we will see explicitly in Sec. 3.3 for weak coupling, the current scaling is entirely determined by that of the components of the eigenfunctions at the sites where the reservoirs are attached. At the critical point, these exhibit a different scaling than those in the bulk of the chain, because of their multifractal nature [197]. As a consequence, there is a mismatch with respect to Eq. (2.125) against the results from the isolated system, obtained by the authors of Ref. [31] using the spatial spread of a localised wavepacket. We have discussed in Sec. 2.2.3 and Appendix A how to link this quantity to the Kubo conductivity. The proof relies on the space-translational invariance of the system, which is not present in the AAH or GAAH models, but can be restored for quantities averaged over φ. The calculations in the closed environment for the AAH model at critical point give, instead of subdiffusion, an exponent pointing to diffusion, but an anomalous density profile, hinting to superdiffusion [31]. We emphasise again that the disagreement is due to the different behaviours of the components of the eigenfunctions in the bulk

and in the boundaries. In this case, the interchange in the limit of infinite time and infinite system size discussed in Sec. 2.2.2 for the conductivities in open and closed environment leads to drastic different results [176].

For $\alpha \neq 0$, the GAAH model features a mobility edge in energy, separating the regions of completely delocalised and localised states in the same spectrum, which can be found analytically to be [36]

$$E_c = \frac{1}{\alpha}\text{sign}(\lambda)(|t_h| - |\lambda|). \tag{3.2}$$

The richer phase diagram of the GAAH model has been originally explored in the linear response regime through Landauer-Büttiker approach with NEGF in Ref. [198], and schematically depicted in Fig. 3.1. We notice that, since the study has been conducted at high temperatures, there is no dependence on the chemical potential or the energy in the diagram. A possible thermodynamic application of the model was first studied in Ref. [199], where the different statistics of the bosonic baths induces large energy current rectification. However, the heat and electric transport properties of the model had not been explored yet at finite low temperatures, where the possibility of tuning the position of the mobility edge can become relevant in the context of quantum thermal machines.

As previously discussed in Sec. 2.1.3 and depicted in Fig. 2.6, energy filtering is a central concept in thermoelectric energy conversion: in order to obtain a strong thermoelectric response, it is necessary to allow only particles in a finite energy window to flow [38, 39]. The opportunity of realising an extremely efficient energy filter through a mobility edge has been considered for the first time for the mobility edge associated with the metal-insulator transition of the Anderson model [119, 200, 201]. Here, random disorder localises only the low-energy part of the spectrum, while high-energy states remain extended. This leads to an asymmetric transmission function and hence a diverging thermopower in the vicinity of the mobility edge, which separates the localised, insulating states from the extended, conducting ones. The Anderson metal-insulator transition occurs in three spatial dimensions [119], while in lower dimensions, and in the absence of interparticle interactions, all states are localised in the thermodynamic limit [23]. Remarkably, the GAAH model exhibits a mobility edge even in one spatial dimension, whose position in energy can be known precisely.

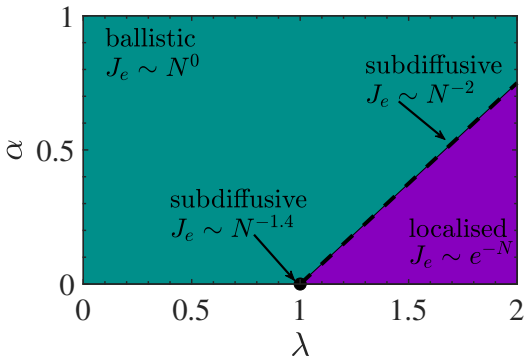

Figure 3.1: Phase diagram of the high temperature non-equilibrium electric transport properties of the GAAH model. The ballistic region is separated from the localised region by a subdiffusive line with $\alpha_G = 2$, and $\alpha_G = 1.4$ at $\alpha = 0$ (AAH model). The results are obtained within Landauer's framework and averaged over different realisations, by integrating φ from 0 to 2π. Adapted from Ref. [198]

Furthermore, conducting states in the case of the GAAH model support ballistic transport, whereas those in the three-dimensional Anderson model support diffusive transport. For these reasons, we have decided to investigate the low temperature thermoelectric properties of the model, exploring its capability as working medium in a quantum thermal machine.

3.1 Thermoelectric effects in the GAAH model

As described in Sec. 2.1.1, we consider a tight-binding model with GAAH on-site potential, and a bilinear system-bath coupling between the first site of the chain and the left L bath, at temperature and chemical potential $T+\Delta T, \mu+\Delta\mu$, and between the last site and the right R bath, at T, μ. We assume bath spectral densities independent on the energy in WBL approximation, in such a way that the only relevant parameter relative to the baths in the calculation of the transmission function in NEGF matrix representation is the system-bath coupling strength γ.

The pivotal calculation for our results is in fact the transmission function $\tau_{LR}(E)$, which is independent of the temperature and the chemical potential of the reservoirs. In Fig. 3.2 we display the spectrum of the system and the corresponding transmission function for two different pairs of values of λ and α, choosing $b = \tau$ throughout the dissertation, where $\tau = (\sqrt{5}+1)/2$ is the golden ratio. We see that the mobility edge and the clusters of ballistic states lying above it generally give rise to a highly asymmetric transmission profile, which is conducive to a large thermoelectric response.

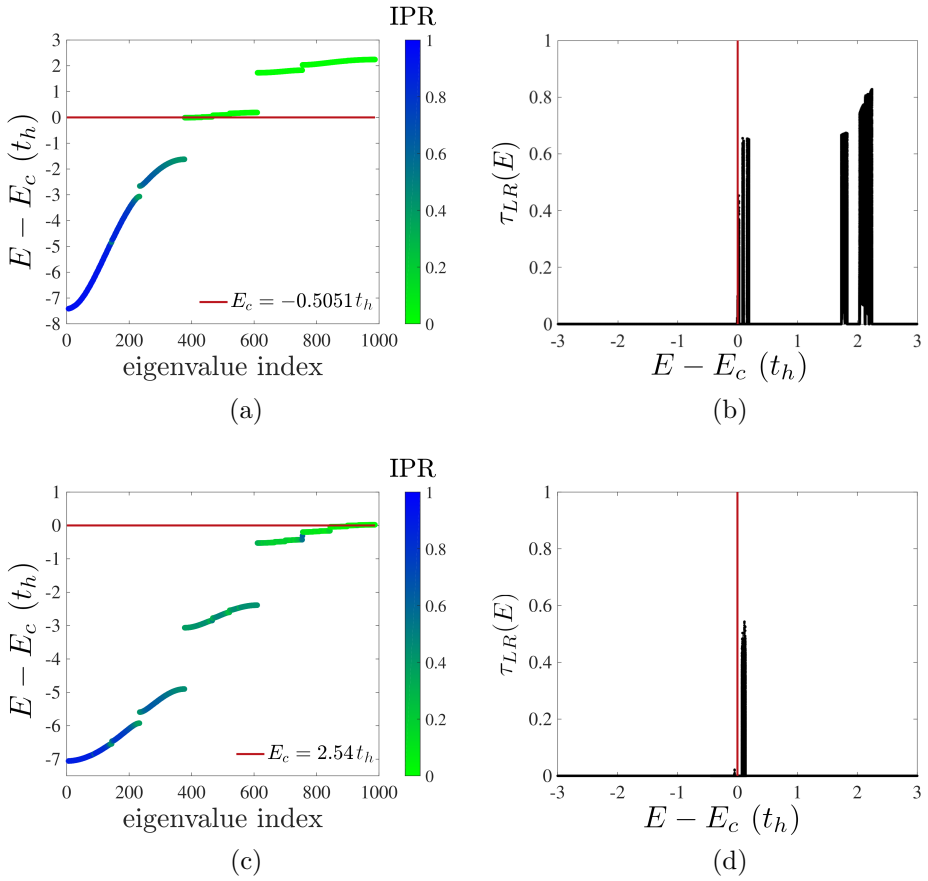

Figure 3.2: Spectra for single GAAH wires of length $N = 987$, generated with (a) $\lambda = -0.8\ t_h$, $\alpha = 0.792$, $\varphi = 0$ (dashed vertical line in Fig. 1.7), and (c) $\lambda = -1.4\ t$, $\alpha = 0.330$, $\varphi = 0$. The mobility edge is shown by the red line. (b)-(d) The transmission functions associated respectively to the first and second configuration, averaged at every energy over 40 values of the phase φ, as described in the main text. Conduction is clearly possible only at energies that support extended eigenstates.

The choice of the two parameters in the model, moreover, gives control over the structure of the spectrum, determining the position of the mobility edge and the number of ballistic states above it.

At this point, a note on terminology is in order. For simplicity, henceworth we refer to the clusters of ballistic states lying above the mobility edges as "bands". Strictly speaking, these groups of states do not satisfy the usual definition of a band, because they do not tend to a continuum in the thermodynamic limit in the rigorous mathematical sense, due to their fractal structure. Nevertheless, as discussed above and shown in Sec. 3.2, this structure has little effect on thermodynamic properties such as efficiency, thus we make no strict distinction in terminology.

Since the GAAH model has a large parameter space, we focus on a single, representative example rather than performing an exhaustive study. In what follows, we consider

the particular configuration displayed in Fig. 3.2a, corresponding to the dashed vertical slice we saw in Fig. 1.7 with $\alpha = 0.792$, for a chain of 987 sites. The mobility edge E_c sits within a group of closely packed eigenvalues, with several other ballistic bands. We work in a regime of intermediate system-bath coupling, $\gamma = t_h$. As shown later in Sec. 3.1.3, modifying γ merely rescales the currents without qualitatively affecting the transport behaviour. In the following, we use this transmission function to analyse the thermoelectric properties of the GAAH wire in different temperature regimes, via the transport coefficients given by Eqs. (2.39)–(2.41). All quantities shown in this section are obtained numerically and ultimately averaged over the phase φ by integrating between 0 and 2π and dividing by 2π. The averaging procedure reduces the sample-to-sample fluctuations in the finite size realisations of the model, and it restores translational symmetry.

3.1.1 Low-temperature performance

We begin by studying the low-temperature behavior, choosing $T = 0.1\ (t_h/k_B)$. This temperature regime is relevant for experiments involving ultracold atoms in optical lattices [14] and allows to clearly distinguish the non-trivial spectral structures reflected in the behaviour of the transport coefficients. We observe in Fig. 3.3 that the electrical and thermal conductances closely follow the structure of the transmission function, with significant transport occurring only within the conducting bands around and above the mobility edge. Furthermore, we notice that the Wiedemann-Franz law does not hold here. This is due to the highly discontinuous transmission function of the system, determined by the fractal properties of its spectrum. We conjecture this violation to be a general feature of quasiperiodic systems, which we will observe also in the case of the Fibonacci model in Ch. 4. This structure of the transmission function is also responsible for the relatively small values of the electric conductance compared to the peak values of $\tau_{LR}(E)$ plotted in Fig. 3.2b.

The most dramatic effect due to the energy filter is evident in the Seebeck coefficient S plotted in Fig. 3.4a, which assumes finite values around the mobility edge. We also notice the magnitude of S rising when the chemical potential is tuned far below or above the mobility edge. Even when μ lies on the insulating side, some of the delocalised states participate in transport because of the non-zero temperature, generating a small but finite conductance. As the mobility of the electrons decreases, the

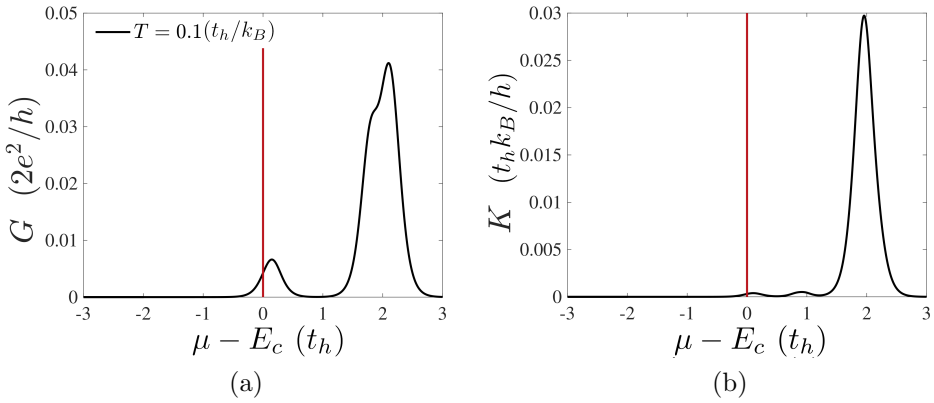

Figure 3.3: (a) Electric conductance and (b) thermal conductance as a function of chemical potential at fixed temperature $T = 0.1(t_h/k_B)$. The mobility edge is shown by the red line.

voltage necessary to stop their flux increases, leading to a large Seebeck factor according to Eq. (2.41). In the region far above E_c, the charge carriers flow in the opposite direction to the heat carriers, leading to negative values for S. The figure of merit ZT also exhibits a divergence below the mobility edge, as shown in Fig. 3.4b. This yields an extremely efficient thermal machine, yet in a region of negligible electrical conductance and thus vanishing power. Features more interesting for the realisation of a useful device are instead visible when the chemical potential is tuned above the mobility edge. In this region, the engine has finite conductance, while the asymmetry of the transmission function gives rise to a figure of merit $ZT \approx 10$ just above the mobility edge. We observe, moreover, two higher peaks of $ZT \approx 60$ and $ZT \approx 40$ corresponding respectively to the upper and lower edges of the first and second ballistic bands above the mobility edge. Such values of ZT correspond to efficiencies far exceeding those recorded in recent experiments [12]. This is, however, also due to the presence of phonons in the mesoscopic systems, where they behave as heat carrier in parallel with electrons. As they are uncharged, they do not contribute to the charge conductance or to the thermopower, but do contribute to the total thermal conductance, which appears in the denominator of ZT, reducing in such a way the values of the thermoelectric figure of merit.

From the study of low-temperature transport, it is clear that by tuning the chemical potential it is possible to obtain an extremely efficient autonomous thermal machine at finite power output. In order to study the machine's performance more systematically, we now focus on the conditions for generating the maximum power, seen already in Eq. (2.70). In the linear-response regime with fixed ΔT, the power is maximised

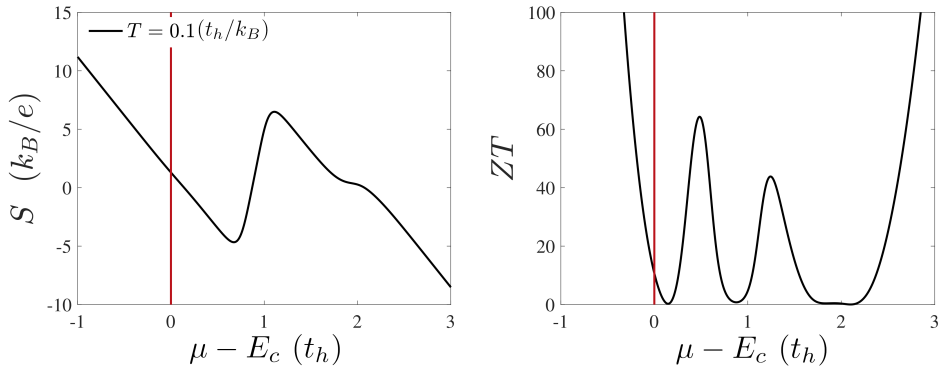

Figure 3.4: (a) Seebeck factor and (b) thermoelectric figure of merit as a function of chemical potential at fixed temperature $T = 0.1(t_h/k_B)$. The mobility edge is shown by the red line.

when $\Delta\mu = -eS\Delta T/2$. Since this value depends on the chemical potential through S, our goal is to find the best thermal machine, or, equivalently, the optimal μ in order to obtain the maximum power output. In Fig. 3.5, we plot the maximum power and corresponding efficiency Eq. (2.68) as a function of μ, at the fixed temperature $T = 0.1$ and bias $\Delta T = 0.01$ (t_h/k_B). We distinguish two cases according to whether the charge current is positive (left to right) or negative (right to left) according to our conventions. In the former case, the temperature gradient drives particle transport above the chemical potential, leading to power extraction for $\mu_L < \mu_R$, (since $S > 0$, $\Delta\mu < 0$). In the latter case, the thermal gradient causes holes below the chemical potential to migrate from left to right, which generates power so long as $\mu_L > \mu_R$ ($S < 0$, $\Delta\mu > 0$). Two points that are particularly suitable for the realisation of the thermal machine are marked with blue circles in Fig. 3.5: one in the region of positive J_N, the other for negative J_N. Here, the machine produces the highest values of electric power, with an efficiency reaching $\eta^{(h)} \approx 0.4\eta_C^{(h)}$. The strong thermoelectric response of the system at these two points is due to the lowermost and uppermost edges of the ballistic bands, respectively. Indeed, at low temperatures, it seems preferable to exploit the band edges rather than the mobility edge, since the power is significantly lower in the vicinity of E_c.

3.1.2 Effect of increasing temperature

In this section, we explore the performance of the quasiperiodic machine at higher temperatures. As displayed in Fig. 2.4a, in the linear-response regime the temperature

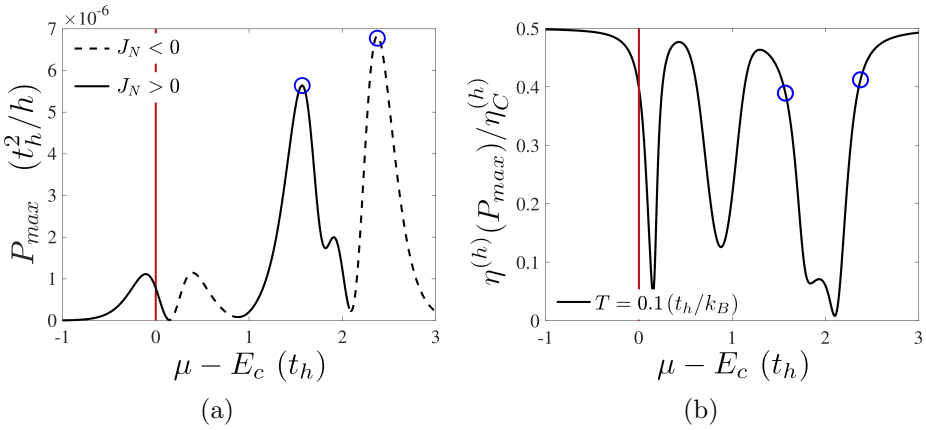

Figure 3.5: (a) Maximum power and (b) efficiency at maximum power as a function of chemical potential at fixed temperature $T = 0.1$ and bias $\Delta T = 0.01(t_h/k_B)$. Blue circles mark the points of absolute maximum power. The mobility edge is shown by the red line.

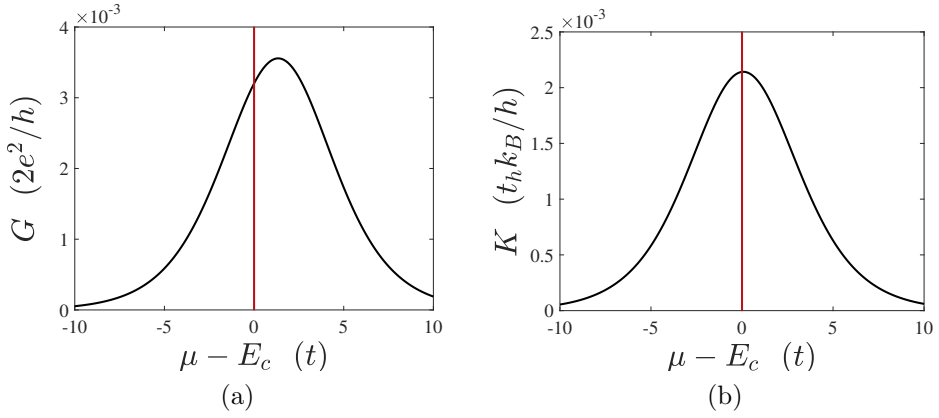

Figure 3.6: (a) Electric conductance and (b) thermal conductance as a function of chemical potential at fixed temperature $T = 2.0(t_h/k_B)$. The mobility edge is shown by the red line.

fixes the width of $f'(E)$, which determines the energy window centred on μ within which transport takes place. As T increases, the gaps between the bands are no longer resolved and the sharp features of G and K displayed in Fig. 3.3 are broadened and reduced in magnitude, as we see in Fig. 3.6 for $T = 2.0(t_h/k_B)$. As a result of this thermal broadening, the conductance is non-vanishing even for $\mu < E_c$ and the thermopower exhibits a weaker slope.

In order to meaningfully compare the thermoelectric performance of the GAAH wire at different temperatures, we vary T while fixing the ratio $\Delta T/T = 0.1$, thus also ensuring that we remain in the linear-response regime. For each value of T and ΔT, we find the chemical potential, μ^*, and bias, $\Delta\mu = -eS(\mu^*)\Delta T/2$, that maximise power output. As before, we distinguish situations where $J_N > 0$ and $J_N < 0$ — corresponding to heat transport by particles or holes, respectively — performing a

separate maximisation for each case. In Fig. 3.7, we show the maximum power and the corresponding efficiency as a function of temperature. We first focus on cases where $J_N > 0$. The power grows linearly at high temperature, while μ^* decreases, as shown in the inset of Fig. 3.7. The drop in efficiency visible around $T \lesssim t_h/k_B$ is due to the particular structure of the spectrum: here, the transport window includes both ballistic bands, leading to a more symmetric transmission function. The thermodynamic coefficients related to this point, which occurs for $T = 0.5t_h/k_B$, are reported in Fig. 3.8. At even higher temperature, μ^* lies below E_c on the localised side, and the whole structure of the spectrum is exploited. All ballistic bands are included in the transport window (giving high power), but the transmission profile remains asymmetric and enhances the thermoelectric response (giving high efficiency). Therefore, the properties of the GAAH model are here essential to obtain an efficient thermal machine with finite power output at high temperature. We repeat this study of maximum power for chemical potentials where $J_N < 0$, shown by the dashed blue lines in Fig. 3.7. The machine initially produces more power in this region, but as the temperature increases the recorded power output assumes values closer to those of the previous case and we see the two lines overlap in the plot, since the transport window broadens to covers the whole spectrum. The efficiency at maximum power converges to the CA bound, i.e., $\eta_C^{(h)}/2$, more quickly than in the case where $J_N > 0$. Moreover, the optimal chemical potential increases with temperature, with μ^* moving well above the uppermost edge of the ballistic region for large T. Therefore, the strong thermoelectric response here is due mainly to the band edge.

Nevertheless, the presence of the mobility edge still enhances efficiency. In order to show this, we compute analogous data for a clean tight-binding wire, $\{V_n\}_{n=0}^N = 0$, and $t_h = \gamma$ as before. We have commented its transmission function already in Fig. 2.3. In this case, particle-hole symmetry is broken at the edges of the spectrum located at energies $E = \pm 2t_h$. This leads to two perfectly symmetric points of maximum power, whose distance from the center of the spectrum at $E = 0$, one below and the other above, increases with temperature. As shown in Fig. 3.9, the efficiency saturates the CA bound at high temperature, while the maximum power is higher than for the GAAH model due to the larger number of conducting states. However, at low and intermediate temperatures where the spectral characteristics can be resolved, the thermoelectric efficiency of the clean wire, due exclusively to the presence of band

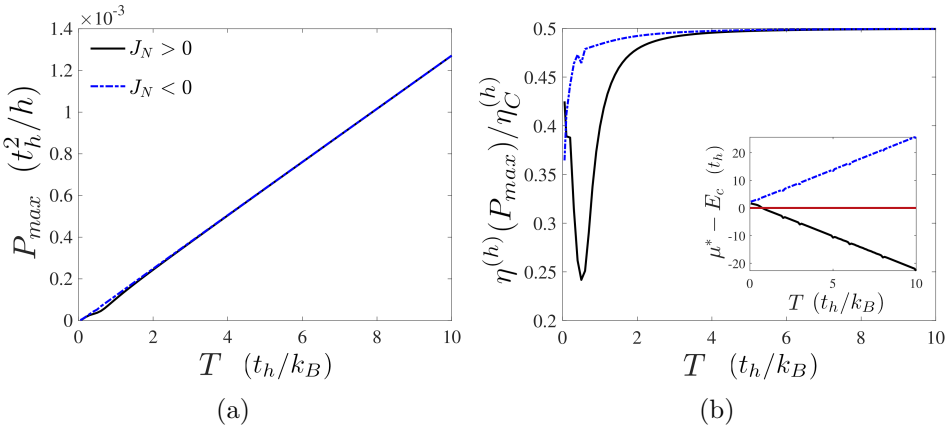

Figure 3.7: (a) Absolute maximum power and (b) corresponding efficiency at maximum power as a function of temperature with $\Delta T/T = 0.1$. The solid black lines show results obtained by optimising the power only over values of μ that give rise to a particle current flowing from the hot to the cold bath, $J_N > 0$. The dashed blue lines are instead obtained by restricting the maximisation to $J_N < 0$. The chemical potential yielding this maximum power is shown in the inset.

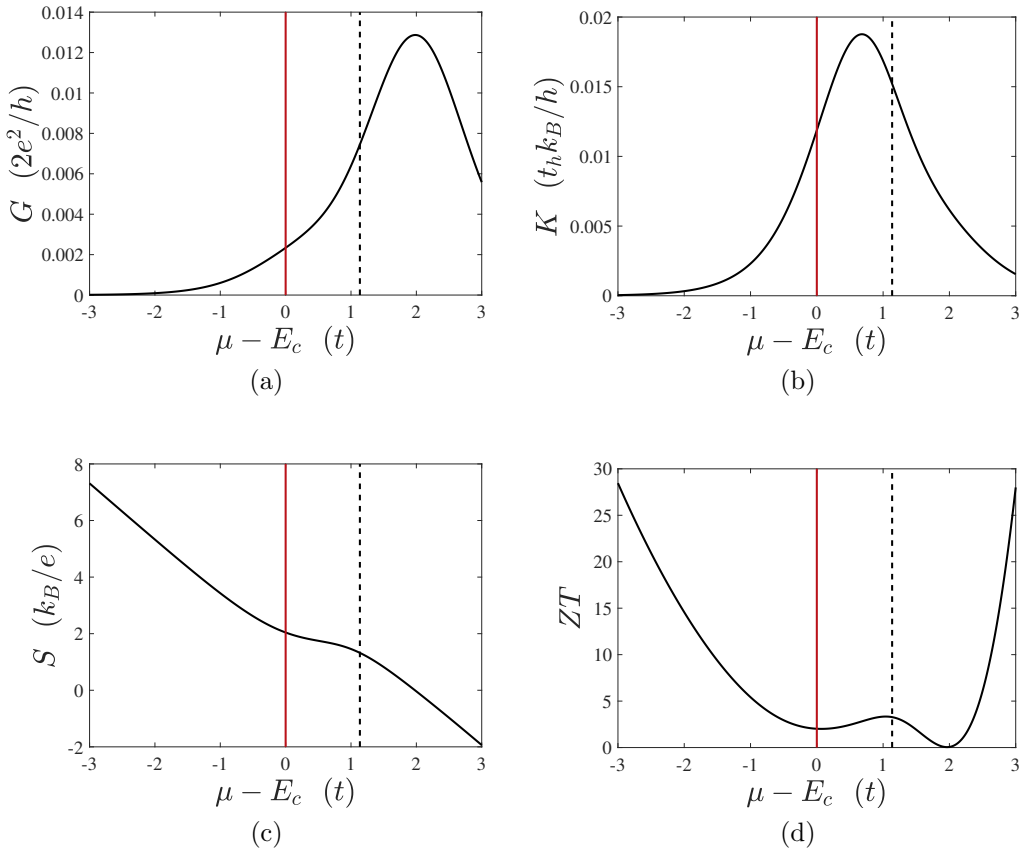

Figure 3.8: The efficiency at maximum power output for $J_N > 0$, indicated by the black solid line in Fig. 3.7, reaches a minimum at temperature $T = 0.5(t_h/k_B)$. We show the thermodynamic coefficients at this temperature: (a) electric conductance, (b) thermal conductance, (c) Seebeck factor, and (d) figure of merit. The mobility edge is shown by the red line, while the dashed black vertical line indicates the chemical potential maximising the power output $\mu^* = 1.14t_h$ and used to compute the minimum of the curve in Fig. 3.7.

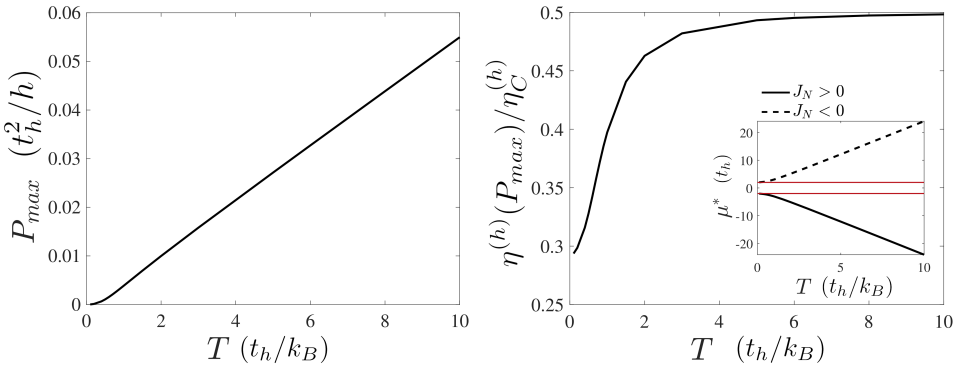

Figure 3.9: (a) Absolute maximum power and (b) efficiency at maximum power, as in Fig. 3.7 but using a clean (i.e., nondisordered) wire as a working medium. Identical values for positive and negative current are obtained at symmetric chemical potentials relative to the center of the conducting region (inset).

edges, is lower than for a quasiperiodic system supporting a mobility edge also.

Our proposal for the quasiperiodic quantum heat engine with mobility edge could be experimentally tested using ultracold neutral atoms trapped in bichromatic optical lattices. On this platform, it is possible to engineer one-dimensional quasiperiodic systems with a mobility edge by various means, e.g. by lowering the primary lattice depth so that hopping processes beyond nearest-neighbour play a role [52, 53, 68, 107, 121, 122, 125], and the specific GAAH potential in (3.1) has been recently realised [35]. These systems all share similar spectral features and thus should display thermoelectric properties similar to those studied in this chapter if integrated in the two-terminal set-up for particle and heat diffusion measurements which has been developed for cold atoms in a parallel and independent set of experiments [14, 202–205]. For example, if we assume the same nearest-neighbour interaction term $t_h \sim h \times 500$ Hz adopted in the laboratory for ^{40}K atoms at 0.15 T_F [53], where T_F is the Fermi temperature, our units for temperature read 1 $t_h/k_B \sim 0.1\ T_F$. Working in the linear-response regime simplifies our theoretical analysis, but it determines a very low power output ($t_h^2/h \sim 2.0 \times 10^{-28}$ W). Large biases have been demonstrated in the ultracold atom toolbox for transport measurement [202] and power could then be considerably increased.

3.1.3 Dependence on system-bath coupling

The study of the proposed quasiperiodic thermoelectric is characterised by a large number of parameters to control and tune in order to reach the highest possible efficiency at finite power output. In the previous sections we show the properties of the thermal machine computed at an intermediate coupling regime, with γ fixed equal to t_h. The analysis of the efficiency is, in fact, independent of this choice. In order to show this, we compute the Onsager coefficients of the same system keeping the temperature and chemical potential constant and changing just the strength of the coupling between the central chain and the reservoirs. We have found that the forms of L_{11}, L_{12} and L_{22} as function of chemical potential remain the same regardless of γ, up to an overall factor. A change in the coupling constant affects just the magnitude of the coefficients, as it is evident from the conductance plotted in Fig. 3.10a. The magnitude initially increases with γ, but, after reaching a maximum at an optimum γ^*, it drops as the particles begin to be scattered back to the reservoirs without entering the central region because of the high impedance mismatch. The same kind of behaviour is observed also for the other coefficients L_{12} and L_{22} in all temperature ranges. Quantities deriving from a ratio of the Onsager coefficients, such as the thermopower S and the figure of merit ZT, are thus independent of γ, as shown in Fig. 3.10b. As a consequence, in the limit of large system size it is possible to maximise the power output of the machine while keeping its efficiency constant, just by tuning the coupling of the chain to the baths in the set-up. In Fig. 3.10c and Fig. 3.10d we collect, for different values of γ, results for the efficiency at maximum power $\eta^{(h)}(P_{max})$ and the maximum power P_{max} at fixed chemical potential μ which gives the highest value for the electric power output when $T = 0.1\ t_h/k_B$. The corresponding value of the chemical potential is the same at every γ and the efficiency remains constant apart from small numerical fluctuations, as expected. We see, instead, the power rising linearly for small γ, reaching the highest value at $\gamma \sim 2.0\ t_h$, and subsequently decaying with a power law. The parameter γ can be then fixed without loss of generality, and, moreover, can be used to control the maximum power output without affecting the efficiency of the thermal machine.

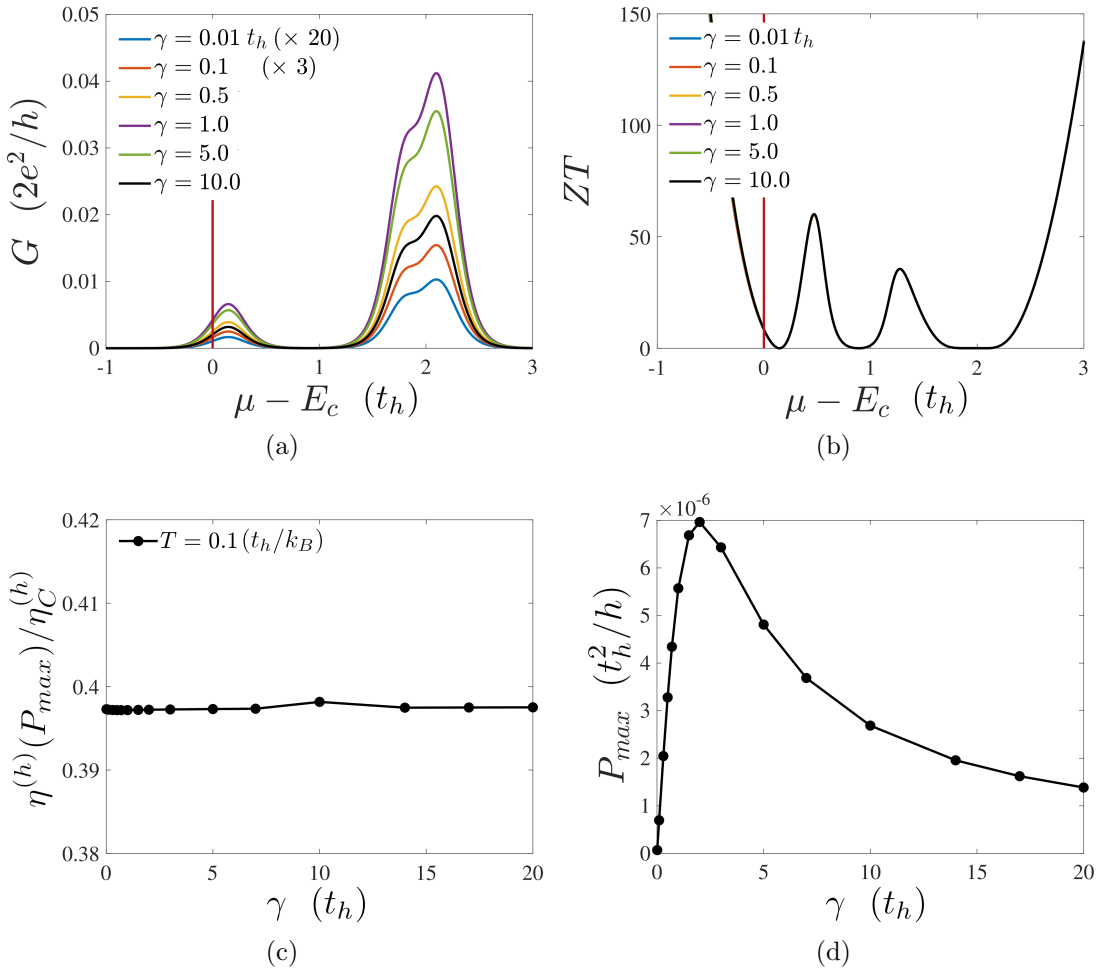

Figure 3.10: Dependence of the thermoelectric properties on the system-bath coupling strength γ, fixing the temperature at $T = 0.1\ t_h/k_B$. (a) Electrical conductance as a function of the distance between the chemical potential and the mobility edge, indicated by the red line, obtained for multiple choices of γ. All curves have the same form and differ only in their magnitude. (b) Figure of merit around the mobility edge for different γ. Since the Onsager coefficients are modified by the same pre-factor, their combination is γ-independent and the different curves completely overlap. (c) As a consequence of the same argument, the efficiency at maximum power as a function of the system-bath coupling, for a fixed chemical potential, $\mu - E_c = 1.57\ t_h$, remains constant with γ is changed. (d) Maximum power transferred by the machine. It is evident that it is possible to tune the system-bath coupling in such a way to optimise power without changing efficiency.

3.2 Phenomenological transmission function

A general property of quasiperiodic one-dimensional models is that their spectrum exhibits fractal properties, which are reflected in the fine-grained structure of the transmission function. While these fractal properties depend on the exact choice of the quasiperiodic potential, the asymmetry of the transmission function and the occurrence of bands of ballistic states are generic to many one-dimensional quasiperiodic systems with a mobility edge. In this and in the following section, we demonstrate that the behaviour of the thermoelectric coefficients observed above, in particular, the divergence of thermopower and figure of merit, are generic to any system showing these characteristics, generalising the concept of quasiperiodic thermal machine beyond the specific potential chosen in Eq. (3.1).

The fractal spectrum of the GAAH model is reflected by the position of the peaks in the transmission function. Here we show that the fine-grained structure of this fractal spectrum is unimportant for the physics described above. To that end, we study the transport properties of the set-up by modelling its transmission function with a series of boxcar functions of height and width corresponding to the different ballistic regions of the GAAH model. By construction, these boxcar functions lack any fine structure whatsoever. In Fig. 3.11a, the boxcar approximation is plotted together with the exact transmission function from Fig. 3.2b. With this phenomenological transmission function, we now calculate the transport properties. Fig. 3.11b shows the electrical conductance G as obtained from the phenomenological approach along with the exact value of G for the GAAH model, showing excellent agreement up to an overall scale factor. The factor occurs because, due to the fractal nature of the spectrum of the GAAH model, the integral of the true transmission function of the GAAH model is a fraction of that of the boxcar transmission function. Other Onsager coefficients obtained from the phenomenological model also differ by the same overall factor. This, in turn, means that quantities defined as a ratio of the Onsager coefficients show excellent agreement with the GAAH model. This is shown in Fig. 3.11c for the Seebeck factor, and in Fig. 3.11d for the efficiency at maximum power.

This exercise shows that the physics analysed in previous section is not a specific property of the GAAH model that we have considered here. Any system with similar coarse-grained features in its transmission function will show the same qualitative

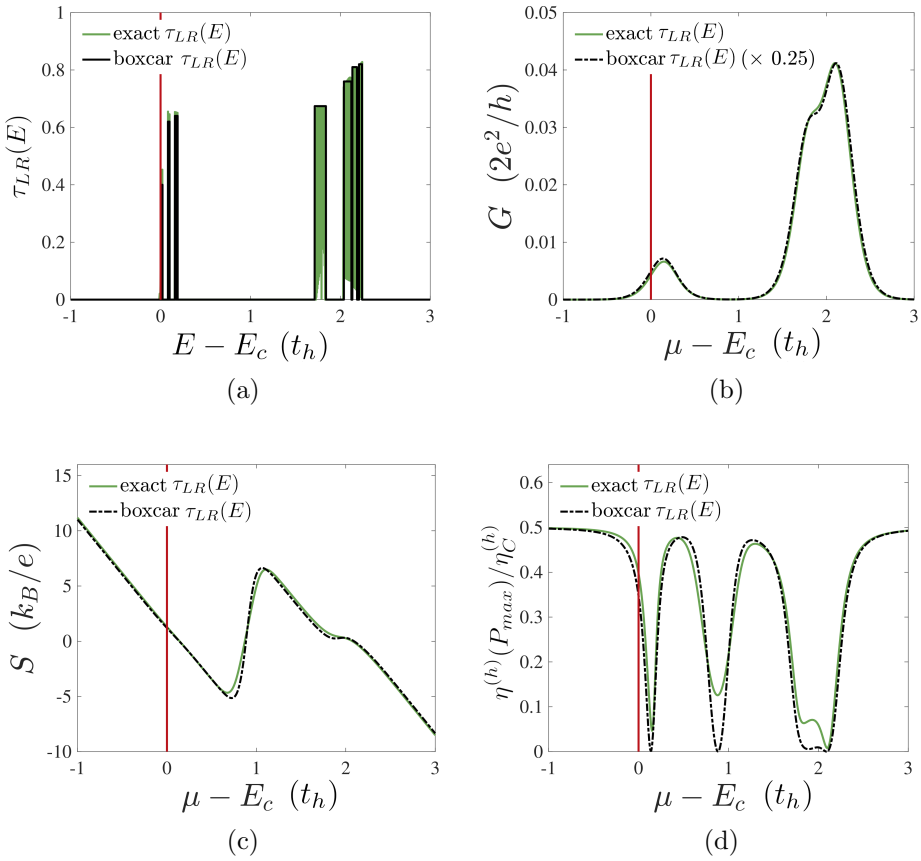

Figure 3.11: (a) The transmission function for the set-up in the same configuration as in the main text computed with NEGF (green lines), overlapped by a series of boxcar (black lines) following its profile. Comparison of (b) the electric conductance, (c) the Seebeck factor and (d) efficiency at maximum power obtained from the calculated transmission (solid green line) and from the boxcar approximation (dashed black lines). The position of the mobility edge is shown by the red line.

behaviour. Such transmission functions are expected in other quasiperiodic one-dimensional systems with a mobility edge separating ballistic and localised states. Hence, our results exemplify the thermoelectric properties of all such systems.

3.3 Analytical results in the weak-coupling limit

The phenomenological transmission function can also be arrived at more microscopically in the weak system-bath coupling limit. The particle and heat currents in a one-dimensional system among two fermionic reservoirs, within the WBL approximation and in the weak system-bath coupling limit, can be in fact expressed directly as

a function of the eigenstates of the isolated system [31]:

$$J_e = 2e\gamma \sum_{\ell=1}^{N} \frac{\Phi_{L\ell}^2 \Phi_{R\ell}^2}{\Phi_{L\ell}^2 + \Phi_{R\ell}^2} \big(f_L(E_\ell) - f_R(E_n)\big), \tag{3.3}$$

$$J_q = 2\gamma \sum_{\ell=1}^{N} \frac{\Phi_{L\ell}^2 \Phi_{R\ell}^2}{\Phi_{L\ell}^2 + \Phi_{R\ell}^2} (E_\ell - \mu)\big(f_L(E_\ell) - f_R(E_\ell)\big), \tag{3.4}$$

where $\Phi_{\nu\ell},\ \nu = L, R$ is the component of the n-th eigenstate on the first ($\nu = L$) or the last ($\nu = R$) site of the chain. In the linear-response regime, we thus obtain the Onsager coefficients for reference values of μ and T:

$$L_{11} = 2\gamma e^2 T \sum_{\ell=1}^{N} \frac{\Phi_{L\ell}^2 \Phi_{R\ell}^2}{\Phi_{L\ell}^2 + \Phi_{R\ell}^2} (-f'(E_\ell)), \tag{3.5}$$

$$L_{12} = 2\gamma e T \sum_{n=1}^{N} \frac{\Phi_{L\ell}^2 \Phi_{R\ell}^2}{\Phi_{L\ell}^2 + \Phi_{R\ell}^2} (E_\ell - \mu)(-f'(E_\ell)), \tag{3.6}$$

$$L_{22} = 2\gamma T \sum_{\ell=1}^{N} \frac{\Phi_{L\ell}^2 \Phi_{R\ell}^2}{\Phi_{L\ell}^2 + \Phi_{R\ell}^2} (E_\ell - \mu)^2(-f'(E_\ell)). \tag{3.7}$$

The expressions above are strictly valid only in the weak system-bath coupling regime. Note that they only depends on the absolute values of the single-particle eigenvectors of the system at sites where the baths are attached, namely, the first and the last sites.

In Sec. 2.1, we have described the importance of breaking the symmetry between the dynamics of the electrons above and below the chemical potential, or, in other words, the electron-hole symmetry, in order to obtain a good thermoelectric. A simple way to realise this effect is to put an energy filter on the central system to prevent the transmission at certain energies. This may be achieved by a band edge or a mobility edge. Here we analytically demonstrate the enhancement of thermoelectric effects due to this mechanism. In the weak coupling regime it is easy to verify that they depend only over the first and the last sites, however, for larger γ, the only error is an overall multiplicative factor, which is the same for all the currents and Onsager coefficients (see Sec. 3.1.3). Considerations about quantities defined through ratios of the Onsager coefficients can be then regarded as generic, since these prefactors cancel each other.

It is evident that in order to get a coefficient L_{12} different from zero the eigenstates

need to behave differently for energy above or below the chemical potential μ. With this condition, the Seebeck coefficient, which is introduced in Eq. 2.41 and enters quadratically in the definition of the figure of merit, can assume finite values. If the spectrum of the system contains an isolated cluster of eigenstates, the strongest thermoelectric effects arise when the chemical potential is placed at their edges, since there are no states contributing below or above a certain index ℓ^* in the sum appearing in Eqs. (3.5)-(3.7). On the other hand, for a system exhibiting a mobility edge at $E_c = E_{\ell^*}$ the eigenfunctions scale with the system size N as follows:

$$\begin{aligned} \Phi^2_{\nu\ell} &\sim e^{-N} \quad \text{if} \quad \ell < \ell^*, \\ \Phi^2_{\nu\ell} &\sim \frac{1}{N} \quad \text{if} \quad \ell > \ell^*. \end{aligned} \tag{3.8}$$

The sums can be then split into two parts: the terms for $\ell < \ell^*$ and for $\ell > \ell^*$. The former terms will go to zero as N increases, while the latter will converge to a finite value.

We now make the further assumption that the eigenfunctions $\Phi_{\nu\ell}$ contribute approximately the same weight for each value of $\ell > \ell^*$ in Eqs. (3.5)-(3.7). The Onsager coefficients for large enough N can be thus approximated, up to a proportionality constant, by

$$L_{11} \propto \gamma \, \frac{e^2 T}{N} \sum_{\ell>\ell^*}^{N} (-f'(E_\ell)), \tag{3.9}$$

$$L_{12} \propto \gamma \, \frac{eT}{N} \sum_{\ell>\ell^*}^{N} (E_\ell - \mu)(-f'(E_\ell)), \tag{3.10}$$

$$L_{22} \propto \gamma \, \frac{T}{N} \sum_{\ell>\ell^*}^{N} (E_\ell - \mu)^2(-f'(E_\ell)). \tag{3.11}$$

We display in Fig. 3.12 the comparison between the exact computation carried out through the Landauer-Büttiker integrals and the predictions of the above equations. We notice that the proportionality constant, independent on the system size, is the same for all three Onsager coefficients. As a consequence, it does not affect quantities such as the thermopower, the figure of merit or the efficiency. Therefore, we see that we only require the single-particle eigenvalues of the system to accurately recover the essential physics, up to a proportionality constant.

Now, we take one further step of approximation. We note that the single-particle

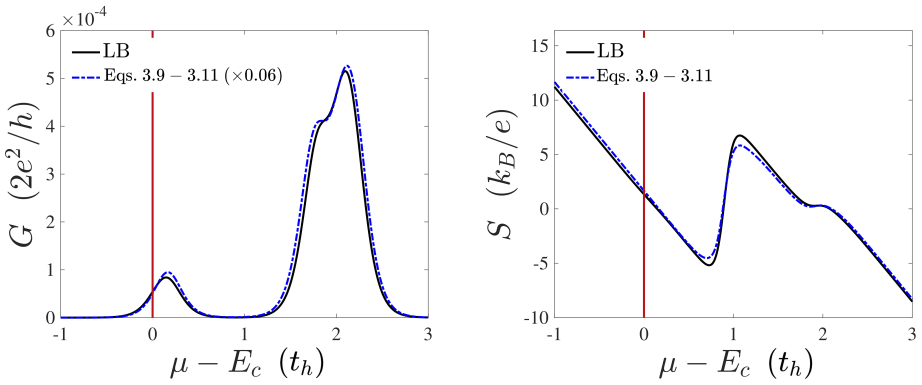

Figure 3.12: Comparison between the transport coefficients computed through the exact Landauer-Büttiker integrals (solid black line), and the approximated forms in Eqs. (3.9)–(3.11) (dashed blue line). (a) Electrical conductance. (b) Seebeck coefficient. The parameters of the system are the same as in the main text, but with a weak coupling of $\gamma = 0.01\ t_h$. The proportionality factor of 0.06 in (a) is a free parameter, which encapsulates the microscopic details of the eigenfunctions that are neglected in the approximations. The position of the mobility edge is shown by the red line.

eigenvalues occur in clusters, as evidenced by the ballistic bands in Fig. 3.2b. Due to quasiperiodicity, these eigenvalue clusters have a finer self-similar structure. We now choose to completely ignore this finer structure and replace the summations in Eqs. (3.9), (3.10), (3.11) by integrals over the width of each ballistic band. This amounts to phenomenologically modelling the transmission function by a series of boxcar functions, as done in Sec. 3.2. With this simplified assumption, we can derive closed-form analytical expressions for the contribution from each boxcar function to the Onsager coefficients L_{11} and L_{12}. To state the result concisely, we define the following three functions:

$$A = \tanh\left(\frac{\mu - E_1}{2k_BT}\right),$$
$$B = \tanh\left(\frac{E_2 - \mu}{2k_BT}\right),$$
$$C = \log\left[\cosh\left(\frac{\mu - E_1}{2k_BT}\right)\operatorname{sech}\left(\frac{E_2 - \mu}{2k_BT}\right)\right].$$

The contribution to L_{11} and L_{22} from a band of ballistic states between E_1 and E_2 is

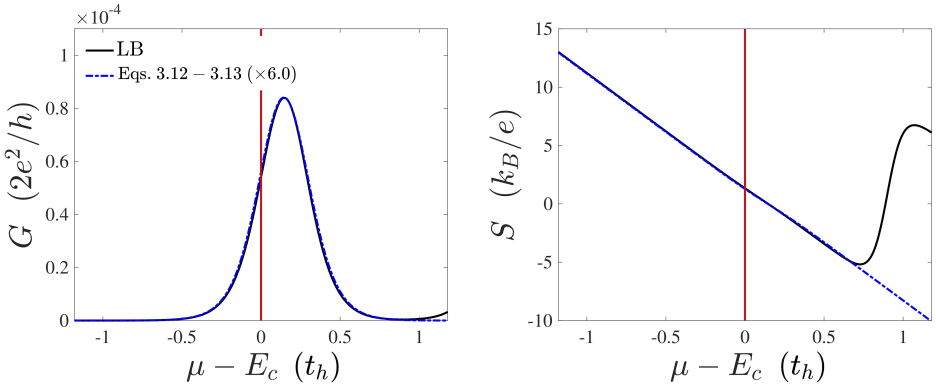

(a) (b)

Figure 3.13: (a) Electrical conductance and (b) Seebeck coefficient at low temperature $T = 0.1\ t_h/k_B$ and $\gamma = 0.01\ t_h$. The quantities are computed through the exact Landauer-Büttiker integrals (solid black line), and the analytical formulae in Eqs. (3.12) and (3.13) (dashed blue line). The proportionality factor of 6.0 in (a) is a free parameter, which reflects the fractal structure of the transmission function that is neglected in the boxcar approximation. The position of the mobility edge is shown by the red line.

then given by

$$L_{11} \propto \frac{e^2 T\gamma}{N}\left[A + B\right], \tag{3.12}$$

$$L_{12} \propto \frac{eT\gamma}{N}\left[(E_1 - \mu)A + (E_2 - \mu)B + 2k_B TC\right]. \tag{3.13}$$

To show the correctness of these results, we plot the conductance G and Seebeck coefficient S for chemical potentials μ close to the mobility edge. At low temperatures, only one cluster contributes, and this contribution should match that obtained from the above analytical formulae, up to a proportionality constant for G. Plots of G and S as obtained from the above formula are shown in Fig. 3.13 along with the exact results. Indeed, we see that G is qualitatively identical up to a proportionality constant, while S is both qualitatively and quantitatively the same. The Seebeck coefficient starts to deviate for higher μ due to contributions from the next cluster of ballistic states. This can be remedied by adding another boxcar function corresponding to the next cluster, as done in obtaining Fig. 3.11c. This analysis reinforce the conjecture that similar thermoelectric characteristics will occur in other quasiperiodic systems displaying a mobility edge.

Chapter 4

Fibonacci heat engine

We proceed with the exploration of the possible application of quasiperiodic potentials in quantum heat management by focusing on the diagonal Fibonacci chain, introduced in Sec. 1.4. In this Chapter, we consider its non-interacting limit, and, after a review of the known results on the anomalous particle and spin transport in the model, we analyse in Sec. 4.1 the emergence of thermoelectric effects within the approach of Sec. 2.1. Then, motivated by experiments in molecular nanoelectronics, we investigate the consequences of introducing incoherent inelastic effects which lead to dephasing. These can be easily incorporated within our framework through voltage-temperature Büttiker probes, that are presented in Sec. 4.2. In Sec. 4.3, we discuss how the presence of dephasing noise from inelastic scattering modifies the highly non-trivial transport properties of the Fibonacci model, and, in particular, how it can be used to enhance refrigeration in the device in certain favourable thermodynamic configurations. These results have been first presented in Ref. [206].

We restate that in the tight-binding diagonal Fibonacci chain the lattice energies $\{V_l\}_{l=1}^{N}$ assume two alternating values u_A or u_B, whose sequence is generated by the Fibonacci substitution rule,

$$\begin{aligned} u_A &\to u_A u_B \\ u_B &\to u_A, \end{aligned} \tag{4.1}$$

while the first neighbour hopping t_h is constant. Differently from the paradigmatic AAH, this model escapes localisation, while the quasiperiodicity of the potential in-

duces multifractal spectrum and eigenstates at every u_A and u_B, in the sense described in Sec. 1.2.1. Therefore, one may assume control over a single parameter $u_A = -u_B = u$ without loss of generality. It is known, since the pioneering study of Abe and Hiramoto [30], that the spectral criticality in this model gives rise to anomalous transport exponents varying continuously with the potential strength u [207]. We replicate these results in Fig. 4.1a, where we evaluate the mean square displacement of a wavepacket initially localised at the center of the chain, $\Delta x^2(t) = \sum_l \left[(l - N/2)^2 \ |\Psi_l(t)|^2\right]$. We consider the isolated chain and compute the unitarily evolved state with the Fibonacci matrix Hamiltonian $\mathbf{\Psi}(t) = \exp\left(-it\mathbf{H}_s/\hbar\right)\mathbf{\Psi}(0)$. The vector $\mathbf{\Psi}(t)$ contains the component of the wavepacket over the $l = 1, \ldots, N$ site of the chain, and $\Psi_l(0) = \delta_{lN/2}$. As discussed in Sec. 2.2.3 and Appendix A, in presence of translational invariance this quantity yields the same information of the spread of correlations connected to the Green-Kubo electric conductivity. The exponent in the scaling fit $\Delta x^2(t) \sim t^\nu$ can then be employed to discern the transport regime. In particular, $\nu = 2$ points to ballistic behaviour and $\nu = 1$ to standard diffusion, $1 < \nu < 2$ implies superdiffusive transport, and $0 < \nu < 1$ implies subdiffusive transport. We note that the fits are performed for times before the boundaries of the system are reached and the curves saturate. As u increases, we observe that the transport slows down, and correspondingly the saturation happens at longer times. In Fig. 4.1b we show the ν extracted from the fits of the $\Delta x^2(t)$ curves, as a function of u. The exponent ν tends to 2 for $u \to 0$, and then decreases continuously towards 0 (absence of transport) for increasing u, with two regimes: superdiffusive ($\alpha > 1$ for $u \lesssim 1.5$) and subdiffusive ($\alpha < 1$ for $u \gtrsim 1.5$). In Ref. [32], it has been verified that the same exponent can be extracted from single realisations of the Fibonacci potential. However, here and in the following we perform the averaging procedure followed in in Refs. [134, 208] and described in Sec. 1.4 to formally restore translational invariance. Operationally, we consider an "infinite" sequence with $N_\infty \gg N$ generated directly from Eq. (4.1) and cut out finite samples of length N starting from the first site, then from the second, etc. Discarding the reflection symmetric examples and the symmetric partners of the samples already stored, we can identify $N/2$ (or $(N-1)/2$ for odd N) distinct samples to average over.

Spin transport in the open environment has been analysed through a phenomenological Lindblad master equation in Ref. [32]. In this setting, multifractality determines again a scaling of the current that smoothly varies from superdiffusive to subdiffusive

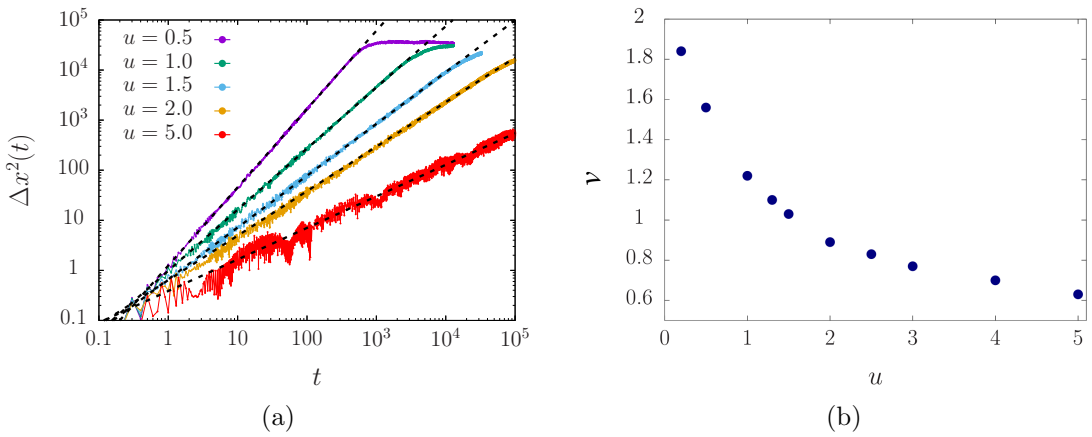

(a) (b)

Figure 4.1: (a) Mean squared displacement Δx^2 of a state initially localised at the middle of a non-interacting Fibonacci chain of $N = 1001$ sites is computed in time for different example values of the potential strength u. The dashed lines in the log-log plot show the fits $\Delta x^2 \sim t^\nu$. We notice the curves saturating at low u as the wavepacket has spread over the entire system, where the fast dynamics makes the finite size of the system visible at shorter times. (b) The extracted exponent ν varies continuously with u, indicating anomalous diffusion.

through standard diffusion with increasing u. However, as in the case of the AAH, it is highlighted a dependence of the scaling exponents on the number theoretic properties of the set of chosen N, and the quantitative mismatch with the results from the isolated chain.

In the context of quantum thermal machines, the multifractality of the spectrum, reflected in the transmission function, suggests the possible capability of the Fibonacci chain as working medium. Therefore, we investigate steady-state thermoelectric transport in the Fibonacci model in presence of both temperature and chemical potential bias. Arrangements of nucleotides in synthetic DNA molecules generated by the same Fibonacci substitution rule have in fact already been proposed to realise nanoelectric devices [131, 132], with related numerical studies mostly limited to electric transport [209, 210]. If we want to consider thermoelectric devices based on this type of structures, however, we must consider that in single DNA molecules, transport is characterised by a concurrence of coherent and incoherent mechanisms, determined by the interaction between conducting electrons and "environmental" degrees of freedom such as the other electrons, nuclei or the solvent [211–214]. These many-body effects collectively introduce noise that might consist of loss of phase coherence, and momentum and energy exchange. It has been demonstrated in various contexts that this noise from the environment can assist transport. The examples of such environmental

assisted or dephasing enhanced transport include natural photosynthetic complexes [41, 42, 215–219], molecular junctions [44, 220, 221], photonic crystals [46, 47, 222], trapped ions [48, 223], and also boundary-driven spin chains at infinite temperature [49–51]. However, the implications of this effect for thermoelectricity — an intrinsically finite-temperature phenomenon — have received comparatively little attention. Here we ask if the inevitable presence of dephasing noise due to inelastic scattering can be used to enhance thermoelectric performance in quasiperiodic quantum thermal machines.

4.1 Coherent thermoelectric transport

We first reproduce the regime of anomalous transport in absence of dephasing within Landauer's framework for a two-terminal device. The Fibonacci chain is attached to a hot and a cold reservoir in WBL approximation in the same configuration where we studied the GAAH model in Sec. 3.1, and we compute electric and heat currents in linear response through the transport coefficients and the applied biases. The existing calculations focus on the infinite temperature case [32], and surprisingly, to our knowledge, the survival of the anomalous diffusion has not been demonstrated at finite temperatures. In the following, we work in a regime of intermediate system-bath coupling, $\gamma = t_h = 1$. However, the choice of γ within linear response and WBL approximation only rescales the currents without qualitatively affecting the transport behaviour, as verified in Sec. 3.1.3. From our numerics, we observe that the self-similar structure of the spectrum in the Fibonacci model is reflected on the transmission function $\tau_{LR}(E)$. An example of the transmission function for a chosen value of Fibonacci potential strength is shown in Fig. 4.2.

The calculation of currents requires an integration over energy of the transmission function multiplied by the Fermi-Dirac distributions. Due to the near-discontinuous nature of the transmission, this integration becomes challenging for large system sizes. Nevertheless, the system sizes we have been able to access are large enough to extract the asymptotic transport exponents α_G and α_K, introduced in Eq. (2.106) and Eq. (2.107). In Fig. 4.3a and Fig. 4.3b, we show J_e and J_q as function of system size N at different Fibonacci potential strengths $u = 0.5, 1.0, 1.5, 2.0, 4.0$. The thermodynamic parameters are $T = 1.0$, $\Delta\mu = 0.1$ and $\Delta T = 0.1$. We select different chemical

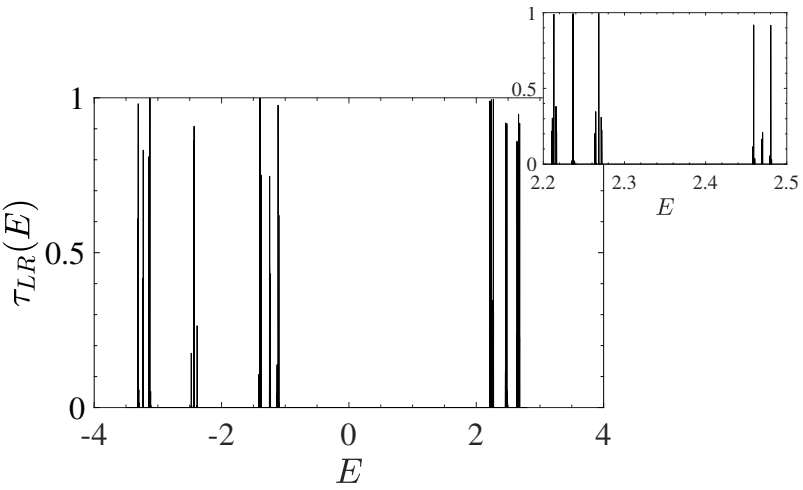

Figure 4.2: Example of zero-dephasing transmission function $\tau_{LR}(E)$ of a single Fibonacci chain realisation of size $N = 200$, at $u = 2.0$. In the inset, we explicitly show the self-similarity of the structure by zooming on a portion of the energy axis.

potentials for every value of u, since the choice of μ along the energy axis affects only a pre-factor in the currents and not their scaling exponent, leaving the plots qualitatively equivalent. We observe in Fig. 4.3c that the transport exponents α_G (blue dots) and α_K (red stars) collapse onto the same trend. We notice that the exponent α_G and α_K vary continuously with u, from superdiffusive ($\alpha_{G/K} < 1$) to subdiffusive ($\alpha_{G/K} > 1$) behaviour through normal diffusion ($\alpha_{G/K} = 1$). In Fig. 4.3d, we show that this data collapse occurs independently of temperature. Thus, we prove that the anomalous transport behaviour observed previously at infinite temperature survives at finite temperatures in both the electric and thermal transport.

The Landauer-Büttiker framework we have adopted has not only the advantage to allow the study of charge and heat currents at finite temperature but in what follows it will also allow us to study the effect of dephasing in a systematic way by introducing Büttiker probes.

4.2 Büttiker probes

The idea of introducing additional electron reservoirs as probes to mimic dephasing noise was first described by Büttiker [224], and then applied to extended conductors by D'Amato and Pastawski [225, 226]. The additional reservoirs are treated as conventional baths, which receive particles and re-introduce them into the central system after scrambling their phase. The probes are "fictitious" in the sense that their par-

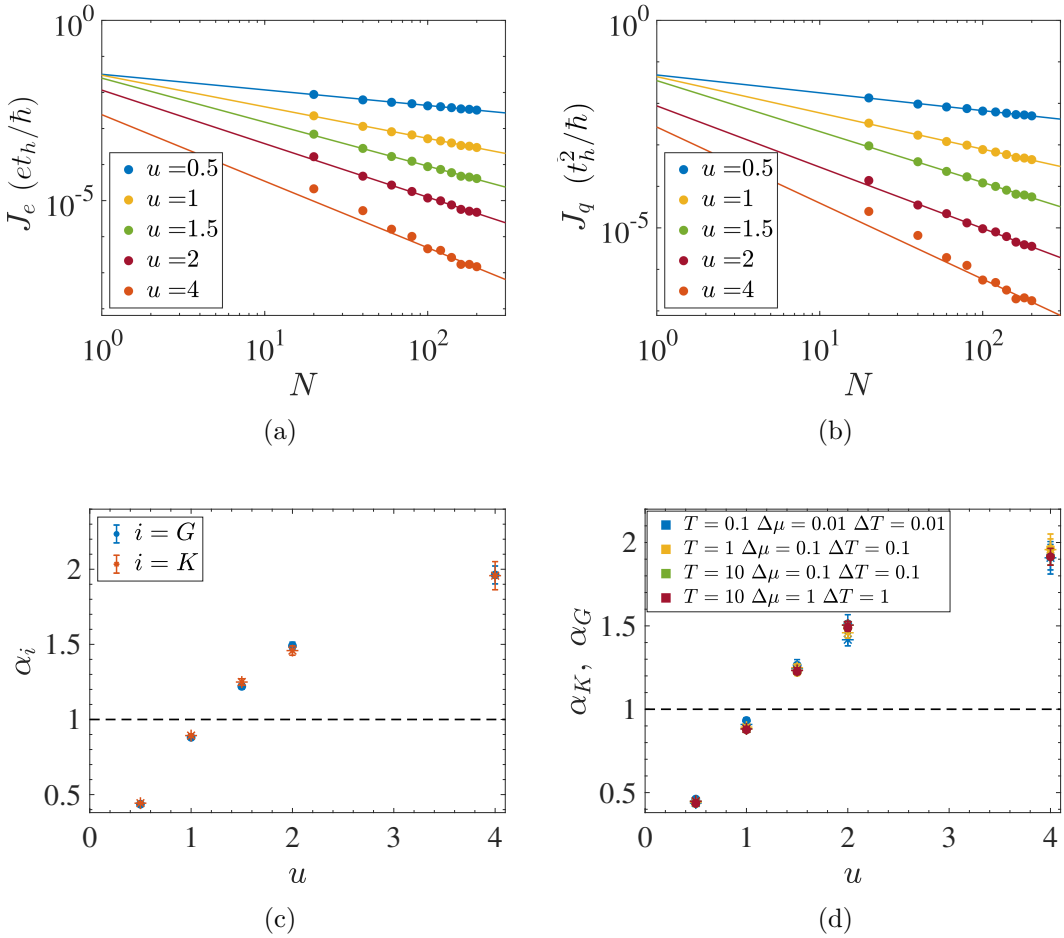

Figure 4.3: (a)-(b) Scaling with N of coherent heat and electric currents in the Fibonacci model with hopping parameter $t_h = 1$ and coupling to the baths $\gamma = 1$, for different potential strengths u, indicated in the color legend. The thermodynamic parameters are $T = 1$, $\Delta T = 0.1$, $\Delta\mu = 0.1$. The chemical potentials are respectively $\mu = -2, -2.4, -2.8, -3.3, -5.2$. (c) Scaling exponent extracted from the electric $G \sim N^{-\alpha_G}$ (blue dots) and thermal conductance $K \sim N^{-\alpha_K}$ (red stars) associated to the currents in (a)-(b), at the same parameters. The dashed line indicates the value of α at which transport is diffusive. The error bars are given by the asymptotic error in the fits. (d) Scaling exponents for G (dots) and K (stars) computed in different thermodynamic configurations given by the colors in the legend. We notice that they do not depend on the thermodynamic configurations.

ticle distributions are self-consistently determined in such a way to mimic different types of incoherent scattering processes. We consider again the configuration and formalism introduced in Sec. 2.1 to study coherent transport, and, in particular, the total Hamiltonian of the extended region composed of system and baths is given by the same Eq. (2.18). However, the index ν covers now both "real" left (L) and right (R) baths, and the N probes, $\nu = L, R, 1, ..., N$. Each probe $n = 1, ..., N$ is a fermionic bath with Hamiltonian analogous to Eq. (2.19) and spectral function analogous to Eq. (2.30), and is coupled to the n-th site of the chain through

$$\hat{H}_{Fn} = \sum_{\lambda} (t_{\lambda n} \hat{a}_n^\dagger \hat{D}_{\lambda n} + \text{h.c}), \tag{4.2}$$

with $t_{\lambda n}$ the amplitude for electrons to tunnel from the n-th lead onto the wire. The electric and heat currents flowing through the system are given by the Landauer-Büttiker integrals in Eq. (2.2) and Eq. (2.11) extended to multiple terminals

$$J_e = \frac{2e}{h} \sum_{\nu} \int dE \tau_{L\nu}(E)[f_L(E) - f_\nu(E)], \tag{4.3}$$

$$J_q = \frac{2}{h} \sum_{\nu} \int dE (E - \mu_L) \tau_{L\nu}(E)[f_L(E) - f_\nu(E)], \tag{4.4}$$

where $f_{L/R}(E)$ are the Fermi-Dirac distributions of the left and right physical reservoirs, and $f_n(E)$ the occupation probabilities of the probes. The collection of transmission functions $\tau_{\nu'\nu}(E)$ is found via a generalisation of the NEGF approach to a multi-terminal set-up. The formula in Eq. (2.28) thus becomes

$$\tau_{\nu\nu'}(E) = \text{Tr}\big\{\mathbf{\Gamma}_\nu(E)\mathbf{G}_S^\dagger(E)\mathbf{\Gamma}_{\nu'}(E)\mathbf{G}_S(E)\big\}, \tag{4.5}$$

where the NEGF $\mathbf{G}_S(E)$ was defined in Eq. (2.25). The indices $\nu, \nu' = L, R, 1, ..., N$ here run over the real left (L) and right (R) baths, and the Büttiker probes $(1, ..., N)$. Given the structure of the coupling with the central system in Eq. (4.2), the self-energies of the the probes $\mathbf{\Sigma}_n(E)$ $(n = 1, ...N)$ are given in WBL approximation by one constant non-zero element matrices when in lattice basis, $[\mathbf{\Sigma}_n(E)]_{nn} = -i\gamma_d/2$, while $[\mathbf{\Gamma}_n(E)]_{nn} = \gamma_d$. The generalised transmission functions can be then simplified

as

$$\begin{aligned}
\tau_{LR}(E) &= \gamma^2 \ |[\mathbf{G}_S(E)]_{1N}|^2 \\
\tau_{nL}(E) &= \gamma\gamma_d \ |[\mathbf{G}_S(E)]_{n1}|^2 \\
\tau_{nR}(E) &= \gamma\gamma_d \ \ |[\mathbf{G}_S(E)]_{nN}|^2 \\
\tau_{nn'}(E) &= \gamma_d^2 \ \ |[\mathbf{G}_S(E)]_{nn'}|^2.
\end{aligned} \tag{4.6}$$

We assign $\tau_{\nu\nu}(E) = 0$, since these terms do not contribute to the currents, and $\tau_{\nu\nu'}(E) = \tau_{\nu'\nu}(E)$, since the tunnelling process is symmetric. The only formal difference between real baths and probes is that their occupation $f_n(E)$ is not necessary a Fermi-Dirac distribution with temperature T_n and chemical potential μ_n as free parameters, but it is self-consistently determined by imposing some conditions on the currents flowing towards them,

$$J_{e,n} = \frac{2e}{h} \sum_{\nu} \int dE \tau_{n\nu}(E)[f_n(E) - f_\nu(E)], \tag{4.7}$$

$$J_{q,n} = \frac{2}{h} \sum_{\nu} \int dE (E - \mu_n) \tau_{n\nu}(E)[f_n(E) - f_\nu(E)]. \tag{4.8}$$

The conditions depend on the type of incoherent effect desired. Incoherent elastic scattering, where the electrons lose memory of their phase but conserve their energy, is recreated by cancelling the contribution to the electric current at each energy with the so-called "dephasing probe" [220]. Operationally, this translates into deriving the occupation of the N probes from the solution of the N equations $\tau_{n\nu}(E)[f_n(E) - f_\nu(E)] = 0$, at each energy E. For the other cases of incoherent effects, one requires instead the specific form $f_n(E) = \{1 + \exp[(E - \mu_n)/k_B T_n]\}^{-1}$ and solves the conditions for T_n and μ_n. When a chemical potential bias is applied to the system, incoherent inelastic scattering is introduced by setting the net electric currents towards each probe to zero $J_{e,n} = 0$, using a "voltage probe" [45, 212, 227]. If a temperature bias is also present, as in the context of thermal machines, we encode non-dissipative inelastic scattering by further cancelling the heat currents going in to the probes. In this case, the average transfer of charge and heat from and towards the probes is zero, but single electrons exchange energy and momentum besides losing phase coherence. In the following, we implement this so-called "voltage-temperature

probe" [211], imposing then

$$J_{e,n} = \frac{2e}{h} \sum_{\nu} \int dE \tau_{n\nu}(E)[f_n(E) - f_\nu(E)] = 0, \tag{4.9}$$

$$J_{q,n} = \frac{2}{h} \sum_{\nu} \int dE (E - \mu_n) \tau_{n\nu}(E)[f_n(E) - f_\nu(E)] = 0. \tag{4.10}$$

These $2N$ non-linear equations do not posses a proof of existence and uniqueness of the solution, contrary to the case of the voltage probe [228, 220]. We restrict then the study to linear response regime, as suggested by the algorithm in Ref. [229], by Taylor-expanding the Fermi-Dirac distributions of each probe and bath. Once solved the system of $2N$ linear equation, we plug the set of solutions $\{T_n, \mu_n\}_{n=1}^{N}$ into Eqs. (4.3)–(4.4). To extract the transport coefficients, we re-write the physical currents in Eqs. (4.3)–(4.4) as in Eqs. (2.44)–(2.45). We first calculate electric and heat currents setting $\Delta T = 0$, $\Delta\mu \neq 0$, and calculate them again a second time, setting $\Delta T \neq 0$, $\Delta\mu = 0$. We see that the first calculation allows extraction of G and Π. Knowing G and Π, the second calculation allows extraction of S and K. We investigate then the possibility of dephasing-enhanced transport in the Fibonacci model in presence of the voltage-temperature Büttiker probes. Henceforth, we will refer to the system-probe coupling parameter γ_d as "dephasing strength". However, the conditions implemented on the currents mimic incoherent inelastic scattering events, leading to energy relaxation (at single electron level, but not on average) beside the loss of phase coherence. It should be noted that this is fundamentally different from local pure dephasing Lindblad dissipators, most often used in the context of quantum information, which allow energy transfer even on average.

4.3 Introducing dephasing

4.3.1 Dephasing enhanced transport

A heuristic argument to understand the behaviour of the infinite-temperature conductivity after adding dephasing was introduced in Ref. [50] for spin transport with dephasing and dissipation modelled via Lindblad equations. Here, we revisit the argument considering electric current under a voltage bias. As first seen in Eqs. (2.104)–(2.106), the phenomenological diffusion equation for the electric current induced by a

voltage bias in absence of dephasing $J_e = \sigma(N)\Delta\mu/N$, can be generalised to anomalous transport regimes with $\sigma(N) \sim N^{1-\alpha_G}$. It is known that sufficient dephasing changes anomalous transport behaviour to normal diffusive behaviour. For a given dephasing strength γ_d, one can associate a characteristic length N_d, beyond which coherence is quickly destroyed, so that transport becomes diffusive with well-defined $\sigma(\gamma_d)$. This argument gives

$$\sigma(N, \gamma_d) \sim \begin{cases} N^{1-\alpha_G} & N < N_d \\ \sigma(\gamma_d) & N > N_d \end{cases}, \tag{4.11}$$

The behaviour should be continuous across N_d, so that at $N = N_d$ it must hold that $\sigma(\gamma_d) \sim N_d^{1-\alpha_G}$. Considering $t_d \sim 1/\gamma_d$ to be the time between incoherent scattering events, N_d can be heuristically estimated by the spatial spread of a small perturbation in the system within this time in absence of coupling to baths [50]. This gives $N_d \sim \gamma_d^{-1/(\alpha_G+1)}$. As a result, for small dephasing strength, we get the following dependence of conductivity on the dephasing strength,

$$\sigma(\gamma_d) \sim N_d^{1-\alpha_G} \sim \gamma_d^{(\alpha_G-1)/(\alpha_G+1)}. \tag{4.12}$$

Thus, the dependence of conductance on the dephasing strength is dictated by the nature of transport in the absence of dephasing. If the transport in the absence of dephasing is either ballistic ($\alpha_G = 0$) or superdiffusive ($\alpha_G < 1$), in the regime of small γ_d, the conductivity decays to zero as γ_d increases. But in the case of subdiffusion ($\alpha_G > 1$), the conductivity increases and consequently reaches a maximum at intermediate γ_d before decaying for large γ_d. Thus, dephasing enhanced transport is expected in the regime where the transport was subdiffusive in absence of dephasing. Behavior consistent with above heuristic description has already been observed in various systems within the framework of local Lindblad equations, which can be thought to model the infinite temperature limit, and local pure dephasing Lindblad dissipators [49–51, 230, 231]. This includes a recent study on the Fibonacci model [51]. We stress again that our set-up is fundamentally different from this class of descriptions. In the set-up of these previous works, energy exchange with the sources of dephasing is allowed, even on average. However, in our set-up with the voltage-temperature Büttiker probes, both electric and heat currents into the probes are zero on average.

Therefore, neither particle exchange nor energy exchange with the sources of dephasing are allowed on average. Despite this, we expect the heuristic phenomenology of dephasing enhanced transport given above to hold in our set-up. Moreover, although the above phenomenology has been discussed in terms of electric conductivity, we expect to see enhancement of thermal conductivity also as a function of dephasing strength, before it eventually decays to zero for large dephasing strength.

We now numerically explore the possibility of dephasing enhanced transport in the our set-up. The number of transmission functions to compute from Eq. (4.6) at every energy E grows as N^2, which limits our study to $N \sim 200$. Despite this, we find that our numerics are well converged at this system size and allow for an accurate extraction of transport exponents. In Fig. 4.4, we show the diffusive scaling of electric J_e (left panels) and heat J_q (right panels) currents at different γ_d for potential strength $u = 0.5$ (top panels) and $u = 4.0$ (bottom panels). In the same figures, the dashed line indicates the value of currents in the coherent case. We verify, as evident in the bottom panels, that dephasing enhances heat and electric transport at the potential strength which would otherwise determine subdiffusion, $u = 4.0$. The plots are realized for different μ, at $T = 1.0$, and $\Delta\mu = \Delta T = 0.1$, but changing the thermodynamic variables of the leads does not alter the results in any qualitative way.

Next, we look at the electric and thermal conductivities. We extract the conductivities σ and κ from the linear fits of respectively $\log G$ and $\log K$ versus $-\log N$ up to $N = 200$, for different values of γ_d. While scanning the thermodynamic parameter space, we notice a remarkably sensitive behaviour of the conductivities to temperature T and chemical potential μ, which is more evident as we increase the potential strength u in the subdiffusive regime. In Fig. 4.5 we show σ (in blue) and κ (in red) as a function of γ_d for $u = 4.0$ at different choices of T and μ. In all plots, we see that both the electrical and the thermal conductivities initially increase with γ_d, while they go to zero for large γ_d, as expected from the heuristic argument above. We highlight the position of the highest values of σ and κ with continuous vertical lines of the same color. In Fig. 4.5a and Fig. 4.5b we set the temperature to $T = 0.1$, and take two different values of μ, respectively corresponding to the lower and top end of the spectrum. Surprisingly, we observe the presence of multiple local maxima, whose heights and positions depend on the choice of μ. The same kind of variety in the local peaks arises also at intermediate temperatures and for other choices of chemical

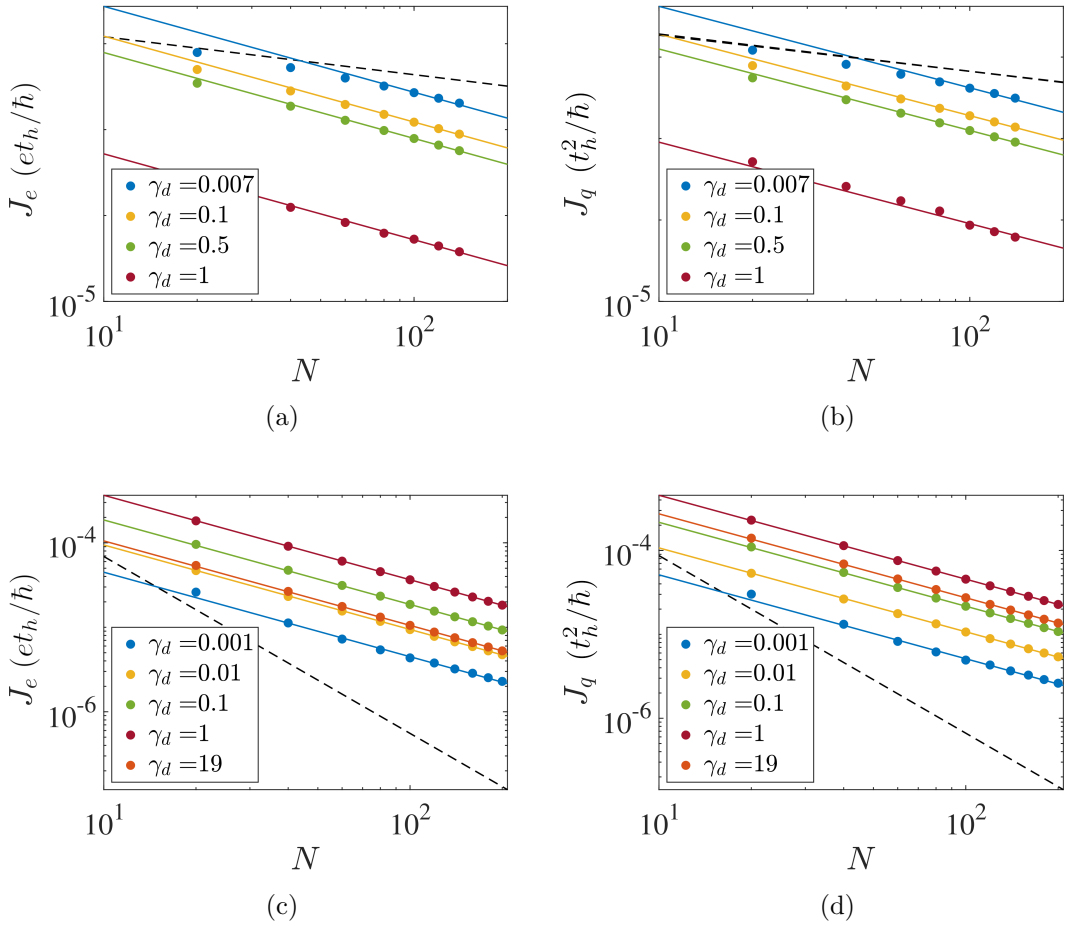

Figure 4.4: Electric (a)-(c) and heat (b)-(d) currents in Fibonacci chains of length N at various dephasing strengths γ_d, indicated in the legends. The dashed line shows the corresponding currents at zero dephasing. Currents become diffusive at any $\gamma_d \neq 0$, so that transport slows down in the superdiffusive regime for $u = 0.5$ (top panel), while is enhanced in the subdiffusive regime for $u = 4.0$ (bottom panel). The thermodynamic parameters are $T = 1.0$, $\Delta T = 0.1$, and $\Delta\mu = 0.1$.

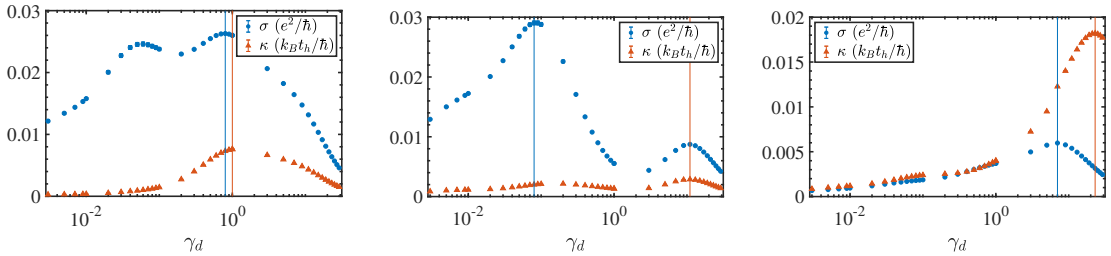

Figure 4.5: The electric (blue) and thermal (red) conductivities extracted from the scaling of the conductances up to a length of $N = 200$, with $u = 4.0$. The continuous lines highlight the dephasing strength γ_d that maximises the corresponding conductivity. The plots are at different thermodynamic configurations: in (a)-(b), $T = 0.1$ and μ is taken at two different points in the energy spectrum, respectively $\mu = -5.2$ and $\mu = 4.3$, while in (c), $T = 10$ and the choice of μ becomes irrelevant (for the specific plot we show $\mu = -5.2$). The error bars on each data point, given from the asymptotic error in the linear fit, are smaller than dot size and not visible in the plots.

potentials. On the other hand, at high temperatures, a single peak appears for each conductivity, with position and height independent of μ, as shown in Fig. 4.5c for $T = 10$. The presence of a single peak is in consistent with previous findings using Lindblad dephasing in Ref. [51].

Linear response transport properties of a fermionic system at chemical potential μ and temperature T are usually governed by the spectrum of the system in the range of the energies $\mu \pm k_B T$, which is approximately the width of the derivative of the Fermi-Dirac distribution with respect to μ, as we already noticed in Fig. 2.4a. Thus, if $k_B T$ is much larger than the bandwidth of the system, transport coefficients become independent of μ. This explains the observed μ independence of high temperature conductivities. On the other hand, this picture suggests that the presence of multiple μ dependent peaks at low temperatures is related to the structure of the effective spectrum given by the collection of transmission functions within the energy window $\mu \pm k_B T$. We therefore deduce that the fractal spectrum of the Fibonacci model, which gives the peculiar near-discontinuous transmission function in the coherent case (see Fig.4.2), is also the reason for the surprising multiple peaks in the conductivities as a function of γ_d. A more microscopic understanding, however, is difficult at finite temperatures. Instead, in the next subsection we discuss another surprising observation from the results, the violation of Wiedemann-Franz law.

4.3.2 Violation of Wiedemann-Franz law

We state again the Wiedemann-Franz law, rewriting Eq. (2.51) in terms of the electric and thermal conductivities,

$$\frac{\kappa}{\sigma T} = \frac{K}{GT} = \mathcal{L}. \tag{4.13}$$

If transport is anomalous, $\mathcal{L}$ does not need to be equal to the Lorenz number $\mathcal{L}_0$, since the conductivities may not be well-defined in that case. In the Fibonacci model, we already find its violation in absence of dephasing, as we expect from the asymmetries in its transmission function.

We observe that the Wiedemann-Franz law is still violated over a wide range even in presence of dephasing, when transport becomes diffusive and both the conductivities are well-defined. This remarkable fact is evident from Fig. 4.5, which shows that even at relatively low temperature $T = 0.1$, the thermal and the electrical conductivities are not proportional to each other. In fact, we find that the maxima in the thermal and the electrical conductivities arise at different positions in parameter space, at both low and high temperatures. The violation of the Wiedemann-Franz law as a function of γ_d at $T = 0.1$ is explicitly shown in Fig. 4.6a and in Fig. 4.6b, respectively for $u = 2.0$, and $u = 4.0$. The $\mathcal{L}$ ratio is smaller than the Lorenz number for a wide range of γ_d, and it is restored to $\mathcal{L}_0$ only at $\gamma_d >> u$. At high temperatures, instead, as in Fig. 4.6c and in Fig. 4.6d the law is violated as expected for the entire range of γ_d we have considered.

We further analyse the deviation by visualising $\mathcal{L}/\mathcal{L}_0$ at different γ_d as a function of temperature with any other parameter fixed, for $u = 2.0$ in Fig. 4.7b and $u = 4.0$ in Fig. 4.7a. The violation for small and zero γ_d can be interpreted considering again the structure of the transmission functions from the collection of real baths and probes in the energy window included into transport at each temperature. At small and zero dephasing, the sharp features of the transmission would prevent the Sommerfeld expansion necessary to directly derive the Wiedemann-Franz law from Eqs.(4.3)-(4.4) at low temperatures. As dephasing increases, however, these features are progressively broadened and the energy windows over which the transmissions are continuous gets larger, so the ratio $\mathcal{L}/\mathcal{L}_0$ is restored to 1.

The fact that thermal and electrical conductivities can have maxima at different values

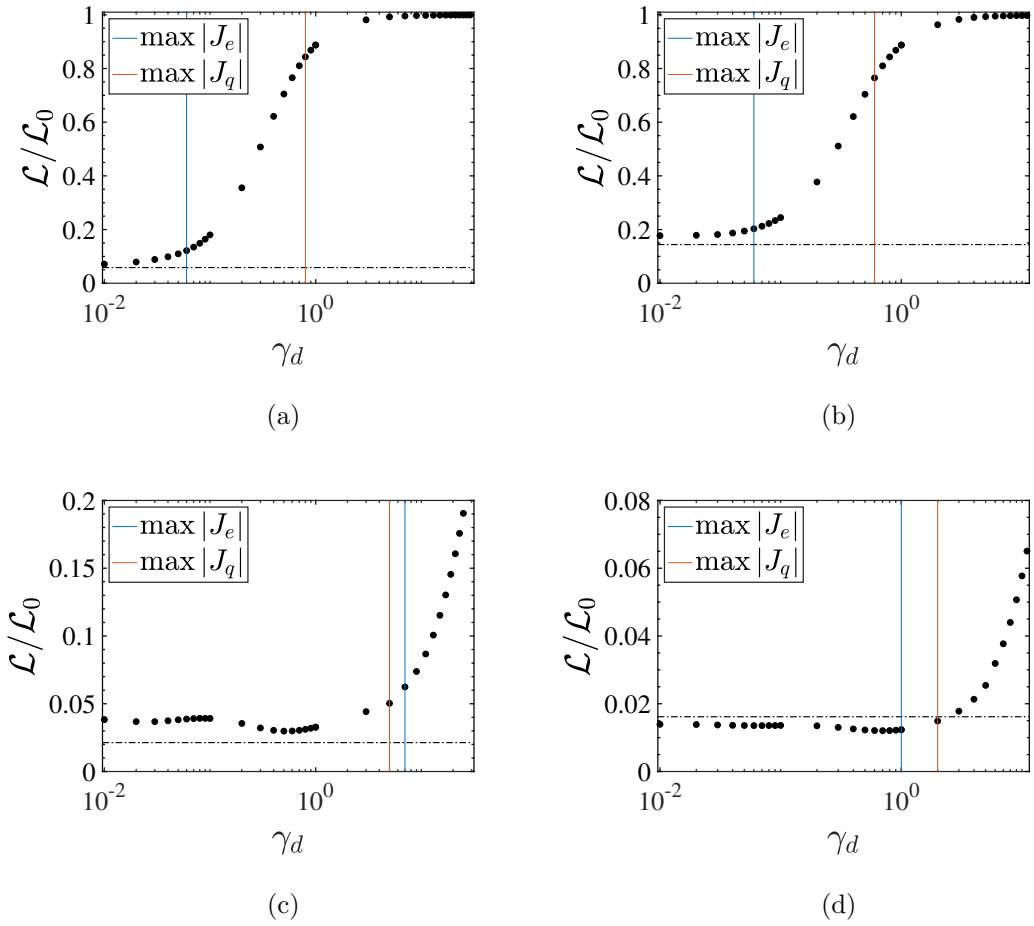

Figure 4.6: Ratio $\mathcal{L} = K/GT$ normalized to the Lorenz number $\mathcal{L}_0 = (\pi k_B)^2/3e^2$ for (a) $u = 4.0$, $\mu = -5.2$, (b) $u = 2.0$, $\mu = -3.3$, at low temperature $T = 0.1$, with $\Delta T = 0.01$, $\Delta\mu = -0.01$. The dashed line indicates the value at zero dephasing. The blue and red vertical continuous lines highlight respectively the position of the maxima of electric and heat current. In (c) and (d) we use the same parameters of the refrigerator configurations in (b)-(c) of Fig. 4.8: (c) $u = 4.0, \mu = -5.2, T = 10, \Delta T = 0.5, \Delta\mu = -1.0$, (d) $u = 4.0, \mu = -3.3, T = 10, \Delta T = 1.0, \Delta\mu = -1.0$

.

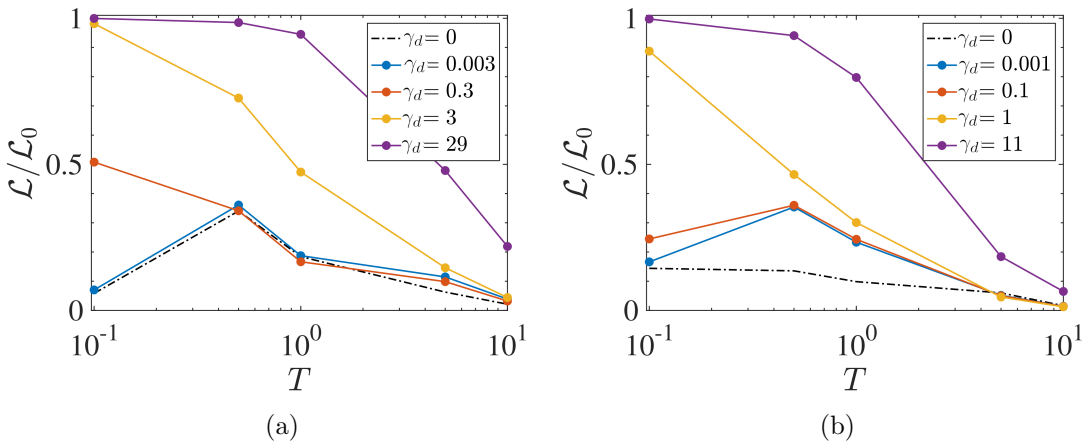

Figure 4.7: Ratio $\mathcal{L}/\mathcal{L}_0$ for different choices of γ_d as a function of temperature at (a) $u = 2.0$, $\mu = -3.3$, (b) $u = 4.0$, $\mu = -5.2$ with constant applied biases $\Delta\mu = 0.01$, $\Delta T = 0.01$.

.

of dephasing strength, translates to values of γ_d where the magnitude of heat current is maximised at low corresponding magnitude of electric current or vice versa. It is clear from the expressions for $\eta^{(h)}$ in Eq. (2.58) and $\eta^{(r)}$ in Eq. (2.72) that situations where the magnitude of heat current and the magnitude of electric current are maximised at different values of γ_d can be advantageous.

4.3.3 Dephasing enhanced refrigeration

As discussed extensively in Sec. 2.1.3, to make a two-terminal device act as either a heat engine or a refrigerator, in absence of dephasing, a key ingredient is asymmetry of the transmission function around the chosen chemical potential. The peculiar transmission function of the Fibonacci model in absence of dephasing, which reflects its fractal spectrum (see Fig. 4.2), shows that it naturally has this property for various choices of chemical potentials, and thus can serve as working medium for a natural refrigerator or heat engine. Introducing incoherent inelastic scattering into the system makes it difficult to extrapolate the energy-filtering properties of the effective spectrum, since it is given by the collective transmissions of the fictitious probes. However, it is still possible to exploit the highly sensitivity of the conductivities to the dephasing strength to individuate particular thermodynamic configurations to realise efficient thermoelectric devices.

A particularly interesting case occurs for parameters where the Fibonacci model in absence of dephasing is subdiffusive and works as a refrigerator. As we have seen in

previous sections, dephasing will increase the currents in this case, making transport diffusive. If the system still acts as a refrigerator it will therefore enhance its cooling rate $-J_q$. Moreover, if the maxima of electrical and heat currents are different, it can even increase the coefficient of performance of the refrigerator, by decreasing in magnitude the power input ($P = -\Delta\mu J_e/e < 0$). In the following, we demonstrate such simultaneous dephasing-induced enhancement of both cooling rate and coefficient of performance in the refrigerating regime. We first scan the parameter space and select configurations which function as refrigerator. The plots in Fig. 4.8 show the absolute values of the electric (blue) and heat (red) currents as a function of γ_d at different thermodynamic parameters. On the right axis, we also show $\eta^{(r)}/\eta_C^{(r)}$, whose value at zero dephasing is indicated by a dashed horizontal line. We observe explicitly in Fig. 4.8a that electrical and heat currents have maxima at different values of dephasing strength. By definition, the coefficient of performance $\eta^{(r)}$ is maximised when the magnitude of heat current is maximum, but the electrical current is away from its maximum. However, $\eta^{(r)}$ for this choice of chemical potentials, temperatures and Fibonacci potential strength ($u = 4.0$), is always below the value obtained in absence of dephasing. In Fig. 4.8b, instead, which shows a refrigerating regime for a different choice of chemical potentials and temperatures at the same value of u, we see $\eta^{(r)}$ enhanced by dephasing for a wide range of γ_d. For $u = 2.0$, we can also find different configurations in Figs. 4.8c- 4.8d where the coefficient of performance is enhanced by the presence of dephasing. Moreover, since u lies in the regime of enhanced transport (see Fig. 4.3d), the presence of dephasing also dramatically increases the cooling rate $-J_q$ of these refrigerating regimes.

We conjecture that this highly non-trivial transport behaviour is associated with the fractal structure of the Fibonacci spectrum. However, it is challenging to find a more microscopically accurate explanation in presence of dephasing at finite temperature. In the case of coherent transport, the details of the system are directly connected to the thermoelectric properties of the non-equilibrium steady state through the transmission function. Conversely, when dephasing is introduced through the probes, transport is determined by the entire collection of transmission functions between reservoirs and probes. This complexity makes the interplay between spectral properties, dephasing, and transport difficult to understand intuitively. Nevertheless, our numerical results clearly indicate that thermal and particle transport behave differently with respect

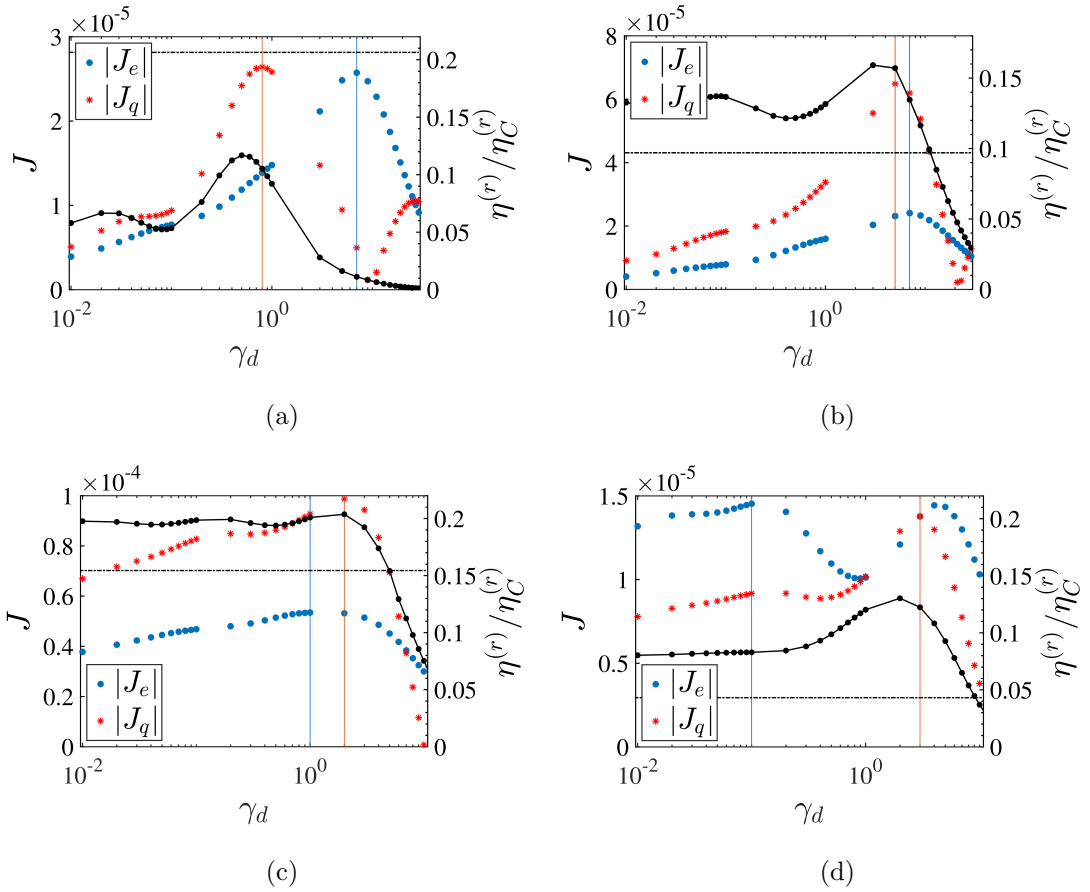

Figure 4.8: Examples of configurations which will function as a fridge, (a)-(b) for $u = 4.0$ and (c)-(d) $u = 2.0$, $N = 200$. The red (blue) dots indicate the magnitude of the heat (electric) current, with its maximum highlighted by a vertical continuous line in the same colour. On the right axis, $\eta^{(r)}$ normalised to the maximum theoretical limit $\eta_C^{(r)}$ is shown in black, and its value at zero dephasing is indicated as a reference with a horizontal dashed line. Parameters: at $u = 4.0$ (a) $\mu = 0, T = 5, \Delta T = 0.1, \Delta\mu = 0.5$, (b) $\mu = -5.2, T = 10, \Delta T = 0.5, \Delta\mu = -1.$, at $u = 2.0$ (c) $\mu = -3.3, T = 10, \Delta T = 1.0, \Delta\mu = -1.0$, (d) $\mu = 2.8, T = 1.0, \Delta T = 0.01, \Delta\mu = 0.1$.

to dephasing. This opens the possibility of enhancing thermoelectric effects by noise. In particular, we have demonstrated a remarkable dephasing-induced-enhancement of both cooling rate and coefficient of performance simultaneously for autonomous refrigeration using the Fibonacci chain as a working medium. Although this finding is specific to certain parameter regimes of the Fibonacci model, we hope that the results might serve more generally as a conceptual guide for the realisation of new synthetic systems for nanoscale heat management based on quasiperiodic potentials.

Chapter 5

Dynamics of the interacting Fibonacci chain

The control reached over the Hamiltonian and the initial conditions in ultracold atom set-ups has provided an ideal platform where to realise quasiperiodic models and probe their non-trivial transport properties from the perspective of dynamics. In these experiments, by tuning the relative depths of the optical lattices trapping the atoms, it is possible to investigate both the non-interacting limit of the models as well as the effect of many-body interactions. The interacting AAH model has been studied in several theoretical works [120, 232–241], and it has been now verified experimentally that its single particle localisation gives rise to a possible many body localisation (MBL) phase [53–56]. Differently from the AAH, there is no delocalisation-localisation transition in the non-interacting Fibonacci model. As discussed in the previous chapter, the Fibonacci potential induces instead critical behaviour of all eigenstates at every potential strength. The transport exponents show a smooth crossover from ballistic to subdiffusive with increase in the potential strength. A natural question, then, is what happens to the transport behaviour of the Fibonacci model in the presence of interactions? How do interactions affect the diagram displayed in Fig. 4.1b from the previous chapter? Different answers to these questions have been proposed in the literature. In the recent work by Varma and Žnidarič, the dynamics of polarised domain walls and the boundary-driven Lindblad equation steady-states reveal diffusion at small interaction strengths [208]. The spectral analysis in Ref. [71] provides, instead, evidence for a localisation transition at finite potential strength, that would constitute a genuine many-body effect, since the non-interacting model does not exhibit

a localised phase. Finally, a nonequilibrium Green's functions approach in Ref. [73] suggests in the Fermi-Hubbard realisation of the model a slow subdiffusive behaviour at high potential strength, determined by the non-trivial spectral properties of the model. Motivated by the lack of experimental results at this moment, we focus on characterising the transport regime of the interacting Fibonacci model with a further approach, exploiting dynamical quantum typicality (DQT). In Sec. 5.1 we study the real-time broadening of the expectation values of local number operators, starting from a nonequilibrium typical state. Via DQT, this quantity is directly related to the spread of density-density correlations and thereby to classification of transport via the Green-Kubo formula in the isolated system, as explained previously in Sec. 2.2.3 and Sec. 2.2.4. We complete the observations from the study of the dynamics with a further investigation respectively on the participation entropy of the system in Sec. 5.2 and the expectation values of both the local occupation and imbalance in the diagonal ensemble in Sec. 5.3. The results presented in this chapter are based on Ref. [242].

We realise the interacting Fibonacci model by adding a nearest neighbour density-density term with strength 2Δ to the tight-binding Hamiltonian, where the on-site energies are generated according to the Fibonacci substitution rule in Eq. (4.1), with $u_A = -u_B = u$,

$$\hat{H} = \sum_{l=1}^{N-1} [t_h(\hat{a}_l^\dagger \hat{a}_{l+1} + \text{h.c.} + 2\Delta \hat{n}_{l+1}\hat{n}_l] + \sum_{l=1}^{N} u_l \hat{a}_l^\dagger \hat{a}_l. \tag{5.1}$$

The numerical study is performed after recasting the fermionic system into a spin 1/2 XXZ model with external magnetic field, as seen in Sec. 2.2.1,

$$\hat{H} = \sum_{l=1}^{N-1} \left[t_h(\hat{s}_l^+ \hat{s}_{l+1}^- + \text{h.c}) + 2\Delta \hat{s}_l^z \hat{s}_{l+1}^z \right] + \sum_{l=1}^{N} u_l \hat{s}_l^z. \tag{5.2}$$

We restrict our calculations to the largest sector of the total Hilbert space with fixed magnetisation $\langle \hat{S}^z \rangle = 0$ and $N/2$ spins up.

5.1 Density-density correlations via typicality

In this section, we study infinite temperature particle transport in the interacting Fibonacci model through the dynamics of density-density correlations, using the DQT

approach. As derived in Sec. 2.2.4, the spatial variance or spread of correlations can be computed as

$$\Sigma^2(t) = 4\sum_{l=1}^{N}\left(l-\frac{N}{2}\right)^2 C_l^{typ}(t), \tag{5.3}$$

$$C_l^{typ}(t) = \frac{1}{2}\Big(n_l(t) - n_l(0)\Big), \tag{5.4}$$

where the expectation value of $\hat{n}_l$ is evaluated on the typical state $|\psi_\infty^s\rangle$ projected onto the subspace where the site $N/2$ is occupied,

$$n_l(t) = \langle\tilde{\psi}_{N/2}^s|\hat{n}_l(t)|\tilde{\psi}_{N/2}^s\rangle \tag{5.5}$$

$$|\tilde{\psi}_{N/2}^s\rangle = \frac{1}{\sqrt{C^s}}\hat{n}_{N/2}\,|\psi_\infty^s\rangle\,. \tag{5.6}$$

Here, the label s indicates vectors in the largest magnetisation sectors. Details on how to modify the expressions in the DQT approach and find the normalisation constant C^s are reported in Appendix B. In practice, we compute the real-time broadening of a density profile initialised in a non-equilibrium configuration presenting a peak at the center of the chain, on top of a uniform background which corresponds to the equilibrium value of the occupation, as depicted schematically in Fig. 2.8.

We generate a single typical state by taking a normalised state vector $|\tilde{\psi}^s\rangle$ with random coefficients and apply the operator $\hat{n}_{N/2}$. We unitarily time evolve this state and calculate the density profile at each time point, from which both $\Sigma^2(t)$ and the autocorrelation $C_{N/2}^{typ}(t)$ can be derived. The dynamical typicality approach allows us to do a long time simulation of a maximum system size of $N = 24$. We fix the hopping term $t_h = 1$, and the interaction strength $\Delta = 0.5$, and investigate the nature of transport as a function of the strength of the potential u. All the results shown are averaged over the collection of the non-equivalent realisations of the Fibonacci model at finite generic length, as described in Sec. 1.4 or at the beginning of Ch. 4. As discussed in Sec. 2.2.3, the relation between the Green-Kubo conductivity and the spatial variance relies on the translational invariance of the system in the thermodynamic limit. Although the Fibonacci model does not exhibit the translational invariance, it is effectively restored by averaging over the various samples.

In Fig. 5.1a, we show $\Sigma^2(t)$ as a function of t at significant values of u, for $N = 24$. As we noticed in Fig. 4.1a in the non-interacting case, for small u, $u \lesssim \Delta$, saturation

occurs at time $\sim N/2$ due to the finite size of the system. Power-law fitting of the data before the saturation yields a superdiffusive exponent, $1 < \nu < 2$ (see plot for $u = 0.2$ in Fig. 5.1a). On increasing u, transport slows down, and therefore it takes a much longer time to hit saturation. For $u \gtrsim \Delta$, we see a clear subdiffusive exponent, $0 < \nu < 1$ (plots for $u = 1.0,\ 2.0$ in Fig. 5.1a) and saturation is not reached within our simulation time scales and system sizes. The crossover from superdiffusive to subdiffusive behaviour seems to arise at $u \approx \Delta$, where from our results there does not seem to be a clear power-law behaviour before saturation occurs. It is possible, at best, to fit two different power-laws at two different time regimes, between $5 \lesssim t \lesssim 10$ with $\nu \sim 1.1$ and between $10 \lesssim t \lesssim 50$ with $\nu \sim 0.5$. The exponents obtained from the power-law fits are given in Fig. 5.1b, which shows the crossover from superdiffusive to subdiffusive transport. At much higher values of u, $u \gg \Delta$, $\Sigma^2(t)$ again quickly saturates to a finite, low value: this signals a lack of spreading of the initially localised quench, $\nu = 0$, thereby pointing at a possible localised regime ($u = 4.0, 8.0$ in Fig. 5.1a), which is reminiscent of the results of Ref. [71]. The fits were performed on the central values of the time axis, neglecting those affected by the finiteness of the system and the initial transient towards equilibrium behaviour. We identified such interval comparing its position and its extension at different N, since saturation must hit at later times for larger sizes, while the transient region is independent on the size. Furthermore, for each fit we considered time windows of increasing widths to verify the stability of the extracted transport exponents.

To highlight the differences between the subdiffusive and the localised regime and to discuss finite-size effects, in Figs. 5.1c and 5.1d, we show $\Sigma^2(t)$ for respectively $u = 1.5$ and $u = 8.0$ at different system sizes. In Fig. 5.1c, the long time power-law growth of $\Sigma^2(t)$ with a subdiffusive exponent is clear for all three system sizes $N = 20, 22, 24$. With increase in system size, the time extent of the power-law growth increases, as expected, and the power-law exponent also converges (to $\nu = 0.3$). However, the different system sizes noticeably do not overlap at any time scale. This is due to the effect of the finite system size coupled with the quasiperiodic potential. As discussed in Ch. 4 and 3, the results for quasiperiodic systems are dependent on the choice of system sizes [31, 32, 243], and particularly, for the Fibonacci potential, on how different the system-sizes are from Fibonacci numbers. This system-size dependence may be reduced by averaging over samples, but the small number of available samples

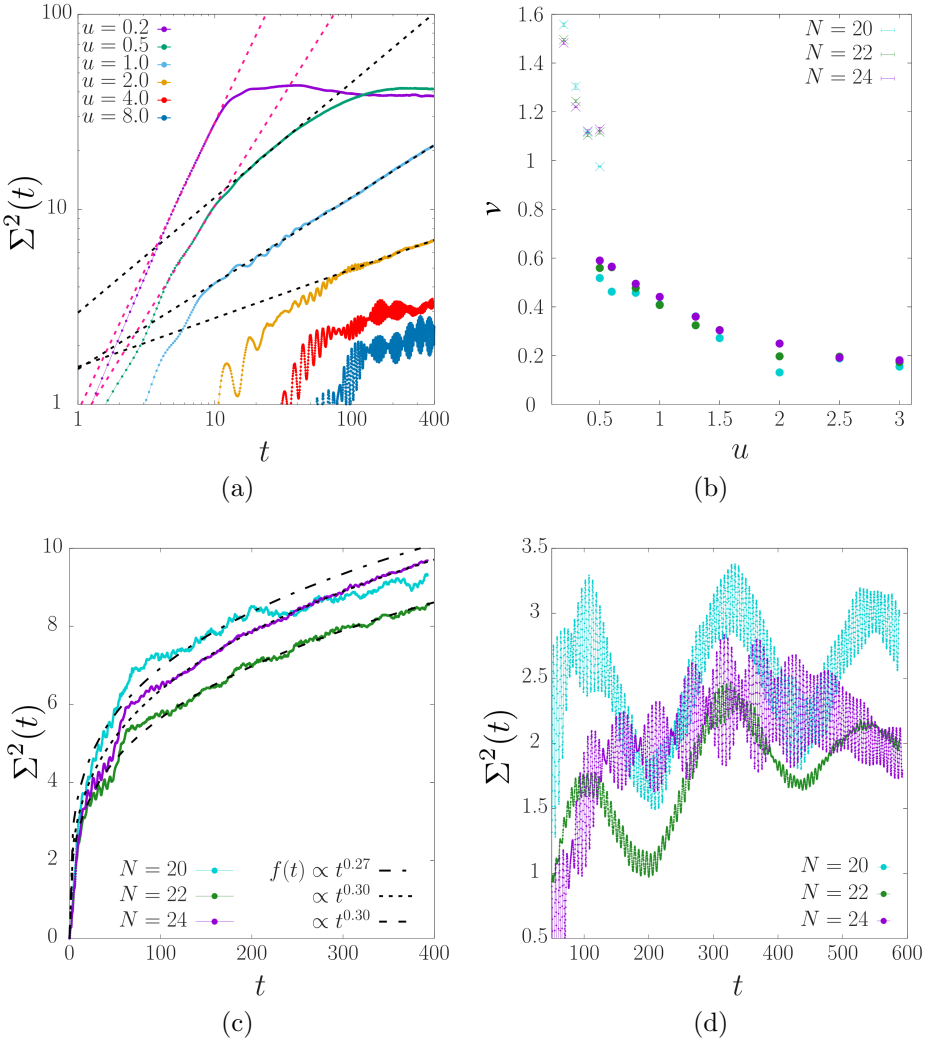

Figure 5.1: (a) Log-log plot of $\Sigma^2(t)$ vs time t at different Fibonacci potential strengths u, for a chain of $N = 24$ spins and $\Delta = 0.5$. The data computed directly from time evolution are shown with continuous lines. We show the corresponding fits of the form of Eq. (2.124) in dotted lines; the short-time fits are shown in pink, while the long-time ones are in black. We notice $\Sigma^2(t)$ growing faster than t at low u, and slowing down as u increases. (b) Exponent ν extracted from the $\Sigma^2(t)$ as a function of the potential strength u. The crosses correspond to the fast dynamics (shown in pink in panel (a)), while the dots are relative to the long-time dynamics (shown in black in panel (a)). The errors of each data point are smaller than the dot size. (c) $\Sigma^2(t)$ is shown at $u = 1.5$ for three different system-sizes in linear scale, along with their corresponding power-law fits. (d) The same quantity is displayed for $u = 8.0$ at three different system sizes $N = 20, 22, 24$ for a longer time in linear scale.

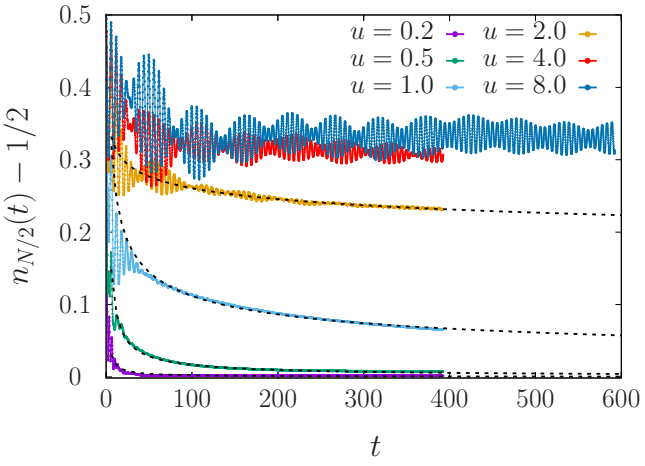

Figure 5.2: Time evolution of $2C_{N/2}(t) = n_{N/2}(t) - \frac{1}{2}$ evaluated on the typical state projected over the subspace where the site at the center of the chain $N/2$ is initially occupied by one particle. At $u = 0.2, 0.5, 1.0, 2.0$, $C_{N/2}(t)$ decays as $t^{-\nu'}$, with respectively $\nu' = 0.92, 0.78, 0.37, 0.086$. The fits are shown in dashed lines. At high u, $C_{N/2}(t)$ does not seem to show any decay up to the longest simulation time.

limits the kind of averaging that is possible to perform in our system sizes. We note that, while this behaviour holds for all values of u, it does not affect our ability to obtain the power-law exponent and that, nevertheless, all the results for the three different system sizes are of the same order of magnitude. In Fig. 5.1d, this same size-dependent effect is shown in the localised regime for $u = 8.0$. Here, we highlight the presence of oscillations, showing no signs of a power-law growth trend.

Next, we look at the density autocorrelation $C_{N/2}(t)$ and characterise transport in terms of the exponent ν', as in Eqs. (2.149)–(2.150). The plots of $2C_{N/2}(t) = n_{N/2}(t) - \frac{1}{2}$ are shown in Fig. 5.2. We observe oscillations on top of a very clear power-law decay for $u < 4.0$. For $u \lesssim \Delta$, the power-law exponent is consistent with superdiffusive transport, $1 > \nu' > 0.5$; for $u \gtrsim \Delta$, the power-law exponent is consistent with subdiffusive transport $0.5 > \nu' > 0$. For $u \gg \Delta$, corresponding to $u = 4.0, 8.0$ in Fig 5.2, we do not see any power-law decay up to the longest time scales that we simulated, thereby suggesting localisation. This is consistent with our results from time scaling of $\Sigma^2(t)$.

In Ref. [71], the spectral properties of the Fibonacci model are studied as a function of the potential strength at a fixed interaction strength of $\Delta = t_h$. Although the Fibonacci potential shows no localisation in absence of interactions, a transition to MBL has been predicted. The question, then, is whether this MBL could be seen at lower interaction strengths. The infinite temperature transport properties at small interac-

tion are investigated in Ref. [208]. This study gives strong evidence that the presence of a small interaction makes transport diffusive at all potential strengths u. This again is very nontrivial, because, in absence of interactions there is a smooth crossover from ballistic to subdiffusive. The question, then, becomes whether transport can become anomalous again at intermediate interaction strengths. One parameter point was shown in favour of this in Ref. [208].

From our investigation at intermediate many-body interaction strength $\Delta = 0.5t_h$, the following picture emerges. For $u \lesssim \Delta$, transport is relatively fast. We find some evidence of superdiffusion in this regime, although the fast transport and the finite system sizes do not allow us to extract a long time transport exponent. Since our results are limited to much smaller system sizes than Ref. [208], we cannot completely rule out the possibility that behaviour becomes diffusive. On increasing u, transport slows down, allowing us to extract long time exponents. For $u \gtrsim \Delta$, we find a strong evidence of subdiffusive transport, consistent with the results at larger values of u in Ref. [208]. The crossover from superdiffusive to subdiffusive behaviour seems to occur at $u \sim \Delta$, where we are unable to extract a single dynamical exponent. On further increasing u, i.e, for $u \gg \Delta$, we find evidence compatible with the presence of a localised phase, as reported in Ref. [71] for higher interaction strength. Subsequently to our investigation, the existence of a transition to a possible MBL phase at an intermediate interaction strength has been suggested in a further study [136].

To summarise, our results strongly suggest that anomalous transport survives in the Fibonacci model in the presence of interactions, and, on further increasing u, i.e, for $u \gg \Delta$, that the system crosses over to a possible MBL phase. In the next sections, we investigate the crossover by means of studies of participation entropy and calculation of observables in the diagonal ensemble.

5.2 Participation entropy

The spectral properties of the Hamiltonian (5.1) have shown evidence of a many-body localisation transition at finite critical potential strength at $\Delta = 1.0$ [71]. This phase would be introduced uniquely by the interplay of quasidisorder and many-body interactions, since localisation is not present in the non-interacting limit of the model. We perform here an analysis similar to Ref. [71], by computing the Rényi-2 participation

entropy of the Fibonacci chain with $\Delta = 0.5$ through exact diagonalisation (ED). These quantities have been used to characterise localisation both in single-particle and in many-body interacting systems [114, 244, 245].

Let $|\ell\rangle$ represent a many-body energy eigenstate. This can be expanded in an arbitrary basis, which we choose to be the configuration-space or computational basis, as $|\ell\rangle = \sum_{k=1}^{D} d_k |\phi_k\rangle$. The probability $p_k = |d_k|^2$ indicates the "participation" of the element $|\phi_k\rangle$ from the arbitrary basis $\{|\phi_k\rangle\}_k$ in the state $|\ell\rangle$. The second Rényi participation entropy (PE) is given by

$$S_2^P = -\ln\Big(\sum_{k=1}^{D} p_k^2\Big). \tag{5.7}$$

If the eigenstate is completely delocalised, $S_2^P/\log(D) \to 1$. On the other hand, if $S_2^P/\log(D) \to D_2$, then the eigenstate is fractal with a fractal dimension of D_2 [246]. For a system showing MBL, the midspectrum energy eigenstates, the region of the Hilbert space that is sampled by the isolated system at infinite temperature, are expected to be fractal with a low fractal dimension. For systems which are neither completely delocalised nor in MBL, $S_2^P/\log(D)$ for the midspectrum eigenstates may not converge to a constant. The study of S_2^P thereby allows one to capture crossover to MBL.

In Fig. 5.3, we plot $S_2^P/\log(D)$ as a function of the potential strength for different system sizes, $N = 14, 16, 18, 20, 22$. All the points are obtained from an average over ~ 200 midspectrum eigenstates, with the exception of the data for $N = 22$ that are averaged over ~ 140 eigenstates. Finally, the PE are averaged over the nonequivalent realisations of the Fibonacci potential. The midspectrum eigenvalues and eigenstates are obtained through the shift-invert algorithm [247]. At very low u, the PE $S_2^P/\log(D)$ is close to 1, but still shows dependence on the system size. At larger values of u, $S_2^P/\log(D)$ decays rapidly with u, and eventually shows a collapse for the different system sizes. Thus two regimes can be identified, corresponding to the transport (either superdiffusive or subdiffusive) and absence of transport regimes found in Sec. 5.1, the latter reminiscent of the many-body localised phase identified in Ref. [71]. More definitive statements about the transition in the thermodynamic limit would require a systematic study of the finite size scaling. In the following, we explore yet another way of characterising the crossover to the localised phase from finite system sizes.

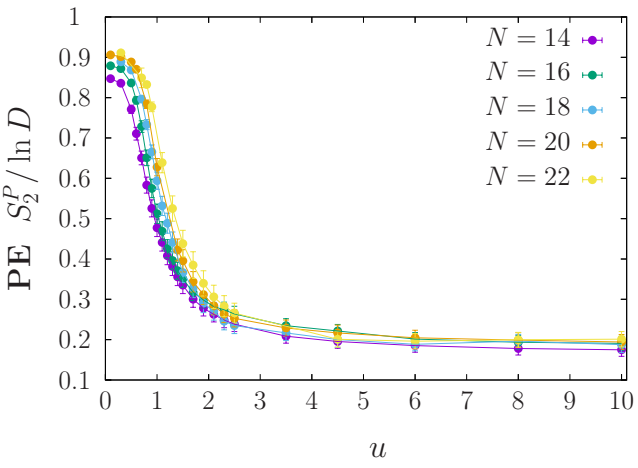

Figure 5.3: Participation entropy $S_2^P / \log D$ associated to the central region of the spectrum for different Fibonacci potential strength u. The curves are displayed for multiple chain sizes.

5.3 Expectation values in the diagonal ensemble

In Sec. 5.1, we obtained finite-time results for the dynamics of the system at different potential strengths u. In the following, we will instead focus on the asymptotic results by using the diagonal ensemble, or infinite time averaged state, to investigate the infinite limit of $n_{N/2}(t)$ of the isolated system initialised in a nonequilibrium state $|\psi\rangle$. We introduce first the notion of diagonal ensemble and how it is connected to the mechanism of equilibration in an isolated system.

We consider an isolated system described by the general Hamiltonian $\hat{H}$, its eigenstates $\{|k\rangle\}$ and corresponding eigenvalues $\{E_k\}$, and an arbitrary local observable $\hat{O}$. We prepare the system in an initial out-of-equilibrium state $|\psi\rangle = \sum_k c_k |k\rangle$, and let it unitarily time-evolve according to

$$|\psi(t)\rangle = \sum_k c_k e^{-iE_k t/\hbar} |k\rangle \,, \tag{5.8}$$

with $c_k = \langle k|\psi\rangle$. The expectation value of the operator will also evolve in time, as follows

$$\langle\psi(t)|\hat{O}|\psi(t)\rangle = \sum_k |c_k|^2 O_{kk} + \sum_{k\neq m} c_k^* c_m e^{i(E_k - E_m)t/\hbar} O_{km}, \tag{5.9}$$

with $O_{km} = \langle k|\hat{O}|m\rangle$. The system equilibrates with respect to the observable $\hat{O}$ when the time evolution of its expectation value converges to a stable value given by the

following long-time average

$$\bar{O} = \lim_{t\to\infty} \frac{1}{t} \int_0^t \langle\psi(t')|\hat{O}|\psi(t')\rangle \, dt'. \tag{5.10}$$

If the spectrum is not degenerate, or, alternatively, does not include an extensive amount of degeneracies, the phase in the second term of Eq. (5.9) averages to zero in the long-time limit, thus $\bar{O}$ reduces to

$$\bar{O} = \sum_k |c_k|^2 O_{kk} = \mathrm{Tr}\left\{\hat{O}\hat{\rho}_{DE}\right\} = \langle\hat{O}\rangle_{DE}\,. \tag{5.11}$$

The equilibration value of $\hat{O}$ corresponds to its expectation value in the diagonal ensemble relative to the initial state $|\psi\rangle$,

$$\hat{\rho}_{DE} = \sum_k |c_k|^2 \, |k\rangle \langle k| = \sum_k |\langle k|\psi\rangle|^2 \, |k\rangle \langle k|\,. \tag{5.12}$$

The system is said to have thermalised with respect to the observable $\hat{O}$ if its asymptotic value is undistinguishable from the thermal ensemble average,

$$\bar{O} = \langle\hat{O}\rangle_{eq}\,. \tag{5.13}$$

A deep fundamental understanding of thermalisation in isolated systems is still missing. However, it is now generally accepted that it occurs under a certain set of conditions on the observable $\hat{O}$, known as eigenstate thermalisation hypothesis [65], that will be presented in detail in the next chapter. For the moment, we only mention that in the MBL phase, instead, systems fail to thermalise, since their many-body eigenstates localise in the computational basis, and conventional statistical mechanics breaks down [64].

From the above discussion, we understand how it is possible to infer from expectation values in the diagonal ensemble if the system reaches absence of transport at high values of the Fibonacci potential strength u, or rather exhibits a region of slow dynamics. However, the computation of O_{DE} requires full ED of the Hamiltonian, so our results are limited to the system sizes $N = 10, 12, 14, 16, 18$, up to a maximum of 20 obtained only at $u \geq 2.0$.

We focus on the occupation number at half chain $\hat{n}_{N/2}$, considering the diagonal

ensemble for the typical state in Eq. (5.6). The occupation of the initial state is 1 by construction, and it will eventually reach the equilibrium value of ~ 0.5 in the case of thermalisation. The results are shown in Fig. 5.4a for different potential strengths as a function of the inverse of the system size. At low $u \lesssim 1$, the value of the observable at infinite time decreases with N and we are able to extrapolate the infinite-size limit result through a fit of the form $\sim 1/N^{\gamma}$; the fits are shown with dotted lines in Fig. 5.4a and extrapolate to 0.5, indicating that the system thermalises in the thermodynamic limit. At larger u, we do not assume a form for the finite size scaling of $n_{N/2}$ and thus we do not extrapolate the infinite-size limit.

We also consider the imbalance [52, 53], a density correlation function defined as

$$I(t) = \frac{4}{N} \sum_{j=1}^{N} \langle \psi(0) | (\hat{n}_j(T) - 1/2)(\hat{n}(0) - 1/2) | \psi(0) \rangle \,, \tag{5.14}$$

which in the case of initial Néel state, represented in the computational basis as $|\psi\rangle = |{\downarrow}{\uparrow}{\downarrow}{\uparrow}{\downarrow} \ldots\rangle$, can be written as the following operator

$$\hat{I} = [\hat{n}_e - \hat{n}_o]/N, \tag{5.15}$$

where $\hat{n}_{e/o} = \sum_{l_{e/o}} \hat{n}_l$ is the number of particles at the even (e) or odd (o) sites. We compute the initial imbalance $I(t = 0) = \langle \psi | \hat{I} | \psi \rangle$, and derive its infinite time limit from its expectation values in the diagonal ensemble associated to the Néel state. The initial value at $t = 0$ is 1 and will eventually reach the equilibrium value of 0 if there is thermalisation. We show the infinite-time limit of the imbalance in Fig. 5.4b as a function of $1/N$. The results are similar to those from $\hat{n}_{N/2}$ and the random typical state. At low u, it is possible to extrapolate the imbalance in the thermodynamic limit, giving 0. However, at larger potential strength, namely for $u > 4$, the data shows a lack of decay with N, up to the system sizes we have access to, and supports our results obtained in Sec. 5.1 pointing to absence of transport in the system and localisation.

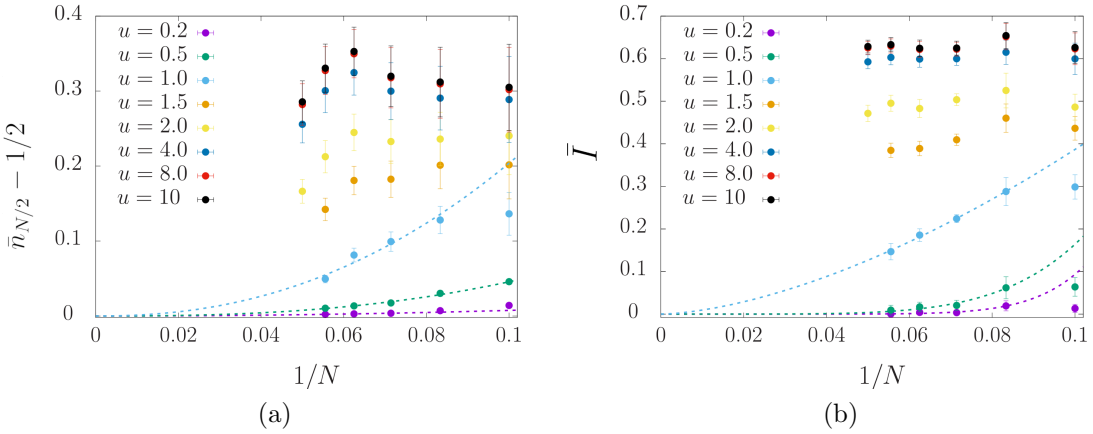

Figure 5.4: (a) Expectation value of the occupation at half chain $\hat{n}_{N/2}$ in the diagonal ensemble associated to the initial typical state, which gives the infinite time limit of the operator. The dotted lines indicate extrapolation for $N \to \infty$ for the first three values of u, described by $1/N^{\gamma}$ with $\gamma = 2.81, 2.59, 2.23$ for increasing u. (b) Expectation value of the imbalance $\hat{I}$ in the diagonal ensemble for the initial Néel state, with the same color code of (a). Again, the dotted lines represent the fits $1/N^{\gamma}$ we use to extrapolate the value of $\bar{I}$ in the thermodynamic limit, with $\gamma = 8.73, 5.47, 1.61$ for increasing u.

Chapter 6

Spin helix states in single-impurity XXZ model

While the previous chapters of the thesis have been focused on exotic potentials exhibiting quasiperiodic order, we return here to a simpler model, which, however, plays a fundamental role in physics. The anisotropic Heisenberg, or XXZ, model has been devised to understand ferromagnetic and antiferromagnetic behaviour, and represents the archetype to describe strongly correlated systems in quantum mechanics. The XXZ model is a one-dimensional quantum 1/2-spin chain with anisotropic interactions and zero external magnetic field. The details of this type of Hamiltonian were first mentioned in Sec. 2.2.1, we write here the one specific to the XXZ model adopting the same notation,

$$\hat{H}_{XXZ} = \sum_{l=1}^{N} \left[\hat{s}_l^x \hat{s}_{l+1}^x + \hat{s}_l^y \hat{s}_{l+1}^y + \Delta \hat{s}_l^z \hat{s}_{l+1}^z \right], \tag{6.1}$$

where J_{xy} has been chosen equal to 1, and Δ indicates the anisotropy. Even in absence of disorder or quasidisorder, the competition between coherent and incoherent effects leads to a rich variety of transport behaviours, dictated by integrability [175]. As discussed in Sec. 2.2.3, integrable systems exhibit an extensive set of local conserved quantities, which can determine a non-vanishing Drude weight in the thermodynamic limit, and, consequently, ballistic transport [248]. These systems possess a underlying structure that often allows for analytical treatment, in particular, the XXZ model was the first physical model to be solved via Bethe ansatz [249, 250]. At zero temperature, its spin transport properties are thus well understood [250], with a tran-

sition from ballistic in the gapless phase (present only in the $\langle \hat{S}^z \rangle = 0$ sector, for $\Delta \leq 1$) to insulating behaviour ($\Delta > 1$ in the $\langle \hat{S}^z \rangle = 0$ sector). Furthermore, a finite lower bound for the spin Drude weight has been found analytically in sectors away from $\langle \hat{S}^z \rangle = 0$ for every Δ at infinite and finite temperature, implying overall ballistic transport [248, 251]. For the zero magnetisation sector at higher temperatures, most studies tackle separately two regimes. In the so-called weakly-interacting regime $0 < \Delta < 1$, the presence of quasi-local conserved quantities has been formally established [252], determining again a finite Drude weight and ballistic transport at infinite temperature. In the strongly-interacting regime $\Delta \geq 1$, an impressive amount of numerical investigations has been conducted in the limit of infinite temperature, including DQT approach [167, 184], open system boundary-driving [253], generalised hydrodynamics [254–256], and finite-time tDMRG [257]. The results suggest diffusive transport, and, at $\Delta = 1$, superdiffusion with a precise exponent characteristic of the Khandar-Parisi-Zhang (KPZ) universality class, which has been observed also in magnetic materials [258], ultracold atoms [259], and quantum digital simulators [260]. The complete dependence of the transport properties on finite temperature and the nature of the subleading terms in the ballistic regions remain, on the other hand, subject of open and intense studies [175].

In the last years, some of these investigations have been conducted on physical platforms. The degree of tunability, the length of coherence times, and the ability to prepare non-equilibrium configurations on set-ups as trapped ions [261], impurity atoms in diamond [262], and, especially, ultracold atoms [57–59, 75, 263], has reached a level that establishes these systems as analogue quantum simulators to test the transport properties of quantum Hamiltonians. The dynamics of the XXZ model has been recently probed for the first time over a large range of anisotropies in a beautiful and celebrated experiment performed by Jepsen *et al.* [75]. Highly non-equilibrium configurations were prepared by imprinting on the chain of atoms a winding magnetisation profile with adjustable wavelength. The so-called spin helix states are pure states, and display a strong energy dependence on the wavelength of the winding. The transport regimes reconstructed from the measures, however, are in contrast with the predictions from linear response theory described above. Indeed, spin helix states are highly non-trivial configurations not fully investigated yet.

The progress in the experimental platforms has also renewed the interest in equilibra-

tion and thermalisation in isolated many-body systems [64]. Initially brought away from equilibrium, they relax again following the underlying microscopic dynamics, according to the transport behaviour of the conserved quantities, which is dictated by their conservation laws. For such reason, integrable models will reach equilibrium in a different way from non-integrable ones. In particular, while integrable systems retain complete memory of the initial conditions, sufficiently complex Hamiltonians equilibrate and thermalise to the microcanonical thermal prediction at their initial energy. This interplay has been investigated in seminal experiments demonstrating that integrability inhibits thermalisation [60], and that an integrability-breaking perturbation is enough to bring the system to thermal equilibrium [67]. The accepted framework to interpret the process of thermalisation is known as eigenstate thermalisation hypothesis. Given the sensitivity of integrability to perturbations, the XXZ model represents in this context a playground where to systematically investigate the transition to thermalisation, and the effect on transport.

The presence of a magnetic impurity on a single spin site, in particular, has been shown to break integrability in the XXZ model [264, 265], while, interestingly, leaving the high-temperature transport regimes of the system unaltered [265]. Motivated by the groundbreaking experimental results mentioned above, we aim to probe transport in the single impurity model when initialised to the same spin helix states prepared in the laboratory by Jepsen *et al.*. In particular, in contrast with the integrable case of the experiment, the single impurity model is expected to thermalise at the energy of the initial spin helix state, which can be controlled by the winding parameter. Thus, we wonder if it is possible to exploit thermalisation to numerically extract equilibrium dynamical properties at precise energies, which can be selected by preparing the appropriate spin helix state. Usually, this type of study requires large numerical resources even for pure states, as in the DQT approach, since it is necessary to wait for equilibration under unitary time-evolution. Here, we circumvent these difficulties via kernel polynomial method (KPM), which allows to resolve in the frequency domain physical quantities as correlation functions, from which the equilibrium transport exponents can be extracted in the limit of zero frequency.

We start in Sec. 6.1 with a theoretical overview on the eigenstate thermalisation hypothesis, showing its most relevant predictions. We proceed discussing how the mechanism has been numerically verified on the XXZ model subject to a single mag-

netic impurity, and the known implications on spin transport. In Sec. 6.2, we describe in more details the experiment of Jepsen *et al.*, and their results, providing a stronger motivation for our study. Finally, in Sec. 6.3 we investigate global spectral properties of the single impurity XXZ model, and dynamical quantities relative to the spin helix states. We compute all the relevant physical quantities using the KPM, introduced in Sec. 2.3. We extract transport exponents from the correlation functions in the microcanonical and diagonal statistical ensembles, and compare with those from the single spin helix states. The preliminary results exposed in this chapter have not been published yet, but will constitute the basis for an upcoming article.

6.1 Integrability breaking and thermalisation

The topic of how thermalisation could emerge in quantum systems evolving under unitary dynamics has fascinated the statistical mechanics community for almost a century, and still is an intense field of research [266]. The mechanism leading the isolated system to an asymptotic state undistinguishable from a finite temperature Gibbs ensemble by local or linear response measurements lacks a rigorous understanding. Neverthless, there has been some progress. In particular, the most established framework available is the eigenstate thermalisation hypothesis (ETH). ETH is a conjecture on the form of the matrix elements of an observable on the eigenbasis, which would ensure expectation values and correlation functions to coincide with their thermal finite-temperature counterparts. The idea dates back to Von Neumann, when, reinterpreting quantum mechanically the main notions of statistical mechanics, he also suggested to focus on physical observables, rather than wavefunctions or density matrices [267]. A crucial study was published much later by Deutsch, inspired by Berry [268] and based on random matrix theory, where he reveals a relation between diagonal elements of matrix observables and microcanonical averages [269]. The current formulation, however, was finalised by Srednicki [270].

Given the basis of eigenstates $\{|n\rangle\}$ of the Hamiltonian $\hat{H}$, and the relative eigenvalues $\{E_n\}$, the ETH can be formulated as an ansatz for the matrix elements of a local observable $\hat{O}$,

$$O_{nm} = \langle n|\hat{O}|m\rangle = O(\bar{E})\delta_{nm} + e^{-S(\bar{E})/2} f_O(\bar{E}, \omega) R_{nm}, \tag{6.2}$$

where $\bar{E} = (E_m + E_n)/2$, $\omega = E_m - E_n$, $S(\bar{E})$ is the thermodynamic entropy of the the system, and R_{nm} a complex or real random variable with zero mean and unit variance, while $O(\bar{E})$ and $f_O(\bar{E}, \omega)$ are two smooth functions. In particular, since, by continuity, it will not vary over a small energy interval, $O(\bar{E})$ is related to the expectation value from the microcanonical ensemble taken at energy $E = \bar{E}$. The second term, due to the appearance of the entropy, is exponentially small with system size, and connected to the dynamical properties of the observable, in particular, correlation functions will depend on $|f_O(\bar{E}, \omega)|^2$. It is now generally expected that the above ansatz will hold for all the observable for which statistical mechanics applies. Systems that do not thermalise, instead, do not follow ETH. Integrable systems, for example, which possess extensive sets of local conserved quantities, after equilibration are described by a generalised Gibbs ensemble [271], thus retaining information about the initial state. Analogously, systems that display many-body localisation (MBL) escape thermalisation [64].

We consider an isolated system with $N \gg 1$ degrees of freedom, whose Hamiltonian is non-integrable and away from a MBL transition. There may be global symmetries, however, their only effect is to reduce the Hilbert space into independent subsectors, as discussed in Sec. 2.2.1, such that the following analysis can be carried out independently for each of them. We initialise the system in an arbitrary state $|\psi\rangle = \sum_k c_k |k\rangle$, which will unitarily time-evolve as

$$|\psi\rangle = \sum_k c_k e^{-iE_k t/\hbar} |k\rangle \,, \tag{6.3}$$

where $c_k = \langle k|\psi\rangle$. As discussed in Sec. 5.3 in Eqs. (5.9)–(5.11), given a local operator $\hat{O}$, the system equilibrates when its long-time averaged expectation value $\bar{O}$ on the arbitrary initial state converges to a stable value, given by the expectation value on the diagonal ensemble relative to $|\psi\rangle$,

$$\bar{O} = \sum_k |c_k|^2 O_{kk} = \mathrm{Tr}\{\hat{O}\rho_{DE}\} = \langle \hat{O} \rangle_{DE} \,, \tag{6.4}$$

where we reiterate the expression for completeness,

$$\hat{\rho}_{DE} = \sum_k |c_k|^2 |k\rangle \langle k| = \sum_k |\langle k|\psi\rangle|^2 |k\rangle \langle k| \,. \tag{6.5}$$

As seen in Eq. (5.13), thermalisation implies, instead, that the asymptotic value can be obtained from a statistical ensemble average,

$$\bar{O} \to O_{mc}(E) = \mathrm{Tr}\left\{\hat{O}\hat{\rho}_{mc}\right\}, \tag{6.6}$$

with $O_{mc}(E)$ the expectation value of $\hat{O}$ in the microcanonical ensemble,

$$O_{mc}(E) = \frac{1}{\rho(E)}\sum_{k=1}^{D}\delta(E-E_k)O_{kk} = \frac{1}{\rho(E)}\sum_{k^*}O_{k^*k^*}, \tag{6.7}$$

where $\rho(E)$ is the density of states, and the indices k^* are such that the corresponding eigenergies belong to a small energy window around E, $E_{k^*} \in [E-\delta E_{mc}, E+\delta E_{mc}]$. The ensemble is characterised by the parameter E, but, equivalently, it can be associated to a microcanonical temperature,

$$\beta(E) = \left.\frac{d\mathcal{S}_{mc}(E')}{dE'}\right|_{E'=E}, \tag{6.8}$$

with $\mathcal{S}_{mc}(E) = \ln\left[\rho(E)dE\right]$ the microcanonical entropy given by Boltzmann's relation, where $\rho(E)dE$ corresponds to the number of microstates in the small energy interval dE. Generic systems with short-range interactions satisfy ensemble equivalence, thus other ensemble in statistical mechanics can be used to describe the thermal expectation value, in particular the canonical state at inverse temperature $\beta(E)$.

We verify now that Eq. (6.6) can be derived as a consequence of the ETH ansatz. We invoke Eq. (6.2) in the expression for the asymptotic value $\bar{O}$ from Eq. (6.4), and obtain

$$\bar{O} = \sum_k |c_k|^2\left[O(E_k) + e^{-S(E_n)/2}f_O(E_n,0)R_{nn}\right] \simeq \sum_k |c_k|^2 O(E_k), \tag{6.9}$$

where the second term is suppressed exponentially because of the factor $e^{-S(\bar{E})/2}$. We observe a dependence on the initial state through the probabilities $|c_k|^2$, nevertheless, independently on the actual values of the coefficients c_k, the ETH ansatz leads to

$$\bar{O} \simeq O_{mc}(\langle E\rangle), \tag{6.10}$$

as long as the $|c_k|^2$ are narrowly distributed around the average energy $\langle E\rangle = \langle\psi|\hat{H}|\psi\rangle$,

and the energy fluctuations are sub-extensive with the N degrees of freedom of the system,

$$\begin{aligned} \delta E &= \sqrt{\langle\psi|\hat{H}^2|\psi\rangle - (\langle\psi|\hat{H}|\psi\rangle)^2} \\ \langle E\rangle \sim N, \quad &\frac{\delta E^2}{\langle E\rangle^2} \sim \frac{1}{N}. \end{aligned} \tag{6.11}$$

This condition is generally satisfied in systems with short-range interactions. Since $O(E)$ is a smooth function of the energy, we can Taylor-expand the diagonal elements of $\hat{O}$ around the mean energy of the initial state,

$$O_{kk} \simeq O(E_k) \simeq O(\langle E\rangle) + (E_k - \langle E\rangle)\frac{\partial O(E_k)}{\partial E_k}\bigg|_{\langle E\rangle} + \frac{1}{2}(E_k - \langle E\rangle)^2\frac{\partial^2 O(E_k)}{\partial E_k^2}\bigg|_{\langle E\rangle}. \tag{6.12}$$

When we insert the above expression in Eq. (6.9), we obtain

$$\begin{aligned} \bar{O} &\simeq O(\langle E\rangle) + \frac{1}{2}\delta E^2\frac{\partial^2 O(\bar{E})}{\partial \bar{E}^2}\bigg|_{\langle E\rangle} \\ &\simeq O_{mc}(\langle E\rangle) + \frac{1}{2}\left[(\delta E)^2 - (\delta E_{mc})^2\right]\frac{\partial^2 O(\bar{E})}{\partial \bar{E}^2}\bigg|_{\langle E\rangle}, \end{aligned} \tag{6.13}$$

where δE_{mc} are the sub-extensive energy fluctuations in the microcanonical ensemble, due to the finite size of the system [65]. From this result, we observe that the ETH ansatz guarantees thermalisation at the level of expectation values, meaning that the long-time averaged expectation values will agree to the thermal ensemble prediction at the energy set by the initial state up to sub-extensive corrections.

The ETH provides further predictions on the two-point correlation functions, and, consequently, on the dynamical properties of the system at thermal equilibrium. We consider, initially, the correlation function evaluated on the diagonal ensemble, which encodes the properties of the system once reached equilibration, starting from the arbitrary state $|\psi\rangle$,

$$C_{DE}(t,\psi) = \langle\hat{O}(t)\hat{O}\rangle_{DE} - \langle\hat{O}(t)\rangle_{DE}\langle\hat{O}\rangle_{DE}. \tag{6.14}$$

When expanding on the eigenbasis, the expression reads,

$$\begin{aligned} C_{DE}(t,\psi) &= \sum_{k,m} |c_k|^2 e^{-it(E_m-E_n)/\hbar} O_{km} O_{mk} - \left(\sum_k |c_k|^2 O_{kk} \right)^2 \\ &= \sum_{k,m\neq k} |c_k|^2 e^{-it(E_m-E_n)/\hbar} |O_{km}|^2 + \sum_k |c_k|^2 (O_{kk})^2 - \left(\sum_k |c_k|^2 O_{kk} \right)^2, \\ &= \sum_k |c_k|^2 C_k(t) + (\delta O_{DE})^2, \end{aligned} \tag{6.15}$$

where in the second equality we separated the terms $m = k$ from $m \neq k$ in the sum. The first term contains, analogously to $\bar{O}$, a weighted sum over the $|c_k|^2$, narrowly distributed around the average energy $\langle E \rangle$, of a quantity parametrised by a single eigenstate, $C_k(t)$. The second constitutes the fluctuation of the operator in the diagonal ensemble, $(\delta O_{DE})^2$, which can in general be shown to scale as the equilibrium statistical fluctuations $(\delta O_{mc})^2$ [65]. We apply on the first term the off-diagonal ETH ansatz from Eq. (6.2),

$$\begin{aligned} C_k(t) &= \langle k|\hat{O}(t)\hat{O}|k\rangle - \langle k|\hat{O}(t)|k\rangle \langle k|\hat{O}|k\rangle = \sum_{m\neq k} e^{it(E_k-E_m)/\hbar} |O_{km}|^2 \\ &= \sum_{m\neq n} e^{-i\omega t/\hbar} e^{-S(E_k+\omega/2)} \left| f_O(E_k+\omega/2,\omega) \right|^2 |R_{km}|^2, \end{aligned} \tag{6.16}$$

where we wrote $\omega = E_m - E_k$ and $\bar{E} = (E_k + E_m)/2 = E_k + \omega/2$. Since $f_O(\bar{E},\omega)$ is a continuous function, we can perform again a Taylor expansion around $\langle E \rangle$, and finally obtain from the last line of Eq. (6.15),

$$C_{DE}(t,\psi) \simeq C_k(t) + \left. \frac{\partial^2 C_k(t)}{\partial E_k^2} \right|_{\langle E \rangle} (\delta E)^2 + (\delta O_{DE})^2, \tag{6.17}$$

where the single eigenstate correlation function is evaluated at the eigenvalue compatible with the mean energy of the state $|\psi\rangle$, $E_k = \langle E \rangle$. From the definition of expectation values in the microcanonical ensemble given in Eq. (6.7), the corresponding correlation function,

$$C_{mc}(t,E) = \langle \hat{O}(t)\hat{O} \rangle_{mc} - \langle \hat{O}(t) \rangle_{mc} \langle \hat{O} \rangle_{mc}, \tag{6.18}$$

can be written as [65],

$$C_{mc}(t,E) \simeq C_k(t) + (\delta O_{mc})^2, \tag{6.19}$$

where $C_k(t)$ is evaluated at the eigenstate compatible with $E = E_k$. The ETH thus implies that thermalisation occurs also at the level of correlation functions,

$$C_{DE}(t, \psi) \simeq C_{mc}(t, \langle E \rangle), \tag{6.20}$$

where $\langle E \rangle = \langle \psi | \hat{H} | \psi \rangle$, with fluctuations due to the finite system size. Effectively, correlation functions thermalise to the prediction on a single eigenstate with corresponding eigenenergy $E_k = \langle E \rangle$.

We conclude the analysis of thermalisation according to the ETH by considering the fact that it is also possible to define a correlation function over a single generic state,

$$C_\psi(t) = \langle \psi | \hat{O}(t) \hat{O} | \psi \rangle - \langle \psi | \hat{O}(t) | \psi \rangle \langle \psi | \hat{O} | \psi \rangle \,. \tag{6.21}$$

We observe, however, that this expression does not recover $C_{DE}(t, \psi)$ when infinite-time averaged. The diagonal ensemble can be reconstructed, instead, from the following [272],

$$\begin{aligned} \overline{\langle \hat{O}(t + \tau/2) \hat{O}(t - \tau/2) \rangle} &= \lim_{t \to \infty} \frac{1}{t} \int_0^t \langle \psi | \hat{O}(t' + \tau/2) \hat{O}(t' - \tau/2) | \psi \rangle \\ &= \sum_{km} |c_k|^2 e^{i\tau(E_k - E_m)/\hbar} |O_{km}|^2 = \langle \hat{O}(\tau) \hat{O} \rangle_{DE} \,, \end{aligned} \tag{6.22}$$

which, differently from computing $C_{DE}(\tau, \psi)$ as in Eq. (6.14), requires a long-time average for every value of τ.

The occurrence of the eigenstate thermalisation has been verified by a large body of numerical investigations on strongly correlated systems in the non-integrable regime, ranging from interacting spin chains [273, 274], to two dimensional Ising model in trasversed fields [275, 276] and lattice of interacting hard-core bosons [277, 278]. The studies usually involve evaluation via ED of the diagonal [279, 278], and off-diagonal [276, 280] matrix elements of local operators in the energy eigenbasis. In particular, from a delicate binning procedure [272, 276], one can extract the smooth function $f_O(E, \omega)$, which dictates the dynamics of the correlation functions, and carries information on fluctuation-dissipation relations [65], and the multipartite entanglement structure of the energy eigenstates [272].

6.1.1 ETH in the single impurity model

Notably, thermalisation as prescribed by the ETH has also been demonstrated to occur in originally integrable systems when subject to local perturbations, in particular, in the XXZ model with a single magnetic defect [66]. It was already known from statistical spectral analysis that the presence of a single magnetic impurity away from the margins of the chain would induce integrability-breaking [264, 281, 282]. The authors of Ref. [66] have performed a step further and verified ETH on the single-impurity Hamiltonian,

$$\hat{H}_{SI} = \hat{H}_{XXZ} + w\hat{s}^z_{N/2}, \tag{6.23}$$

featuring a magnetic defect at the center of the chain with field strength w. Specifically, the diagonal matrix elements of global or locally constraint (with support away from the impurity) observables in the perturbed eigenstates have been shown to follow a smooth function of the energy, which corresponds to the microcanonical prediction for the integrable model [66]. The off-diagonal elements were also found compliant to the ETH [66], and, more interestingly, characterised in the case of the spin-current operator by a system size-independent $|f_{J_N}(\bar{E}, \omega N)|^2/N$ at $\bar{E} \sim 0$ [283]. This behaviour has been interpreted as a manifestation of previous observation in the single-impurity model of ballistic infinite-temperature spin transport in linear response regime [265]. Indeed, the emergence of ballistic behaviour in a system fulfilling ETH has generated some puzzlement, since the expectation on physical grounds is that incoherent effects and complexity will lead to diffusive incoherent transport. The results have been reconciled in a picture where the perturbed model inherits statistical mechanics and transport properties of the integrable model as a consequence of an anomalous thermalisation [283, 284]. We will not add further details to this concept, since for our studies we limit to exploit the crucial fact that local observables and dynamical correlations away from the impurity will thermalise to the statistical predictions of the unperturbed XXZ model.

6.2 XXZ model on ultracold atoms

Ultracold atoms trapped in optical lattices represent the most promising platform where to realise spin chain Hamiltonians, and investigate fundamental questions on

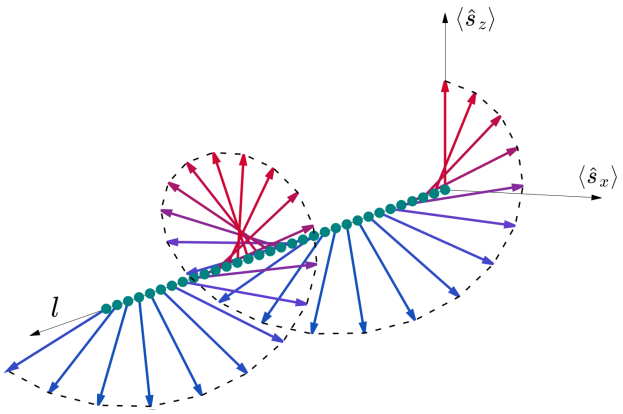

Figure 6.1: Schematic representation of the magnetisation profile of the spin-helix states realised in the experiment of Ref. [75]. The spin vector winds in the $s^x - s^z$ plane as a function of the position along the chain of atoms. In the following, we denote the period of the winding, or helicity parameter, by λ.

isolated quantum dynamics, many-body localisation, and thermalisation [285]. A remarkable example is the versatile analogue quantum simulator realised by Jepsen *et al.* [75, 286, 287]. The dynamics of the XXZ model Hamiltonian is reproduced on one-dimensional arrays of ultracold ^{7}Li atoms trapped by optical lattices. The depth of a lattice controls the rate of spin-exchange, the first term in Eq. (6.1), while the applied magnetic field in a given direction adjusts the anisotropy parameter Δ. The details of the set-up allow for a unprecedented degree of tunability, and to explore for the first time the system over a wide range of parameter values.

In the beautiful experiment described in Ref. [75], the transport properties of the system are probed by preparing highly non-equilibrium spin-helix states at $t = 0$, and letting them evolve according to the intrinsic unitary dynamics, described by $\exp\left(-it\hat{H}_{XXZ}/\hbar\right)$. A winding magnetisation in the $s^x - s^z$ plane is thus initially imprinted along the chain with wavelength λ, henceforth indicated as helicity parameter. A schematic representation of the resulting magnetic profile is depicted in Fig. 6.1. Frozen snapshots in time of the expectation values of the local magnetisation along the chain $\langle \hat{s}_l^z \rangle$ are reconstructed via spin-imaging measures. The characteristic decay timescale τ of the profile is evaluated as a function of the helicity. The exponent in the dispersion relation $\tau \sim \lambda^\alpha$ yields an indication of the nature of transport, with $\alpha = 1$ pointing to ballistic transport, $\alpha = 2$ to a diffusive process, while the in-between values to anomalous diffusion, respectively superdiffusion ($1 < \alpha < 2$) and subdiffusion ($\alpha > 2$).

Some of the findings from the experiment are in contrast with the theoretical predictions for the XXZ model. In particular, a smooth increase in α from 1 (ballistic) to 2 (diffusive) occurs for positive anisotropies $0.55 < \Delta < 1$, and continues with $\alpha > 2$ for $\Delta > 1$, signalling subdiffusion. The studies for long-time linear-response transport at high temperatures mentioned at the beginning of the chapter indicate, instead, a sharp transition from ballistic to diffusion at $\Delta = 1$ [254, 257], where the KPZ hydrodynamic exponent is expected [258]. The authors argue that the two classes of results are fundamentally different, since the initial state in the experiment is a pure state far from equilibrium, and not a highly mixed states. Indeed, these impressive results give rise to new questions on the far-from-equilibrium dynamical regime, and the effect of finite temperature.

This experiment can be considered analogous to the numerical simulation performed in Sec. 5.1 to investigate the survival of anomalous transport in the interacting Fibonacci model, after a quench represented by a peaked density profile over a uniform background. In that case, however, the nature of the initial pure state, a projected typical state, allowed us to map the decay of the density perturbation directly to the correlations evaluated in the thermal ensemble at infinite temperature.

6.3 Results in presence of single impurity

The set-up of the experiment described in the previous section will be now reconstructed in our framework, adopting the single-impurity Hamiltonian in Eq. (6.23) rather than the clean XXZ model of Eq. (6.1). As discussed in Sec. 6.1.1, the single magnetic impurity at the centre of the chain breaks integrability, and ETH is fulfilled. Global observables and observables away from the impurity thermalise to the predictions of the microcanonical ensemble of the unperturbed clean system, thus yielding the same dynamical behaviour. In this preliminary study, we focus on the parameter region where the clean model displays diffusive spin transport, fixing $\Delta = 1.3$ in Eq. (6.23). Moreover, ideally following the experiment, we will perform our simulations in the full Hilbert space.

The spin helix state in the full Hilbert space can be written as a product state on the

computational basis,

$$|\psi_\lambda\rangle = \bigotimes_{l=1}^{N} \left[\cos(\pi l/\lambda) \, |\downarrow_l\rangle - \sin(\pi l/\lambda) \, |\uparrow_l\rangle \right], \tag{6.24}$$

with l is the position index along the chain. The expectation value of the local spin at site l at time $t = 0$ is thus,

$$\langle\psi_\lambda|\vec{\hat{s}}_l|\psi_\lambda\rangle = -\left(\sin(2\pi l/\lambda), 0, \cos(2\pi l/\lambda)\right), \tag{6.25}$$

where we notice that for $\lambda = 2$ the Néel state appears, $|\psi_2\rangle = |\uparrow_1 \downarrow_2 \uparrow_3 \downarrow_4 \ldots\rangle$. Remarkably, the spin-helix states exhibit a dependence of their mean energy on the helicity parameter, which effectively allows in numerical and physical experiments to tune the initial energy of the system. We show it here in Fig. 6.2a for the single impurity model, $E_\lambda = \langle\psi_\lambda|\hat{H}_{SI}|\psi_\lambda\rangle$, considering $N = 24$ spins and an impurity field strength $w = 1.58$. For the impurity strength w, we follow Ref. [265], where parameters in this range have been shown not to alter the transport regime of the model. The local density of states (lDOS) $\rho_{\psi_\lambda} = \sum_k |c_k^\lambda|^2 \delta(E - E_k)$ also varies with λ, displaying in Fig. 6.2b a broader gaussian form at lower λ, which progressively shrinks into more irregular peaks at higher λ. However, since ETH is verified [66, 283], we expect the the distribution of all the sets $\{|c_k^\lambda|^2\}_k$ to be narrowly distributed around E_λ in the limit of large system size, and the conditions in Eq. (6.11) fulfilled. The lDOS has been computed with the KPM, as exposed in detail in Sec. 2.3.1, where we provide a recipe to compute the moments of its Chebyshev expansion.

As explained in Sec. 6.1, it is possible to assign to each energy E a microcanonical inverse temperature $\beta(E) = 1/k_B T(E)$, the characteristic parameter of the statistical ensemble towards which the system will thermalise, with E the energy of the initial state. The relation is defined through the density of states (DOS) and the microcanonical entropy, as indicated in Eq. (6.8). The DOS of the single impurity model, computed via KPM, is displayed in Fig. 6.3a. The method allows to obtain the result without any binning procedure, directly as a smooth function on an arbitrarily set of points, including the E_λ shown earlier in Fig. 6.2a. Therefore, we can derive the microcanonical temperature $T(\lambda) = T(E_\lambda)$ as a function of the helicity. Within ETH, we can probe microcanonical expectation values, or, equivalently, canonical expecta-

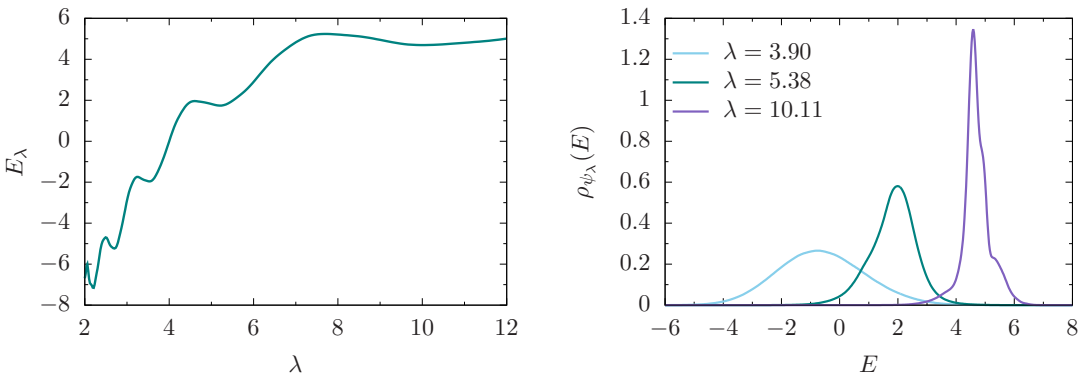

(a) (b)

Figure 6.2: (a) Mean energy of the spin helix state, $E_\lambda = \langle\psi_\lambda|\hat{H}_{SI}|\psi_\lambda\rangle$, as a function of the helicity. A clear dependence is shown, that, in the context of ETH, allows to tune the microcanonical predictions at which the observables will thermalise, once the system has been initialised with $|\psi_\lambda\rangle$. (b) Local densities of states for three different spin helix states. These quantities have been obtained directly as smooth functions of the energy from the KPM, using $N_C = 280$ moments. In both figures, $N = 24$, $\Delta = 1.3$, $w = 1.58$.

tion values, given the equivalence of the ensembles, at respectively arbitrary energy or arbitrary temperature, by choosing the helicity of the initial state. We observe in Fig. 6.3b that the divergence in temperature occurs approximately at $\lambda \sim 3.94$, which corresponds to the energy where we have the largest availability of states, or, in other words, where the DOS and the microcanonical entropy reach their maximum.

We verify now explicitly the occurrence of thermalisation at the level of the observable expectation values, according to ETH. We imagine to initialise the system with $|\psi_\lambda\rangle$, and let it evolve. We imagine also to follow the evolution with time of the expectation value of the local observable $\hat{O}$. After a certain amount of time has passed, $\hat{O}$ has reached the equilibrium value, given by its expectation value in the diagonal ensemble of the initial state,

$$O_{DE}(\psi_\lambda) = \sum_k |c_k^\lambda|^2 |O_{kk}|^2. \tag{6.26}$$

Since ETH is fulfilled, $O_{DE}(\psi_\lambda)$ will correspond to the value of the smooth function $O_{mc}(E)$, yielding the microcanonical expectation value, evaluated at energy $E = E_\lambda$. In our framework, we do not need to wait for long times, since the KPM evaluates directly expectation values as functions in the energy domain, as exposed in detail in Sec. 2.3.2. Therefore, we can directly probe the microcanonical expectation values at different energies by tuning the helicity. Indeed, we observe in Fig. 6.4a that for a local observable away from the impurity, $\hat{O} = \hat{s}^z_{N/4}$, the $O_{DE}(\psi_\lambda)$ computed at different

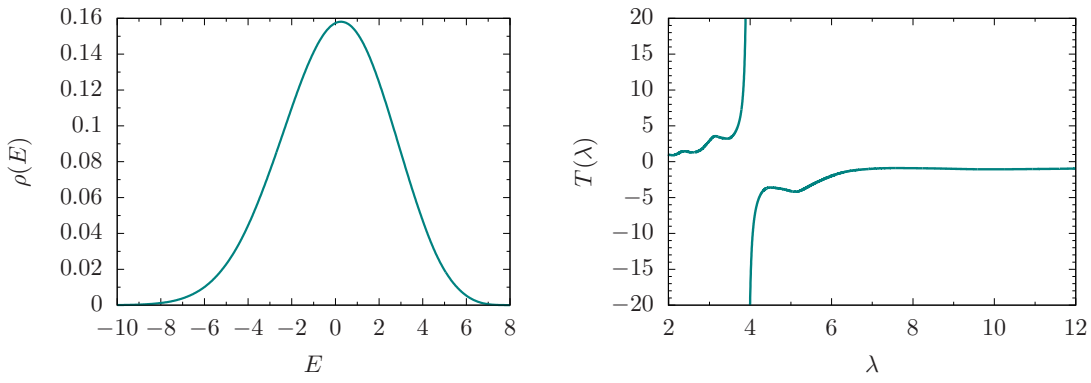

(a) (b)

Figure 6.3: (a) DOS for the single-impurity model with $\Delta = 1.3$, $w = 1.58$, obtained via KPM using $N_C = 80$ moments, and $R = 1$ random state to perform the stochastic evaluation of trace. (b) Microcanonical temperature obtained from the DOS through the relation in Eq. (6.8), evaluated over the set of spin helix state mean energies. This determines $T(\lambda) = T(E_\lambda)$ as a function of the helicity.

helicities (violet dots) lie on the continuous microcanonical prediction (green solid line). Moreover, in this case the microcanonical prediction for the single impurity model agrees with that for the clean unperturbed model at the same parameters $\Delta = 1.3$, $N = 24$, but $w = 0$ (dashed black line). If we consider the local magnetisation at the site where we placed the defect, $\hat{O} = \hat{s}^z_{N/2}$, we still verify thermalisation to $O_{mc}(E_\lambda)$, however, this does not correspond anymore to the same microcanonical expectation values of the unperturbed XXZ model. Finally, we mention that, since in the context of ETH $O_{mc}(E)$ is a continuous function, we can obtain the expectation value of the diagonal ensemble of Fig. 6.4 from

$$O_{DE}(\psi_\lambda) = \int dE \rho_{\psi_\lambda}(E) O_{mc}(E), \tag{6.27}$$

which yields the same result of Eq. (6.26) [193].

We finally focus on the correlation functions, in order to extract indications on the dynamics of the system, as performed in Jepsen *et al.* experiment. In this calculation, the KPM demonstrates its full capability. Instead of evaluating a correlation function $C(t)$ in time for long times, we study its Fourier transform in the frequency domain,

$$C(\omega) = \int dt e^{i\omega t} C(t). \tag{6.28}$$

The KPM returns directly the function at all frequencies, and the limit on the time

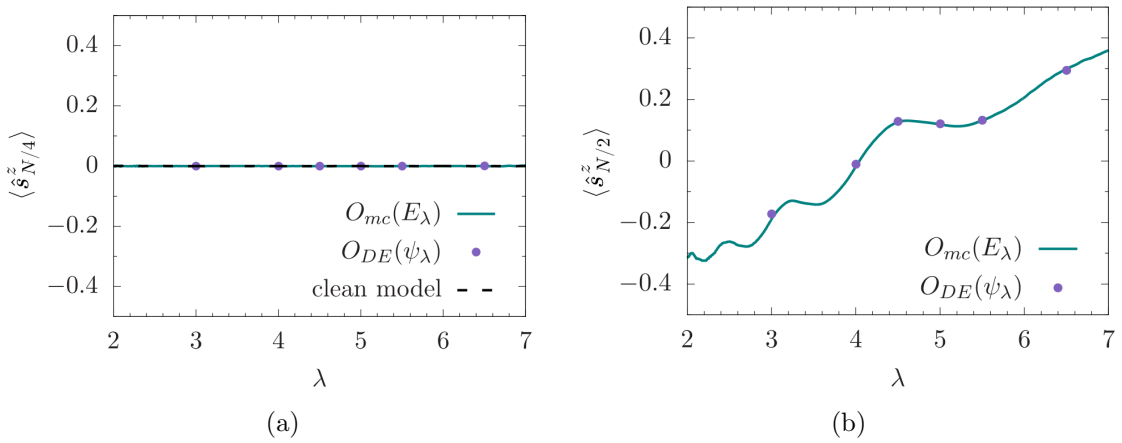

Figure 6.4: Thermalisation at the level of the observables implies that the expectation value in the diagonal ensemble associated to the initial state $O_{DE}(\psi_\lambda)$ (violet dots) corresponds to the microcanonical prediction at the initial energy $O_{mc}(E_\lambda)$ (continuous green line). We show this correspondence on a series of different helicities for $\Delta = 1.3$, $w = 1.58$. (a) The local observable is away from the impurity $\hat{O} = \hat{s}^z_{N/4}$, in this case the microcanonical prediction is the same as in the clean model (dashed black line). (b) Observable on the impurity site, $\hat{O} = \hat{s}^z_{N/2}$. All the quantities are evaluated via KPM, with $N_C = 300$ for $O_{DE}(\psi_\lambda)$, and $N_C = 100$ for $O_{mc}(E_\lambda)$ ($R = 50$ in (a), while in (b) $R = 1$). Calculations are performed in the full Hilbert space at $N = 24$ spins.

scale translates into a problem of resolution of the Chebyshev expansion, which is related to the number of moments used. As discussed in Sec. 2.3, features at energy scales smaller than $\sim 1/N_C$ will not appear in the KPM approximation. The advantage is that a single calculation gives the possibility of extracting transport exponents in ω. Via Fourier tranform, a power law scaling for long times translates into a power law scaling at small frequencies. In particular, the exponent ν' in the correlation decay described in Eq. (2.150), and used in Fig. 5.2 to distinguish the transport regimes of the interacting Fibonacci model in the previous chapter, becomes $\nu'_\omega = 1 - \nu'$ in the scaling for small ω [175]. Therefore, we classify the transport regime of the process according to the scaling exponent of the correlation for $\omega \to 0$, following [288, 289],

$$C(\omega) \sim \omega^{-\nu'_\omega} \begin{cases} 0 < \nu'_\omega < 1/2 \text{ superdiffusion} \\ \nu'_\omega = 1/2 \text{ diffusion} \\ 1/2 < \nu'_\omega \text{ subdiffusion.} \end{cases} \tag{6.29}$$

We study three different correlation functions for local observables, all encountered in the discussion on ETH of Sec. 6.1. The Fourier transform of the correlation in the microcanonical ensemble $C_{mc}(\omega, E)$ depends also on the mean energy parameter,

while the one from the diagonal ensemble $C_{DE}(\omega, \psi)$ depends on the initial state. In addition, we consider the Fourier transform of the correlation function evaluated on a single state as in Eq. (6.21), $C_{\psi_\lambda}(\omega)$. In Sec. 2.3.3, we have provided extensive details on the procedure to compute these quantities, while here we limit to comment the results. We focus on a local observable away from the impurity, in order to probe equilibrium dynamical predictions equivalent to those of the unperturbed XXZ model. We assume in the following $\hat{O} = \hat{s}^z_{N/4}$.

In order to corroborate the above discussion, we show in Fig. 6.5 the correlation function in the microcanonical ensemble as a function of ω, for a fixed energy $\bar{E}_\lambda = 1.8$, at different numbers of Chebyshev moments. We notice that, increasing N_C, we reach perfect overlap between the different orders of the KPM approximation at the extremes of the frequency axis, while we cannot capture the central peak. From the scaling in Eq. (6.29), it is in fact evident the presence of a divergence at $\omega = 0$. The KPM approximations model this divergence with a narrower and narrower Gaussian as N_C increases, never reaching convergence. We observe from the log-log scale of Fig. 6.5b that it is possible to individuate a range of small frequencies where the curve converges, and that can be in principle fitted by a power law. However, we detect the curve becoming less and less regular, with increasing oscillations as we add more moments. This is a finite-size effect: the KPM approximation has hit a number of moments N_C where it is able to resolve the discreteness of the energy levels in the spectrum, which appear continuous at all scales only in the thermodynamic limit. In the following, we perform the power law scaling by compromising between the extension of the frequency window where we have convergence, and the quality of the curve. In general, this has lead us to use the data from the approximation for $N_C = 400$ Chebyshev moments on the frequency range where it shows convergence with the $N_C = 800$ approximation, for example $\omega \sim 0.25 - 1$ in Fig. 6.5.

Within ETH, we can extract equilibrium dynamical predictions in an energy resolved way, using the diagonal ensemble of the spin helix state with appropriate helicity. In this preliminary phase of the study, we start by investigating the transport properties at infinite-temperature. Therefore, we select from Fig. 6.4 a spin helix state whose λ corresponds to the divergence in temperature, in particular, $\lambda_1 = 3.94$, and compute the correlation function in the diagonal ensemble. Analogously to the case of the

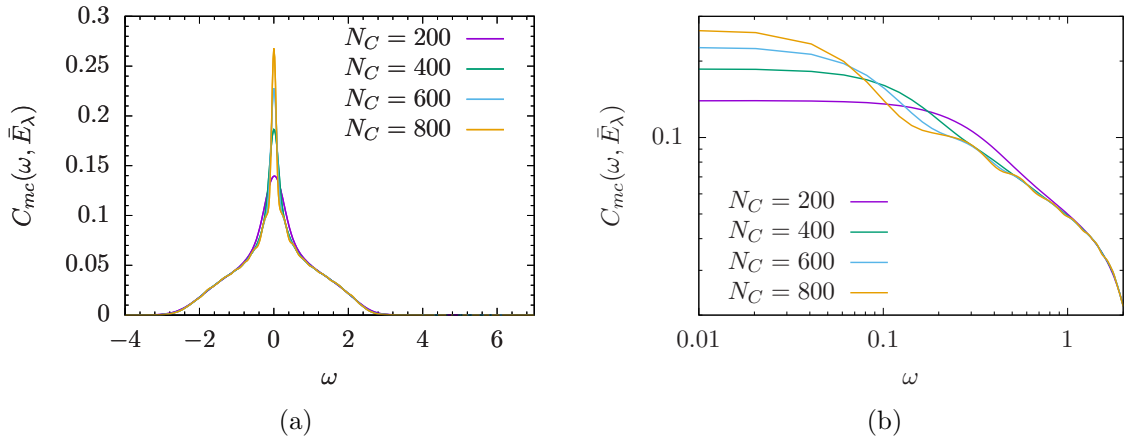

(a) (b)

Figure 6.5: Example correlation function for $\hat{s}^z_{N/4}$ in the microcanonical ensemble as a function of ω, and fixed energy $\bar{E}_\lambda = 1.8$, for $\Delta = 1.3$ and $w = 1.58$. The number of moments used in the KPM is shown in the color legend. We observe in (a) in linear, and (b) log-log scale, that the divergence at $\omega = 0$ cannot be captured. As evident in (b), it exists a window of small frequencies where the approximation has reached convergence, but it is subject to more oscillations for increasing number of Chebyshev moments N_C, due to finite-size effects. In order to perform a power law fitting, we need to compromise between extension of the convergence window and quality of the curve. We have used a single random state in the stochastic evaluation of trace $R = 1$.

expectation value in Eq. (6.27), we can verify the equivalence

$$C_{DE}(\omega, \psi_\lambda) = \int dE \rho_{\psi_\lambda}(E) C_{mc}(\omega, E). \tag{6.30}$$

As expected, we see it overlap in Fig. 6.6a with the microcanonical correlation at the corresponding energy $E_{\lambda_1} = -0.38$, with fluctuations due to the finite size. In Fig. 6.6b, we derive from a power law fitting transport exponent ν'_ω in agreement with previous theoretical studies indicating diffusion at $\Delta > 1$ [167, 184, 253]. We also observe a good agreement between the exponents extracted in the two different ensembles, $\nu'_\omega = 0.50$ for the diagonal, and $\nu'_\omega = 0.52$ for the microcanonical, which manifests ETH directly in the dynamical properties of the system.

We conclude our exploratory study with a calculation of the correlation function on the single helix state, which yields information on the far-from-equilibrium dynamics. We choose, in particular, the same λ_1 corresponding to infinite microcanonical temperature. Since the limited amount of moments available up to now does not allow to properly verify convergence, we are not able to draw definitive conclusions yet. However, we observe in Fig. 6.7 indication of a transport exponent indicating, rather than diffusion, subdiffusion. We have obtained $\nu'_\omega = -1.22$ fitting the KPM

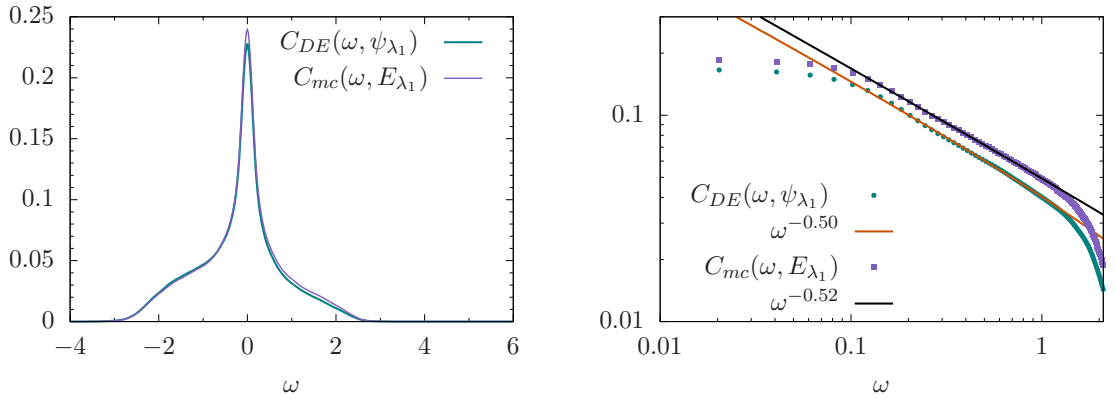

Figure 6.6: (a) Overlap between the correlation function in the diagonal ensemble $C_{DE}(\omega, \psi_{\lambda_1})$, and in the microcanonical ensemble at fixed energy, $C_{mc}(\omega, E_{\lambda_1})$, for the system at $\Delta = 1.3$ and $w = 1.58$. The helicity $\lambda_1 = 3.94$ corresponds in Fig. 6.2a to $E_{\lambda_1} = -0.38$, and in Fig. 6.3b to infinite temperature. (b) In log-log scale, we fit the functions from KPM (indicated by markers) with power laws $C(\omega) \sim \omega^{-\nu'_\omega}$, represented by the solid lines. We have used $R = 1$, $N_C = 400$.

approximation with $N_C = 200$ moments, and $\nu'_\omega = -1.24$ with $N_C = 300$. This result, despite non-conclusive, seems in striking contrast with the infinite-temperature equilibrium predictions, and leaves open the question of spin dynamics in regimes far-from-equilibrium.

However, we have showed that our methodology, exploiting ETH and spin helix states, allows for the extraction of transport exponents in an energy resolved way. Furthermore, we have established the KPM as a powerful method to investigate far-from-equilibrium dynamics. In the future, we will continue developing these results by investigating other regions of the parameter space, with $\Delta < 1$ and $\Delta = 1$, and by systematically exploring the dependence of the transport exponents on the helicities. Moreover, we would like to perform a scaling analysis with system-size, to analyse the effect of the fluctuations in the results, included in the ETH formulations.

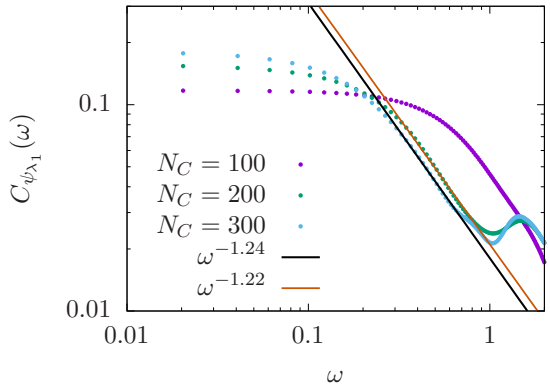

Figure 6.7: Correlation function evaluated on the single spin helix state at $\lambda = 3.94$ for a XXZ spin chain at $\Delta = 1.3$ and $w = 1.58$. The KPM approximations obtained with increasing number of moments N_C are indicated by markers in different colors in the legend. The solid lines represent the power law fits $C_{\psi_{\lambda_1}}(\omega) \sim \omega^{-\nu'_\omega}$ respectively for $N_C = 200$ (yellow line), and $N_C = 300$ (black line). The exponents suggest subdiffusive behaviour.

Conclusions

We have dedicated most of the thesis to the study of non-equilibrium particle and heat transient and steady-state transport properties of Hamiltonians subject to quasiperiodic potentials.

It has been known for long time that such models display uncommon properties as multifractal spectrum and critical eigenstates, which can lead to a localisation transition in one-dimension, mobility edge, or anomalous diffusion. However, they have gathered increasing attention only in recent years, because of the experimental realisation on ultracold atoms trapped in optical lattices, and their relevance in modelling synthetic DNA sequences, which are candidates for the assemblance of molecular electronic junctions.

Quasiperiodic models are now established as primary examples to explore the regime of anomalous transport and its consequences [32, 176, 231, 290]. In particular, it has been shown that multifractality, present also at the critical point of Anderson transition [291], prevents in these systems the agreement between the two standard ways of classifying transport behaviour, via time scaling of the spread of correlation in the the isolated system at thermodynamic limit, and via system size scaling of conductance in the steady-state of the open system [176]. However, previous studies in literature were essentially limited to particle or spin current, with little investigation on the heat or energy transport, and the implications of quasiperiodicity for thermoelectric effects.

Therefore, we have analysed coupled heat and electric currents in the tight-binding limit of quasiperiodic models in a two-terminal configuration, standard in mesoscopic physics. We have worked in Landauer-Büttiker framework with NEGF, which appears to represent the most effective formalism, given the simple structure of the

Hamiltonian matrices, the finite-temperature character of the phenomenon, and the possibility to incorporate dephasing from incoherent scattering. We have fully characterised thermoelectric effects in linear response regime, and demonstrated the large capability of these systems as working medium in quantum thermal machines, due, essentially, to the asymmetries in the transmission function. The asymmetry can also be drastic in case of a mobility edge, as in the GAAH model, where it acts as energy filter on a wide range of values for the thermodynamic variables. The discontinuities in the transmission function provoke large deviations from the Wiedemann-Franz law, which usually constraints to small values the figure of merit quantifying the efficiency of the heat-to-work-conversion. We intuitively map the fragmented structure of the transmission function to the fractality of the spectrum, that seems to have an impact even when these features are effectively broadened in presence of incoherent scattering from Büttiker probes. Despite the suppression of the anomalous transport in favour of standard diffusion, we have found in the Fibonacci chain a non-trivial dependence of the thermal and electric conductivities on the strength of the dephasing from these incoherent scattering events, different from clean or disordered models [50]. Non-trivial results have also been found in a subsequent study similar to ours on the AAH and GAAH models [292]. There is, however, a lack of complete quantitative understanding of this picture. Earlier studies have shown an analytical relation between multifractal indexes and dynamical properties in the quasiperiodic models, in particular, with the diffusion exponents of an initially localised wavepacket in the isolated system [207]. Future studies could be dedicated towards establishing a similar more fundamental link between the structure of the transmission function and quasiperiodicity. The position of the singularities appearing in the transmission, in fact, are directly connected to the divergences in the figure of merit through the Wiedemann-Franz law. Furthermore, even in presence of ballistic states, we have obtained a low power output, due to the structure of the transmission. The analysis of the thermal machine performance could be then extended to far-from-equilibrium scenarios in order to assess the full non-linear response of the system in presence of large bias, which would considerably enhance the power. Outside of linear response regime, the ability to tune the transmission profile of quasiperiodic systems by changing their Hamiltonian parameters could prove crucial in obtaining high efficiency at finite power output [39].

The realisation of quasiperiodic potentials on ultracold atoms trapped in optical lat-

tices, whose relative depths can tune the strength of interactions, has naturally offered a versatile testbed where to investigate the interplay between many-body effects and quasidisorder, in particular the possible emergence of a many-body localisation (MBL) phase, and how it would be fundamentally different from the same phenomenon induced by random disorder [239]. In particular, indications of a MBL transition have been experimentally observed in the interacting AAH model [53–56], which would belong to a new type of universality class [70]. The Fibonacci model is more difficult to realise on the same platform, although a theoretical proposal was recently suggested [293]. Therefore, there have not been opportunities to experimentally probe the dynamics in the interacting version of the model, and verify how many-body interaction terms affect the anomalous diffusion. On the numerical and theoretical side, there have been only few works exploring the problem, whose findings do not reconcile in a unified picture. A MBL transition was predicted at increasing values of the potential and fixed interaction strength [294], while at small interactions strong evidence were found of transport becoming diffusive [208]. Both results are not intuitive, since in absence of interactions the model exhibits no localisation and a smooth crossover from ballistic to subdiffusive. Indeed, a slow subdiffusive dynamics was observed in the Fermi-Hubbard realisation of the model, induced by the multifractality of the spectrum [73].

The question, then, is whether transport can become anomalous again at intermediate interaction strengths. We have contributed towards filling the gap by investigating in this regime density-density correlations at infinite temperature using the dynamical quantum typicality approach. Our findings provided strong evidence of a possible crossover to MBL with increasing Fibonacci potential, preceded by a regime of anomalous subdiffusive transport. However, more definitive results on the occurence of MBL would require the study of larger systems up to longer times, which is beyond current state-of-the-art numerical techniques. Given the peculiar spectral properties of this class of models, a study of the energy dependence of the transport properties is a very promising direction for a subsequent investigation, for example using open system techniques [295, 296]. Moreover, all present studies of transport properties are limited to infinite or zero temperature [72, 208, 297], while the finite temperature transport properties are other interesting but challenging directions for future work.

This study has inevitably lead our interests closer to the physics of many-body systems

beyond the specific case of quasiperiodic potentials. Driven by the technical advances, there has been a renovated combined theoretical and experimental strive towards the fundamental topics of thermalisation, and non-equilibrium phenomena [64]. In particular, we were inspired by the experiment conducted by Jepsen *et al.* on their analogue simulator of quantum Hamiltonians based on ultracold atoms [75]. Here, dynamical aspect of the XXZ model were probed by preparing initial spin helix states, exhibiting a winding magnetisation pattern with adjustable wavelength or helicity. Their exciting results, in contrast with the predictions of linear response regime, inspired us to build a numerical experiment which employs the same type of spin helix states. We focus, however, on the XXZ model with a local magnetic impurity, which is known to break integrability, thus fulfilling the eigenstate thermalisation hypothesis (ETH) while preserving the infinite-temperature transport properties of the clean model [66, 265]. Within ETH, the mean energy of the initial state, here controlled by the helicity, sets the energy or microcanonical temperature of the statistical ensemble the system will thermalise to. We expose in the thesis our first results, showing that it is possible to extract the infinite temperature exponent from the equilibrium dynamical properties of the spin helix states, by tuning the appropriate helicity. We use the kernel polynomial method (KPM), a powerful technique we have been recently gotten acquainted with, that allows to investigate the dynamical quantities in the frequency rather than time domain. In the same framework, we are also able to examine the far-from-equilibrium dynamics, evaluating the correlation functions on the single spin helix states. All of these considerations are part of a preliminary study, that we are currently corroborating with more systematic calculations, and extending to test the properties of the system at finite microcanonical temperatures.

In conclusions, we have demonstrated that, despite living in one-dimension, quasiperiodic models display an extremely rich transport behaviour, which offers possibilities for practical applications in quantum thermal machines, and also a testbed where to explore fundamental questions on how localisation transitions arise in presence of many-body interactions. Their full potential for quantum thermodynamics remains to be uncovered. On the other hand, we have studied thermalisation on the XXZ model in presence of an integrability-breaking term, when probed by spin helix states, and exploited this mechanism to propose a scheme to extract its transport properties. In doing so, we have proved the KPM to be a promising technique to investigate different

dynamical regimes in quantum many-body systems.

Acknowledgements

My first acknowledgement undoubtedly goes to John Goold, my PhD advisor. I am deeply grateful for his patient guidance, his creative enthusiasm and his thoughtful support. I feel extremely lucky to have been part of the research group he has built in Trinity, a bunch of incredible people and physicists and a joyful environment for discussions and new ideas.

I would also like to thank Archak Purkayastha and Mark Mitchison for their constant help and for everything they taught me. I express my gratitude towards Francesca Pietracaprina and Géraldine Haack for offering me the opportunity of working together and their support throughout our projects. I owe special thanks to Gabriel Landi for inviting me to give my first public seminar ever, and for his insightful perspectives on my research along the years. I thank Stephen Clark, Krissia Zawadzki, and Silvia Pappalardi for the help during my last work.

I thank all the past and current members of QuSys, especially Artur, Laetitia, Giacomo, Oisín, Nathan and, last but not least, Alessandro, for the time spent together at the office and outside. Special mention to Maria and Marlon, my left and right desk, with whom I shared so many sorrows and laughs (and pints).

I am grateful to all the other friends I made in Ireland, both in Dublin and in Belfast, and to the friendships I always carry with me from Trieste and Palermo.

Finally, I thank for their invaluable support my beloved family, to whom this thesis is dedicated: my parents Anna and Vincenzo, and my sister Arianna.

Bibliography

[1] R. Kosloff and A. Levy, Annu. Rev. Phys. Chem. **65**, 365 (2014).

[2] M. T. Mitchison, Contemp. Phys. (2019), 10.1080/00107514.2019.1631555.

[3] M. O. Scully, K. R. Chapin, K. E. Dorfman, M. B. Kim, and A. Svidzinsky, Proc. Nat. Acad. Sci. **108**, 15097 (2011).

[4] N. Brunner, M. Huber, N. Linden, S. Popescu, R. Silva, and P. Skrzypczyk, Phys. Rev. E **89**, 032115 (2014).

[5] L. A. Correa, J. P. Palao, D. Alonso, and G. Adesso, Sci. Rep. **4**, 3949 (2014).

[6] N. Killoran, S. F. Huelga, and M. B. Plenio, J. Chem. Phys. **143**, 155102 (2015).

[7] R. Biele, C. A. Rodríguez-Rosario, T. Frauenheim, and A. Rubio, npj Quantum Mater. **2**, 38 (2017).

[8] A. Ghosh, C. L. Latune, L. Davidovich, and G. Kurizki, Proc. Nat. Acad. Sci. **114**, 12156 (2017).

[9] N. Yunger Halpern, C. D. White, S. Gopalakrishnan, and G. Refael, Phys. Rev. B **99**, 024203 (2019).

[10] J. Klatzow, J. N. Becker, P. M. Ledingham, C. Weinzetl, K. T. Kaczmarek, D. J. Saunders, J. Nunn, I. A. Walmsley, R. Uzdin, and E. Poem, Phys. Rev. Lett. **122**, 110601 (2019).

[11] A. Ronzani, B. Karimi, J. Senior, Y.-C. Chang, J. T. Peltonen, C. Chen, and J. P. Pekola, Nature Physics **14**, 991 (2018).

[12] M. Josefsson, A. Svilans, A. Burke, E. A. Hoffmann, S. Fahlvik, C. Thelander, M. Leijnse, and H. Linke, Nat. Nanotechnol. **13** (2018).

[13] N. Mosso, H. Sadeghi, A. Gemma, S. Sangtarash, U. Drechsler, C. Lambert, and B. Gotsmann, Nano Letters **19**, 7614 (2019).

[14] J.-P. Brantut, C. Grenier, J. Meineke, D. Stadler, S. Krinner, C. Kollath, T. Esslinger, and A. Georges, Science **342**, 713 (2013).

[15] L. D. Hicks and M. S. Dresselhaus, Phys. Rev. B **47**, 12727 (1993).

[16] R. Bosisio, C. Gorini, G. Fleury, and J.-L. Pichard, New Journal of Physics **16**, 095005 (2014).

[17] N. Nakpathomkun, H. Q. Xu, and H. Linke, Phys. Rev. B **82**, 235428 (2010).

[18] A. I. Boukai, Y. Bunimovich, J. Tahir-Kheli, J.-K. Yu, W. A. Goddard III, and J. R. Heath, Nature **451**, 168 (2008).

[19] A. I. Hochbaum, R. Chen, R. D. Delgado, W. Liang, E. C. Garnett, M. Najarian, A. Majumdar, and P. Yang, Nature **451**, 163 (2008).

[20] G. Benenti, G. Casati, K. Saito, and R. S. Whitney, Phys. Rep. **694**, 1 (2017).

[21] N. W. Ashcroft, N. D. Mermin, and R. Smoluchowski, Physics Today **30**, 61 (1977).

[22] G. Semeghini, M. Landini, P. Castilho, S. Roy, G. Spagnolli, A. Trenkwalder, M. Fattori, M. Inguscio, and G. Modugno, Nat. Phys. **11**, 554 EP (2015).

[23] E. Abrahams, P. W. Anderson, D. C. Licciardello, and T. V. Ramakrishnan, Phys. Rev. Lett. **42**, 673 (1979).

[24] J. Bellissard, B. Iochum, E. Scoppola, and D. Testard, Communications in Mathematical Physics **125**, 527 (1989).

[25] M. Kohmoto, B. Sutherland, and C. Tang, Phys. Rev. B **35**, 1020 (1987).

[26] H. Hiramoto and M. Kohmoto, Int. J. Mod. Phys. B **06**, 281 (1992).

[27] B. Simon, Advances in Applied Mathematics **3**, 463 (1982).

[28] A. Avila and S. Jitomirskaya, in *Mathematical Physics of Quantum Mechanics* (Springer Berlin Heidelberg, 2005) pp. 5–16.

[29] Y. Last, Commun. Math. Phys. **164**, 421 (1994).

[30] H. Hiramoto and S. Abe, Journal of the Physical Society of Japan **57**, 230 (1988).

[31] A. Purkayastha, S. Sanyal, A. Dhar, and M. Kulkarni, Phys. Rev. B **97**, 174206 (2018).

[32] V. K. Varma, C. de Mulatier, and M. Žnidarič, Phys. Rev. E **96**, 032130 (2017).

[33] S. Aubry and G. André, Ann. Israel Phys. Soc **3**, 18 (1980).

[34] M. Rossignolo and L. Dell'Anna, Phys. Rev. B **99**, 054211 (2019).

[35] F. A. An, K. Padavić, E. J. Meier, S. Hegde, S. Ganeshan, J. Pixley, S. Vishveshwara, and B. Gadway, Physical Review Letters **126**, 040603 (2021).

[36] S. Ganeshan, J. H. Pixley, and S. Das Sarma, Phys. Rev. Lett. **114**, 146601 (2015).

[37] A. Jagannathan, Rev. Mod. Phys. **93**, 045001 (2021).

[38] G. D. Mahan and J. O. Sofo, Proc. Natl. Acad. Sci **93**, 7436 (1996).

[39] R. Whitney, Phys. Rev. Lett. **112**, 130601 (2014).

[40] M. Zebarjadi, K. Esfarjani, M. S. Dresselhaus, Z. F. Ren, and G. Chen, Energy Environ. Sci. **5**, 5147 (2012).

[41] E. Collini, Chem. Soc. Rev. **42**, 4932 (2013).

[42] G. D. Scholes and C. Smyth, The Journal of Chemical Physics **140**, 110901 (2014).

[43] D. Nozaki, C. G. da Rocha, H. M. Pastawski, and G. Cuniberti, Physical Review B **85**, 155327 (2012).

[44] J. K. Sowa, J. A. Mol, G. A. D. Briggs, and E. M. Gauger, Phys. Chem. Chem. Phys. **19**, 29534 (2017).

[45] M. Kilgour and D. Segal, The Journal of Chemical Physics **143**, 024111 (2015).

[46] D. N. Biggerstaff, R. Heilmann, A. A. Zecevik, M. Gräfe, M. A. Broome, A. Fedrizzi, S. Nolte, A. Szameit, A. G. White, and I. Kassal, Nature Communications **7**, 11282 (2016).

[47] S. Viciani, S. Gherardini, M. Lima, M. Bellini, and F. Caruso, Scientific Reports **6**, 37791 (2016).

[48] N. Trautmann and P. Hauke, Phys. Rev. A **97**, 023606 (2018).

[49] M. Žnidarič and M. Horvat, The European Physical Journal B **86**, 67 (2013).

[50] M. Žnidarič, J. J. Mendoza-Arenas, S. R. Clark, and J. Goold, Annalen der Physik **529**, 1600298 (2017).

[51] A. M. Lacerda, J. Goold, and G. T. Landi, Phys. Rev. B **104**, 174203 (2021).

[52] H. P. Lüschen, S. Scherg, T. Kohlert, M. Schreiber, P. Bordia, X. Li, S. Das Sarma, and I. Bloch, Phys. Rev. Lett. **120**, 160404 (2018).

[53] T. Kohlert, S. Scherg, X. Li, H. P. Lüschen, S. Das Sarma, I. Bloch, and M. Aidelsburger, Phys. Rev. Lett. **122**, 170403 (2019).

[54] M. Schreiber, S. S. Hodgman, P. Bordia, H. P. Lüschen, M. H. Fischer, R. Vosk, E. Altman, U. Schneider, and I. Bloch, Science **349**, 842 (2015).

[55] H. P. Lüschen, P. Bordia, S. S. Hodgman, M. Schreiber, S. Sarkar, A. J. Daley, M. H. Fischer, E. Altman, I. Bloch, and U. Schneider, Phys. Rev. X **7**, 011034 (2017).

[56] H. P. Lüschen, P. Bordia, S. Scherg, F. Alet, E. Altman, U. Schneider, and I. Bloch, Phys. Rev. Lett. **119**, 260401 (2017).

[57] S. Hild, T. Fukuhara, P. Schauß, J. Zeiher, M. Knap, E. Demler, I. Bloch, and C. Gross, Physical Review Letters **113**, 147205 (2014).

[58] T. Fukuhara, A. Kantian, M. Endres, M. Cheneau, P. Schauß, S. Hild, D. Bellem, U. Schollwø"ck, T. Giamarchi, C. Gross, I. Bloch, and S. Kuhr, Nature Physics **9**, 235 (2013).

[59] U. Schneider, L. Hackermˇ'ller, J. P. Ronzheimer, S. Will, S. Braun, T. Best, I. Bloch, E. Demler, S. Mandt, D. Rasch, and A. Rosch, Nature Physics **8**, 213 (2012).

[60] T. Kinoshita, T. Wenger, and D. S. Weiss, Nature **440**, 900 (2006).

[61] S. Trotzky, Y.-A. Chen, A. Flesch, I. P. McCulloch, U. Schollwöck, J. Eisert, and I. Bloch, Nature Physics **8**, 325 (2012).

[62] A. Polkovnikov, K. Sengupta, A. Silva, and M. Vengalattore, Reviews of Modern Physics **83**, 863 (2011).

[63] C.-C. Chien, S. Peotta, and M. D. Ventra, Nature Physics **11**, 998 (2015).

[64] D. A. Abanin, E. Altman, I. Bloch, and M. Serbyn, Reviews of Modern Physics **91**, 021001 (2019).

[65] L. D'Alessio, Y. Kafri, A. Polkovnikov, and M. Rigol, Advances in Physics **65**, 239 (2016), https://doi.org/10.1080/00018732.2016.1198134 .

[66] M. Brenes, T. LeBlond, J. Goold, and M. Rigol, Physical Review Letters **125**, 070605 (2020).

[67] Y. Tang, W. Kao, K.-Y. Li, S. Seo, K. Mallayya, M. Rigol, S. Gopalakrishnan, and B. L. Lev, Physical Review X **8**, 021030 (2018).

[68] X. Li, X. Li, and S. Das Sarma, Phys. Rev. B **96**, 085119 (2017).

[69] D.-L. Deng, S. Ganeshan, X. Li, R. Modak, S. Mukerjee, and J. H. Pixley, Ann. Phys. (Berl.) **529**, 1600399 (2017).

[70] V. Khemani, D. Sheng, and D. A. Huse, Physical Review Letters **119**, 075702 (2017).

[71] N. Macé, N. Laflorencie, and F. Alet, SciPost Phys. **6**, 50 (2019).

[72] J. Vidal, D. Mouhanna, and T. Giamarchi, Phys. Rev. Lett. **83**, 3908 (1999).

[73] J. Settino, N. W. Talarico, F. Cosco, F. Plastina, S. Maniscalco, and N. Lo Gullo, Phys. Rev. B **101**, 144303 (2020).

[74] T. Heitmann, J. Richter, D. Schubert, and R. Steinigeweg, Zeitschrift für Naturforschung A **75**, 421 (2020).

[75] P. N. Jepsen, J. Amato-Grill, I. Dimitrova, W. W. Ho, E. Demler, and W. Ketterle, Nature **588**, 403 (2020).

[76] A. Weiße, G. Wellein, A. Alvermann, and H. Fehske, Reviews of Modern Physics **78**, 275 (2006).

[77] E. Schrödinger and R. Penrose, *What is Life?: With Mind and Matter and Autobiographical Sketches*, Canto (Cambridge University Press, 1992).

[78] P. J. Lu and P. J. Steinhardt, Science **315**, 1106 (2007).

[79] B. Grünbaum and G. C. Shephard, *Tilings and Patterns* (Dover Publications, Incorporated, 2016) p. 720.

[80] R. Berger, Memoirs of the American Mathematical Society **0**, 0 (1966).

[81] R. Penrose, The Mathematical Intelligencer **2**, 32 (1979).

[82] R. M. Robinson, Inventiones Mathematicae **12**, 177 (1971).

[83] R. Ammann, B. Grünbaum, and G. C. Shephard, Discrete Comp Geom **8**, 1 (1992).

[84] D. Shechtman, I. Blech, D. Gratias, and J. W. Cahn, Phys. Rev. Lett. **53**, 1951 (1984).

[85] L. Bendersky, Physical Review Letters **55**, 1461 (1985).

[86] T. Ishimasa, H.-U. Nissen, and Y. Fukano, Physical Review Letters **55**, 511 (1985).

[87] D. Levine and P. J. Steinhardt, Phys. Rev. Lett. **53**, 2477 (1984).

[88] J. Cahn, J. Mater. Res. Technol. **106**, 975 (2001).

[89] E. Maciá, Reports on Progress in Physics **69**, 397 (2005).

[90] E. Maciá, ISRN Condensed Matter Physics **2014**, 1 (2014).

[91] Y. K. Vekilov and M. A. Chernikov, Physics-Uspekhi **53**, 537 (2010).

[92] L. Bindi, N. Yao, C. Lin, L. S. Hollister, C. L. Andronicos, V. V. Distler, M. P. Eddy, A. Kostin, V. Kryachko, G. J. MacPherson, W. M. Steinhardt, M. Yudovskaya, and P. J. Steinhardt, Scientific Reports **5**, 9111 (2015).

[93] L. Bindi, P. J. Steinhardt, N. Yao, and P. J. Lu, Science **324**, 1306 (2009).

[94] H. Bohr, *Almost Period Functions (AMS/Chelsea Publication)* (American Mathematical Society, 1999).

[95] M. Y. Azbel, Physical Review Letters **43**, 1954 (1979).

[96] M. Kohmoto, L. P. Kadanoff, and C. Tang, Phys. Rev. Lett. **50**, 1870 (1983).

[97] S. Ostlund, R. Pandit, D. Rand, H. J. Schellnhuber, and E. D. Siggia, Phys. Rev. Lett. **50**, 1873 (1983).

[98] D. Tanese, E. Gurevich, F. Baboux, T. Jacqmin, A. Lemaître, E. Galopin, I. Sagnes, A. Amo, J. Bloch, and E. Akkermans, Phys. Rev. Lett. **112**, 146404 (2014).

[99] F. Baboux, E. Levy, A. Lemaître, C. Gómez, E. Galopin, L. L. Gratiet, I. Sagnes, A. Amo, J. Bloch, and E. Akkermans, Physical Review B **95**, 161114 (2017).

[100] V. Goblot, A. Štrkalj, N. Pernet, J. L. Lado, C. Dorow, A. Lemaître, L. Le Gratiet, A. Harouri, I. Sagnes, S. Ravets, A. Amo, J. Bloch, and O. Zilberberg, Nature Physics **16**, 832 (2020).

[101] Y. E. Kraus and O. Zilberberg, Phys. Rev. Lett. **109**, 116404 (2012).

[102] Y. E. Kraus, Y. Lahini, Z. Ringel, M. Verbin, and O. Zilberberg, Phys. Rev. Lett. **109**, 106402 (2012).

[103] M. Verbin, O. Zilberberg, Y. E. Kraus, Y. Lahini, and Y. Silberberg, Phys. Rev. Lett. **110**, 076403 (2013).

[104] M. Verbin, O. Zilberberg, Y. Lahini, Y. E. Kraus, and Y. Silberberg, Phys. Rev. B **91**, 064201 (2015).

[105] M. Modugno, New Journal of Physics **11**, 033023 (2009).

[106] G. Roati, C. D'Errico, L. Fallani, M. Fattori, C. Fort, M. Zaccanti, G. Modugno, M. Modugno, and M. Inguscio, Nature **453**, 895 (2008).

[107] Y. Wang, J.-H. Zhang, Y. Li, J. Wu, W. Liu, F. Mei, Y. Hu, L. Xiao, J. Ma, C. Chin, and S. Jia, Physical Review Letters **129**, 103401 (2022).

[108] A. Y. Gordon, S. Jitomirskaya, Y. Last, and B. Simon, Acta Mathematica **178**, 169 (1997).

[109] A. Avila, "The absolutely continuous spectrum of the almost mathieu operator," (2008).

[110] S. Y. Jitomirskaya, The Annals of Mathematics **150**, 1159 (1999).

[111] J. Sokoloff, Physics Reports **126**, 189 (1985).

[112] D. R. Hofstadter, Phys. Rev. B **14**, 2239 (1976).

[113] P. G. Harper, Proc. Phys. Soc. A **68**, 874 (1955).

[114] B. Kramer and A. MacKinnon, Reports on Progress in Physics **56**, 1469 (1993).

[115] D. J. Thouless, Journal of Physics C: Solid State Physics **5**, 77 (1972).

[116] S. Ganeshan, K. Sun, and S. D. Sarma, Physical Review Letters **110**, 180403 (2013).

[117] C. M. Soukoulis and E. N. Economou, Phys. Rev. Lett. **48**, 1043 (1982).

[118] R. Riklund, Y. Liu, G. Wahlstrom, and Z. Zhao-bo, Journal of Physics C: Solid State Physics **19**, L705 (1986).

[119] P. W. Anderson, Phys. Rev. **109**, 1492 (1958).

[120] J. Settino, N. Lo Gullo, A. Sindona, J. Goold, and F. Plastina, Phys. Rev. A **95**, 033605 (2017).

[121] J. Biddle, B. Wang, D. J. Priour, and S. Das Sarma, Phys. Rev. A **80**, 021603 (2009).

[122] J. Biddle and S. Das Sarma, Phys. Rev. Lett. **104**, 070601 (2010).

[123] X. Deng, S. Ray, S. Sinha, G. Shlyapnikov, and L. Santos, Physical Review Letters **123**, 025301 (2019).

[124] S. Gopalakrishnan, Physical Review B **96**, 054202 (2017).

[125] J. Biddle, D. J. Priour, B. Wang, and S. Das Sarma, Phys. Rev. B **83**, 075105 (2011).

[126] D. J. Boers, B. Goedeke, D. Hinrichs, and M. Holthaus, Phys. Rev. A **75**, 063404 (2007).

[127] S. Das Sarma, S. He, and X. C. Xie, Phys. Rev. Lett. **61**, 2144 (1988).

[128] S. Das Sarma, S. He, and X. C. Xie, Phys. Rev. B **41**, 5544 (1990).

[129] X. Cai and Y.-C. Yu, Journal of Physics: Condensed Matter **35**, 035602 (2022).

[130] X. Li and S. D. Sarma, Physical Review B **101**, 064203 (2020).

[131] E. Maciá, Phys. Rev. B **74**, 245105 (2006).

[132] A.-M. Guo and Q.-f. Sun, Phys. Rev. B **86**, 115441 (2012).

[133] N. Macé, A. Jagannathan, P. Kalugin, R. Mosseri, and F. Piéchon, Physical Review B **96**, 045138 (2017).

[134] N. Macé, A. Jagannathan, and F. Piéchon, Phys. Rev. B **93**, 205153 (2016).

[135] G. R. Goodson, *Chaotic dynamics: fractals, tilings and substitutions* (Cambridge University Press, 2017).

[136] A. Štrkalj, E. V. H. Doggen, I. V. Gornyi, and O. Zilberberg, Phys. Rev. Research **3**, 033257 (2021).

[137] F. Piéchon, M. Benakli, and A. Jagannathan, Physical Review Letters **74**, 5248 (1995).

[138] J. Janarek, D. Delande, and J. Zakrzewski, Physical Review B **97**, 155133 (2018).

[139] R. Landauer, IBM Journal of Research and Development **1**, 223 (1957).

[140] M. Büttiker, Y. Imry, R. Landauer, and S. Pinhas, Physical Review B **31**, 6207 (1985).

[141] H. van Houten, L. W. Molenkamp, C. W. J. Beenakker, and C. T. Foxon, Semicond. Sci. Technol. **7**, B215 (1992).

[142] M. A. Popp, A. Erpenbeck, and H. B. Weber, Scientific Reports **11**, 2031 (2021).

[143] P. Reddy, S.-Y. Jang, R. A. Segalman, and A. Majumdar, Science **315**, 1568 (2007).

[144] Y. Dubi and M. Di Ventra, Rev. Mod. Phys. **83**, 131 (2011).

[145] R. Bosisio, G. Fleury, and J.-L. Pichard, New J. Phys. **16**, 035004 (2014).

[146] H. B. Callen, *Thermodynamics and an Introduction to Thermostatistics,* (Wiley, New York, 1985).

[147] K. Yamamoto and N. Hatano, Phys. Rev. E **92** (2015).

[148] D. A. Ryndyk, *Theory of Quantum Transport at Nanoscale*, Vol. 184 (Springer, 2016).

[149] S. Datta, *Electronic transport in mesoscopic systems* (Cambridge university press, 1997).

[150] Y. Meir and N. S. Wingreen, Phys. Rev. Lett. **68**, 2512 (1992).

[151] G. J. Snyder and E. S. Toberer, Nat. Mater. **7**, 105 EP (2008).

[152] A. Shakouri, Annu. Rev. Mater. Res. **41**, 399 (2011).

[153] S. R. De Groot and P. Mazur, *Non-equilibrium thermodynamics* (Courier Corporation, 2013).

[154] L. Onsager, Phys. Rev. **37**, 405 (1931).

[155] G. D. Mahan, *Many Particle Physics (Physics of Solids and Liquids)* (Springer, 2007) p. 785.

[156] V. Balachandran, R. Bosisio, and G. Benenti, Phys. Rev. B **86**, 035433 (2012).

[157] R. S. Whitney, Physical Review B **87**, 115404 (2013).

[158] R. S. Whitney, Physical Review B **91**, 115425 (2015).

[159] M. Esposito, K. Lindenberg, and C. V. den Broeck, EPL (Europhysics Letters) **85**, 60010 (2009).

[160] M. Josefsson, A. Svilans, H. Linke, and M. Leijnse, Physical Review B **99**, 235432 (2019).

[161] H. J. Goldsmid, *Introduction to thermoelectricity*, Vol. 121 (Springer, 2010).

[162] C. Van den Broeck, Phys. Rev. Lett. **95**, 190602 (2005).

[163] F. L. Curzon and B. Ahlborn, Am. J. Phys. **43**, 22 (1975).

[164] L. E. Bell, Science **321**, 1457 (2008).

[165] M. Toda, R. Kubo, R. Kubo, M. Toda, and N. Saito, *Statistical Physics II Nonequilibrium Statistical Mechanics* (Springer, 2012).

[166] R. Kubo, Journal of the Physical Society of Japan **12**, 570 (1957).

[167] R. Steinigeweg, EPL (Europhysics Letters) **97**, 67001 (2012).

[168] R. Steinigeweg, F. Jin, D. Schmidtke, H. De Raedt, K. Michielsen, and J. Gemmer, Phys. Rev. B **95**, 035155 (2017).

[169] J. Richter, F. Jin, L. Knipschild, J. Herbrych, H. De Raedt, K. Michielsen, J. Gemmer, and R. Steinigeweg, Phys. Rev. B **99**, 144422 (2019).

[170] J. Richter, D. Schubert, and R. Steinigeweg, Phys. Rev. Research **2**, 013130 (2020).

[171] A. Gubin and L. F. Santos, American Journal of Physics **80**, 246 (2012).

[172] T. Giamarchi, *Quantum Physics in one dimension* (Clarendon/Oxford, 2003).

[173] G. Giuliani and G. Vignale, *Quantum Theory of the Electron Liquid* (Cambridge University Press, 2005).

[174] Nicolas Borghini, "Topics on Nonequilibrium Physics," Universität Bielefeld, Fakultät für Physik (2016).

[175] B. Bertini, F. Heidrich-Meisner, C. Karrasch, T. Prosen, R. Steinigeweg, and M. Žnidarič, Reviews of Modern Physics **93**, 025003 (2021).

[176] A. Purkayastha, J. Stat. Mech.: Theory Exp. **2019**, 043101 (2019).

[177] P. Mazur, Physica **43**, 533 (1969).

[178] M. Suzuki, Physica **51**, 277 (1971).

[179] B. S. Shastry, Physical Review B **73**, 085117 (2006).

[180] M. Žnidarič, A. Scardicchio, and V. K. Varma, Physical Review Letters **117**, 040601 (2016).

[181] S. Paeckel, T. Köhler, A. Swoboda, S. R. Manmana, U. Schollwöck, and C. Hubig, Annals of Physics **411**, 167998 (2019).

[182] C. Bartsch and J. Gemmer, Phys. Rev. Lett. **102**, 110403 (2009).

[183] P. Reimann, Phys. Rev. E **97**, 062129 (2018).

[184] R. Steinigeweg, H. Wichterich, and J. Gemmer, EPL (Europhysics Letters) **88**, 10004 (2009).

[185] P. Reimann, Physical Review Letters **99**, 160404 (2007).

[186] S. Sugiura and A. Shimizu, Physical Review Letters **111**, 010401 (2013).

[187] K. Fabricius and B. M. McCoy, Physical Review B **57**, 8340 (1998).

[188] S. Roche, Physical Review B **59**, 2284 (1999).

[189] A. Ferreira, J. Viana-Gomes, J. Nilsson, E. R. Mucciolo, N. M. R. Peres, and A. H. C. Neto, Physical Review B **83**, 165402 (2011).

[190] J. H. García, L. Covaci, and T. G. Rappoport, Physical Review Letters **114**, 116602 (2015).

[191] E. Gull, S. Iskakov, I. Krivenko, A. A. Rusakov, and D. Zgid, Physical Review B **98**, 075127 (2018).

[192] J. E. Sobczyk and A. Roggero, Physical Review E **105**, 055310 (2022).

[193] Y. Yang, S. Iblisdir, J. I. Cirac, and M. C. Bañuls, Physical Review Letters **124**, 100602 (2020).

[194] I. Papaefstathiou, D. Robaina, J. I. Cirac, and M. C. Bañuls, Physical Review D **104**, 014514 (2021).

[195] C. Chiaracane, M. T. Mitchison, A. Purkayastha, G. Haack, and J. Goold, Phys. Rev. Research **2**, 013093 (2020).

[196] Y. Lahini, R. Pugatch, F. Pozzi, M. Sorel, R. Morandotti, N. Davidson, and Y. Silberberg, Phys. Rev. Lett. **103**, 013901 (2009).

[197] F. Mirlin and Alexander, Rev. Mod. Phys. **80**, 1355 (2008).

[198] A. Purkayastha, A. Dhar, and M. Kulkarni, Phys. Rev. B **96**, 180204 (2017).

[199] V. Balachandran, S. R. Clark, J. Goold, and D. Poletti, Phys. Rev. Lett. **123**, 020603 (2019).

[200] U. Sivan and Y. Imry, Phys. Rev. B **33**, 551 (1986).

[201] K. Yamamoto, A. Aharony, O. Entin-Wohlman, and N. Hatano, Phys. Rev. B **96**, 155201 (2017).

[202] M. Lebrat, P. Grišins, D. Husmann, S. Häusler, L. Corman, T. Giamarchi, J.-P. Brantut, and T. Esslinger, Phys. Rev. X **8**, 011053 (2018).

[203] S. Krinner, T. Esslinger, and J.-P. Brantut, J. Phys. Condens. Matter **29**, 343003 (2017).

[204] M. Kanász-Nagy, L. Glazman, T. Esslinger, and E. A. Demler, Phys. Rev. Lett. **117**, 255302 (2016).

[205] S. Krinner, D. Stadler, D. Husmann, J.-P. Brantut, and T. Esslinger, Nature **517**, 64 (2014).

[206] C. Chiaracane, A. Purkayastha, M. T. Mitchison, and J. Goold, Physical Review B **105**, 134203 (2022).

[207] F. Piéchon, Phys. Rev. Lett. **76**, 4372 (1996).

[208] V. K. Varma and M. Žnidarič, Phys. Rev. B **100**, 085105 (2019).

[209] M. Saha and S. K. Maiti, J. Phys. D: Appl. Phys. **52**, 465304 (2019).

[210] M. Saha and S. K. Maiti, Physica E: Low-dimensional Systems and Nanostructures **93**, 275 (2017).

[211] R. Korol, M. Kilgour, and D. Segal, The Journal of Chemical Physics **145**, 224702 (2016).

[212] H. Kim and D. Segal, The Journal of Chemical Physics **146**, 164702 (2017), https://doi.org/10.1063/1.4981022 .

[213] L. Xiang, J. L. Palma, C. Bruot, V. Mujica, M. A. Ratner, and N. Tao, Nature Chemistry **7**, 221 (2015).

[214] C. Bruot, J. L. Palma, L. Xiang, V. Mujica, M. A. Ratner, and N. Tao, Nature Communications **6**, 8032 (2015).

[215] M. B. Plenio and S. F. Huelga, New J. Phys. **10** (2008), 10.1088/1367-2630/10/11/113019.

[216] P. Rebentrost, M. Mohseni, I. Kassal, S. Lloyd, and A. Aspuru-Guzik, New J. Phys. **11**, 033003 (2009).

[217] F. Caruso, A. W. Chin, A. Datta, S. F. Huelga, and M. B. Plenio, The Journal of Chemical Physics **131**, 105106 (2009).

[218] A. W. Chin, S. F. Huelga, and M. B. Plenio, Philosophical Transactions of the Royal Society A: Mathematical, Physical and Engineering Sciences **370**, 3638 (2012).

[219] E. Zerah-Harush and Y. Dubi, The Journal of Physical Chemistry Letters **9**, 1689 (2018).

[220] M. Kilgour and D. Segal, The Journal of Physical Chemistry C **119**, 25291 (2015).

[221] M. Kilgour and D. Segal, The Journal of Chemical Physics **144**, 124107 (2016).

[222] F. Caruso, A. Crespi, A. G. Ciriolo, F. Sciarrino, and R. Osellame, Nature Communications **7**, 11682 (2016).

[223] E. Zerah-Harush and Y. Dubi, Phys. Rev. Research **2**, 023294 (2020).

[224] M. Büttiker, Phys. Rev. B **33**, 3020 (1986).

[225] C. J. Cattena, R. A. Bustos-Marún, and H. M. Pastawski, Phys. Rev. B **82**, 144201 (2010).

[226] J. L. D'Amato and H. M. Pastawski, Phys. Rev. B **41**, 7411 (1990).

[227] H. Kim, M. Kilgour, and D. Segal, The Journal of Physical Chemistry C **120**, 23951 (2016).

[228] P. A. Jacquet and C.-A. Pillet, Phys. Rev. B **85**, 125120 (2012).

[229] R. Korol, M. Kilgour, and D. Segal, Computer Physics Communications **224**, 396 (2018).

[230] J. J. Mendoza-Arenas, T. Grujic, D. Jaksch, and S. R. Clark, Phys. Rev. B **87**, 235130 (2013).

[231] M. Žnidarič, Physical Review B **105**, 045140 (2022).

[232] Y. Yoo, J. Lee, and B. Swingle, Phys. Rev. B **102**, 195142 (2020).

[233] T. Cookmeyer, J. Motruk, and J. E. Moore, Phys. Rev. B **101**, 174203 (2020).

[234] M. Žnidarič and M. Ljubotina, Proceedings of the National Academy of Sciences **115**, 4595 (2018).

[235] M. Lee, T. R. Look, S. P. Lim, and D. N. Sheng, Physical Review B **96**, 075146 (2017).

[236] Y. B. Lev, D. M. Kennes, C. Klöckner, D. R. Reichman, and C. Karrasch, EPL (Europhysics Letters) **119**, 37003 (2017).

[237] P. Naldesi, E. Ercolessi, and T. Roscilde, SciPost Phys. **1**, 010 (2016).

[238] V. Mastropietro, Phys. Rev. Lett. **115**, 180401 (2015).

[239] S. Iyer, V. Oganesyan, G. Refael, and D. A. Huse, Phys. Rev. B **87**, 134202 (2013).

[240] M. Tezuka and A. M. García-García, Phys. Rev. A **85**, 031602 (2012).

[241] J. X. Zhong and R. Mosseri, Journal of Physics: Condensed Matter **7**, 8383 (1995).

[242] C. Chiaracane, F. Pietracaprina, A. Purkayastha, and J. Goold, Phys. Rev. B **103**, 184205 (2021).

[243] J. Sutradhar, S. Mukerjee, R. Pandit, and S. Banerjee, Phys. Rev. B **99**, 224204 (2019).

[244] D. J. Luitz, N. Laflorencie, and F. Alet, Journal of Statistical Mechanics: Theory and Experiment **2014**, P08007 (2014).

[245] D. J. Luitz, N. Laflorencie, and F. Alet, Phys. Rev. B **91**, 081103 (2015).

[246] D. J. Luitz, F. Alet, and N. Laflorencie, Phys. Rev. Lett. **112**, 057203 (2014).

[247] F. Pietracaprina, N. Macé, D. J. Luitz, and F. Alet, SciPost Phys. **5**, 45 (2018).

[248] X. Zotos, F. Naef, and P. Prelovšek, Physical Review B **55**, 11029 (1997).

[249] H. Bethe, Zeitschrift f˘’r Physik **71**, 205 (1931).

[250] B. S. Shastry and B. Sutherland, Physical Review Letters **65**, 243 (1990).

[251] J. Sirker, R. G. Pereira, and I. Affleck, Physical Review B **83**, 035115 (2011).

[252] T. Prosen, Physical Review Letters **106**, 217206 (2011).

[253] M. Žnidarič, Phys. Rev. Lett. **106**, 220601 (2011).

[254] S. Gopalakrishnan and R. Vasseur, Physical Review Letters **122**, 127202 (2019).

[255] E. Ilievski, J. D. Nardis, M. Medenjak, and T. Prosen, Physical Review Letters **121**, 230602 (2018).

[256] U. Agrawal, S. Gopalakrishnan, R. Vasseur, and B. Ware, Physical Review B **101**, 224415 (2020).

[257] M. Ljubotina, M. Žnidarič, and T. Prosen, Nature Communications **8** (2017), 10.1038/ncomms16117.

[258] A. Scheie, N. E. Sherman, M. Dupont, S. E. Nagler, M. B. Stone, G. E. Granroth, J. E. Moore, and D. A. Tennant, Nature Physics **17**, 726 (2021).

[259] D. Wei, A. Rubio-Abadal, B. Ye, F. Machado, J. Kemp, K. Srakaew, S. Hollerith, J. Rui, S. Gopalakrishnan, N. Y. Yao, I. Bloch, and J. Zeiher, Science **376**, 716 (2022).

[260] N. Keenan, N. Robertson, T. Murphy, S. Zhuk, and J. Goold, "Evidence of kardar-parisi-zhang scaling on a digital quantum simulator," (2022).

[261] R. Blatt and C. F. Roos, Nature Physics **8**, 277 (2012).

[262] R. Schirhagl, K. Chang, M. Loretz, and C. L. Degen, Annual Review of Physical Chemistry **65**, 83 (2014).

[263] M. A. Nichols, L. W. Cheuk, M. Okan, T. R. Hartke, E. Mendez, T. Senthil, E. Khatami, H. Zhang, and M. W. Zwierlein, Science **363**, 383 (2019).

[264] L. F. Santos, Journal of Physics A: Mathematical and General **37**, 4723 (2004).

[265] M. Brenes, E. Mascarenhas, M. Rigol, and J. Goold, Physical Review B **98**, 235128 (2018).

[266] J. Eisert, M. Friesdorf, and C. Gogolin, Nature Physics **11**, 124 (2015).

[267] J. von Neumann, The European Physical Journal H **35**, 201 (2010).

[268] M. V. Berry and M. Tabor, Proceedings of the Royal Society of London. A. Mathematical and Physical Sciences **356**, 375 (1977).

[269] J. M. Deutsch, Physical Review A **43**, 2046 (1991).

[270] M. Srednicki, Journal of Physics A: Mathematical and General **32**, 1163 (1999).

[271] L. Vidmar and M. Rigol, Journal of Statistical Mechanics: Theory and Experiment **2016**, 064007 (2016).

[272] M. Brenes, S. Pappalardi, J. Goold, and A. Silva, Physical Review Letters **124**, 040605 (2020).

[273] A. Khodja, R. Steinigeweg, and J. Gemmer, Physical Review E **91**, 012120 (2015).

[274] R. Steinigeweg, J. Herbrych, and P. Prelovšek, Physical Review E **87**, 012118 (2013).

[275] R. Mondaini, K. R. Fratus, M. Srednicki, and M. Rigol, Physical Review E **93**, 032104 (2016).

[276] R. Mondaini and M. Rigol, Physical Review E **96**, 012157 (2017).

[277] M. Rigol, V. Dunjko, and M. Olshanii, Nature **452**, 854 (2008).

[278] L. F. Santos and M. Rigol, Physical Review E **82**, 031130 (2010).

[279] H. Kim, T. N. Ikeda, and D. A. Huse, Physical Review E **90**, 052105 (2014).

[280] W. Beugeling, R. Moessner, and M. Haque, Physical Review E **91**, 012144 (2015).

[281] L. F. Santos and A. Mitra, Physical Review E **84**, 016206 (2011).

[282] E. J. Torres-Herrera and L. F. Santos, Physical Review E **89**, 062110 (2014).

[283] M. Brenes, J. Goold, and M. Rigol, Physical Review B **102**, 075127 (2020).

[284] K. Mallayya, M. Rigol, and W. D. Roeck, Physical Review X **9**, 021027 (2019).

[285] I. Bloch, J. Dalibard, and W. Zwerger, Reviews of Modern Physics **80**, 885 (2008).

[286] P. N. Jepsen, W. W. Ho, J. Amato-Grill, I. Dimitrova, E. Demler, and W. Ketterle, Physical Review X **11**, 041054 (2021).

[287] P. N. Jepsen, Y. K. E. Lee, H. Lin, I. Dimitrova, Y. Margalit, W. W. Ho, and W. Ketterle, Nature Physics **18**, 899 (2022).

[288] D. J. Luitz and Y. B. Lev, Annalen der Physik **529**, 1600350 (2017).

[289] D. Sels and A. Polkovnikov, Physical Review E **104**, 054105 (2021).

[290] V. K. Varma, S. Pilati, and V. E. Kravtsov, Phys. Rev. B **94**, 214204 (2016).

[291] F. Evers and A. D. Mirlin, Reviews of Modern Physics **80**, 1355 (2008).

[292] M. Saha, B. P. Venkatesh, and B. K. Agarwalla, Physical Review B **105**, 224204 (2022).

[293] K. Singh, K. Saha, S. A. Parameswaran, and D. M. Weld, Physical Review A **92**, 063426 (2015).

[294] N. Macé, F. Alet, and N. Laflorencie, Phys. Rev. Lett. **123**, 180601 (2019).

[295] J. J. Mendoza-Arenas, M. Žnidarič, V. K. Varma, J. Goold, S. R. Clark, and A. Scardicchio, Phys. Rev. B **99**, 094435 (2019).

[296] M. Brenes, J. J. Mendoza-Arenas, A. Purkayastha, M. T. Mitchison, S. R. Clark, and J. Goold, Phys. Rev. X **10**, 031040 (2020).

[297] J. Vidal, D. Mouhanna, and T. Giamarchi, Phys. Rev. B **65**, 014201 (2001).

Appendices

A Spread of wavepacket in the noninteracting system

In this appendix, we show how the spread of correlation defined in Eq. (2.120) reduces to the mean square displacement of a initially localised wavepacket from Eq. (2.126) for one-dimensional non-interacting systems. We consider then a non-interacting tight-binding Hamiltonian $\hat{H}_S$ as in Eq. (2.12), which can be written in matrix form $\mathbf{H}_S$ on the lattice basis as done in Eq. (2.13). We diagonalise the Hamiltonian,

$$\mathbf{\Phi}^T \mathbf{H}_S \mathbf{\Phi} = \boldsymbol{D}, \qquad \boldsymbol{D} = \mathrm{diag}\{E_\ell\}_{\ell=1}^N, \tag{A.1}$$

where the single-particle eigenvectors are found from the columns of the matrix $\mathbf{\Phi}$, and the eigenvalues from $\{E_\ell\}_\ell$. In the new basis, the Hamiltonian reads,

$$\hat{H}_S = \sum_{\ell=1}^{N} E_\ell \hat{A}_\ell^\dagger \hat{A}_\ell, \tag{A.2}$$

where $\hat{A}_\ell = \sum_{p=1}^N \Phi_{p\ell} \hat{a}_p$ are the fermionic annihilation operators in the eigenbasis. The two time density correlation at finite temperature β and chemical potential μ can be simplified as follows

$$\begin{aligned} C_{pq}(t) &= \langle \hat{n}_p(t) \hat{n}_q \rangle_{eq} - \langle \hat{n}_p \rangle_{eq} \langle \hat{n}_q \rangle_{eq} \\ &= \sum_{\ell,\ell'=1}^{N} \Phi_{\ell p} \Phi_{\ell q} \Phi_{\ell' p} \Phi_{\ell' q} e^{it(E_\ell - E_{\ell'})/\hbar} [1 - f(E_{\ell'})] f(E_\ell), \end{aligned} \tag{A.3}$$

after applying the Wick's theorem,

$$\langle \hat{a}_p^\dagger(t_p)\hat{a}_q(t_q)\hat{a}_m^\dagger(t_m)\hat{a}_n(t_n)\rangle = \langle \hat{a}_p^\dagger(t_p)\hat{a}_q(t_q)\rangle \langle \hat{a}_m^\dagger(t_m)\hat{a}_n(t_n)\rangle + \langle \hat{a}_p^\dagger(t_p)\hat{a}_n(t_n)\rangle \langle \hat{a}_q(t_q)\hat{a}_m^\dagger(t_m)\rangle , \tag{A.4}$$

and the following relations

$$\begin{aligned}\langle \hat{a}_p^\dagger(t_p)\hat{a}_q(t_q)\rangle &= \sum_{\ell=1}^{N} \Phi_{\ell p}\Phi_{\ell q} e^{iE_\ell(t_p-t_q)/\hbar} f(E_\ell) \\ \langle \hat{a}_p(t_p)\hat{a}_q^\dagger(t_q)\rangle &= \sum_{\nu=1}^{N} \Phi_{\nu p}\Phi_{\nu q} e^{iE_\ell(t_p-t_q)/\hbar}(1-f(E_\ell))\end{aligned} \tag{A.5}$$

with $f(E) = \{1+\exp[\beta(E-\mu)]\}^{-1}$ the Fermi-Dirac distribution. Now, we take the infinite temperature limit $\beta \to 0$ of Eq. (A.3), and shift the labels to consider the correlation between the middle of the chain $q = N/2$ and the $p = l + N/2$ as in Eq. (2.121),

$$\begin{aligned}C_l(t) &= \frac{1}{4}\sum_{\ell,\ell'=1}^{N} \Phi_{\ell l}\Phi_{\ell N/2}\Phi_{\ell' l}\Phi_{\ell' N/2} e^{it(E_\ell - E_{\ell'})/\hbar} \\ &= \frac{1}{4}\Big(\sum_{\ell'=1}^{N} \Phi_{\ell' l}\Phi_{\ell' N/2} e^{-itE_{\ell'}/\hbar}\Big)\Big(\sum_{\ell=1}^{N} \Phi_{\ell l}\Phi_{\nu N/2} e^{itE_\ell/\hbar}\Big) \\ &= \frac{1}{4}|\Psi_l(t)|^2,\end{aligned} \tag{A.6}$$

where

$$\Psi_l(t) = \sum_{\ell=1}^{N} \Phi_{\ell l}\Phi_{\ell N/2} e^{-itE_\ell/\hbar}. \tag{A.7}$$

The dynamics of each $\Psi_l(t)$ corresponds to evolution according to

$$i\frac{d\Psi_l(t)}{dt} = \sum_{r=1}^{N} [\mathbf{H}_S]_{rp}\Psi_p(t), \tag{A.8}$$

starting from the initial condition $\Psi_l(0) = \delta_{lN/2}$. Thus, from Eq. (A.6) we derive that the two time density correlation at infinite temperature we use to classify transport in the interacting system is directly proportional to $|\Psi_l(t)|^2$ in single-particle systems:

$$|\Psi_l(t)|^2 = 4C_l(t). \tag{A.9}$$

Physically, $|\Psi_l(t)|^2$ gives the probability of finding a particle at site p, after initializing the system with a single particle located at site $N/2$. From above, and Eq.Eq. (2.120), we see that, for a noninteracting system, $\Sigma^2(t) = \Delta x^2(t)$. But unlike $\Delta x^2(t)$, $\Sigma^2(t)$ is well defined also in the presence of interactions.

B Density correlations in the half-filled sector

The quantum dynamical typicality (QDT) approach for the density-density correlation reviewed in Sec. 2.2.4 does not make use of the fact that the quantum spin Hamiltonian under study is number conserving. For a large enough number conserving system, the biggest contribution to the density-density correlation in Eq. (2.147) comes from the half-filled sector. It is plausible that in such case, one can completely restrict the calculation to the half-filled sector, thus saving computational resources and pushing forward the system size. In complete analogy to Sec. 2.2.4, we define a typical state in the half-filled subsector

$$|\psi^s\rangle = \frac{1}{D^s}\sum_{k=1}^{D^s} c_k\,|\phi_k^s\rangle\,, \qquad D^s = \frac{N!}{(N/2)!(N/2)!}, \tag{B.1}$$

where $\{|\phi_k^s\rangle\}_{k=1}^{D^s}$ is an orthonormal basis in the half-filled sector. The new normalization constant C^s in

$$|\tilde{\psi}_{N/2}^s\rangle = \frac{1}{\sqrt{C^s}}\,|\psi_{N/2}^s\rangle\,, \qquad |\psi_{N/2}^s\rangle = \hat{n}_{N/2}\,|\psi^s\rangle\,, \tag{B.2}$$

is given by

$$\begin{aligned} C^s &= \langle\psi_{N/2}^s|\psi_{N/2}^s\rangle = \langle\psi^s|\hat{n}_{N/2}|\psi^s\rangle \approx \overline{\langle\psi^s|\hat{n}_{N/2}|\psi^s\rangle} \\ &= \frac{Tr[\hat{n}_{N/2}]}{D^s} = \frac{(N-1)!}{\frac{N-1}{2}!\frac{N-1}{2}!}\frac{\frac{N}{2}!\frac{N}{2}!}{N!} = \frac{1}{2}. \end{aligned} \tag{B.3}$$

As before, we have

$$|\tilde{\psi}_{N/2}^s\rangle \approx \sqrt{2}\,|\psi_{N/2}^s\rangle\,. \tag{B.4}$$

However, the background occupation of sites $q \neq N/2$ is now less than $1/2$, as it is possible to notice by reproducing the result of Eq. (2.145) in the half-filled sector:

$$\begin{aligned} n_r^s(0) &= \langle \tilde{\psi}^s_{N/2} | \hat{n}_r | \tilde{\psi}^s_{N/2} \rangle \approx 2 \langle \psi^s_{N/2} | \hat{n}_r | \psi^s_{N/2} \rangle \\ &= 2 \langle \psi^s | \hat{n}_r \hat{n}_{N/2} | \psi^s \rangle \approx 2 \overline{\langle \psi^s | \hat{n}_r \hat{n}_{N/2} | \psi^s \rangle} \\ &= 2 \frac{Tr[\hat{n}_r \hat{n}_{N/2}]}{D^s} = \frac{(N-2)!}{\frac{N-2}{2}! \frac{N}{2}!} \frac{\frac{N}{2}! \frac{N}{2}!}{N!} \\ &= \frac{1}{2} \Big(1 - \frac{1}{N-1} \Big). \end{aligned} \tag{B.5}$$

Finally, in analogy with Eq. (2.147), we are able to define

$$\begin{aligned} C_l^s(t) &= \frac{1}{2} (n_l^s(t) - n_l^s(0)), \qquad l \neq N/2 \\ &\approx \frac{1}{2} \Big[n_l^s(t) - \frac{1}{2} \Big(1 - \frac{1}{N-1} \Big) \Big], \end{aligned} \tag{B.6}$$

where $n_l^s(t)$ is the expectation value of the operator $\hat{n}_l$ at time t, starting from the initial state given by $|\tilde{\psi}^s_{N/2}\rangle$. For a large enough system, we expect $C_l^s(t) \approx C_l(t)$. By directly comparing simulations performed for a short time interval on a chain of size $N = 20$ both in the total Hilbert space and in the largest sector at half-filling, we have confirmed our conjecture.